AN ABSTRACT OF THE THESIS OF

Ayal Anis for the degree of Doctor of Philosophy in Oceanography presented on December 13, 1993.

Title: Mixing, Energetics and Scaling in the Upper Oceanic Boundary Layer.

Redacted for Privacy

Abstract approved: _____

James N. Moum

The upper oceanic boundary layer (OBL) is the interface between the atmosphere and the ocean. Understanding of the physical processes in the OBL is of utmost importance, especially for accurate parametrization of turbulence fluxes in models. In order to shed new light on the physics of the OBL the approach taken in this study was to examine an extensive observational data set, collected under different atmospheric and sea state conditions.

During quasisteady nighttime convective forcing conditions the mean structure of θ was superadiabatic in the upper 20-40% of the OBL with a well mixed layer (ML) below. This structure of θ was steady throughout each night of the experiment. Current shear in the ML was smaller or equal to the detection limit of the instrument, however, a large increase in shear was observed near the base of the ML. In contrast to the nighttime OBL, the daytime OBL was stratified and had a significant shear.

Turbulence kinetic energy (TKE) dissipation rate, ϵ, followed convective scaling (i.e. $\epsilon \sim J_b^0$) in the ML. Although ϵ near the surface followed in some

cases the expected constant stress layer scaling, in a large number of cases enhanced dissipation rates were observed. In these cases ϵ followed roughly an exponential decay with depth.

New inferences about the physics of the OBL were made from the observational results. The differences between daytime and nighttime suggest that mixing of heat and momentum by the mechanically (wind) produced turbulence is relatively inefficient and a "slab" model may be an inadequate representation of the OBL. In contrast, during nighttime, mixing is much more efficient and a "slab" model appears to be adequate.

Two new and independent estimates of the vertical heat flux profile during nighttime convective forcing conditions were made. Both estimates are consistent and suggest that the nondimensional heat flux has a linear depth dependence of the form $1 + a_h(z/D)$, where z is the depth, D is the ML depth, and a_h is a constant with a mean value of 1.13.

Energy budget considerations in the diurnally deepening ML show that wind related processes (e.g. surface wind stress, waves, Langmuir cells) need to be taken inot account in addition to convection. A simple parameterization in terms of the wind power, E_{10}, suggests that about 4% of E_{10} enter the OBL. Of this roughly 85% ($\sim 0.034E_{10}$) is dissipated, while the remaining 15% ($\sim 0.006E_{10}$) is available for mixing.

Two new wave-turbulence interaction models are proposed to explain the enhanced near surface dissipation rates, leading to two scaling schemes for ϵ. The first mechanism is downward transport by swell of high levels of turbulence created by wave breaking at the surface. In the second mechanism energy is drawn from the wave field to the mean flow via wave stresses, and then drawn from the mean flow via the turbulence production term.

Mixing, Energetics and Scaling in the Upper Oceanic Boundary Layer

by

Ayal Anis

A THESIS

submitted to

Oregon State University

in partial fulfillment of

the requirements for the

degree of

Doctor of Philosophy

Completed December 13, 1993

Commencement June 1994

APPROVED:

Redacted for Privacy

Professor of Oceanic and Atmospheric Sciences in charge of major

Redacted for Privacy

Dean of College of Oceanic and Atmospheric Sciences

Redacted for Privacy

Dean of Graduate School

Date thesis is presented December 13, 1993

Typed by Ayal Anis

ACKNOWLEDGMENTS

First and foremost I thank Jim Moum who provided excellent guidance, advice, suggestions and personal support and encouragement along the 6+ years I have spent at OSU. He was especially helpful when I felt I was grinding water (i.e. beating a dead horse). Knowingly or not he has also introduced me to biking, which sometimes overwhelmed me, by providing his older 10 speed (it will finnaly return to its legal owner, I promise). I am also thankful to Jeffrey Barnes, Roland deSzoeke, Murray Levine, Clayton Paulson, Edward Taylor, and Phillip Whanger for willingly being members of my committee. Their advice and availability whenever needed are truely acknowledged.

Hydrographic data for this study was collected almost exclusively with the Chameleon and the older version, the Rapid Sampling Vertical Profiler (RSVP). The western avenue techno gang is responsible for the success of this part and their help all along the way is greatfully aknowledged (oh, gone are those long nights of calibrations). Members of this faithful team are Jose Baer, Ray Kreth, Ed Lewellyn, Mike Neeley-brown, Ramesh, and Rob Butler. Thanks guys. I am also grateful to the captain and crew of the R/V *Wecoma* for providing help during our exepriments, and to Ann Gargett and the captain and crew of the CSS *Vector* who allowed us shiptime in the midst of one of their own experiments.

I am grateful to many other faculty members who provided professional and other help. I am especially indebted to Richard Dewey, Tom Dillon, Dave Hebert, Bob Miller, Laurie Padman, and Bill Smyth for helpful discussions.

Dave, Laurie and Bill willingly suffered through some early versions of papers presented in this thesis and provided helpful comments and suggestions for improvements.

Special thanks are due to the Gerson Meerbaum Foundation for Oceanography, the Hebrew University of Jerusalem , Israel, for providing two years of very much needed financial support.

Dave Reinert prepared figures for publications, and while he may not know it he will get more of those. Thanks to Dottore (a.k.a. Russ Desiderio) I was introduced to the Blues, which since then is one of my favorite types of music. Thanks also for the rides to the aquatic center when Dixon recreation center closed for the breaks.

All the students whom I have interacted with, starting at the early days when offices were in Ballard Hall, were friendly, helpful and supportive. Everyone – Vassilis Zervakis (excellent Greek food, way better than any of the Greek restaurants in S.F.), Fred Bahr (ah, that "scenery" in the Bahamas), Julie McClean (who unsatisfied with the slow pace here left in order to graduate ahead of us by half a year), Terry Sullivan, Chaojiao Sun, Peter Zavialov (all three being officemates during one period or another), Robin Tokmakian, Rodrigo Nũnez, Hongbo Qi, Ed Zaron, Jorge Mesias, Shusheng Luan, Donna Witter, Alberto Mestas-Nũnez – thank you all.

The radio stations KLCC and KBVR kept me from closing my eyes and performing some serious face plants into the keyboard during the last months. Thanks specifically to Marcelino Suzuki, the Raggea show D. J., and to the weekend Blues D. Js. for playing great stuff and also providing tickets to the movies almost every week during the last couple of months. Dixon recreation center, with it new aquatic facilities, deserves a special thank

you since it provided refreshing lunch (and dinner) breaks. Fine Corvallis establishments, e.g. the Beanery, the New Morning Bakery, Squirrel's, The Peacock, Woodstock's, Bomb's Away, helped by providing a fun atmosphere.

The most important support, and lots of it, did come from my wife, Ruthy, and kids, Idan, Yoed and Dor. You were unbelievably patient while I was going about my business (or should I say science). However, I regret spending too little time with you, much less than I would have liked to. I hope, and believe, that this aspect may soon improve. I am also thankful to my parents and parents-in-law for their all around help and I apologize for taking the grandchildren away for so long.

TABLE OF CONTENTS

LIST OF FIGURES

LIST OF FIGURES (continued)

LIST OF FIGURES (continued)

LIST OF FIGURES (continued)

LIST OF TABLES

LIST OF TABLES (continued)

MIXING, ENERGETICS AND SCALING IN THE UPPER OCEANIC BOUNDARY LAYER

I. GENERAL INTRODUCTION

The upper ocean boundary layer (OBL) is the part of the ocean which is directly influenced by surface forcing. Being the interface through which heat and momentum are exchanged between the atmosphere and the ocean, the OBL is a key player in both oceanic and atmospheric models. Therefore, only a complete understanding of the physics in the OBL will enable one to forecast accurately large scale oceanic and atmospheric phenomena. A simple approach taken by many oceanic models is to assume that the OBL mimics the atmospheric boundary layer (ABL) over land. However, recent evidence suggests that in many cases the OBL is not simply an upside down version of the ABL. This is not surprising - one might expect that the very fact that the ocean has a free surface will result in differences from flows near solid boundaries. For example, wind blowing over the water surface induces surface gravity waves and Langmuir circulations. Both mechanisms are unique to the OBL and can greatly enhance air-sea fluxes and mixing in the OBL.

The aim of this study to shed light on mixing processes and energetics in the OBL. For this purpose field studies were conducted under a variety of atmospheric and sea state conditions. As a result an extensive data set was collected by intensively profiling the OBL with a vertical microstructure profiler (RSVP; Caldwell et al. 1985). The RSVP provides detailed information on temperature and conductivity and microscale velocity fluctuations. From

these quantities a picture of the hydrodynamic and turbulence fields in the OBL can be inferred and provide the necessary experimental background.

The thesis presents four separate studies which are related through the objective of understanding the physics in the OBL. Chapter II focuses on the deepening phase of the diurnal mixed layer (ML). In chapter III the superadiabatic ocean surface layer (OSL) of the convective OBL is discussed. Chapter IV investigates the vertical structure of the OBL during convection and the implications on the vertical heat flux and entrainment rates. Prospects for scaling turbulence kinetic energy (TKE) dissipation rate, $\epsilon(z)$, in the OBL during different atmospheric and sea state conditions are discussed in chapter V. A summary and general conclusions are presented in chapter VI.

Chapter II, titled "Diurnal Mixed Layer Deepening", examines ML deepening during nighttime convective conditions. Theoretically predicted deepening, assuming convective forcing alone, underestimates the observed deepening. Similarly, an estimate of the energy budget in the ML, including TKE dissipation, results in an apparent imbalance if convection is the sole forcing mechanism. Surface wind stress, surface waves, and Langmuir circulations are discussed and shown to be consistent with the additional energy required to close the budget. If these processes, which are all wind related, can be simply parameterized in terms of E_{10}, the wind energy flux at 10 m height, then approximately 4% of E_{10} is required to account for potential energy increases and dissipation losses during deepening. Of this, about 85% ($\sim 0.034E_{10}$) is effectively dissipated, while the remaining 15%

($\sim 0.006E_{10}$) is available for mixing. Reassessment of ML deepening, driven by combined wind and convective forcing, results in a relatively good agreement with the observations.

In chapter III, titled "The Superadiabatic Surface Layer of the Ocean During Convection", a clear identification of the relatively weak superadiabatic potential temperature gradient in the OSL during convection is made. The superadiabatic gradient, with a mean value of -1.8×10^{-4} K m^{-1}, is shown to be a consistent feature of the convective boundary layer persisting throughout each night of the experiment. A comparison with the atmospheric surface layer (ASL) during convection is made and suggests that although the temperature structure of the OSL qualitatively mimics that of the ASL the dynamics do not (this is explored further in chapter V).

Chapter IV, titled "Prescriptions for Heat Flux and Entrainment Rates in the Upper Ocean During Convection" is a detailed investigation of the upper ocean during convection. A major result of this study indicates that although a "slab" type model may be an adequate representation of the convective OBL it may be inadequate for a wind stress driven OBL. Two independent estimates of the vertical heat flux profile in the convective OBL are made. Both estimates are consistent and suggest that the nondimensional vertical heat flux has a linear depth dependence of the form $1 + a_h(z/D)$, where z is the depth, D is the ML depth, and a_h is a constant with a mean value of 1.13. An estimate of the entrainment rate, derived from observed quantities, results in $\sim 1 \times 10^{-5}$ m s^{-1} and is within a factor of 2 of estimates derived from alternative formulations.

In chapter V, titled "Scaling $\epsilon(z)$ near the Surface of the Ocean", the OBL, subjected to a variety of atmospheric and sea conditions, is examined.

The rate of TKE dissipation, ϵ, is found to exhibit a range of behaviours under the different forcing conditions. In some experiments, in the vicinity of the ocean's surface, ϵ is closely balanced by the wind stress production of TKE. In contrast, a relatively large number of cases reveal enhanced dissipation rates with ϵ decaying exponentially with depth. In these instances the simple scaling laws predicted for turbulence near a solid surface severely underestimate turbulence mixing near the ocean surface. In an attempt to explain the high TKE dissipation rates it is suggested that surface waves are important. Two different mechanisms of wave-turbulence interactions are proposed to explain the behaviour of ϵ near the surface and lead to two scaling schemes. The first mechanism requires high levels of TKE, created by wave breaking at the surface, to be transported downwards away from the surface by the motion of the swell. This transport is then locally balanced by ϵ. In the second mechanism energy from the wave field is drawn to the mean flow, via wave stresses, and then drawn from the mean flow by the turbulence production term, which is balanced by ϵ.

II. DIURNAL MIXED LAYER DEEPENING

Abstract

Intensive profiling of the oceanic boundary layer reveals that deepening of the diurnal mixed layer (ML) is initiated each night by convective conditions. However, predictions of the time dependent ML depth, $D(t)$, from consideration of convective forcing alone underestimate the observed ML depth. Similarly, consideration of the energy budget in the ML, including turbulence kinetic energy dissipation, results in an apparent imbalance if convection is assumed to be the sole forcing mechanism. Although advective effects cannot be ruled out it is unnecessary to invoke unresolved advective processes to account for the imbalance. Wind related processes, such as surface wind stress, surface waves, and Langmuir circulations, are suggested to balance the energy budget, and are shown to be consistent with the additional energy required. Approximately 4% of E_{10}, the wind energy flux at 10 m height, is required to account for potential energy increases and dissipation losses during deepening. Of this, roughly 85% ($\sim 0.034E_{10}$) is effectively dissipated, while the remaining 15% ($\sim 0.006E_{10}$) is available for mixing. By comparison, Richman and Garrett (1979), using field and laboratory experiments and a model for the momentum and energy transfer by the wind to the ocean, suggested an input to the ocean of $4-9\%$ of E_{10} (including the energy that goes into wave breaking). A simple formulation of $D(t)$, including both convective and wind forcing, yields good agreement between $D(t)$ and the observed ML depth if about half of the surface buoyancy flux due to convection and about $0.005 - 0.01E_{10}$ are available for mixing.

II.1. Introduction

Mixing and restratification in the upper ocean boundary layer (OBL) are the direct results of surface forcing, namely the wind energy and heating or cooling. Early and widely quoted laboratory studies by Kato and Phillips (1969) indicated that turbulence resulting from a mechanically applied surface stress, τ_0, caused entrainment of denser fluid into the developing mixed layer (ML). The rate of ML deepening was found to be $\propto u_*^3$ ($u_* \equiv \sqrt{(\tau_0/\rho)}$ is the friction velocity), with about 0.0015 of the energy flux supplied by the surface stress converted into potential energy (PE) of the deepening ML. For comparison, studies of wind mixing in the ocean show a range of values between 0.0012 (Denman and Miyake 1973) and 0.01 (Turner 1969) for the fraction of wind energy flux, $E_{10} = \tau_0 U_{10}$ (U_{10} is the wind speed at 10 m height), converted into PE of the ML.

In addition to wind mixing, cooling of the ocean's surface may lead to mixing resulting from convectively generated turbulence. Most of our knowledge pertaining to convective MLs comes from laboratory and atmospheric boundary layer (ABL) experiments. These studies have shown that buoyant plumes, generated near the surface due to heating, rise through the ML overshooting into the stable inversion layer (e.g. Deardorff et al. 1969). As a result of the overshooting, fluid above the inversion is entrained into the ML, effectively causing the ML to grow. ML growth in the ABL (e.g. Stull 1988) is often characterized by a slow initial growth phase of about 2 hours in the early morning during which the strongly stably stratified nocturnal layer is burned off. Then, rapid growth of the ML is observed and its height may rise at rates up to 1 km per 15 minutes. At the end of this phase the ML height remains roughly constant throughout most of the

afternoon. At sunset, when turbulence production by buoyancy ceases, the ML depth decreases and the stable nocturnal boundary layer develops.

Convectively driven MLs in the ocean are observed during nighttime (Shay and Gregg 1986; Lombardo and Gregg 1989; Anis and Moum 1992 [chapter III], 1993b [chapter IV]) and during cold air outbreaks (e.g. Shay and Gregg 1984a, 1984b, 1986, for convection in a warm-core Gulf Stream ring; Anati and Stommel 1970, Schott and Leaman 1991, and Leaman and Schott 1991, for deep convection in the Mediterranean; Clarke and Gascard 1983, and Gascard and Clarke 1983, for deep convection in the Labrador sea). An additional form of naturally occuring convection is in leads in pack ice (Morison et al. 1992). In this case destabilizing buoayancy fluxes result from dense surface water formation due to salt rejection when the surface freezes.

In contrast to wind driven MLs, convectively driven MLs have been shown to be the only truly well-mixed layers and therefore unable to support a significant current shear (André and Lacarrère 1985; Anis and Moum 1993b [chapter IV]). Compared to studies of convective MLs in the laboratory and ABL, detailed studies of the deepening phase of convective oceanic MLs have not been conducted due to the difficulties involved in oceanic measurements. However, a study by Lombardo and Gregg (1989) showed that the duration of the ML deepening phase (referred to by the authors as the entrainment stage) was between $4 - 16$ hours with an average of 9 hours. During the deepening phase turbulence kinetic energy (TKE) dissipation rate, ϵ, was lower than during the period when the ML depth was roughly steady (their

equilibrium stage). It was suggested that this is consistent with some of the energy released by convection going into PE of the ML and some into internal waves.

Observations indicate that a certain amount of preconditioning of the upper ocean is required for significant convective penetration into the OBL. Preconditioning or weakening of the near surface density gradients is achieved by cumulative mixing prior to the onset of convection. For example, preconditioning in the northwestern Mediterranean takes place in late fall and early winter as a result of the cold, dry and strong Mistral winds blowing out of the Rhône valley and the Tramontane winds from the Pyrenees. These winds rapidly cool and effectively remove the heat stored in the upper water layers, while also itensifying the cyclonic circulation in the near surface water (e.g. Clarke and Gascard 1983; Swallow and Caston 1973). This sets up conditions for deep convection in late winter (Clarke and Gascard 1983). The amount of preconditioning needed is not clear; however, an instructive example indicates the minimum temperature gradient not to be exceeded for convection to penetrate: for a convective nighttime ML driven by surface cooling of $\sim$ 200 W m^{-2} and reaching a depth of 50 m after 12 hours the initial stable temperature gradient better not exceed a couple mK per meter. Preconditioning in the case of a diurnal convective ML may be accomplished by either wind stress or surface wave driven turbulence, Langmuir circulation, or a combination of these. Both surface waves (Kitaigorodskii et al. 1983; Thorpe 1992; Anis and Moum 1993c [chapter V]) and Langmuir circulations (Weller and Price 1988) may affect a considerable part of the OBL.

However, the role of wind stress, surface waves, and Langmuir circulations evidently is not limited to preconditioning only, and it is possible

that these contribute to active mixing during convective ML deepening as well. Moreover, near surface turbulence generated by either wind stress of surface waves might be transported downward to the base of the ML by the sinking convective plumes. This may in turn lead to enhanced ML deepening by providing an effective way to communicate TKE from the surface to the base of the deepening ML. Support for the importance of wind related turbulence during nighttime convective conditions was furnished by the fact that scaling ϵ by a combination of convective and wind stress scalings seemed to work best while scaling by either of these alone was less successful (Lombardo and Gregg 1989). Observational evidence also suggests that Langmuir circulations occur less often when diurnal stratification is strongest (Smith et al. 1987).

It is the objective of this study to examine mixing and turbulence in the deepening nighttime convective OBL, as revealed by observations at an open ocean site in the Pacific Ocean. For this matter we have focused our attention specifically on the rate of ML deepening and on the energetics of the deepening ML. The basic result is that although deepening was initiated every night by convection resulting from sea surface cooling, it was too rapid to be accounted for solely by convection. Examination of the energy budget in the deepening ML revealed an apparent imbalance between the increase in PE and the available energy from the convectively generated dense fluid near the surface. The apparent imbalance was larger still when TKE dissipation was taken into account. From examination of a strongly convecting ML in a warm core ring, Gregg (1987) reported an apparent imbalance between the observed change in density and the net density flux across the ocean's surface. Observing that entrainment rates were too large to be consistent with $\bar{\epsilon}$ in

the convectively dominated part of the ML, Gregg concluded that either the change in PE was overestimated or convection was not the only process deepening the ML. Joyce and Stalcup (1985) reported a similar problem with the heat budget; to balance the heat budget for the same warm core ring they had to invoke a lateral heat flux in the upper ocean.

Since ML deepening in our experiment was observed to be initiated by the onset of convective conditions, advective effects are believed not to be a major contributor to ML deepening. Instead we show that wind related processes, such as surface wind stress, surface waves, and Langmuir circulations, are consistent with the additional energy required to close the budget and therefore need to be considered.

Experimental details are described briefly in section II.2 followed, in section II.3, by a description of the meteorological and oceanographic background conditions. The diurnal cycle and the vertical structure of the hydrodynamic field and ϵ in the OBL are described in section II.4. In section II.5 we consider the energetics in terms of the deepening ML and compare with atmospheric and laboratory studies and other oceanic experiments. Possible energy sources in the OBL, additional to convection, are discussed and mixing ratios, in terms of the energy flux from the wind, are suggested and compared with those from other studies in section II.6. A reassessment of ML deepening as a function of combined convective and wind forcing is made in section II.7. Discussion and conclusions are presented in section II.8.

II.2. Experimental details

As part of the Tropic Heat II experiment, a large set of oceanic microstructure data was collected from the R/V *Wecoma* while steaming south toward the equator (Park et al. 1987). A total of 1128 profiles were obtained along 140° W, between 17° and 6° N, while maintaining nearly continuous 24-hour a day profiling from March 13 to 20. The vertical profiles, to a depth of about 200 m, were made using the freely falling Rapid-Sampling Vertical Profiler (RSVP) (Caldwell et al. 1985). At the ship speed of about 2.5 m s^{-1}, and time interval of about 6-7 minutes between profiles, the horizontal separation between profiles was on the order of 1000 m.

The RSVP provided microscale measurements of temperature and conductivity (from which salinity, potential temperature, θ, and potential density, σ_θ, were computed) and microscale shear of two mutually perpendicular horizontal velocity components (from which $\epsilon(z)$ was computed using the isotropic relations $\epsilon = 7.5\nu\overline{(\partial u'/\partial z)^2}$ or $\epsilon = 7.5\nu\overline{(\partial v'/\partial z)^2}$, were ν is the kinematic viscosity and u' and v' are mutually perpendicular horizontal velocity perturbations; Tennekes and Lumley 1972). The vertical resolution is < 1 cm, temperature resolution is 0.5 mK, salinity resolution is 0.6×10^{-3} psu, σ_θ resolution is 4×10^{-4} kg m^{-3} and the noise level of $\epsilon(z)$ estimates is less than 1×10^{-9} m^2 s^{-3}. Measurements from *Wecoma*'s hull-mounted acoustic Doppler current profiler (ADCP) provided estimates of the horizontal current velocity components at depth intervals of 4 m (T. Chereskin, personal communication).

Continuous shipboard measurements of meteorological data complemented the hydrographic and turbulence measurements. These included wind velocity, air temperature and humidity, short and long-wave radiation and sea surface temperature and conductivity (kindly provided by C. A. Paulson and F. L. Bahr).

II.3. Meteorological and oceanographic background

II.3.1. Meteorological conditions

Moderate winds from the northeast prevailed throughout the experiment and 30 minute averages of wind speed ranged from 4.5 to 10.5 m s^{-1}. Daytime and nighttime averages were 7 to 9 m s^{-1} except for one day (day 3) with a lower average daytime wind speed of 5 m s^{-1}. The surface wind stress, $\tau_0 = \rho_a C_d {U_{10}}^2$, ($\rho_a$ is the air density, C_d is a drag coefficient dependent on wind speed and stability, and U_{10} is the wind speed at a height of 10 m ; Large and Pond 1981) varied between 0.03 and 0.17 Nm^{-2} (Fig. II.1a) while daytime and nighttime averages were between 0.07 and 0.12 Nm^{-2}, except for day 3 which had a lower average of 0.04 Nm^{-2} (Table II.1). Air temperature increased steadily from about 22 to 27 °C (Fig. II.1b), following the general heating trend of the sea surface temperature (SST; measured from the thermistor on the ship's ADCP). Although somewhat obscured by the general increase in air temperature, one can observe the diurnal cycle in the trace of the air-sea temperature difference. During the whole extent of the experiment the sea surface was cooler than the air with air-sea temperature differences varying between -0.1 and -2.8 °C (Fig. II.1b). Average air-sea temperature differences were generally larger in magnitude during nighttime compared to daytime (Table II.1).

The net upward heat flux from the surface of the ocean, J_q^0, is given by the sum of the fluxes of four individual processes

$$J_q^0 = J_q^{sw} + J_q^{lw} + J_q^s + J_q^e. \tag{1}$$

J_q^{sw}, the net shortwave radiation flux, was calculated from direct measurements of incoming solar radiation from which the reflected part was

subtracted assuming a value of 0.06 for the albedo (Payne 1972). The net longwave radiation, J_q^{lw}, was calculated from direct measurements of incoming infrared radiation and subtraction of the outgoing infrared radiation, estimated using Stefan-Boltzmann law with the temperature of seawater measured at 5 m depth and an emissivity value of 0.97. J_q^s and J_q^e, the sensible and latent heat fluxes respectively, were calculated from bulk aerodynamic equations using transfer coefficients corrected for atmospheric surface layer stability and wind speed (Large and Pond 1982).

The contribution of the sensible heat flux to J_q^0 varied between 0 to 30 Wm^{-2} (Fig. II.1c). Daytime averages were between 2 and 13 Wm^{-2}, while nighttime averages were slightly larger with values between 8 and 18 Wm^{-2} (mainly due to the larger air-sea temperature difference during nighttime). The net longwave radiation constituted a larger part of the net surface heat flux, varying between 6 and 75 Wm^{-2} (Fig. II.1c), with daytime and nighttime mean values of 18-52 Wm^{-2} and 16-35 Wm^{-2}, respectively. The main contributions to J_q^0, were from net shortwave radiation (during daytime) and from latent heat flux (during both daytime and nightime) as evidenced from the 30 minute averages of J_q^{sw}, J_q^e (Fig. II.1c) and J_q^0 (Fig. II.1d) and the daytime and nighttime mean values of these quantites (Table II.1). Daytime means of J_q^0, ranged from -230 to -585 Wm^{-2}, a factor of about 2.5, while during convective nighttime conditions J_q^0 varied only by about 25% with mean values between 166 and 212 Wm^{-2} (Table II.1).

The vertical turbulence buoyancy flux at the ocean surface, J_b^0, was calculated following Dorrestein's (1979) formulation

$$J_b^0 = \frac{-g}{\rho_w}\left[s\beta(P - \frac{J_q^e}{L_e}) - \frac{\alpha}{C_p}J_q^0 + \alpha\Delta T\ P\right], \qquad (2)$$

where g is the gravitational acceleration, ρ_w is the seawater density, s is

the salinity mass ratio ($0.034 - 0.035$), β is the haline contraction coefficient ($0.75-0.76$), P is the rate of precipitation, L_e is the latent heat of evaporation ($\sim 2.5 \times 10^6$ J kg^{-1}), α is the thermal expansion coefficient of seawater ($2.9-3.2\times10^{-4}$ K^{-1}), C_p is the specific heat of seawater at constant pressure ($\sim 4 \times 10^3$ J kg^{-1} K^{-1}), and ΔT is the temperature of precipitated water minus the SST. Because rainfall was negligible during the experiment, the terms in (2) involving precipitation were dropped, resulting in the following simplified formula

$$J_b^0 = \frac{g}{\rho_w}\left(s\beta\frac{J_q^e}{L_e} + \frac{\alpha}{C_p}J_q^0\right). \tag{3}$$

In the simplified form (3), the surface buoyancy flux has two contributions: the first accounts for the effect of salinity change in the surface layer due to evaporation and the second accounts for the heating/cooling of the sea surface. During a diurnal cycle J_b^0 varied between -4.7×10^{-7} (daytime) and 2.3×10^{-7} m^2 s^{-3} (nighttime) (Fig. II.1e). The salinity term, J_s^0, contributed only a small part of the total surface buoyancy flux (Fig. II.1e), and accounted for 5 to 10% of the daytime and nighttime average values of J_b^0 (Table II.1).

If TKE in the OBL is produced solely by wind stress and surface buoyancy flux, a useful length scale is the Monin-Obukhov length

$$L \equiv \frac{-u_*^3}{\kappa J_b^0}, \tag{4}$$

which is negative during convection ($u_* \equiv \tau_0/\rho_w$ is the ocean surface friction velocity and von Kármán's constant is $\kappa \simeq 0.4$). During convection, L defines the depth at which the wind stress and the surface buoyancy flux are of equal importance, such that for $z > L$ wind stress is the main TKE source, while for $z < L$ buoyancy is the main TKE source. Thirty-minute averages of L ranged between -4 and -24 m during nighttime, and nighttime averages

were between −10.6 and −17.5 m (Table II.1). Sea-state conditions were moderate throughout the experiment with swells with significant heights between 1.7 and 2.7 m and wind-waves with significant heights between 0.6 and 0.9 m (Table II.1).

II.3.2. Oceanographic conditions

During our experiment SST increased by about 4 °C, from 23 to 27 °C, (Fig. II.1b) and sea surface salinity (SSS; measured from the R/V *Wecoma* at 5 m depth) increased from about 34 to 35 psu (Fig. II.1f). The general trend of increase in SST and SSS, attributed to the southward passage of latitudes from 17°N to 6°N, is typical for the time of the year during which the experiment was carried out (mid March). This is evident from comparison of our data to Levitus' (1982) for the winter season (Figs. II.2b and II.2f) which repesents the mean values of SST and SSS for the months February, March and April. Although the observed increase in SST and SSS, from start to end of the experiment, was slightly larger than that of Levitus', they compensate each other such that σ_θ at the sea surface, calculated from either our or Levitus' data, show a similar net decrease from start to end (Fig. II.1f).

The observed SST and SSS were modulated by features with typical time scales on the order of a few hours (equivalent to a few tens of km in horizontal length scale) and amplitudes of $O(0.01 - 0.1$ °C) (Fig. II.1b) and $O(0.01 - 0.1$ psu) (Fig. II.1f), respectively. Two relatively sharp front-like features are evident in the SST signature at times 74.4 and 75.5 (Fig. II.1b). The first front, with a temperature increase of about 0.5 °C, was accompanied by a decrease in SSS of about 0.1 psu, resulting in a decrease in density of 0.2 kg m^{-3} (Fig. II.1f). The second temperature front (about

0.8 °C), although larger in magnitude than the first, was accompanied by a large increase in SSS of 0.5 psu, and hence resulted in a relatively smaller increase in density of 0.1 kg m^{-3} (Fig. II.1f). These front-like features could be traced at much larger depth; for example the contours plots (not shown) of σ_θ showed domelike shaped maxima at depths of about 50-60 m.

Inspection of the large scale vertical structure of the OBL revealed a relatively diffused seasonal pycnocline, at depths between 40-80 m, during the first two and half days of the experiment (from day 73.0 to day 75.5). However, during the remainder of the experiment (from day 75.5 to day 79.0) the pycnocline was relatively sharp and deepened gradually from about 60 to 100 m. Variability in the strength and depth of the pycnocline are most probably related to the large scale variability encountered while the ship was on her way south. Mean vertical density gradients near the top of the seasonal pycnocline were roughly between -0.05 and -0.15 kg m^{-4}, and resulted mainly from the temperature gradients with only a relatively small contribution from salinity gradients.

Estimates of zonal currents, in the upper 120 m, ranged from 0.0 to 0.45 m s^{-1} in magnitude and changed direction from a westward to an eastward flow at a latitude of about 11° N. This seems consistent with the meridional position of the transition from the westward flowing north equatorial current to the eastward flowing north equatorial countercurrent (e.g. Wyrtki and Kilonsky 1984). Meridional currents, flowing mostly northward, were generally smaller in magnitude (0.0 to 0.3 m s^{-1}) and interspersed with bands of southward flowing currents.

II.4. The diurnal cycle

The daytime phase, during which the ocean surface was heated by solar radiation, lasted between 7 and 8.5 hours. The average downward surface buoyancy flux was between -3.85 and -1.68×10^{-7} m^2 s^{-3} (Table II.1), and produced a relatively weak stable stratification in the OBL. Variability in J_b^0 during daytime was due to cloud coverage which reduced the amount of solar radiation reaching the ocean's surface. The effect of clouds (see the trace of J_q^{sw} in Fig. II.1c) was most pronounced on days 3, 5 and 6 when cloud coverage was between 75 to 100%. Day-to-day variability of mean values of τ_0, mostly due to changes in wind speed with temporal scales of a few hours (Fig. II.1a), was between 0.04 and 0.12 N m^{-2}.

During nighttime, heat loss from the surface, reaching a quasisteady state after a short transition period of about 2-3 hours, resulted in destabilizing convective conditions for 15.5-17 hours each night. During the quasisteady state of about 11.5-13 hours the variability in J_b^0 was small (Fig. II.1e) with nighttime mean values of J_b^0 of 1.35–1.65 $\times$ 10^{-7} m^2 s^{-3}. Winds with smaller night-to-night than day-to-day variability produced mean surface stresses of 0.07–0.11 N m^{-2}. The surface wave field was similar during nighttime and daytime (Table II.1) with waves in the general direction of the wind.

To investigate the diurnal cycle of the vertical structure of the OBL, the influence of horizontal variability was removed as follows: first each single profile of salinity, θ, and σ_θ, was referenced to the average value of the respective quantity in the mixed part of the OBL by subtracting that value. The resulting referenced profiles were then averaged in time. A clear diurnal cycle of the vertical structure of θ emerges from the contour plot of hourly

averages (Fig. II.2a). Since there was essentially no diurnal cycle in salinity (Fig. II.2b), the density structure (Fig. II.2c) followed that of the potential temperature closely. During daytime a relatively shallow mixed layer (up to about 10 m deep) developed at the top of the OBL. Density, beneath the shallow ML, increased roughly linearly with depth at an average rate of about $2 - 6 \times 10^{-4}$ kg m^{-4} until the sharp interface of the top of the pycnocline was reached (Fig. II.3a). During nighttime, when destabilizing convective conditions prevailed, overturns with vertical scales of a few meters (up to 15-20 m) and potential temperature differences of up to about 0.015 K relative to the water below or above were observed in the OBL (Fig. II.4a). The mean temperature structure of the nighttime OBL was superadiabatic (statically unstable) between the surface and a depth of 10-25 m (about $1 - 2L$), while deeper the OBL was well mixed (nearly neutrally stratified) to the base of the ML, D, at depths 40-90 m (Anis and Moum 1992 [chapter III]).

Hourly estimates of the averaged squared buoyancy (Brunt-Väisäla) frequency, N^2, were between 2 and 6 $\times 10^{-6}$ s^{-2} in the daytime OBL. During nighttime N^2 was slightly negative in the superadiabatic part of the OBL, while in the well mixed part $N^2 \sim 0$. The shear magnitude, defined as $S = [(\partial U/\partial z)^2 + (\partial V/\partial z)^2]^{1/2}$, was larger in the stratified daytime OBL ($S \sim 2 - 10 \times 10^{-3}$ s^{-1}), than in the well mixed nighttime OBL ($S < 2 \times 10^{-3}$ s^{-1}) (Anis and Moum 1993b [chapter IV]). Since generally higher values of buoyancy frequency were compensated by higher shear values in the OBL, no significant diurnal cycle of the gradient Richardson number, $Ri = N^2/S^2$, was observed. Hourly estimates of Ri were mostly smaller than 1 during either nighttime or daytime.

Estimates of TKE dissipation rates near the surface (depths 6.5 to 15-25 m) were larger than could be accounted for by the production rate of TKE by surface winds during daytime, while during nighttime they were larger than the sum of the production rate by surface winds and surface buoyancy flux (Anis and Moum 1992 [chapter III], 1993c [chapter V]). Deeper than 15-25 m a pronounced diurnal cycle was observed; during daytime ϵ decreased relatively rapidly with depth, while during nighttime ϵ decreased at a much slower rate (Fig. II.2d). Nighttime average values of ϵ in the ML, away from the superadiabatic ocean surface layer (OSL) and the entrainment zone, scaled reasonably well with J_b^0 (Anis and Moum 1992 [chapter III]). A closer inspection indicated that the scaled dissipation rate, ϵ/J_b^0, decreased linearly with the scaled depth, z/D (Anis and Moum 1993b [chapter IV]). Near the base of the OBL, during daytime and nighttime, ϵ decreased by an order of magnitude or more.

II.5. Mixing energetics and deepening of the ML

II.5.1. Potential energy considerations

When a turbulent fluid progresses into a stably stratified environment, mixing of fluid properties such as temperature and humidity (in the atmosphere) or temperature and salinity (in the ocean) takes place. This will tend to homogenize the fluid and erase the stable stratification at the expense of TKE lost to the increase of PE of the deepening ML. Another part of the TKE may go to production of internal waves and some will be eventually dissipated into heat. Likely sources for turbulence mixing may be wind shear or daytime convection in the ABL, and current shear and nighttime convection in the OBL. Additional energy sources for mixing the upper OBL include surface waves (e.g. Anis and Moum 1993c [chapter V]) and Langmuir circulations (Langmuir 1938; Weller and Price 1988). Helical circulations, somewhat similar to oceanic Langmuir circulations, have been observed in the ABL during conditions of combined surface heating and strong winds (e.g. Stull 1988).

Changes in density and PE as functions of time in the OBL (and similarly in the ABL) can be calculated from the vertical density profile, $\rho_i(z)$, at some initial time (taken here for simplicity as $t = 0$), and the density profile, $\rho(z,t)$, at some later time, t. For simplicity we assume there is no change in density beneath the base of the ML, i.e. $\rho(z,t) = \rho_i(z)$ for $-D > z$, and that after mixing density is homogeneous between the surface and the base of the ML, i.e. $\rho(z,t) = \rho(t)$ for $0 > z > -D$ (see Fig. II.5a for schematic). The net change in density in the ML after time t is given by

$$M(t) = \int_{-D(t)}^{0} \left[\rho(t) - \rho_i(z)\right] dz, \tag{5}$$

where z is the vertical coordinate and is positive upward. In a one-dimensional case, density is changed only by a non-zero surface buoyancy flux or by entrainment from below.

The change in PE per unit area after time t, relative to a fixed reference depth, z_r, below the ML, is

$$W(t) = g \int_{z_r}^{0} [\rho(z,t) - \rho_i(z)](z - z_r)\, dz$$

$$= g \int_{-D(t)}^{0} [\rho(t) - \rho_i(z)](z - z_r)\, dz, \qquad (6)$$

where g is the gravitational acceleration, and the assumptions $\rho(z,t) = \rho_i(z)$ for $-D > z$, and $\rho(z,t) = \rho(t)$ for $0 > z > -D$, were used. Using (5) and the assumption that $\rho(t)$ is uniform with depth in the ML we can rewrite (6) as

$$W(t) = -g \int_{-D(t)}^{0} \rho_i(z)[z + \frac{D(t)}{2}]\, dz + gM(t)(-z_r - \frac{D(t)}{2}) \qquad (7)$$

The first term on the right-hand-side of (7) is the increase in PE due to the homogenization of the initial density profile between the surface and the bottom of the ML. The second term is the change in PE due to the net change in density in the ML. In the following discussion we neglect lateral effects.

II.5.2. ML deepening: no convective forcing $[M(t) = 0]$

The simplest case occurs when energy is supplied at the surface at some rate $F(t)$, all of which goes into raising the PE of the ML, while no net density change in the ML occurs. This implies that the increase in PE is solely due to the homogenization of the density in the layer $0 > z > -D$. Examples of such forcing are stress applied at the surface or energy released by breaking waves at the ocean's surface. In this case a simplified PE equation results

by setting $M(t) = 0$ in (7) so that

$$W(t) = -g \int_{-D(t)}^{0} \rho_i(z)\left[z + \frac{D(t)}{2}\right] dz = \int_0^t F(t')\, dt'. \tag{8}$$

$D(t)$ can now be readily found from (8) if the initial density profile, $\rho_i(z)$, is known.

Examples of ML deepening as a function of time for two simple analytical density profiles follow. The first example is of a density step function where an initial shallow mixed layer of depth h and a constant density ρ_1 is on top of a denser layer with a constant density $\rho_1 + \Delta\rho$ (Fig. II.5b). In this case the ML depth as a function of time is given by

$$D(t) = \frac{2}{gh\Delta\rho} \int_0^t F(t')\, dt' + h. \tag{9}$$

If the rate at which energy is supplied at the surface is independent of time, i.e. $F(t) = constant$, then we find from (9) that the ML will deepen linearly with time, i.e. $D(t) \propto t$.

A more realistic example is one in which an initial shallow mixed layer, h, is atop a layer in which density increases linearly with depth at some rate $-d\rho_i/dz = \gamma > 0$ (Fig. II.5c; see also Fig. II.8). The implicit solution for $D(t)$ in this case is given by the cubic equation

$$D^3(t) - 3h^2 D(t) + 2h^3 = \frac{12}{g\gamma} \int_0^t F(t')\, dt'. \tag{10}$$

For the special case where $h = 0$ the initial density profile is linear throughout and (10) reduces to

$$D(t) = \left(\frac{12}{g\gamma} \int_0^t F(t')\, dt'\right)^{1/3}. \tag{11}$$

If furthermore $F(t) = constant$ then we have simply $D(t) \propto t^{1/3}$. A similar result of $t^{1/3}$ dependence was found by Kato and Phillips (1969)

from dimensional reasoning and the data from their laboratory experiment in which a constant stress was mechanically applied to the surface of a tank with fluid of a uniform density gradient. They argued that the entrainment velocity u_e should be determined by the friction velocity, u^*, the initial density gradient, $(\partial\rho/\partial z)_i$, and the depth of the ML, D. From these an overall Richardson number was defined as $Ri \equiv -g(\partial\rho/\partial z)_i D^2/2\rho u_*^2$, and on dimensional grounds it was proposed that $u_e/u^* = f(Ri)$. From a fit to their data they found that $u_e/u^* = 2.5(Ri)^{-1}$, and using the definition of Ri and that $u_e = dD/dt$ they showed that $D(t) = u_*(15t/N_i^2)^{1/3}$, where $N_i^2 \equiv -g(\partial\rho/\partial z)_i/\rho$.

II.5.3. ML deepening: convective forcing only $[M(t) \neq 0]$

When the BL is subjected to convective forcing alone a change in both the PE and the density of the BL results. The net density change associated with the convectively induced surface buoyancy flux, J_b^0, is

$$M(t) = \int_0^t \frac{\rho}{g} J_b^0(t')\, dt', \tag{12}$$

where ρ is a suitable reference density at the surface, and can be taken as a constant ($\sim$ 1023 kg m^{-3}) without introducing an error larger than 0.1%. We examine next two cases of convective ML deepening: the first case excludes entrainment (section II.5.3.1), while the second case accounts for entrainment deepening (section II.5.3.2). Predictions of $D(t)$ are made for both cases and compared to the observed ML depths (section II.5.4).

II.5.3.1. Deepening without entrainment

If turbulence entrainment at the ML base is neglected, then, at any moment $D(t)$ cannot exceed the depth at which the uniform density in the ML intercepts the initial density profile. This type of deepening is referred

to as thermodynamic (or encroachment) ML growth in the atmospheric literature and explains roughly 80% of the observed ML growth (e.g. Stull 1988). Since in this case the uniform density in the ML at any time t is equal to the initial density at depth $z = -D(t)$, we have

$$\rho(t) = \rho_i\big(-D(t)\big). \tag{13}$$

Combining (5), (12), and (13), we get

$$D\rho_i\big(-D(t)\big) - \int_{-D(t)}^{0} \rho_i(z)\,dz = \int_0^t \frac{\rho}{g} J_b^0(t')\,dt'. \tag{14}$$

ML deepening as a function of time can be determined from (14) once the initial density profile and the surface buoyancy flux are specified. For the case of a density step function (Fig. II.5b), an initial increase in density of the shallow top layer, at a rate of $d\rho/dt = \rho J_b^0(t)/gh$, will occur but without deepening. At some time t_s a sudden deepening, to a depth limited only by the sharp density gradient at the top of the pycnocline, will take place. The time t_s satisfies the condition $h\Delta\rho = \int_0^{t_s} (\rho/g) J_b^0(t')\,dt'$, and is given by $t_s = gh\Delta\rho/b\rho$ for a constant surface buoyancy flux $J_b^0(t) = b$, and by $t_s = (2gh\Delta\rho/a\rho)^{1/2}$ for a linearly increasing buoyancy flux $J_b^0(t) = at$.

For the more realistic initial density profile of Fig. II.5c, the depth of the ML, from (14), is given by

$$D(t) = \left(\frac{2}{\gamma}\int_0^t \frac{\rho}{g} J_b^0(t')\,dt' + h^2\right)^{1/2} = \left(\frac{2}{N_i^2}\int_0^t J_b^0(t')\,dt' + h^2\right)^{1/2}, \tag{15}$$

where N_i is the constant value of Brunt-Väisälä frequency associated with the linearly increasing part of the initial density. When $J_b^0(t) = b$, which closely resembles the quasisteady surface buoyancy flux observed during the major part of each night of our experiment (Fig. II.1e), the depth of the ML, from (15), is

$$D(t) = \left(\frac{2b}{N_i^2}t + h^2\right)^{1/2}. \tag{16}$$

For $J_b^0 = at$, which is a good approximation of the observed period of about 2-3 hours at the begining of each night of the experiment, equation (15) reduces to

$$D(t) = \left(\frac{a}{{N_i}^2}t^2 + h^2\right)^{1/2}. \tag{17}$$

For the special case $h = 0$, i.e. when the initial density profile is linear throughout, the ML depth increases at a rate $\propto t^{1/2}$ for a constant surface buoyancy flux ($D(t) = (2b/{N_i}^2)^{1/2}t^{1/2}$, when $J_b^0(t) = b$), while for a linearly increasing surface buoyancy flux the ML depth increases $\propto t$ ($D(t) = (a/{N_i}^2)^{1/2}t$, when $J_b^0(t) = at$).

II.5.3.2. Entrainment deepening

In the presence of entrainment the above method underpredicts the ML depth. Since fluid is entrained by mixing at the base of the deepening ML, $D(t)$ cannot simply be found from consideration of density conservation alone; the dynamics of turbulence, which was neglected in the case without entrainment, need to be taken into account. The simplest way to do this is by consideration of the energy balance in the ML. Due to the positive surface buoyancy flux denser water is created at the surface at a rate of $(\rho/g)J_b^0(t)$. As a result the rate of increase of available PE of the denser surface water, relative to the reference depth z_r, is simply $-gz_r(\rho/g)J_b^0(t) = -z_r\rho J_b^0(t)$. Assuming that all of the available PE goes to increase the PE of the deepening ML, then, using (7) and (12), the balance at some time t is

$$-g\int_{-D(t)}^{0}\rho_i(z)\left[z + \frac{D(t)}{2}\right]dz + \left(-z_r - \frac{D(t)}{2}\right)\int_0^t \rho J_b^0(t')\,dt'$$
$$= -z_r\int_0^t \rho J_b^0(t')\,dt'. \tag{18}$$

Equation (18) can be rewritten as

$$-g\int_{-D(t)}^{0}\rho_i(z)\left[z + \frac{D(t)}{2}\right]dz = \frac{D(t)}{2}\int_0^t \rho J_b^0(t')\,dt'. \tag{19}$$

Equation (19) can be interpreted as follows: during the sinking of the dense surface water it mixes evenly throughout the ML and as a result the center of mass of the dense fluid created near the surface is lowered by $D(t)/2$ and an amount $[D(t)/2]\int_0^t \rho J_b^0(t')\,dt'$ of available PE energy is released. This released PE, in turn, is consumed by the work $-g\int_{-D(t)}^0 \rho_i(z)\left[z+D(t)/2\right]\,dz$ required to homogenize the initial density profile between the surface and the base of the ML, $D(t)$.

Solutions of (19), using the two forms of initial density profiles from the examples above, are given next. For an initial density step function (Fig. II.5b) the solution is given by

$$D(t) = \frac{h}{1-(1/h\Delta\rho)\int_0^t(\rho/g)J_b^0(t')\,dt'}. \tag{20}$$

In contrast to deepening without entrainment, when no deepening occured until $t = t_s$ (where t_s satisfies the condition $h\Delta\rho = \int_0^{t_s}(\rho/g)J_b^0(t')\,dt'$), entrainment deepening occurs also for $t_s > t > 0$. However, similar to deepening without entrainment, at $t = t_s$, the ML will be completely mixed to the depth of the pycnocline. For an initial profile where density increases linearly with depth beneath an initially shallow ML of depth h (Fig. II.5c), we find

$$D^2(t) - 3h^2 + \frac{2h^3}{D(t)} = \frac{6}{{N_i}^2}\int_0^t J_b^0(t')\,dt' \tag{21}$$

For a constant surface buoyancy flux, $J_b^0 = b$, (21) reduces to

$$D^2(t) - 3h^2 + \frac{2h^3}{D(t)} = \frac{6b}{{N_i}^2}t, \tag{22}$$

and for a linearly increasing surface buoyancy flux, $J_b^0 = at$, equation (21) reduces to

$$D(t)^2 - 3h^2 + \frac{2h^3}{D(t)} = \frac{3a}{{N_i}^2}t^2. \tag{23}$$

If furthermore $h = 0$, (22) reduces to $D(t) = (6b/N_i^2)^{1/2}t^{1/2}$, and (23) reduces to $D(t) = (3a/N_i^2)^{1/2}t$. In this case, the time dependence of entrainment deepening and deepening without entrainment is the same, however, entrainment deepening is faster by a factor of $3^{1/2}$.

II.5.4. Comparison of predicted and observed ML depths

Examination of the entrainment phase during our experiment showed a relatively rapid deepening of the ML associated with the onset of convective nighttime conditions. Once convective conditions set in (i.e when J_b^0 turned positive) erosion of daytime stratification, between the ocean's surface and the top of the seasonal pycnocline, was completed in about 2-3 hours. This resulted in a ML deepening rate of about 8-19 meters per hour. Further deepening was effectively inhibited when the base of the ML reached the top of the strongly stably stratified seasonal pycnocline. At this depth ϵ dropped rapidly (Fig. II.2d) from values close to J_b^0 to values smaller than 10^{-8} m^2 s^{-3}. The relatively rapid deepening of the ML that we observed resulted in a much shorter deepening phase than that observed by Lombardo and Gregg (1989) for similar initial density gradients. They reported durations of 4-16 hours with an average of 9 hours (in their Fig. II.5 deepening of the ML by 40 m took about 10 hours). Moreover, they did not observe any significant deepening of the ML during the initial stage when J_b^0 was positive and increasing (i.e. the first couple of hours each night, referred to by Lombardo and Gregg as the initiation stage). This seems to be very different from our observation of a rapidly deepening ML during the initial stage.

To investigate the deepening phase we have chosen three diurnal cycles when salinity effects were negligible and σ_θ followed θ closely. As an

example, contours of θ and ϵ for one diurnal cycle are presented in Figs. II.6a and II.6b, respectively. In this example the ML deepened by about 45 m in a period of 2.5 hours (Fig. II.6a), during which J_b^0 was positive and increased roughly linearly. Note also the rapid increase of $\epsilon(z)$ which followed closely the deepening of the ML (for example the contour line of $log(\epsilon) = -7.5$ deepened from about 20 to 50 m; Fig. II.6b). Comparison of the predicted and observed deepening of the ML, during the entrainment phase of nights 3, 4, and 5, is presented in Figure II.7. For this purpose the predicted ML depth was estimated for two cases: a) ML deepening without entrainment, calculated numerically using equation (15) and observed $J_b^0(t)$; b) ML deepening by entrainment, calculated numerically using equation (21) and observed $J_b^0(t)$. Observed ML depths were deduced from single profiles (hollow circles), and from the referenced and 20 min averaged density contour trace $\sigma_\theta = 0.001$ kg m^{-3} (filled circles). Two basic results are:

- ML depths appear to be larger than predicted for deepening without entrainment (the dashed line in Fig. II.7);
- ML depths are roughly equal or slightly larger than predicted for entrainment (the solid line in Fig. II.7).

To this point we have not considered forcing mechanisms additional to convection. Nor have we considered TKE dissipation which further reduces the amount of energy available for deepening the ML and increasing its PE. These issues are addressed next by consideration of an energy balance which includes forcing mechanisms and sinks.

II.5.5. Effects of additional energy sources and TKE dissipation

Suppose that in addition to convection there exists a source of energy, F, which may be a function of both depth and time. The energy budget for

the deepening ML, including TKE dissipation, becomes

$$\underbrace{-g\int_{-D(t)}^{0}\rho_i(z)\left[z+\frac{D(t)}{2}\right]dz}_{W_H}+\underbrace{\int_0^t\left(\int_{-D(t')}^{0}\rho\epsilon(z,t')\,dz\right)dt'}_{DISS}$$

$$=\underbrace{\frac{D(t)}{2}\int_0^t\rho J_b^0(t')\,dt'}_{BF}+\underbrace{\int_0^t\left(\int_{-D(t}^{0}F(z,t')\,dz\right)dt'}_{R}. \qquad (24)$$

The LHS of (24) represents energy sinks: W_H is the amount of work needed to homogenize the ML density; $DISS$ is the vertically and time integrated TKE dissipation rate in the ML. The RHS of (24) represents the energy sources: BF is the amount of available PE released due to the sinking of the dense surface water; R represents additional mechanisms which may include shear production, Langmuir cells, surface wind stress and surface wave breaking.

In most oceanic cases changes in PE cannot simply be estimated from the difference between $\rho_i(z)$ and $\rho(z,t)$, the respective density profiles at the beginning and the end of the deepening phase, because of lateral effects; for example, if $J_b^0 = 1\times10^{-7}$ m^2 s^{-3} the rate of increase of density in a ML of 50 m depth is 2×10^{-7} kg m^{-3} s^{-1}, which results in a net density increase of about 2×10^{-3} kg m^{-3} for a period of 3 hours. Such a small density change might easily be masked by lateral effects. Since our observations show that deepening was initiated every night when J_b^0 changed sign, it is suggested that ML deepening was unrelated to lateral processes and any density changes related to these processes need to be removed first. This was effectively done in (7) by assuming that the final density profile in the ML is independent of z, such that $\rho(z,t) = \rho(t)$. This provides a means to estimate W_H from $\rho_i(z)$ directly. However, a more accurate way, from

the standpoint of the observational data, is to estimate W_H using a new density profile $\rho_H(z,t)$ which has the shape of the final density profile, $\rho(z,t)$, and satisfies the condition $\int_{-D(t)}^{0}[\rho_H(z,t) - \rho_i(z)]\,dz = 0$. Once $\rho_H(z,t)$ has been determined W_H can be calculated from (6) and is given by $W_H = g\int_{-D(t)}^{0}[\rho_H(z,t) - \rho_i(z)]z\,dz$. This procedure was used for the three ML deepening phases and the relevant density profiles are presented in Figure II.8. For reference we have also plotted the density profile $\rho_M(z,t)$ (dashed line), resulting from the increase in density in the ML due to the surface buoyancy flux, such that $\int_{-D(t)}^{0}[\rho_M(z,t) - \rho_i(z)]\,dz = \int_0^t(\rho/g)J_b^0(t')\,dt'$. Estimates of W_H ranged from 30 to 43 J m^{-2}, with a mean of 34 J m^{-2} (Table II.2), and in all three cases were roughly equal to $(1-2)BF$. That is, the work done was larger than that available solely from convective forcing.

The apparent imbalance is even larger if TKE dissipation in the ML is taken into account. For that purpose the term $DISS$ in (24) was estimated in two ways: the first assumes that the depth averaged dissipation rate is some fixed fraction r of the surface buoyancy flux, i.e. $\bar{\epsilon}(t) = [1/D(t)]\int_{-D(t)}^{0}\epsilon(z,t)\,dz = rJ_b^0(t)$, so that

$$DISS1 = \int_0^t \rho D(t')\bar{\epsilon}(t')\,dt' = r\rho\int_0^t D(t')J_b^0(t')\,dt'. \qquad (25)$$

A value of $r = 0.44$, as observed by Lombardo and Gregg (1989) for the entrainment phase during their experiment, was used to estimate $DISS1$ for our observations. Since $DISS1$ does not account for the higher TKE dissipation rates observed closer to the surface it may severely underestimate the true dissipation. In an attempt to account for the higher dissipation rates a more realistic estimate of $DISS$ was calculated as

$$DISS2 = \int_0^t\left(\int_{-D(t')}^{z_0}\rho\epsilon(z,t')\,dz\right)dt' + \int_0^t\rho\epsilon(z_0,t')|z_0|\,dt', \qquad (26)$$

where $\epsilon(z_0)$ is the TKE dissipation rate at a depth $z_0 = -10$ m, and our observed values of ϵ were used. Since $\epsilon(z_0)$ was assumed throughout the depth interval $z > z_0$ to avoid potential near surface contamination of the data by the ship's wake, $DISS2$ may still result in an underestimate because $\epsilon(z)$ is probably larger than $\epsilon(z_0)$ in the depth range $z > z_0$. Estimates of $DISS1$ and $DISS2$ based on (25) and (26) are presented in Table II.2. Next, results from relevant convective experiments are compared to those from our study, and additional forcing mechanisms, represented quantitatively by R (eqn. 24), are discussed in section II.6.

II.5.6. Comparison with other convective ML deepening studies

For the purpose of comparison we examined observations made by Shay and Gregg (1984a, 1984b) of a convective OBL forced by a cold air outbreak, and by Lombardo and Gregg (1989) of a nighttime convective OBL. Assuming that convective forcing is solely used for deepening, the predicted depth of the ML for these two experiments is given by (15) for convective deepening without entrainment, and by (21) for convective deepening including entrainment. The predicted and observed ML depths are presented as a function of time in Figure II.9. For reference also plotted are the interface height as a function of time as observed by Deardorff et al. (1969) for convection in water in a laboratory experiment.

Initially the oceanic data seems to follow nonentrainment convective deepening (the first 9 hours of Shay and Gregg's experiment and the first 2 hours of Lombardo and Gregg's experiment). However, in both cases the observed ML depths depart from the nonentrainment curve and get closer to the upper bound curve of entrainment deepening with Shay and Gregg's data even exceeding it at the end of the deepening period. For

comparison, the laboratory data of Deardorff et al. followed nonentrainment ML deepening during the entire deepening period. Values of W_H and BF for the experiments of Shay and Gregg, Lombardo and Gregg, Deardorff et al., and for a numerical model of André et al. (1978) for the Wangara boundary layer data of Day 33, are presented in Table II.3. Comparison of the estimates of W_H and BF suggests that in the oceanic cases the surface buoyancy flux term, BF, is slightly smaller (Shay and Gregg) or slightly larger (Lombardo and Gregg) than the observed amount of work, W_H, needed to homogenize the ML. For comparison, in both the laboratory experiment of Deardorff et al. and the atmospheric experiment of André et al., BF is roughly twice as large as W_H.

Inclusion of TKE dissipation for the oceanic experiments of Shay and Gregg (see also Gregg 1987), and Lombardo and Gregg, suggests that additional energy to that available from BF is needed to balance the budget (24). This is similar to the conclusions from our experiment. Estimates of the additional energy needed are represented by $R1$ and $R2$ (Table II.3), and refer to $DISS1$ and $DISS2$, respectively. For the experiment of Deardorff et al. convection was the sole forcing mechanism as was the case of the experiment of André et al. (except for the relatively shallow ASL in which wind stress might have dominated). For these two experiments we estimated the dissipation term as $DISS1 = W_M - BF$. This results in $\overline{\epsilon} = 0.35 J_b^0$ and $\overline{\epsilon} = 0.39 J_b^0$ for Deardorff et al.'s and André et al.'s experiments, respectively, and is in general agreement with atmospheric values (see Table II.3).

II.6. Mixing in addition to convection

The picture that emerges suggests that for the examples of the atmospheric and laboratory convective boundary layers ML deepening could be explained solely by convective forcing. In contrast, the deepening of the oceanic ML, although apparently initiated by convection, requires additional energy source/s to balance the budget. Although we cannot completely rule out the possibility of advective effects, it seems unlikely that they governed *diurnal* ML deepening initiated each night when J_b^0 became positive. If so, what are the likely additional mechanisms in the oceanic case ? Are they consistent with the additional energy required to balance the budget (R in eqn. 24) ? This problem is addressed next by consideration of: wind stress and breaking surface waves (section II.6.1.), Langmuir cells (section II.6.2.), and turbulence shear production at the base of the deepening ML (section II.6.3.).

II.6.1. Surface wind stress and wave breaking

When the wind blows over the ocean, energy is transferred from the wind through interaction of the surface wind stress, τ_0, with the surface drift current. A number of studies have estimated the ratio, m_w, between the increase in PE of the deepening ML, E_{PE}, and the wind energy flux, E_{10}. Estimates of m_w, from laboratory and oceanic field experiments (Table II.4), range from 0.0012 (Denman 1973) to 0.01 (Turner 1969), a range of about one order of magnitude. An attempt to reconcile the apparent energy imbalance observed in the oceanic ML during convection can now be made. If both convective and wind forcing are available for mixing, the balance between the increase of PE in the ML and the available energy is

$$W_H = ABF + \int m_w E_{10}\, dt, \tag{27}$$

where $ABF = BF - DISS1$ represents the part of BF available for mixing, and $m_w E_{10}$ is the part available for mixing from the wind energy flux. Using (27) and the estimates of W_H, ABF, and E_{10} from our experiment (see Table II.5) results in $m_w = 0.004 - 0.011$ with a mean value of $m_w = 0.006$. For the experiments of Shay and Gregg and Lombardo and Gregg, $m_w = 0.011$ and $m_w = 0.005$, respectively. These values are consistent with the mid to upper range of estimates of m_w in Table II.4.

However, so far the picture is incomplete since surface waves, a source of TKE through either breaking or wave stresses (Anis and Moum 1993c [chapter V]), have not yet been taken into account. In ML models the turbulence energy flux term, $\overline{-w'(p'/\rho_0 + e)}|_{z=0}$ (where $e = 0.5u_i'u_i'$; e.g. Niiler and Kraus 1977), is associated with wave breaking and is commonly lumped together with the surface wind stress term. Both terms are modeled as proportional to E_{10}, and the proportionality constant n_w in Table II.4 represents estimates of the fraction of E_{10} transferred to the ML including the source associated with wave breaking. A different estimate of the energy lost by wave breaking is based on Longuet-Higgins' (1969) theoretical-statistical model for a wave field in an equilibrium state, and is also given in Table II.4. Laboratory measurements suggest, indeed, that most of the energy lost by breaking goes directly into turbulence (e.g. Rapp and Melville 1990). The estimate of Richman and Garrett (1977) is of the net wind energy input to the ML through the wave field, and is based on a model for momentum and energy transfer by the wind to the surface waves and the ML in conjunction with laboratory and field measurements.

The overall energy budget, which accounts for surface waves and includes the higher TKE dissipation rates observed near the surface (see eqn. 26),

reads now

$$W_H + DISS2 = BF + \int n_w E_{10}\, dt. \tag{28}$$

From (28) and the estimates of W_H, $DISS2$, BF, and E_{10} for our experiment (see Table II.5) we find that $n_w = 0.02-0.07$ with a mean value of $n_w = 0.04$. For the experiments of Shay and Gregg and Lombardo and Gregg $n_w = 0.03$ and $n_w = 0.05$, respectively. These estimates are consistent with the range of estimates of n_w in Table II.4. Note however that although the TKE dissipation estimates, $DISS2$, are more realistic than $DISS1$, they may still underestimate the true dissipation as explained earlier. It seems reasonable, therefore, that one may need to use the higher estimates of n_w in Table II.4, at least for the oceanic cases cited.

II.6.2. Mixing by Langmuir cells

Although Langmuir (1938) claimed more than 5 decades ago that these cells, now bearing his name, are possibly the essential mechanism by which the ML is formed, a full understanding of their role as a source of energy and its transfer in the upper ocean has not yet been established. To date the most extensive measurements of Langmuir cells in the OBL were carried out by Weller and Price (1988) from FLIP. They reported downward vertical and downwind horizontal velocities on the order, and at times, in excess of 20 cm s^{-1} in the upper half of the ML. Moreover, they found that on some occasions, when Langmuir cells appeared suddenly, they were able to mix the shallow near surface stratification ($\leq$ 0.05 K m^{-1}) formed by daytime heating. They concluded that Langmuir cells can be an important direct mixing mechanism in the upper one third to one half of the ML, but found no direct evidence for the role of Langmuir cells in mixing at the base of the 40-60 m deep ML. Although unable to calculate accurate Reynolds stresses

associated with the cells, the velocities they observed support conclusions (e.g. Gordon 1970; Pollard 1977) that the Reynolds stress associated with Langmuir cells can be an order of magnitude larger than the instantaneous wind stress.

The importance of Langmuir cells as a mixing mechanism in the upper ocean was demonstrated in a numerical study by Leibovich and Paolucci (1980). Using typical oceanic values as their model parameters, resulted in mixing efficiencies of $m_w = 0.005 - 0.016$ (Table II.4) when the development of the ML was subjected solely to Langmuir circulations. These mixing efficiencies are larger than those resulting from the consideration of mixing by surface wind stress alone. Moreover, the mixing efficiencies associated with Langmuir cells seem to provide enough energy to be consistent with the range of $m_w = 0.004 - 0.011$, estimated from our observations and those of Shay and Gregg and Lombardo and Gregg (section II.6.1). Leibovich and Paolucci suggested that the vertical gradients in the downwind flow associated with Langmuir cells may be responsible for shear flow instabilities and mixing in the ML. Although the contribution of the vertical gradients to the maintenance of ML turbulence has not yet been quantified, the shear magnitude observed by Weller and Price (1988) from *FLIP* was much larger than that of the model profiles of Leibovich and Paolucci.

An alternative way to look at Langmuir cells is by consideration of the possible conversion of kinetic energy carried by the cells to PE of the ML as a result of mixing. If Langmuir circulations can be idealized as a series of counter rotating cells, rotating at a constant radial frequency ω, with circular cross sections of radius r in a plane perpendicular to the wind, then,

the average kinetic energy of a cell per unit surface area, T_L, is given by

$$T_L = \frac{1}{2r} \int_0^{2\pi} \int_0^r \frac{1}{2} \rho \omega^2 r'^2 r' dr' d\alpha, \tag{29}$$

where $d\alpha$ is a small arc section. Performing the integration results in

$$T_L = (\pi/8)\rho(\omega r)^2 r. \tag{30}$$

Langmuir cells have been shown to evolve in time from smaller to larger spatial scales (see Leibovich 1983 for a comprehensive summary of the theory and observations). Streak spacing, i.e. the distance between convergence zones, of the large cells in the ocean was found to be on the order of about 1.5 (Assaf et al. 1971) to 3 (Smith et al. 1987) times the ML depth. The observations of Weller and Price (1988) indicated that the appearance of moderate to large cells was followed by mixing of the near surface stratification. We might assume, then, that the large cells are resposible for most of the mixing and we may take, for our idealized circular cells, $r \sim D/2$ (using an average streak spacing of $4r \sim 2D$). Assuming an angular velocity, ωr, on the order of the vertical velocity, and taking a vertical velocity of 0.05 m s^{-1} for the average wind speeds of about 8 m s^{-1} during our experiment (see Fig. 23 of Weller and Price 1988), we find from (30) that $T_L \sim 20$ J m^{-2} (an average value of $D \sim 40$ was used). If the conversion from kinetic energy of the cells to PE of the ML is, say, 50% efficient we need roughly 2-3 cells to account for the additional energy required for mixing, $R1$ (Table II.2). This results in a decay time of Langmuir cells of about 1 hour.

Langmuir cells have been shown to be highly transient (Weller and Price 1988) and clear determination of their decay rate has not yet been made. However, some observations indicate that individual Langmuir type

features persisted for durations on the order of 1 (Leibovich 1983) to 2 hours (Smith et al. 1987). Although our simple model of conversion of cell kinetic energy to PE of the ML does not provide additional insight into the physics of the mixing process, it gives a consistent order of magnitude argument in agreement with the additional energy needed for the enhanced mixing observed, and reasonable cell decay rates. It is also noted that although Langmuir cells are believed to be primarily mechanically driven, observational evidence suggests that they occur *less* often when diurnal stratification is strongest (Smith et al. 1987). If this is the case they may be found more frequently during destabilizing convective conditions.

II.6.3. Shear generated turbulence at the base of the ML

Additional energy for turbulence mixing and deepening of the ML may be provided by shear production, P, near the base of the ML. Increased levels of shear, supporting this notion, were indeed observed near the base of the ML, while shear in the bulk of the ML was much smaller (Anis and Moum 1993b [chapter IV]). Shear production may, in turn, be balanced by TKE dissipation and buoyancy destruction, i.e. $P = \epsilon - J_b$ (buoyancy destruction, $-J_b$, represents the conversion of turbulence energy into PE of the ML). Support for a simple balance of this type, in the convective OBL, comes from numerical simulations (André and Lacarrère 1985), while a field experiment in the convective ABL provided similar evidence (Zhou et al. 1985). Note that entrainment due to shear generated turbulence at the base of the ML is in addition to entrainment caused by penetrating convection (section II.5.3.2).

Using the simplified TKE equation, $P = \epsilon - J_b$, defining a flux Richardson number $R_f \equiv -J_b/P$, and using a critical value of $R_f = 0.15$

(Osborn 1980), an upper bound on the rate of buoyancy destruction at the base of the ML is given by

$$|J_b(-D)| \leq 0.2\epsilon(-D). \tag{31}$$

Laboratory measurements by Rohr and Van Atta (1987) showed that 0.2 was a good estimate for stratified fluids where $Ri \geq 0.1$. Values of R_i, observed during our experiment near the base of the nighttime deepening ML, were generally on the order of 0.1–1.0.

If the shear dominated layer is of thickness h_s and centered at $z = -D$, the amount of TKE converted to PE is

$$PE^D = \int_0^t \left(\int_{-D-h_s/2}^{-D+h_s/2} -\rho J_b(z,t')\,dz \right) dt' \leq \rho h_s 0.2\epsilon(-D)t, \tag{32}$$

where (31) was used. The numerical simulations of André and Lacarrère (1985) indicate that $h_s \leq 0.3D$. Combined with our observations of $\epsilon(-D) \leq 1\times10^{-7}$ m^2 s^{-3}, an average ML depth of $D = 40$ m during a deepening phase of duration $t = 2.5$ hr, and taking $\rho = 1023$ kg m^{-3}, results in $PE^D \leq 2.2$ J m^{-2}. Although shear production at the base of the ML is likely to occur and we should consider it, it contributes only a relatively small amount of the additional energy needed for mixing (about 8% of the mean value of $R1$; Table II.2).

II.7. Reassessment of ML deepening including mixing in addition to convection

As shown earlier, ML deepening was initiated nightly with the onset of convective conditions, however, it was too rapid to be accounted for by convection alone. Shear generated turbulence near the base of the ML was shown to contribute less than 8% to ML deepening (section II.6.4). On the other hand it was shown that additional wind forcing, through either surface stress, surface waves, Langmuir circulation, or a combination of them, may provide sufficient energy to alleviate the imbalance. Although the exact mechanism of mixing and ML deepening cannot be determined from our experiment, reassessment of the ML depth can nevertheless be made. If the fraction of available energy due to convection is m_c, where $1 > m_c > 0$, and the fraction of available energy from the wind is m_w, then combining (8) and (19) results in

$$-g\int_{-D(t)}^{0}\rho_i(z)\left[z+\frac{D(t)}{2}\right]dz$$

$$=m_c\frac{D(t)}{2}\int_0^t\rho J_b^0(t')\,dt'+m_w\int_0^t E_{10}(t')\,dt', \tag{33}$$

where in (8) we have set $F(t)=m_wE_{10}(t)$.

Equation (33) can be solved for $D(t)$ if $\rho_i(z)$, $J_b^0(t)$, E_{10}, m_c and m_w are known. For the example of an initial shallow ML of depth h with a linear density profile beneath it (Fig. II.5c), we find

$$D^3(t)+\left(-3h^2-\frac{6m_c}{g\gamma}\int_0^t\rho J_b^0(t')\,dt'\right)D(t)$$

$$+\left(2h^3-\frac{12m_w}{g\gamma}\int_0^t E_{10}(t')\,dt'\right)=0. \tag{34}$$

For comparison of the observed ML depths to estimates based on (34) we used 3 estimates $m_w=0.0012$, $m_w=0.005$, and $m_w=0.01$, representing

the range $m_w = 0.0012 - 0.01$ in Table II.4 (we excluded the larger estimates based on Leibovich and Paolucci's model for mixing by Langmuir circulation). The part available for mixing due to convection was estimated in two ways: 1) separately for each night, assuming $m_c = ABF/BF$ and using the estimates of ABF and BF in Table II.5 (this results in $m_c = 0.20$, $m_c = 0.26$, and $m_c = 0.21$, for nights 3, 4, and 5, respectively); 2) as the mean value of $m_c = W_H/BF = 0.46$ and $m_c = W_H/BF = 0.54$, using the estimates of W_H and BF for the experiments of Deardorff et al. (1969) and André et al. (1978) (Table II.3). This results in $m_c = 0.5$.

The results for the case where m_c assumes different values for each night (Fig. II.10), and the results for the case $m_c = 0.5$ (Fig. II.11), indicate that the observed ML deepening can be accounted for when taking into consideration both convective and wind forcing. Coefficients of $m_w \sim 0.01$, representing the upper range of estimates of m_w given in Table II.4, are needed for Nights 3 and 4, while for night 5 lower values of $m_w = 0.001-0.005$ seem to work well. We believe that $m_c \sim 0.5$, deduced from the laboratory and ABL experiments, may better represent the amount of work available for mixing due to convection, since for these experiments effects unrelated to convection were neglegible. In contrast, the values of m_c deduced from oceanic scaling studies of ϵ are lower since observed ϵ is more likely to include additional dissipation related to wind or wave generated TKE.

II.8. Discussion and conclusions

An extensive set of measurements of the hydrodynamic field and of turbulence was made in the OBL covering 6 diurnal cycles. During both daytime and nighttime winds and sea state were moderate. The surface buoyancy flux during daytime was between -3.85 and -1.68 $\times 10^{-7}$ m^2 s^{-3}, and a roughly linear density profile, with density increasing at a rate of $2-5\times10^{-4}$ kg m^{-4}, was observed in the OBL beneath a shallow ML which occupied the upper 10 m or so. After a transition period of 2-3 hours, from daytime to nighttime conditions, convective forcing reached a quasisteady state with nightly mean values of $J_b^0 = 1.3 - 1.7 \times 10^{-7}$ m^2 s^{-3}.

In this study we have focused our attention specifically on the transition phase from stabilizing daytime to destabilizing nighttime convective conditions. During this period, when J_b^0 increased roughly linearly from 0 to its quasisteady nighttime value, deepening of the ML proceeded relatively quickly and was completed in 2-3 hours. This is faster than the 4-16 hours, with an average of 9 hours, found by Lombardo and Gregg (1989) for the deepening of the nighttime ML during their experiment. Comparison of our observed ML depths during the deepening phase to those predicted theoretically revealed that: 1) ML deepening appears to be faster than predicted for deepening without entrainment (the dashed line in Fig. II.7); 2) ML deepening is roughly equal or slightly faster than predicted for entrainment assuming all of the convective forcing is available for mixing (the solid line in Fig. II.7). A similar comparison (Fig. II.9) was made for a diurnal convective OBL (Lombardo and Gregg 1989) and for an OBL in which convection was induced by a cold air outbreak (Shay and Gregg 1984a). In both cases the observed ML depths were larger than

predicted for deepening without entrainment and smaller than predicted for entrainment deepening, except toward the end of the deepening period of Shay and Gregg's experiment when the observed ML depth exceeded that predicted by entrainment. In contrast, the deepening of the ML in a laboratory convection experiment (Deardorff et al. 1969) followed the predicted convective deepening without entrainment (Fig. II.9).

Consideration of the increase in PE of the ML, W_H, at the end of the deepening period, showed it to be larger than could be accounted for by convection alone. For comparison, the laboratory experiment of Deardorff et al. (1969) and the numerical experiment of André et al. (1978), based on data from the Wangara convective ABL experiment, showed that the change in PE could be explained solely by convective forcing. The essential difference between the oceanic and laboratory experiments is that for the latter the sole forcing was by convection. This suggests that additional mixing mechanisms in the OBL played an active role in the deepening of the ML. An estimate of shear generated turbulence at the base of the ML, which may induce additional mixing by working against the stable density stratification from below, provided less than 8% of the additional energy needed. If the additional energy comes from the wind and can be parameterized as $m_w E_{10}$, where E_{10} is the wind energy flux, mixing efficiencies of $m_w = 0.004 - 0.011$ are required . A complementary comparison of the ML depth predicted by combined convective and wind forcing to the observed ML depth results in a similar range of wind mixing efficiencies, m_w (Figs. II.10, II.11). These are higher than suggested by Kato and Phillips' (1969) laboratory experiment, where a constant stress was applied mechanically to the surface, but are consistent with those suggested by other investigators (Table II.4).

Specifically, Turner (1969), based on a direct comparison of the measured wind and its effect on mixing, suggested a value of $m_w = 0.01$.

A different scenario involves Langmuir cells as mixing agents. The capability of mixing by Langmuir cells in the OBL was demonstrated by Weller and Price (1988); their observations indicated that on some occasions, when Langmuir cells appeared suddenly, they were able to mix stable temperature gradients as large as 0.05 K m^{-1}. Assuming a simple model of conversion of kinetic energy of the cells into PE of the ML, we showed that the amount of energy available from this conversion is similar to the additional energy needed for mixing, and that the decay time of a cell is consistent with observations. Estimates of mixing efficiencies from a Langmuir circulation mixing model (Leibovich and Paolucci 1980), sugests that $m_w = 0.005-0.016$ for typical oceanic conditions. These are consistent with the range of mixing efficiencies of $m_w = 0.004-0.011$ resulting from our experiment and the two other oceanic experiments.

Since TKE dissipation is an important energy sink in the OBL, estimates of the TKE dissipation rate, ϵ, were included in the overall energy budget (eqn. 24). Parameterization of the *total* wind energy flux entering the surface of the ocean as $n_w E_{10}$ (where n_w is larger than the mixing efficiency m_w above), resulted in estimates of $n_w = 0.02-0.07$, with a mean of $n_w = 0.04$, required to close the overall budget. Similar estimates of $n_w = 0.03$ and $n_w = 0.05$ were deduced when we used data from the experiments of Shay and Gregg (1984a,b) and Lombardo and Gregg (1989), respectively. These estimates are consistent with estimates of n_w made by other investigators when surface waves are taken into consideration (Table II.4); for example, an estimate based on a model predicting the rate at which energy is lost by

wave breaking for a wave field in equilibrium with the wind (Longuet-Higgins 1969) results in $n_w = 0.04$; an estimate from an attempt by Richman and Garrett (1977) to calculate the actual transfer of wind energy to the ocean through the surface wave field suggests that $n_w = 0.04 - 0.09$.

The general conclusion from our experiment and the two other oceanic experiments cited is that although convective conditions seem to initiate ML deepening, the observed deepening rates cannot be accounted for solely by convection. However, if additional sources of mixing which are consistent with OBL observations are included, the observed ML depth can be explained by a simple combination of convective and wind forcing. Assuming that about half of the convective forcing is available for mixing, as is suggested by the data from the experiments of Deardorff et al. (1969) and André et al. (1987), results in convective and wind forcing contributing roughly equally to deepening of the ML in the oceanic cases examined. A summary of ML deepening formulations due to either convective forcing, wind forcing, or their combination is given in Table II.6.

Unfortunately it is impossible to determine from our observations how the energy from the wind is imparted to the ocean. Likely candidates which are consistent with the additional energy required are wind stress, surface waves, or Langmuir circulations. Although in some cases one of these processes might dominate it is reasonable to expect that in moderate sea conditions all need to be taken into account when considering the energetics in the upper OBL. It is for future work to try and distinguish the conditions when wind stress, wave related, or Langmuir circulation dominate and to what extent they influence mixing in each case. However, if ultimately the wind supplies the energy via either or a combination of these mechanisms,

then roughly 85% ($\sim 0.034E_{10}$) entering the OBL is effectively dissipated, while the remaining 15% ($\sim 0.006E_{10}$) is available for mixing.

Acknowledgments. We are grateful to the Captain and crew of the R/V *Wecoma* for their help during the experiment. This work was supported by National Science Foundation Grants OCE-8608256 and OCE-8716719 and by ONR grant N00014-89J3211. A. A. is also grateful for a personal grant from the Gerson Meerbaum Foundation for Oceanography, the Hebrew University of Jerusalem, Israel.

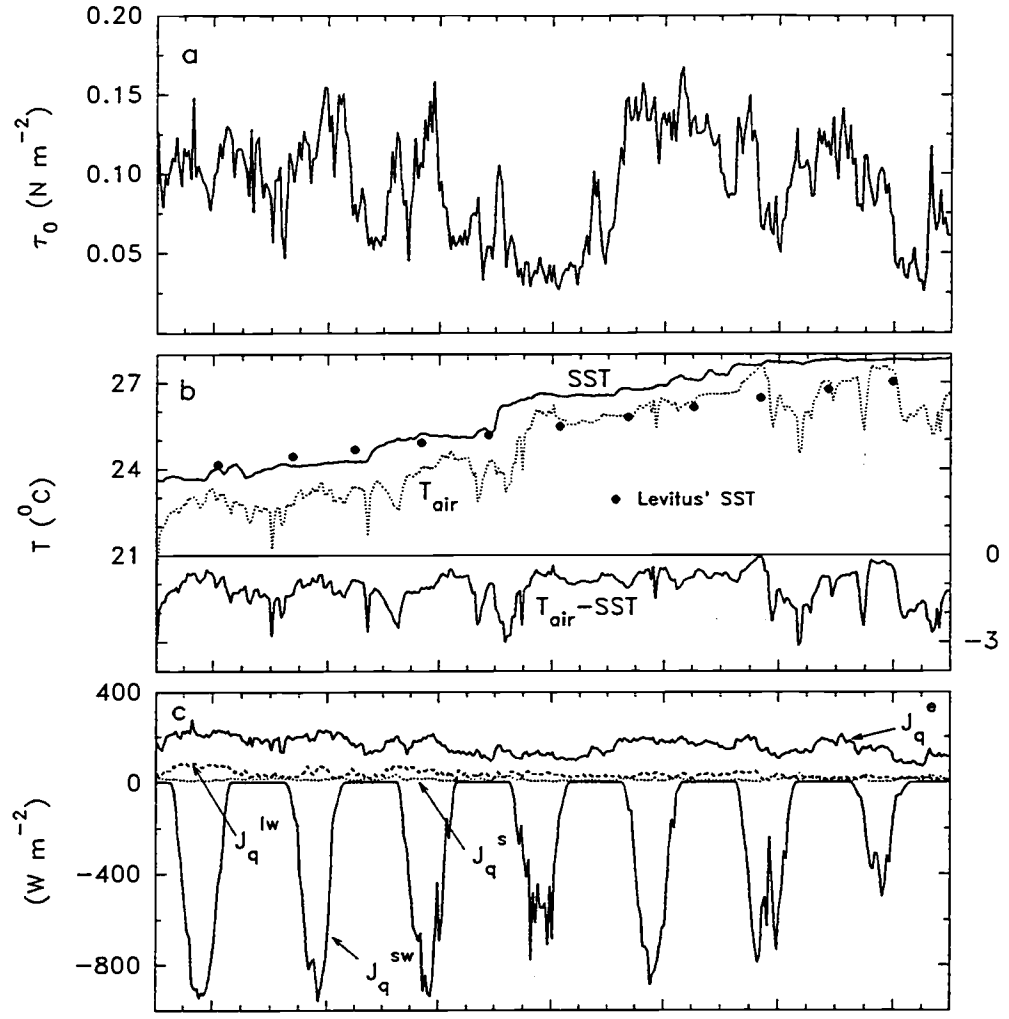

Figure II.1. Thirty-minute averages of shipboard meteorological data for the six diurnal cycles of the experiment. (*a*) Surface wind stress, τ_0. (*b*) Air temperature at 8 m height, T_{air}, and seawater temperature at 5 m depth, SST, and their difference, $T_{air} - SST$. Although the diurnal cycle does not clearly stand out it can be observed in the traces of either the air temperature or the air-sea temperature difference. For comparison purposes we have also plotted the SST data (filled circles) from the climatological atlas of Levitus (1982). (*c*) The heat flux components: J_q^{sw} is the net shortwave radiation, J_q^e is the latent heat flux, J_q^{lw} is the net longwave radiation, and J_q^s is the sensible heat flux. Negative heat flux represents heat input into the ocean while a positive flux represents heat loss.

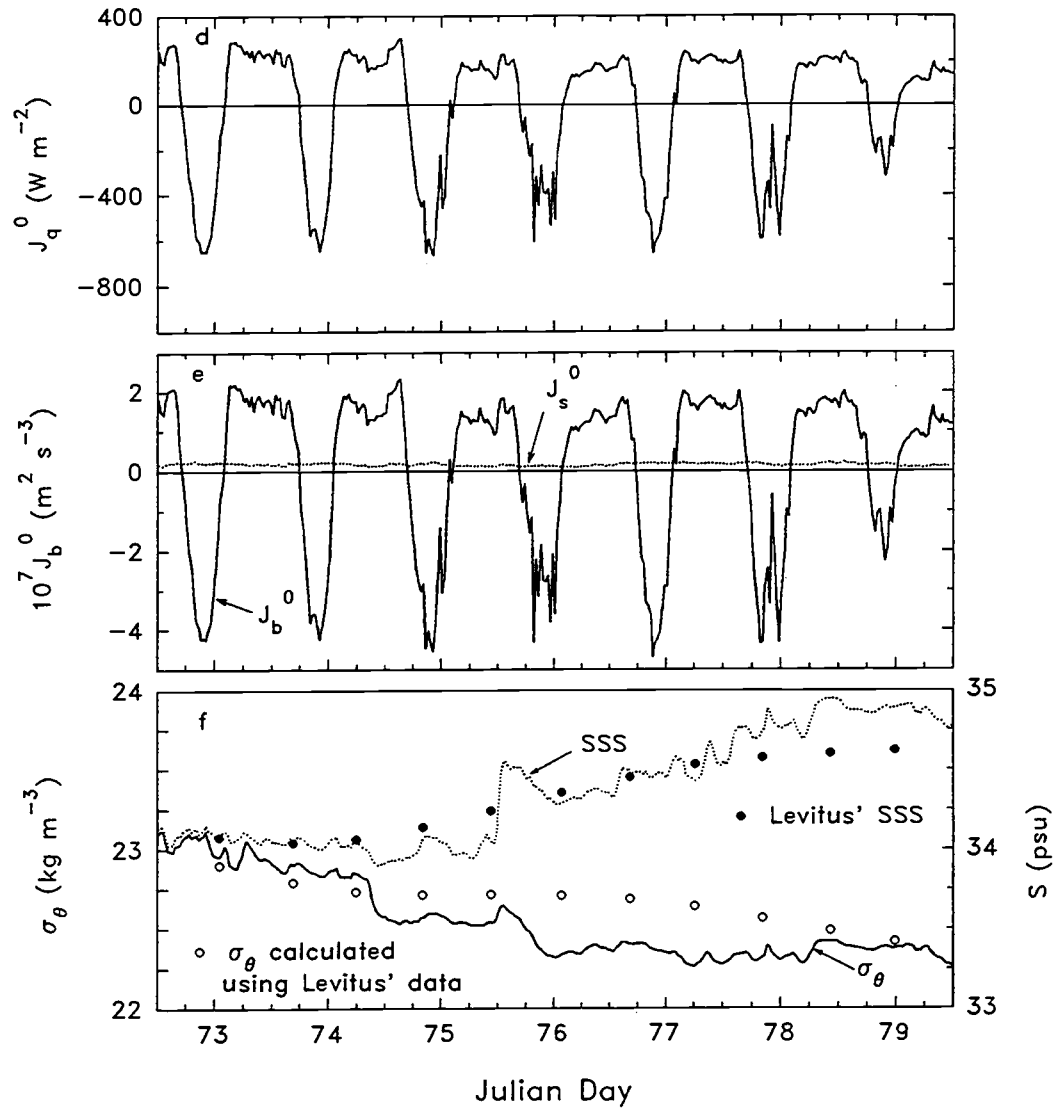

Figure II.1. (continued) (*d*) The net heat flux at the sea surface, J_q^0. (*e*) The net surface buoyancy flux, J_b^0, and the contribution, J_s^0, due to the salinity changes at the sea surface (mainly due to evaporation). Salinity effects account only for a small fraction (5−10%) of the net surface buoyancy flux, while the main contribution is due to the heating/cooling of the sea surface. A positive buoyancy flux represents a mass flux into the surface (e.g. during convection). (*f*) Sea surface salinity, SSS, as measured from the R/V *Wecoma* (dotted line), and the SSS from Levitus' data (filled circles). The sea surface density, σ_θ, was calculated from the observed SST and SSS (solid line) and from Levitus' data (hollow circles). The SST and the SSS from Levitus' atlas represent the climatological mean for the winter season (the months of February, March and April).

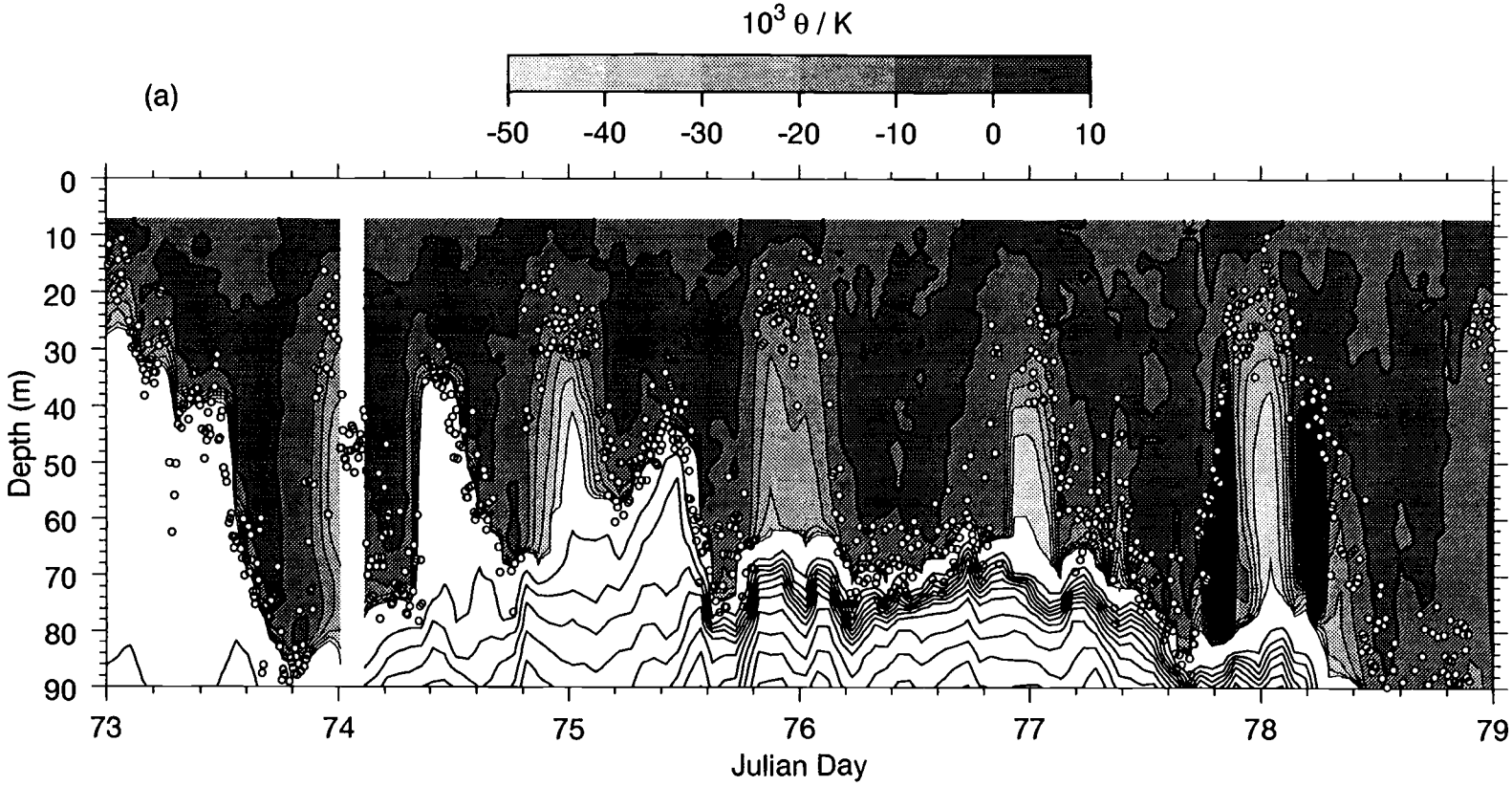

Figure II.2. Panels $(a - c)$ are contour plots of the referenced and hourly averaged finescale vertical structure of θ, salinity, and σ_θ. θ gray shades increments are 0.01 K, and salinity increments are 0.004 psu and were chosen to represent equal contributions to σ_θ (increments of 0.003 kg m^{-3}). The heavy black line represents the value 0 and the circles represent the ML depth as estimated from individual profiles. Contour lines below the ML are at intervals of 1 K, 0.4 psu, and 0.3 kg m^{-3}, for θ, salinity, and σ_θ, respectively. Note the cooler and therefore denser fluid in the upper $20 - 30$ m of the OBL each night resulting in a superadiabatic OSL.

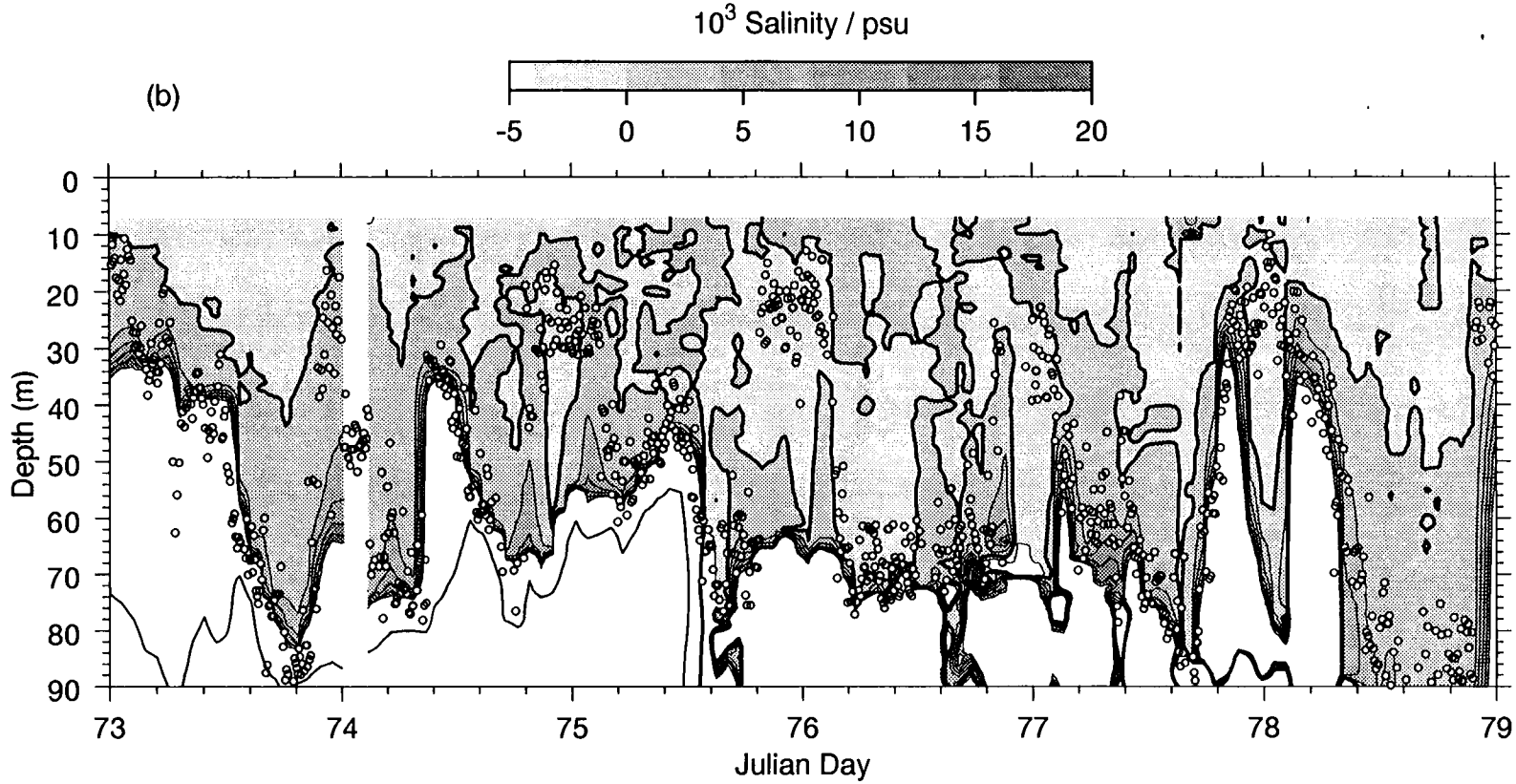

Figure II.2. (continued)

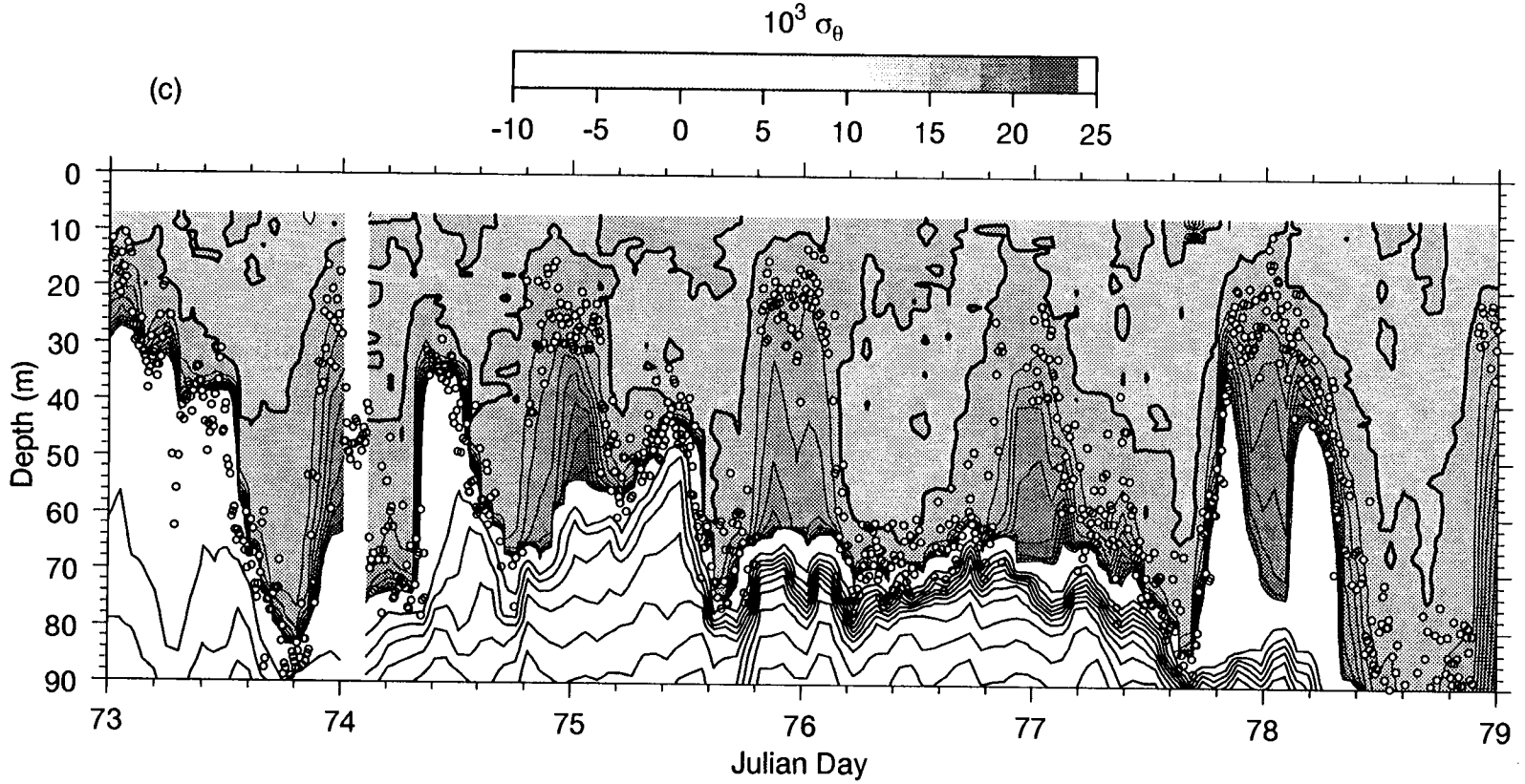

Figure II.2. (continued)

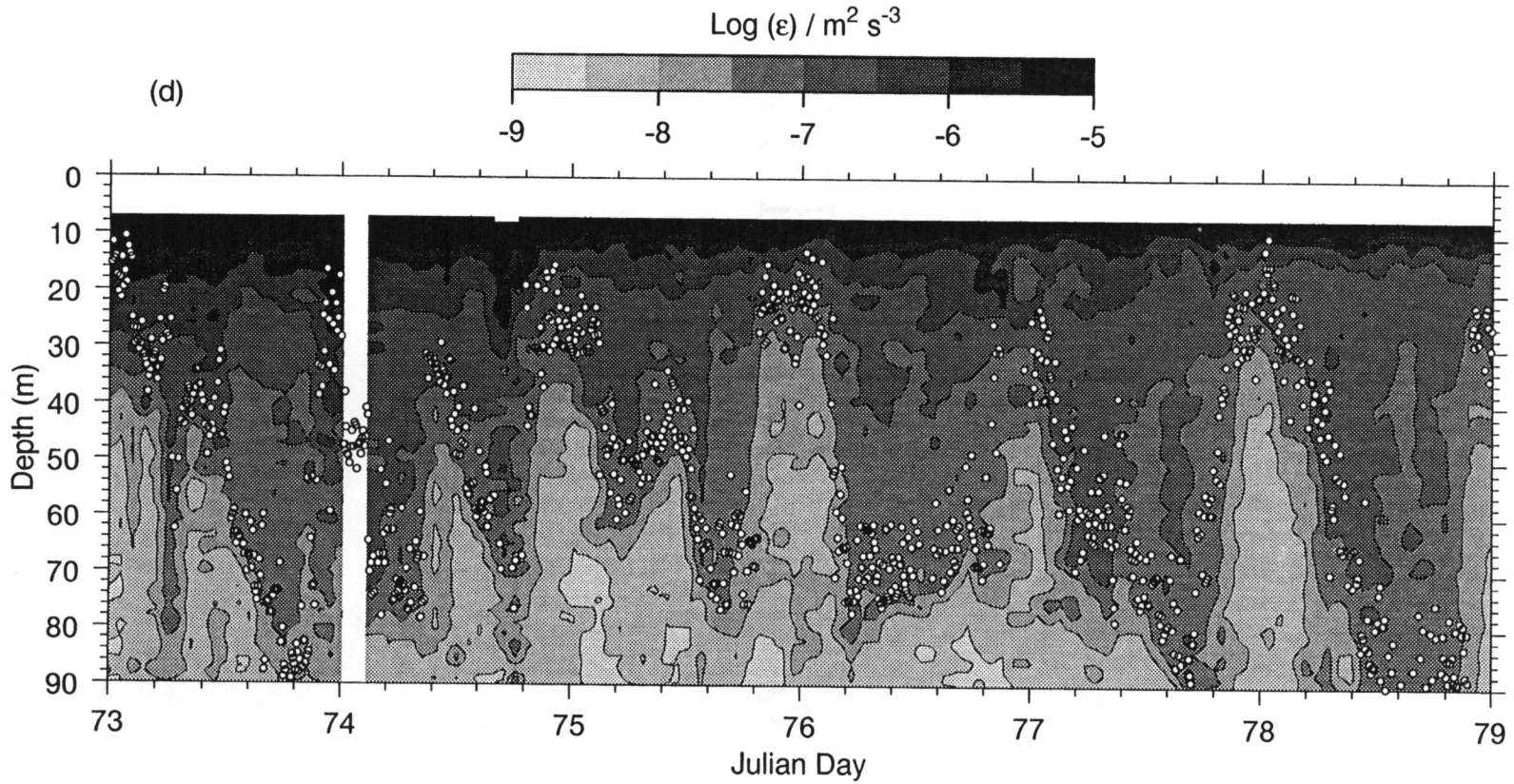

Figure II.2. (continued) Contours of the logarithm of hourly averaged turbulence kinetic energy dissipation rate estimates, ϵ, are presented in panel (d) (shadings are at half decade increments).

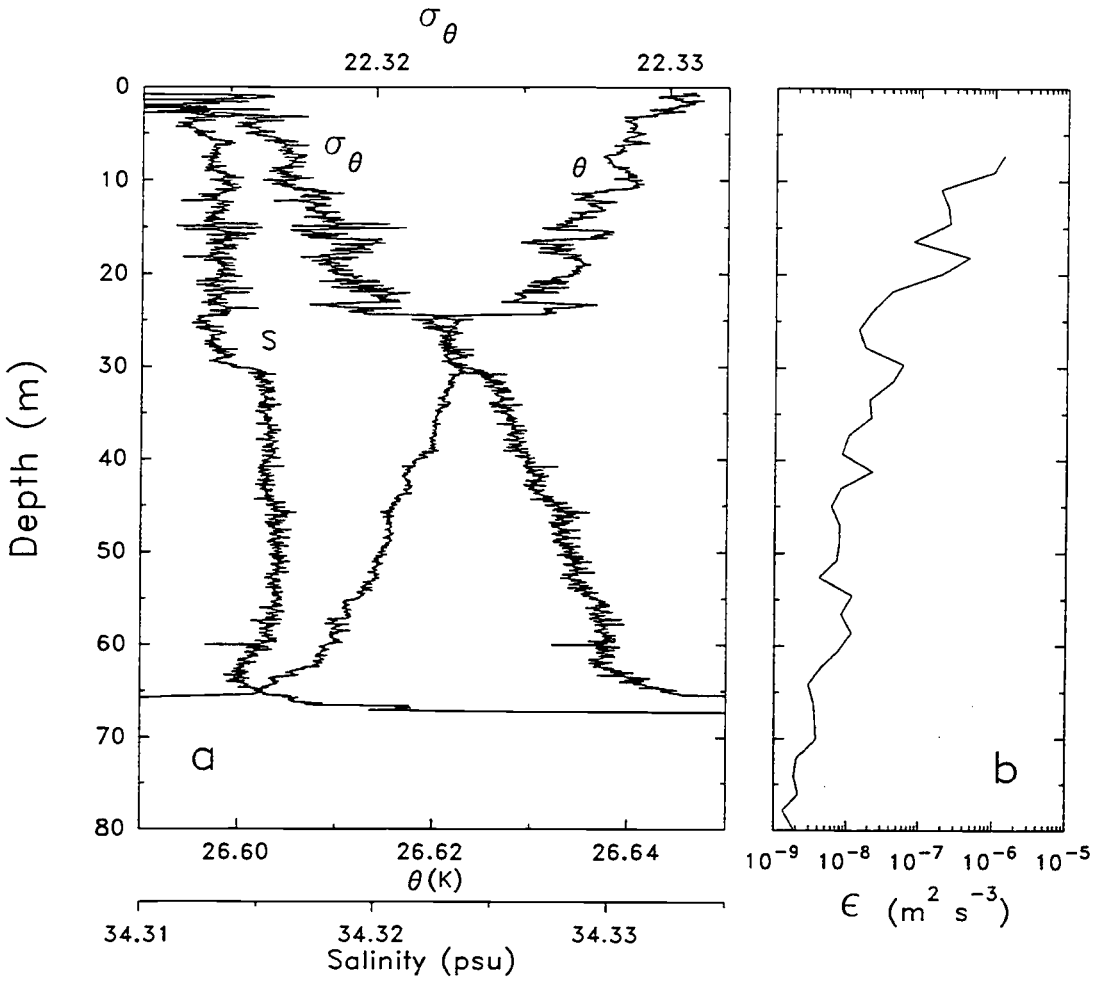

Figure II.3. Typical daytime vertical profiles (a) of θ, salinity, and σ_θ, and (b) of ϵ.

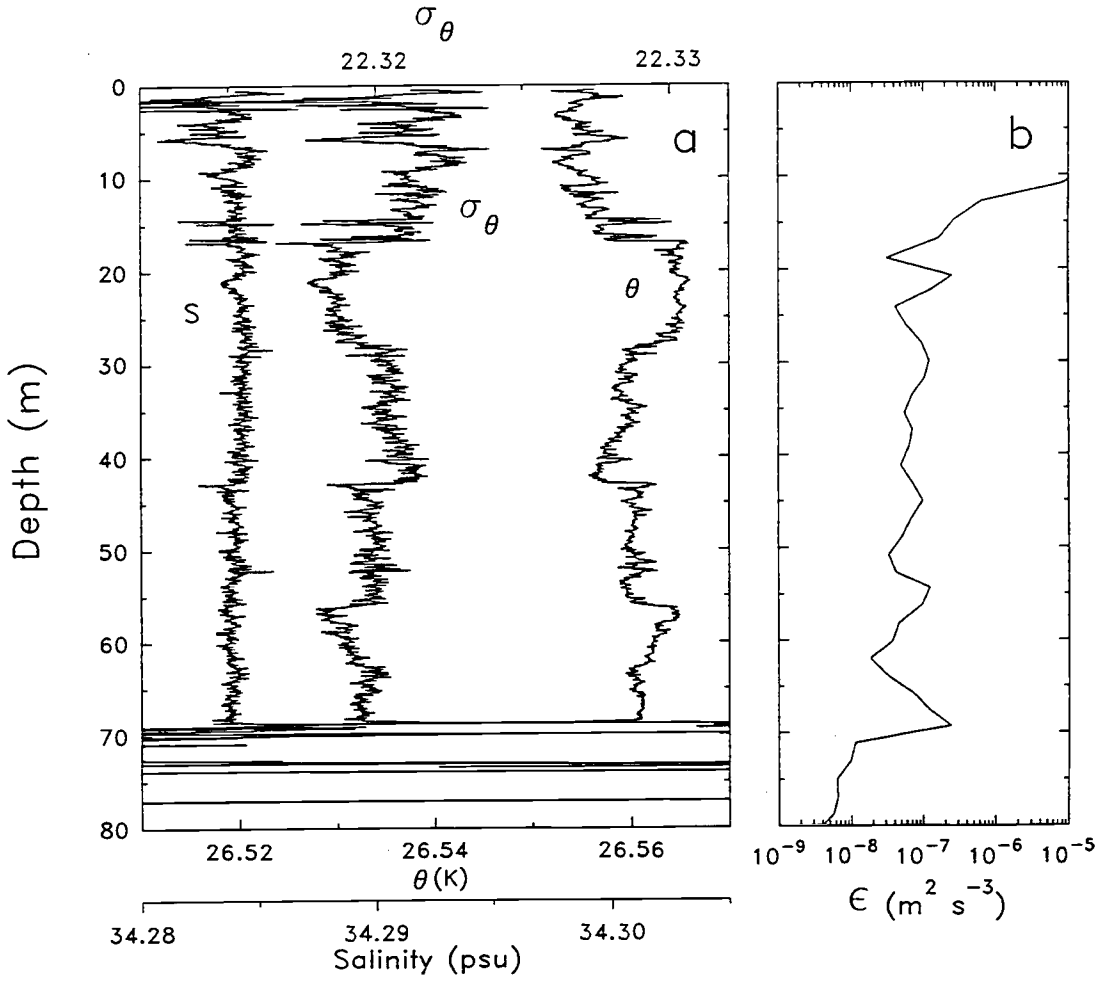

Figure II.4. Similar to Fig. II.3 but for nighttime. Note the relatively uniform profile of ϵ between 20 m and the base of the ML at 70 m, and the cool dense blob of water in the top 15 m.

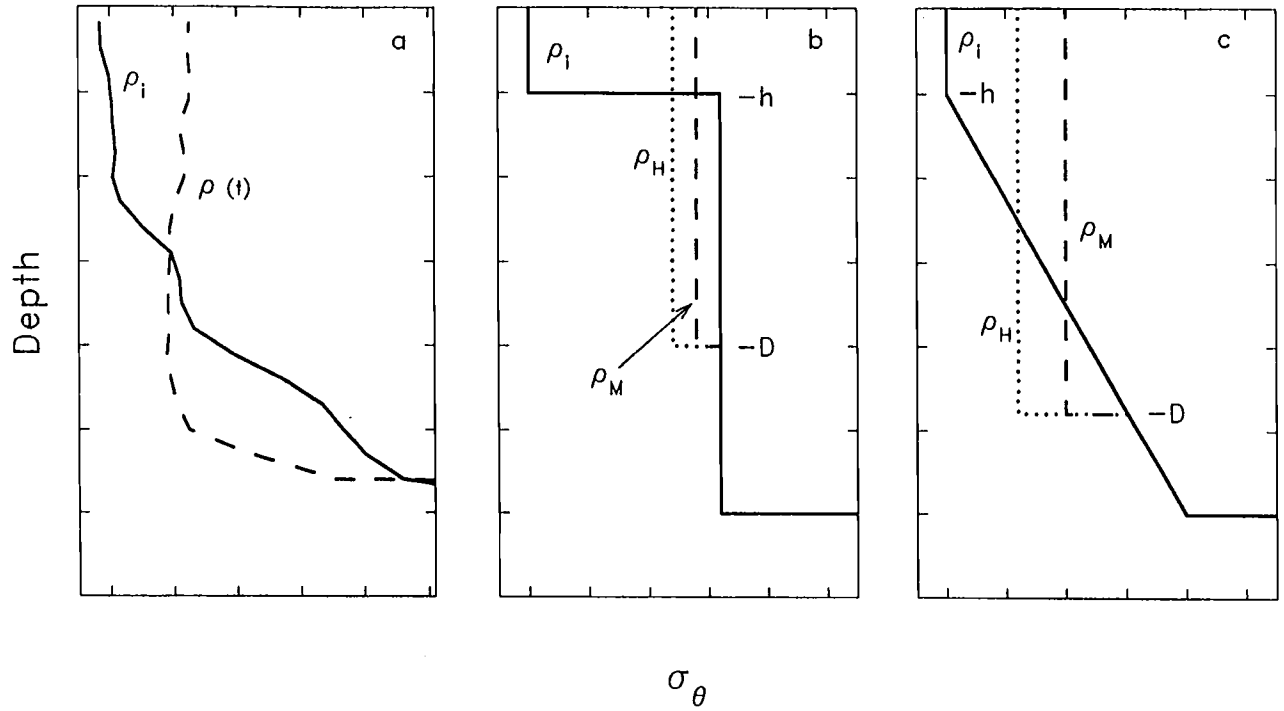

Figure II.5. (a) An example of a typical potential density profiles, ρ_i (solid line), observed just before the onset of convective conditions, and $\rho(t)$ (dashed line), observed at the completion of the deepening of the ML. (b) Schematic of the deepening of an initial two layer density structure. Three profiles are shown: ρ_i (solid line) is the initial density profile; ρ_H (dotted line) is the density profile resulting from the homogenization of ρ_i to a depth of $-D$; ρ_M (dashed line) is similar to ρ_H, however, it accounts also for the change in density due to the surface mass flux. ρ_H may represent wind mixing, while ρ_M may represent convective mixing. (c) Similar to (b) but for an initial density profile, ρ_i, where a shallow ML of depth h is atop a deeper layer in which density increases linearly with depth. Schematic (c) represents fairly well the deepening of the nighttime ML in our experiment. Density and depth scales are in arbitrary units.

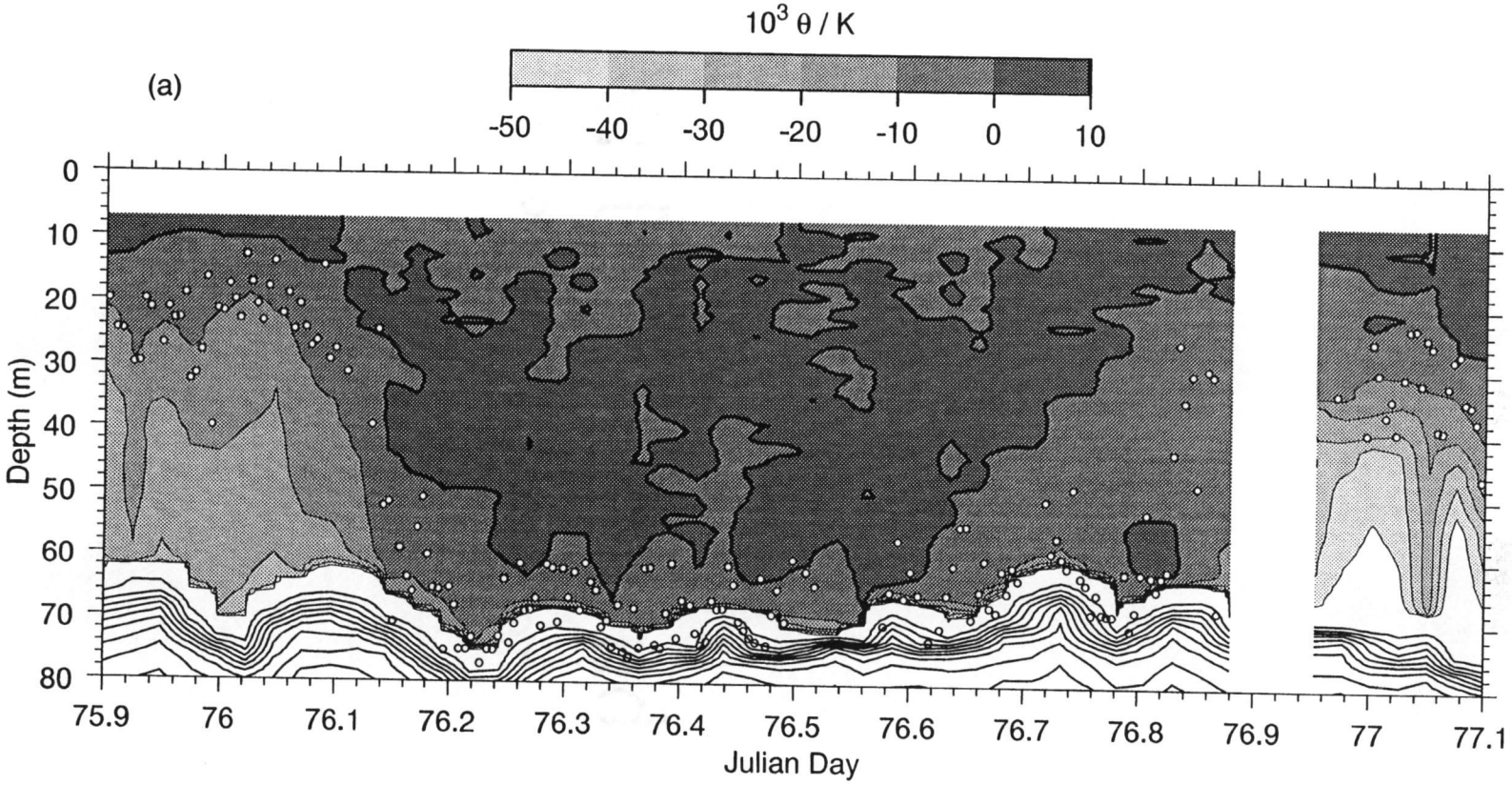

Figure II.6. Similar to Fig. II.2 but for referenced and 20-minute averaged data of one complete diurnal cycle (a) of θ, (b) of ϵ. The rapid deepening is evident in both θ and ϵ, starting at time 76.06 and reaching its final depth at 76.17 (i.e. about two and a half hours later).

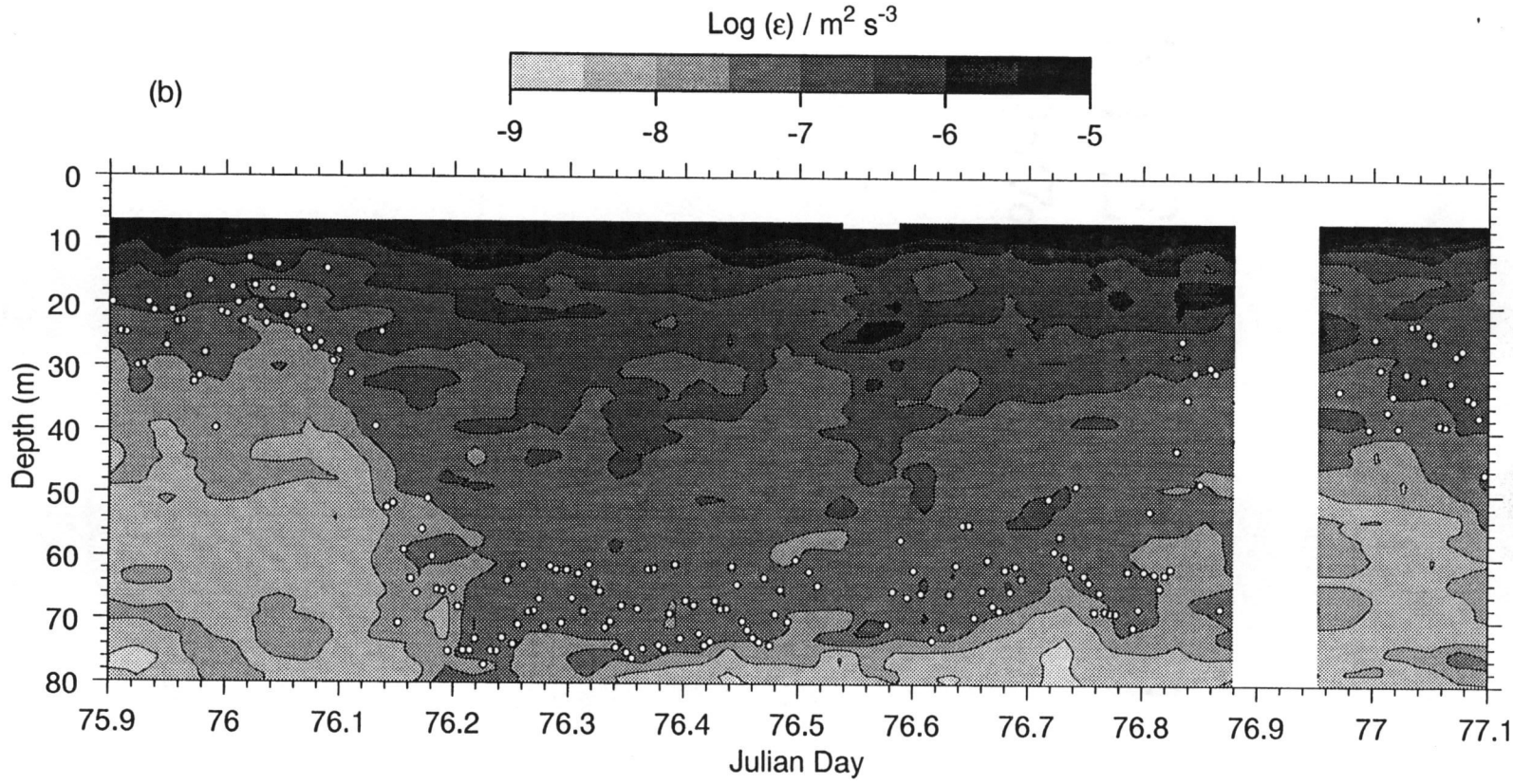

Figure II.6. (continued)

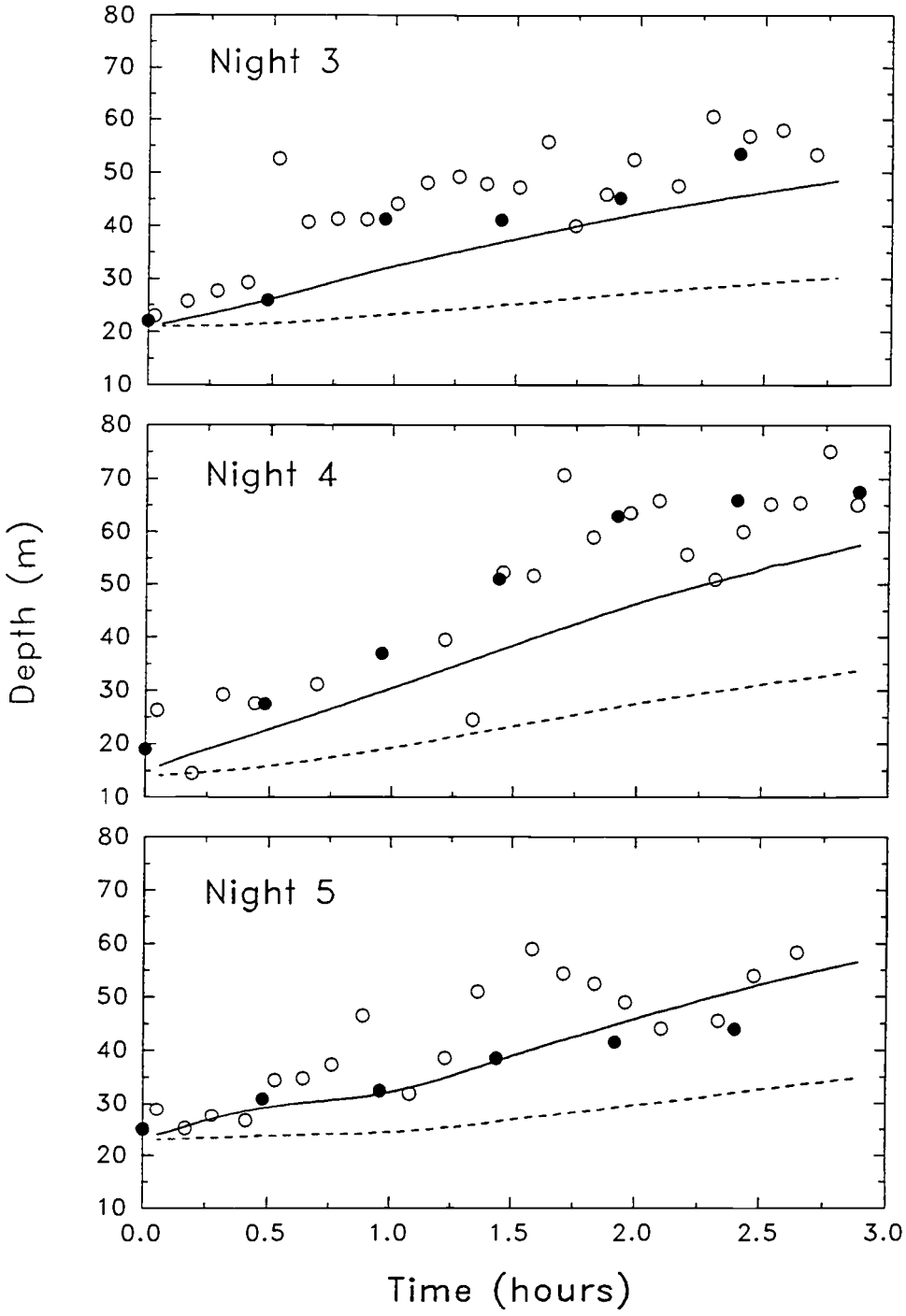

Figure II.7. ML depth, $D(t)$, as a function of time. The dashed line represents ML deepening due to convection without entrainment as predicted by (15), and the solid line represents convective entrainment deepening as predicted by (21). Observed ML depths were deduced from single profiles (hollow circles) and from the contour line $\sigma_\theta = 0.001$ kg m^{-3} of referenced and 20-minute averaged data (filled circles).

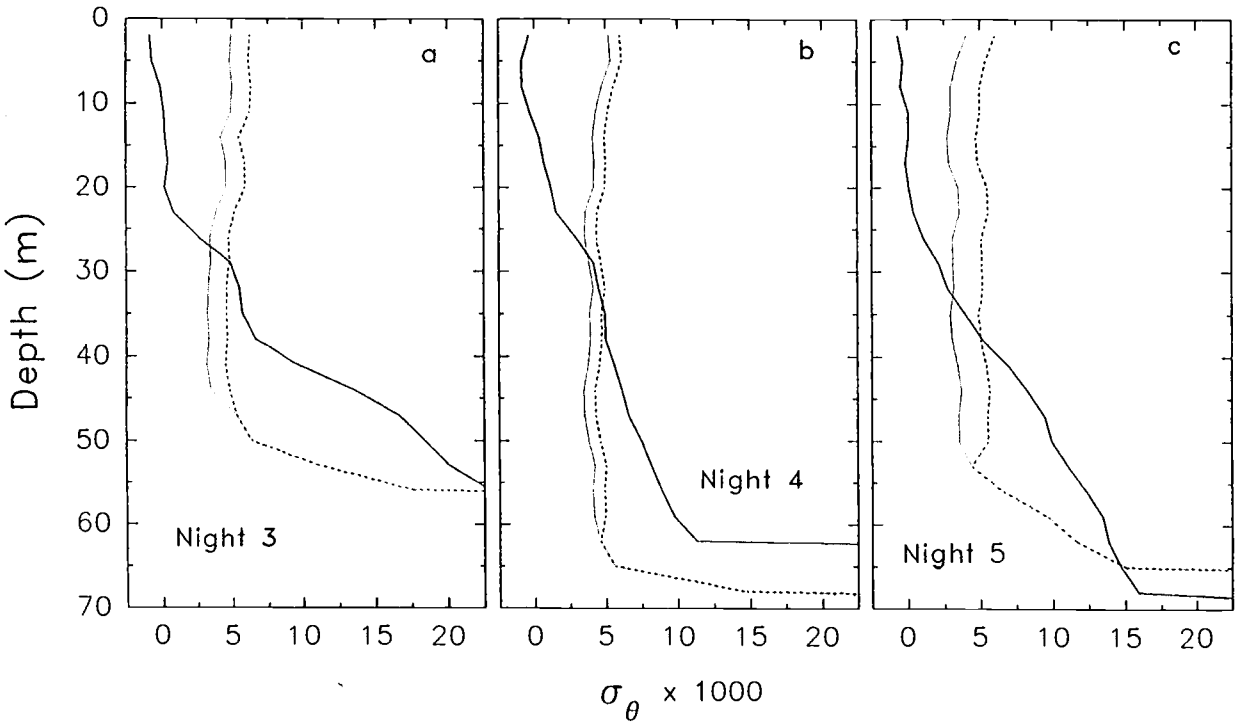

Figure II.8. Potential density profiles at the beginning and at the end of the deepening phase of the three nights of our experiment. The solid line represents the initial density profile, ρ_i, just before the onset of convective conditions. The dotted line represents the density profile ρ_H, and has the shape of the observed density profile at the end of the deepening period, however, without the change in density due to the surface mass flux. The change in density is accounted for in the density profile, ρ_M, represented by the dashed line (see also text). Each profile is a 20-minute average of referenced potential density profiles (about 3 profiles); ρ_i is centered at about 15 minutes before J_b^0 changed sign from negative to positive (i.e. the onset of convective conditions), and ρ_H and ρ_M are centered at about 2.5 hours after the onset of convective conditions. During this time period J_b^0 increased roughly linearly with time.

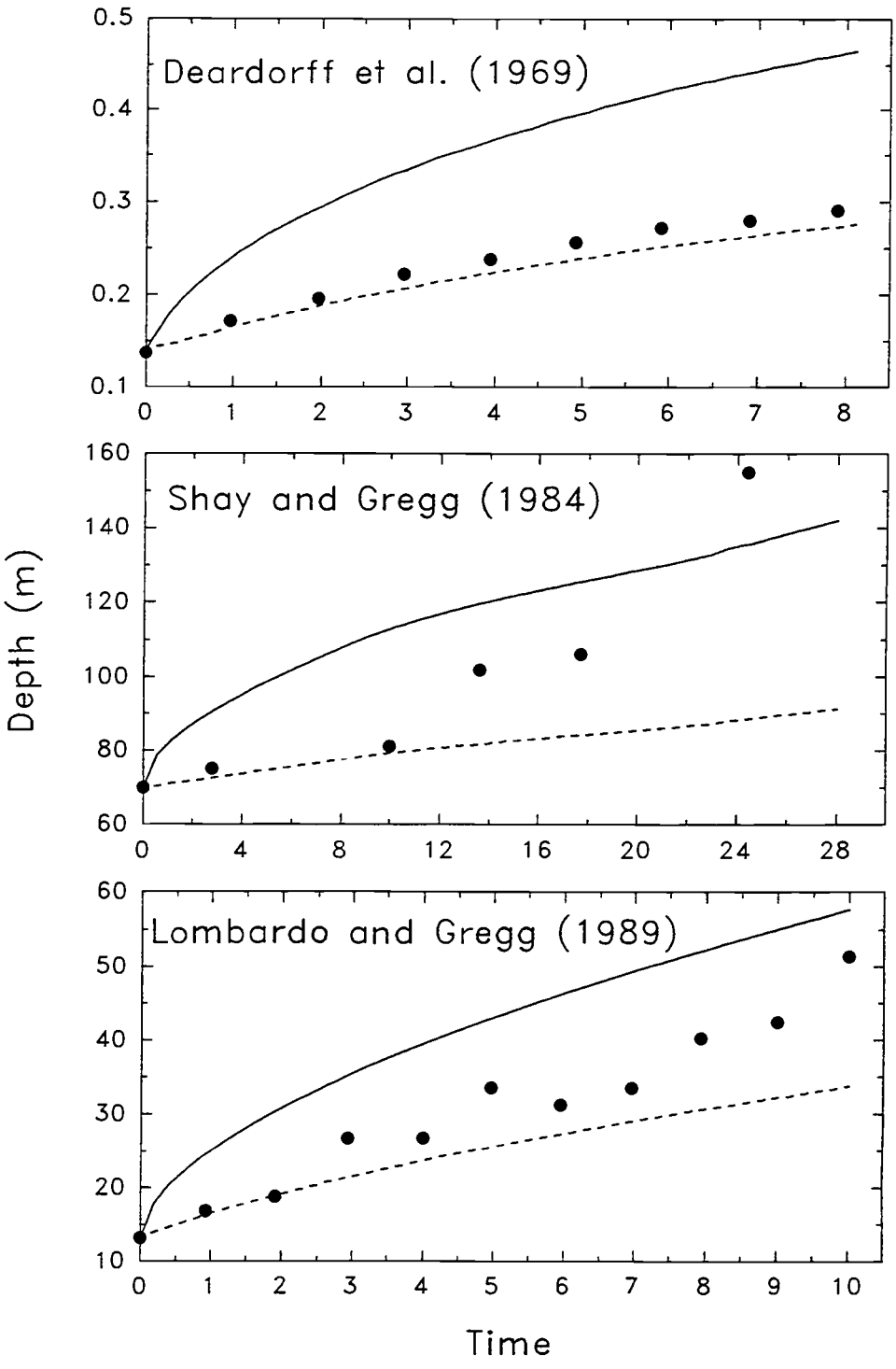

Figure II.9. Similar to Fig. II.7 but for the convective deepening of a ML in a laboratory experiment (top panel), in a warm-core Gulf stream ring (middle panel), and in a diurnal OBL (bottom panel). Filled circles represent the observed ML depths. Time scale for the top panel is in minutes and for the middle and bottom panels in hours.

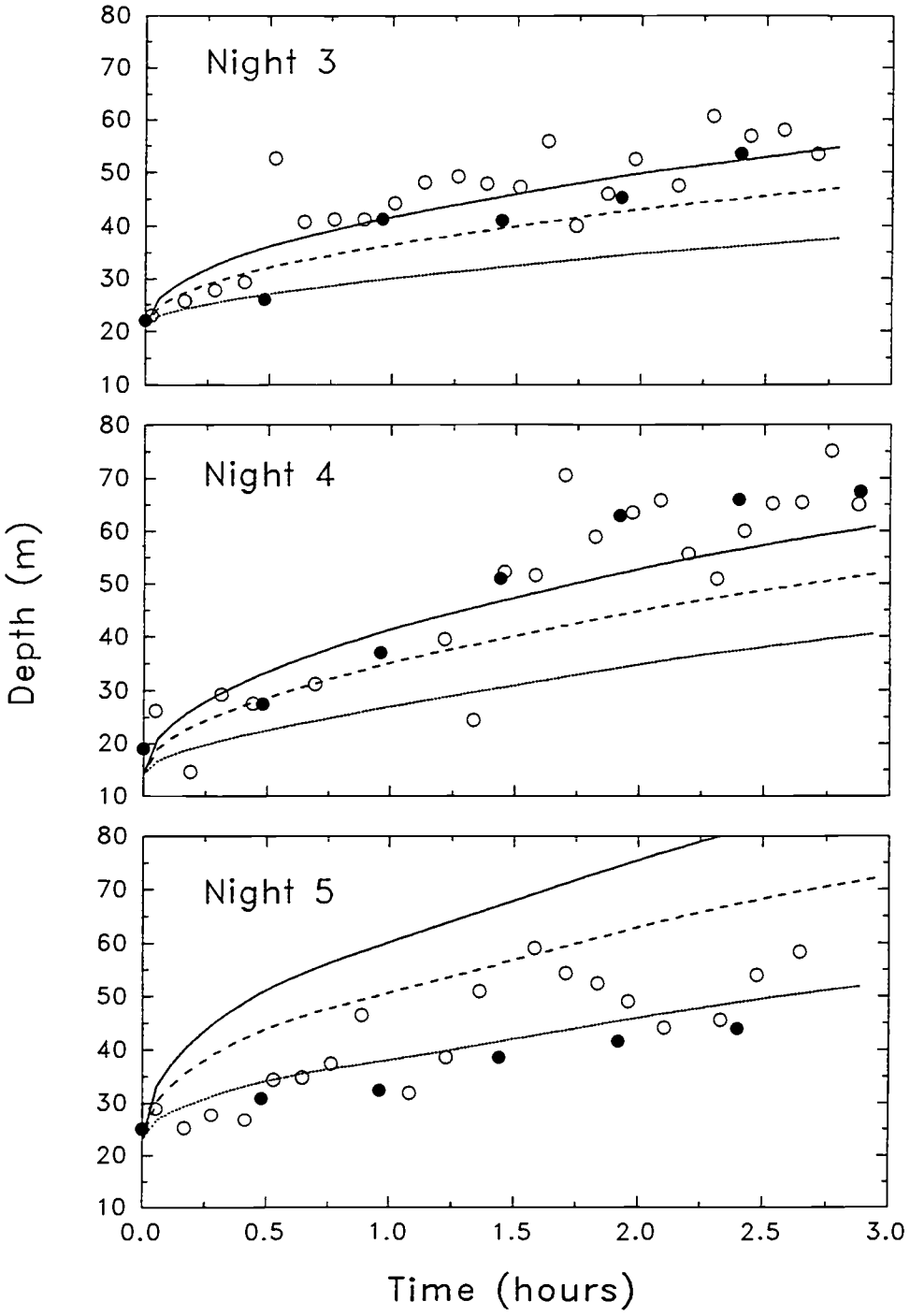

Figure II.10. ML depth as a function of time. Estimates of $D(t)$ were made using (34) with $m_c = 0.20$, $m_c = 0.26$, and $m_c = 0.21$ for nights 3, 4, and 5, respectively. The lower (dotted line), middle (dashed line), and upper (solid line) curves for each night represent the predicted ML depth for $m_w = 0.0012$, $m_w = 0.005$, and $m_w = 0.01$, respectively. Observed ML depths are the same as in Fig. II.7.

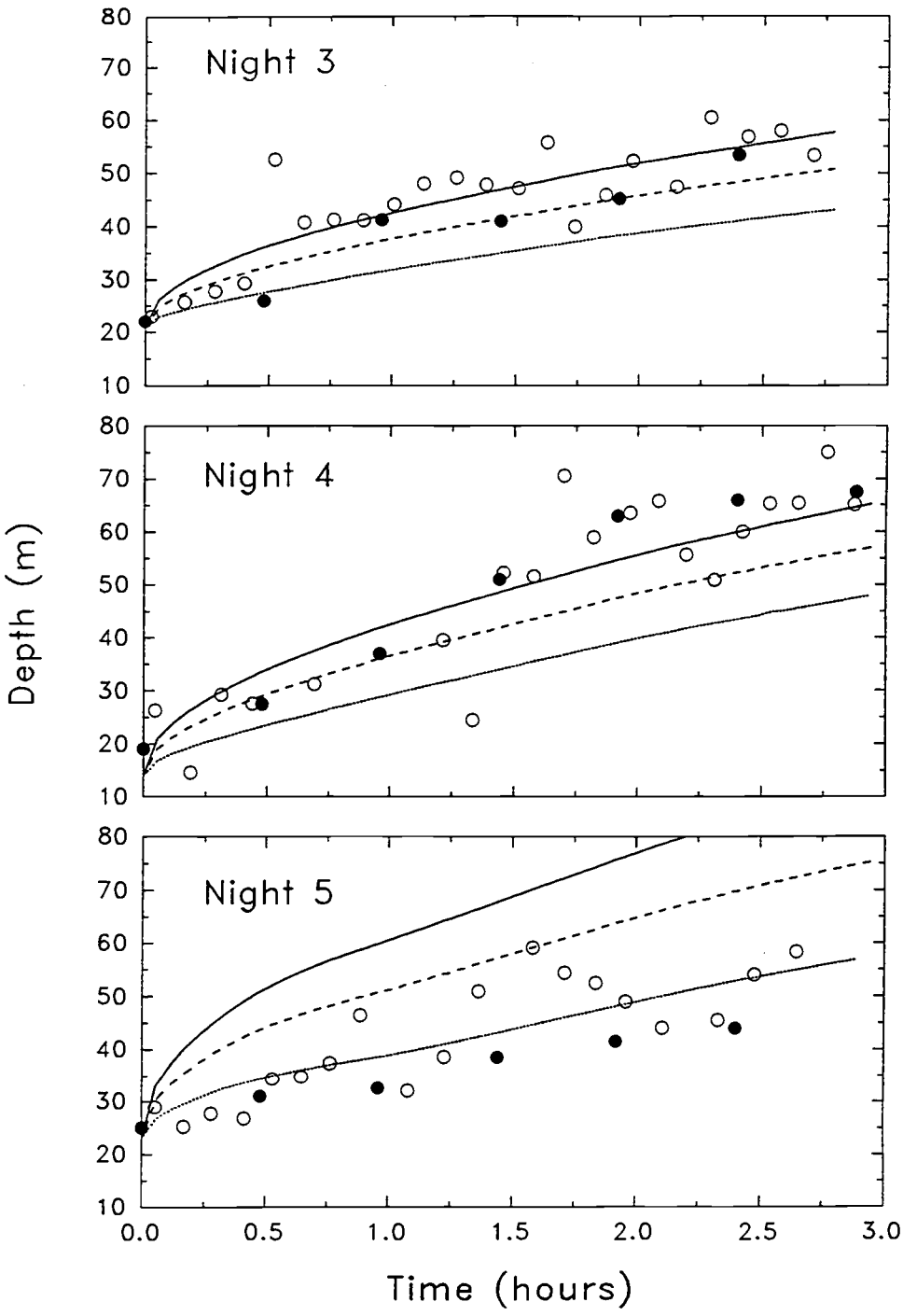

Figure II.11. Similar to Fig. II.10 but with $m_c = 0.5$ for the part of energy available for mixing due to convective forcing. This value of m_c, deduced from laboratory (Deardorff et al. 1969) and atmospheric (Andr'e et al. 1978) experiments, may better represent the actual part of convective forcing going into ML deepening.

Table II.1. Daytime and nighttime averages of the surface wind stress, τ_0, the difference between the air temperature (T_{air}; measured from the R/V *Wecoma*'s mast at 8-m height) and the sea surface temperature (SST; measured from the ship's hull mounted Doppler's thermistor at 5-m depth), $T_{air} - SST$, the shortwave solar radiation, J_q^{sw}, the latent heat of evaporation, J_q^e, the net surface heat flux, J_q^0, the salinity contribution to the surface buoyancy flux, J_s^0, the net surface buoyancy flux, J_b^0, the Monin-Obukhov length, $L \equiv -u_*^3/\kappa J_b^0$ (where $u_* \equiv \sqrt{\tau_0/\rho}$, and $\kappa = 0.4$ is von Kármán's constant), and the significant wave height, H_s (from R/V *Wecoma*'s ship's officers' log).

	τ_0	$T_{air} - SST$	J_q^{sw}	J_q^e	J_q^0	$10^7 J_s^0$	$10^7 J_b^0$	L	H_s (m)	
	N m^{-2}	°C	W m^{-2}	W m^{-2}	W m^{-2}	m^2 s^{-3}	m^2 s^{-3}	m	Swell	Wind-waves
night 1	0.08	−1.84	–	167	212	0.16	1.64	-10.6	2.4	0.8
day 1	0.12	−0.84	−850	203	−585	0.20	−3.85	8.0	2.4	0.7
night 2	0.10	−1.23	–	168	211	0.16	1.65	-14.2	2.7	0.9
day 2	0.11	−1.02	−757	190	−507	0.18	−3.60	7.9	2.4	0.9
night 3	0.08	−1.53	–	126	171	0.12	1.43	-11.7	2.0	0.7
day 3	0.04	−0.69	−559	123	−392	0.12	−2.77	2.3	1.7	0.6
night 4	0.07	−0.88	–	133	166	0.13	1.35	-10.8	1.8	0.6
day 4	0.12	−0.68	−751	183	−524	0.18	−3.70	9.2	1.9	0.9
night 5	0.11	−0.73	–	163	205	0.16	1.54	-17.3	2.2	0.9
day 5	0.07	−1.36	−531	123	−377	0.12	−2.91	5.9	2.2	0.9
night 6	0.11	−0.86	–	179	199	0.18	1.61	-17.5	2.1	0.9
day 6	0.09	−0.28	−399	149	−230	0.15	−1.68	11.4	2.1	0.9

Table II.2. Estimates of the different terms of the energy budget during deepening of the nightly convective ML (units are J m^{-2}). W_H is the amount of work needed to mix the initial density profile, $\rho_i(z)$, into the final density profile $\rho_H(z,t)$ (see also section II.5.5. and Fig. II.8). $DISS1$ and $DISS2$ are the vertically and time integrated dissipation rates in the ML; $DISS1$ was calculated from (25) with $r = 0.44$ (Lombardo and Gregg 1989), while $DISS2$ was calculated using (26) and the observed values of ϵ. BF is the amount of available PE released due to the sinking of the dense surface water. $R1 = W_H + DISS1 - BF$ and $R2 = W_H + DISS2 - BF$ represent the additional amount of energy needed to balance the budget (see eqn. 24). The time interval used for calculations started when J_b^0 changed sign from negative (daytime) to positive (nighttime) and ended about 2-3 hours later when the ML reached its quasisteady depth.

Night	W_H	$DISS1$	$DISS2$	BF	$R1$	$R2$
3	33	16	240	20	29	253
4	43	14	211	19	38	235
5	30	27	156	33	24	153
Mean	34	19	202	24	29	212

Table II.3. Similar to Table II.2 but for data from 4 other convective boundary layer experiments (units are J m^{-2}). $DISS1$ for the experiments of Shay and Gregg and Lombardo and Gregg was calculated using (25) with $r = 0.45$ and $r = 0.44$, respectively. $DISS2$ was estimated as follows: for the first term in (26) (the depth range $z_0 > z > -D$) we used the same parameterization for ϵ as in (25); for the second term in (26) (the depth range $0 > z > z_0$) we used $\epsilon(z_0) = \epsilon(-20\ \text{m}) = 1 \times 10^{-6}\ \text{m}^2\ \text{s}^{-3}$ for Shay and Gregg's experiment, and $\epsilon(z_0) = \epsilon(-10\ \text{m}) = 1 \times 10^{-6}\ \text{m}^2\ \text{s}^{-3}$ for Lombardo and Gregg's experiment. No dissipation measurements were available for the experiments of Deardorff et al. and André et al. However, if convection was the only forcing mechanism (as was the case for the laboratory experiment of Deardorff et al. and for the atmospheric experiment of André et al. in the convective ABL above the surface layer, where wind stress may have dominated), then the dissipation term may be estimated as $DISS1 = BF - W_H$. This results in $\overline{\epsilon} = 0.35 J_b^0$ and $\overline{\epsilon} = 0.39 J_b^0$ for these two experiments, respectively, and compares favorably with $\overline{\epsilon} = 0.2 - 0.6 J_b^0$, found in the numerical simulations of André et al. A somewhat higher value of $\overline{\epsilon} = 0.64 J_b^0$ was observed by Caughey and Palmer (1979) during the 1973 Minnesota and the 1976 Aschurch experiments. The large differences in the magnitude of estimates of similar quantities in different experiments (see also Table II.2) is due to differences in magnitude of the buoyancy flux and integration periods.

Reference	W_H	$DISS1$	$DISS2$	BF	$R1$	$R2$
Shay and Gregg (1984a,b)	2089	1287	3039	1987	1389	3141
Lombardo and Gregg (1989)	87	63	412	114	36	385
Deardorff et al. (1969)	0.11	0.13	—	0.24	—	—
André et al. (1978)	15570	13095	—	28665	—	—

Table II.4. Range of coefficients describing the energy transfer from the wind to the ML; m_w is the ratio between the rate of change of PE of the ML, E_{PE}, and the wind energy flux at 10 m height, $E_{10} = \tau_0 U_{10}$ (m_w is also referred to as the mixing efficiency); n_w is the ratio between the total rate of energy transferred to the ML, E_{ML} (including the energy flux lost by surface wave breaking), and the wind energy flux. The estimate of Longuet-Higgins is of the energy lost by wave breaking and is based on a statistical-theoretical model and the assumption of an equilibrium spectrum of wind-generated waves. Laboratory measurements of breaking waves suggest that most of the wave energy lost through breaking goes into turbulence (e.g. Rapp and Melville 1990). The estimates of Richman and Garrett represent the actual rate of energy imparted to the ML through the surface wave field and are based on a model for the momentum and energy transfer by the wind to the surface waves and the ML, and on field and laboratory experiments. The mixing efficiency estimated by Leibovich and Paolucci is based on a model in which the role of langmuir circulation as the sole mixing mechanism was examined.

Reference	$m_w = E_{PE}/E_{10}$	$n_w = E_{ML}/E_{10}$
Kato and Phillips (1969)	0.0015	-
Longuet-Higgins (1969)	-	0.04
Turner (1969)	0.01	-
Miropolskii (1970)	-	0.01-0.06
Denman (1973)	0.0012	-
Halpern (1974)	0.003-0.004	-
Alexander and Kim (1976)	0.003	-
Garnich and Kitaigorodskii (1977)	-	0.01-0.08
Garwood (1977)	-	0.009
Richman and Garrett (1977)	-	0.04-0.09
Leibovich and Paolucci (1980)	0.005-0.016	-

Table II.5. Energy budget terms (in J m^{-2}) calculated from our data and data from two other oceanic experiments. Values of W_H and BF were defined earlier and are rewritten here from Tables II.2 and II.3. Values in column ABF represent the part of the surface buoyancy flux available for ML deepening and were calculated as $ABF = BF - DISS1$ using the estimates of BF and $DISS1$ from Tables II.2 and II.3. The column $\int m_w E_{10}\, dt$ represents the amount of wind energy used to increase the PE of the ML. The range of values results from the range in the estimates of m_w (Table II.4) (the estimates of $\int m_w E_{10}\, dt$ below do not include mixing due to Langmuir cells). The column $\int n_w E_{10}\, dt$ represents the *total* amount of wind energy entering the ML. The range of values results from the range in the estimates of n_w (Table II.4).

Source	W_H	ABF	$\int m_w E_{10}\, dt$	$W_H + DISS2$	BF	$\int n_w E_{10}\, dt$
Night 3	33	4	5-43	273	20	39-389
Night 4	43	5	4-36	254	19	32-324
Night 5	30	6	8-65	186	33	58-583
Mean	34	5	6-50	236	24	45-454
Shay and Gregg (1984a,b)	2089	700	150-1250	5128	1987	1125-11250
Lombardo and Gregg (1989)	87	51	9-72	449	114	65-648

Table II.6. Summary of various formulations for the ML depth, $D(t)$ (see section II.7). The general formula for wind forcing, convective forcing (without and with entrainment), and combined wind and convective forcing are presented in the first column. The second column presents $D(t)$ for the special case of an initial linear density profile where $\gamma = -d\rho_i/dz$. The third column presents explicit solutions of the ML depth as a function of time for the special cases of a constant wind energy flux, E_{10} =constant, and a linearly increasing buoyancy flux, $J_b^0 = at$. $S_w \equiv \int_0^t E_{10}(t')\,dt'$ and $S_c \equiv \int_0^t \rho J_b^0(t')\,dt'$ are the wind and convective forcing functions, respectively. m_w and m_c represent the fraction available for ML deepening from wind and convective forcing, respectively.

Forcing	General Formula	Initial linear density	E_{10}=constant; $J_b^0 = at$
Wind	$-g\int_{-D(t)}^{0}\rho_i(z)\left[z+D(t)/2\right]dz = m_w S_w(t)$	$D(t) = \left((12m_w/g\gamma)S_w(t)\right)^{1/3}$	$D(t) = (12m_w E_{10}/g\gamma)^{1/3}t^{1/3}$
Convection (no entrainment)	$gD\rho_i\left(-D(t)\right)$ $-g\int_{-D(t)}^{0}\rho_i(z)\,dz = S_c(t)$	$D(t) = \left((2/g\gamma)S_c(t)\right)^{1/2}$	$D(t) = (a\rho/g\gamma)^{1/2}t$
Convection (with entrainment)	$-g\int_{-D(t)}^{0}\rho_i(z)\left[z+D(t)/2\right]dz = m_c(D(t)/2)S_c(t)$	$D(t) = \left((6m_c/g\gamma)S_c(t)\right)^{1/2}$	$D(t) = (3m_c\rho a/g\gamma)^{1/2}t$
Combined (convection+wind)	$-g\int_{-D(t)}^{0}\rho_i(z)\left[z+D(t)/2\right]dz = m_c(D(t)/2)S_c(t) + m_w S_w(t)$	$D^3(t) - (6m_c/g\gamma)S_c(t)D(t) - (12m_w/g\gamma)S_w(t) = 0$	$D^3(t) - (3m_c\rho at^2/g\gamma)D(t) - (12m_w E_{10}t/g\gamma) = 0$

III. THE SUPERADIABATIC SURFACE LAYER OF THE OCEAN DURING CONVECTION

Abstract

Clear identification of the relatively weak superadiabatic potential temperature gradient in the ocean surface layer during convection has been made with the help of intensive vertical profiling measurements at an open ocean site. In the surface layer the superadiabatic gradient, with a mean value of -1.8×10^{-4} K m^{-1}, was a consistent feature of the convective boundary layer persisting throughout each of six consecutive nights. In the well mixed layer, below the surface layer, the observed potential temperature was nearly constant and turbulent kinetic energy (TKE) dissipation rate approximately balanced the production of TKE by the buoyancy flux through the sea surface. In the surface layer the TKE dissipation rate was systematically larger than the production of TKE predicted by wind stress and mixed layer similarity scaling.

III.1. Introduction

In comparison to the convective boundary layer (CBL) of the ocean, the vertical structure of the atmosphere during convection is well-known (Driedonks and Tennekes 1984; Stull 1988). The structure of the atmospheric CBL consists of four layers, each governed by different physics. At the surface is a thin microlayer of air (O(1 cm)) in which molecular processes dominate: molecular conduction of heat, viscous transfer of momentum and molecular diffusion of passive tracers are responsible for the transport between the surface and the lowest few millimeters of the atmosphere. The potential temperature (θ) decrease across the microlayer is very large with temperature gradients on the order of -1×10^4 K m^{-1}. Above the microlayer is an unstable superadiabatic atmospheric surface layer (ASL) (O(10-100 m)) with temperature gradients on the order of $-1 \times (10^{-2} - 10^{-1})$ K m^{-1} (the terms potential temperature, adiabatic and superadiabatic are defined in the caption to Fig. III.1). Within the ASL large scale thermal convection is constrained by proximity to the lower boundary and heat transport is by small scale turbulent eddies; mixing is by forced convection and appears to be explained by Monin-Obukhov similarity scaling (Driedonks and Tennekes 1984; Stull 1988); turbulent fluxes of momentum and heat are constant with height to within 20% throughout the layer (Haugen et al. 1971). Above the ASL is an atmospheric mixed layer (AML; O(1 km)) in which the change of potential temperature with height is small, mixing is dominated by large scale, convectively-driven thermal plumes, and mixing by free convection appears to follow mixed layer similarity scaling (Stull 1988). Atop the AML

is a fourth layer, the entrainment zone, in which intermittent turbulence, overshooting thermals, Kelvin-Helmholtz waves, internal waves and sometimes clouds may be found.

The oceanic analogue to the microlayer is the cool skin (Paulson and Simpson 1981). The cool skin has an average thickness of a few millimeters and temperature gradients of about -300 K m^{-1} (Khundzhua et al. 1977). Recent measurements of turbulence during convection have confirmed the existence of well-mixed layers in the ocean (OML for ocean mixed layer; Shay and Gregg 1986; Lombardo and Gregg 1989), and in a fresh water reservoir (Imberger 1985; Brubaker 1987) which appear to obey mixed layer scaling. However, to date there have been no theoretical or observational studies which provide a consistent framework for an oceanic surface layer (OSL). While there have been hints of anomalously cool water above the mixed layer (Brubaker 1987; Imberger 1985; Shay and Gregg 1986), in each case the temporal and spatial intermittency of these events was not well resolved. If (as suggested by Brubaker, 1987) the isolated cool parcels of fluid near the surface in individual profiles represent "thermals" which form at the surface and subsequently sink into the mixed layer, it might be highly improbable to resolve individual events by profiling measurements. This would also be true if these cool parcels are indicative of the coherent structures near the ocean's surface suggested by Soloviev (1990) or Thorpe et al. (1991). To extract the *mean* structure of the surface layer, our approach was to examine a large number of profiles obtained under conditions during which nighttime convection generated a clear mixed layer where TKE dissipation was approximately equal to the surface buoyancy flux. While acknowledging that the physics of the events in the OSL are not well resolved, a consistent

mean structure persisting over six separate nights was found. Not entirely unexpected, the mean temperature structure of the CBL in the ocean was found to closely resemble that in the atmosphere, at least qualitatively.

Some aspects of the dynamics of the OSL can be deduced from measurements of TKE dissipation rate. It has been suggested (e.g. see Soloviev et al. 1988; Lombardo and Gregg 1989) that, in the OSL, the variation of TKE dissipation rate with depth, $\epsilon(z)$, is proportional to ${u_*}^3/\kappa z$, the production of TKE by surface winds (where $u_* = \sqrt{\tau/\rho_w}$ is the ocean surface friction velocity, τ is the surface wind stress, ρ_w is the density of seawater, $\kappa = 0.4$ is von Karman's constant and z is positive upwards). However others have found evidence for more intense mixing in this depth range (Kitaigorodskii et al. 1983; Gregg 1987). Our observations indicate $\epsilon(z)$ to be consistently larger than predicted by wind stress and mixed layer similarity scaling. Although the temperature structure of the OSL mimics that of the ASL, apparently the dynamics do not. Presumably this results from physical processes related to the proximity of a free surface in the OSL which do not apply to the ASL, most studies of which have been made over land.

Experimental details of our investigation are given in section III.2, followed by a description of the observations in section III.3. In section III.4 we discuss the results and show that these are consistent with recent towed temperature measurements by Soloviev (1990) and Thorpe et al. (1991) which have demonstrated some degree of order in a highly variable temperature field.

III.2. Experimental details

As part of the Tropic Heat experiment in 1987 a large set of hydrographic and turbulence profiles was made from the RV *Wecoma* in the upper Pacific ocean while steaming south toward the equator. The profiles were made using the Rapid-Sampling Vertical Profiler (RSVP) (Caldwell et al. 1985). The RSVP is a 120 cm long and 5 cm in diameter, cylindrical free-falling instrument tethered to the ship with a cable serving as data link and retrieval line. This instrument provides near-microscale measurements of temperature and conductivity (from which salinity and density were computed) and microscale velocity fluctuations (from which $\epsilon(z)$ was computed). The vertical resolution is < 1 cm, temperature resolution is 0.5 mK, salinity resolution is 0.6×10^{-3} psu, σ_t resolution is 0.0004 kg m^{-3} and the noise level of our estimates of $\epsilon(z)$ is less than 1×10^{-9} W kg^{-1}. Vertical profiles were made to a depth of 200 m at a nominal fall speed of the RSVP of 0.8 m s^{-1} while the ship was moving at about 2.5 m s^{-1}. Time interval between profiles was about 6-7 minutes . The hydrographic and turbulence measurements were complemented by continuous shipboard measurements of meteorological data. These included wind velocity, air temperature and humidity, solar and long wave radiation and sea surface temperature and conductivity (C. Paulson and F. Bahr, personal communication). Bulk aerodynamic formulae (Large and Pond 1981) were applied to the surface meteorological data to estimate surface values of wind stress, τ, heat flux, J_q^0, and buoyancy flux, J_b^0.

III.3. Observations

For the study presented here we have analyzed a series of 366 profiles made over 6 consecutive nights during March 1987 along 140°W between 17°N and 7°N. During these nights winds were moderate, varying on average between 7-9 m s^{-1}, the sea surface losing heat at a nightly rate of 166-212 W m^{-2} and J_b^0 was reasonably steady with values of $1.3 - 1.7 \times 10^{-7}$ W kg^{-1}. Nightly mean values of mixed layer depth, D, varied between 50.6 and 82.2 m and the Monin-Obukhov length scale, $L = -u_*^3/\kappa J_b^0$ (negative during convection), varied between -10.6 and -17.5 m (see Table III.1).

III.3.1. Profile to profile variability

A typical set of 10 consecutive vertical profiles of potential temperature made between 01:34 and 02:39 local time, is shown in Fig. III.1 (each profile was referenced to the mixed layer temperature by subtracting the average potential temperature in the mixed layer). The horizontal spatial separation between the profiles is on the order of 900 m. During this section winds were ENE averaging 8-9 m s^{-1} and wind waves and swell had significant wave heights of 0.5 and 2 m respectively. J_b^0 was $1.2 - 1.3 \times 10^{-7}$ W kg^{-1}, $L \sim -9$ m and the depth of the mixed layer was about 45 m. Although some of the profiles show well-mixed sections almost from the sea surface to the base of the mixed layer (e.g. last profile), most of them reveal considerable small scale variability and complexity. In the fourth, fifth and sixth profiles from the left, cold water blobs with a vertical extent from the surface to a depth of 5-12 m and with a temperature difference of -0.01 to -0.015 K, relative to the water below, can be clearly seen. Other profiles (e.g. the second and third from left) show slightly warmer water of about 0.004 K atop cooler water.

III.3.2. Hourly averages: diurnal progression

By averaging the referenced profiles into hourly bins, a clear picture of the temporal development of the oceanic CBL emerges. Fig. III.2 shows such a sequence throughout one diurnal cycle, starting at 14:30 local time and ending the following day at 12:30. It is evident that during daytime, when the surface of the ocean is heated by solar radiation, there is a persistent positive potential temperature gradient ($\partial\theta/\partial z$) throughout most of the upper ocean boundary layer, rendering it statically stable. With the change in sign of surface heat and buoyancy fluxes, during the transition from day to night, $\partial\theta/\partial z$ changes sign from positive to negative in about two hours. $\partial\theta/\partial z$ remains negative throughout the night in the upper 10-25 m (the OSL) until the transition from nighttime to daytime conditions occurs. Between the base of the OSL to the base of the mixed layer the potential temperature is nearly constant, i.e. $\partial\theta/\partial z \sim 0$.

III.3.3. Mean potential temperature and dissipation profiles during convection

To examine the mean structure of the oceanic CBL we considered profiles that were made at night, when the ocean surface was losing heat and J_b^0 was reasonably steady, starting 2 hours after sunset and ending 2 hours before sunrise. The referenced and averaged potential temperature profile from one particular night indicates the small but significant negative departure from the adiabat between the surface of the ocean and a depth of about 24 m, corresponding to about $2L$ (Fig. III.3). Within the superadiabatic layer, salinity was approximately constant within our measurement uncertainty so that potential density (σ_θ) changes were determined chiefly by θ, resulting in a statically unstable OSL. Below the OSL, to the base of the OML, θ

more closely followed an adiabat, although variations in $\partial\theta/\partial z$ are apparent. To demonstrate that the superadiabatic OSL was a consistent feature of all 6 nights in the experiment, we plotted the referenced and averaged profiles together on one plot in Fig. III.4. The mean value of $\partial\theta/\partial z$ within the OSL was -1.8×10^{-4} K m^{-1} over the range $2L < z < -0.5$ m (which covered the upper 20-30% of the CBL).

During nighttime, averaged values of $\epsilon(z)/J_b^0$ in the OML indicated a nearly constant value with depth throughout the mixed layer for each of the 6 nights ($-D < z < 2L$). Nightly means varied between 0.69 ($\pm$0.03) and 0.87 ($\pm$0.09); the mean value over all 6 nights was 0.81 (Table III.1). This value is slightly larger than results from other OML, 0.61 and 0.72 for the Bahamas and ring experiments respectively (Shay and Gregg 1986), 0.44 to 0.65 during different stages of the development of the diurnal OML (Lombardo and Gregg 1989) and 0.45 from the mixed layer of a fresh water reservoir (Imberger 1985). Although mixed layer scaling appears to apply within the OML, $\epsilon(z)$ in the OSL is much larger than either the production of TKE by surface winds ($u_*{}^3/\kappa z$), by surface buoyancy flux (J_b^0) or by their sum (Fig. III.5), as would be predicted by similarity scaling.

III.4. Discussion and conclusions

The existence of a statically unstable surface layer during convection in the ocean might be simply an indication of the slow response of the bulk of the mixed layer to changes in surface temperature caused by changing surface fluxes. In cooling the ocean from above, a superadiabatic temperature gradient must appear somewhere in the upper ocean to span the temperature difference across the surface and the mixed layer. In the few millimeters nearest to the surface, molecular conduction (governed by the fluid's molecular diffusivity $D_\theta \simeq 1.4 \times 10^{-7}$ m^2 s^{-1}) is the main heat transfer mechanism whereas turbulent transport takes over farther away from the surface (i.e in the OSL). In essence, there *must* be a superadiabatic layer because of the heat loss from the surface of the ocean (mainly due to evaporation) and the inability of the turbulence to mix the entire CBL rapidly enough for complete homogenization.

Towed temperature measurements in the upper ocean have yielded some insight into the horizontal (and vertical) structure of the temperature field near the surface (Soloviev 1990; Thorpe et al. 1991). During both stable (usually daytime) and convective (usually nighttime) conditions, the form of coherent structures in the OSL have been inferred by calculating the skewness, S, of the horizontal temperature gradients. Atmospheric and lab measurements in turbulent boundary layers suggest that the sign of the skewness of the temperature gradient measured in the mean flow direction, sgn$[S(\partial T/\partial x)]$, is given by sgn$[\mathbf{x}\cdot(\nabla T \times \omega)]$ (Gibson et al. 1977), where $\mathbf{x}$ is a unit vector in the mean flow direction, ∇T is the mean vertical temperature gradient (normal to the boundary) and ω is the vorticity of the mean flow (in a plane parallel to the boundary). Both studies (Soloviev 1990; Thorpe

et al. 1991) found sgn(S) > 0 in the upper few meters of the oceanic CBL. *If* the structure is as shown in their schematic diagrams, with a positive vertical shear of the mean flow, *then* sgn[$\mathbf{x}\cdot(\nabla T \times \omega)$]=sgn($S$) > 0 *requires* that $\partial T/\partial z < 0$ in the surface layer. Our result of a mean superadiabatic temperature profile (i.e $\partial\theta/\partial z < 0$) in the OSL during unstable convective conditions is consistent with the prediction of $\partial T/\partial z < 0$ and serves to strengthen the proposed structure of coherent eddies in the OSL presented by these authors.

The high dissipation rates in the OSL suggest an imbalance between the production of turbulence, as predicted by wind stress and mixed layer scaling, and the rate at which it is dissipated by viscous forces. This apparent imbalance might be explained by additional processes in the OSL due to the proximity to the free surface of the ocean. Near the free surface of the ocean, wave-induced mean drift may increase effective values of u_* (Churchill and Csanady 1983), Langmuir cells may introduce episodic mixing events (Thorpe 1985; Weller and Price 1988), and surface waves may contribute in a number of ways to intensify turbulence near the surface (Kitaigorodskii et al. 1983; Huang 1986). One or a combination of the above mechanisms might contribute to additional production of turbulence resulting in the high dissipation rates we observed in the OSL. It is also possible that turbulence and pressure transport terms in the TKE equation may have greater influence than we have previously considered. Thus, the physics governing the mixing is likely to be very complex due to the proximity of a free surface, as is suggested by the vertical structure of $\epsilon(z)$ in the OSL. However more observations are required to explain the behaviour of turbulence in the OSL and its proper scaling under different forcing conditions.

Combining the results of this study with previous results, there appears to be a consistent vertical structure of the oceanic CBL which includes 4 regimes. Proceeding toward the surface these are:

i) Stable layer (thermocline) in which $\partial\theta/\partial z > 0$.

ii) Mixed layer in which $\partial\theta/\partial z \sim 0$ and $\epsilon(z)/J_b^0 \sim$ constant .

iii) Superadiabatic surface layer in which $\partial\theta/\partial z < 0$ and $\epsilon(z)$ increases toward the free surface more rapidly than accounted for by the production rates of TKE by surface winds and buoyancy flux at the sea surface.

iv) Cool skin, at the top centimeter or so of CBL, which could not be resolved by our measurements.

The mean value of the potential temperature gradient for all six nights in the superadiabatic layer was $\partial\theta/\partial z \sim -2\times10^{-4}$ K m^{-1}. Although individual vertical profiles of potential temperature are highly variable within the OSL during convection (Fig. III.1), the results of Soloviev (1990) and Thorpe et al. (1991) suggest that the structure has a degree of organization which provides hope in understanding the physics. Our results indicate that the *mean* structure resembles that of the ASL during convection (Fig. III.6 and Table III.2) and complement observations of time/space variability within the OSL.

Acknowledgments. We are grateful to the Captain and crew of the RV *Wecoma* for their support during the experiment and to Dave Hebert, Murray Levine and Laurie Padman for their helpful comments. This work was supported by National Science Foundation grants OCE-8608256 and OCE-8716719.

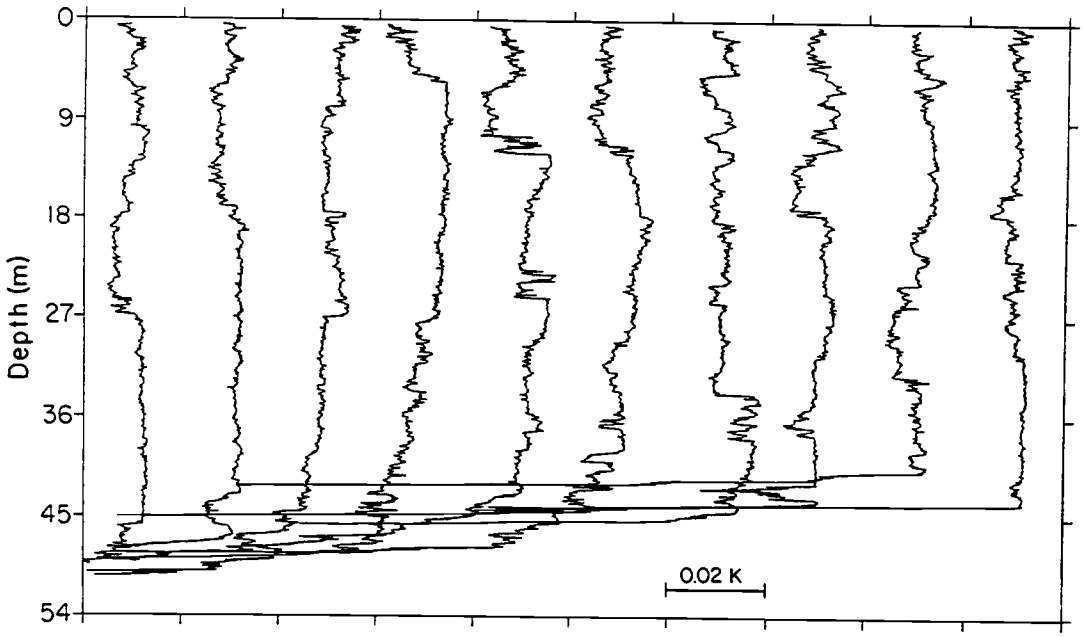

Figure III.1. A typical set of 10 consecutive vertical potential temperature (θ) profiles during nighttime convective conditions. The profiles were taken between local time 01:34 and 02:39 and the horizontal spacing between profiles is about 900 m. Each profile was referenced to the temperature in the mixed layer by subtracting the average potential temperature in the mixed layer ($-D < z < 2L$). Profiles are offset by 0.02 K. The potential temperature θ is the temperature the fluid parcel would have if it was expanded or compressed adiabatically (i.e. without thermal contact with the surrounding fluid) from its existing pressure and temperature to a standard reference pressure. This removes the influence of pressure on temperature and is useful when comparing fluid parcels at different depths and when considering vertical motions of fluid parcels. In an adiabatic layer θ is constant with depth (i.e a vertical line) and in a superadiabatic layer the vertical derivative of θ, $\partial\theta/\partial z$, is negative.

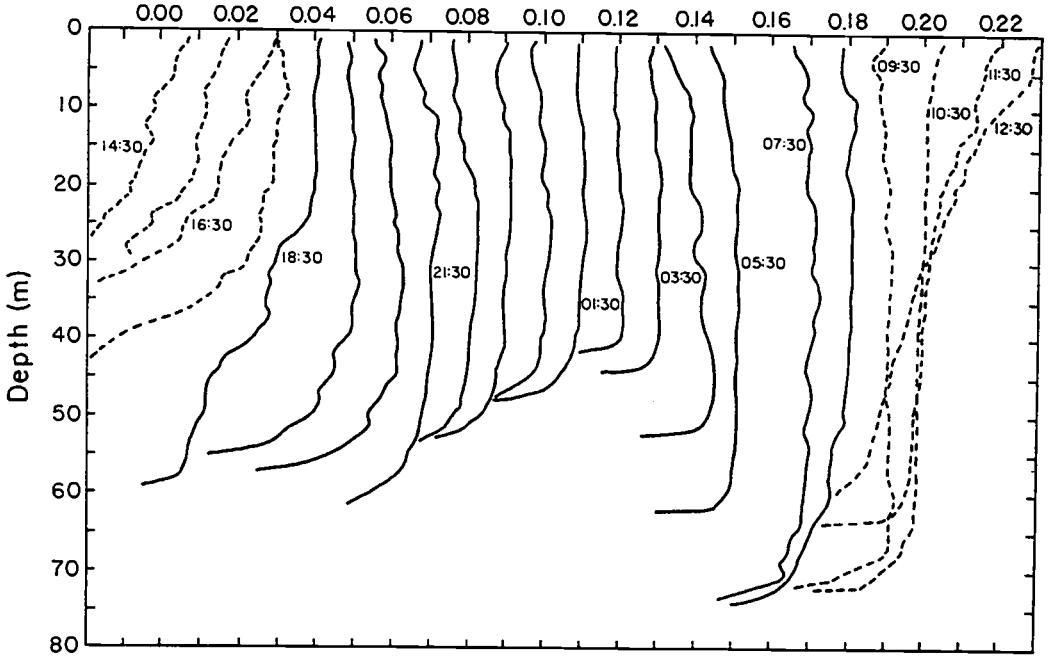

Figure III.2. A sequence of referenced and hourly averaged θ profiles throughout one diurnal cycle, starting at 14:30 local time and ending the following day at 12:30. Solid lines are nighttime profiles and broken lines are daytime profiles; profiles are offset by 0.01 K. From this sequence it is observed that the small superadiabatic potential temperature gradient, in the upper part of the profiles, is a persistent feature throughout the night (but away from transition periods). The transition time from $\partial\theta/\partial z > 0$ during daytime, to $\partial\theta/\partial z < 0$ during nighttime (and vice versa) is on the order of 2 hours. The 06:30 profile is missing due to instrumentation problems.

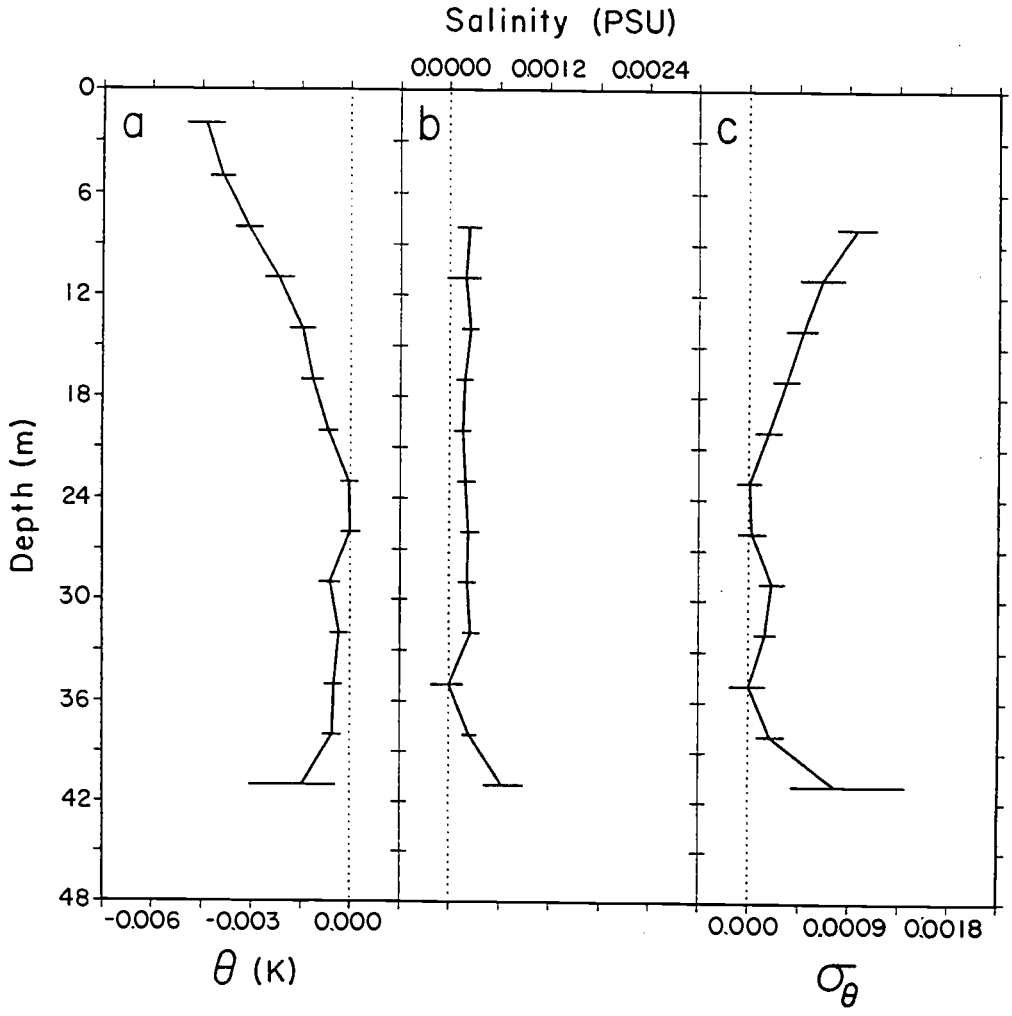

Figure III.3. Referenced and averaged potential temperature, (a) θ, salinity, (b) S, and potential density, (c) σ_θ for night 3 (78 profiles). θ, S and σ_θ are plotted relative to their extrema within the mixed layer. Error bars are 95% bootstrap confidence limits. The potential density, σ_θ, is calculated from θ and S. θ and S scales were chosen to represent equal contributions to σ_θ. Salinity values from depths shallower than 6.5 m were omitted due to possible contamination of the conductivity measurements by air bubbles. The weak superadiabatic potential temperature structure of the surface layer has been clearly extracted, by subtracting from each profile the average value of θ in the mixed layer ($-D < z < 2L$) for each profile, before ensemble averaging into 3 m depth bins. This procedure effectively removed any effects of large scale horizontal gradients.

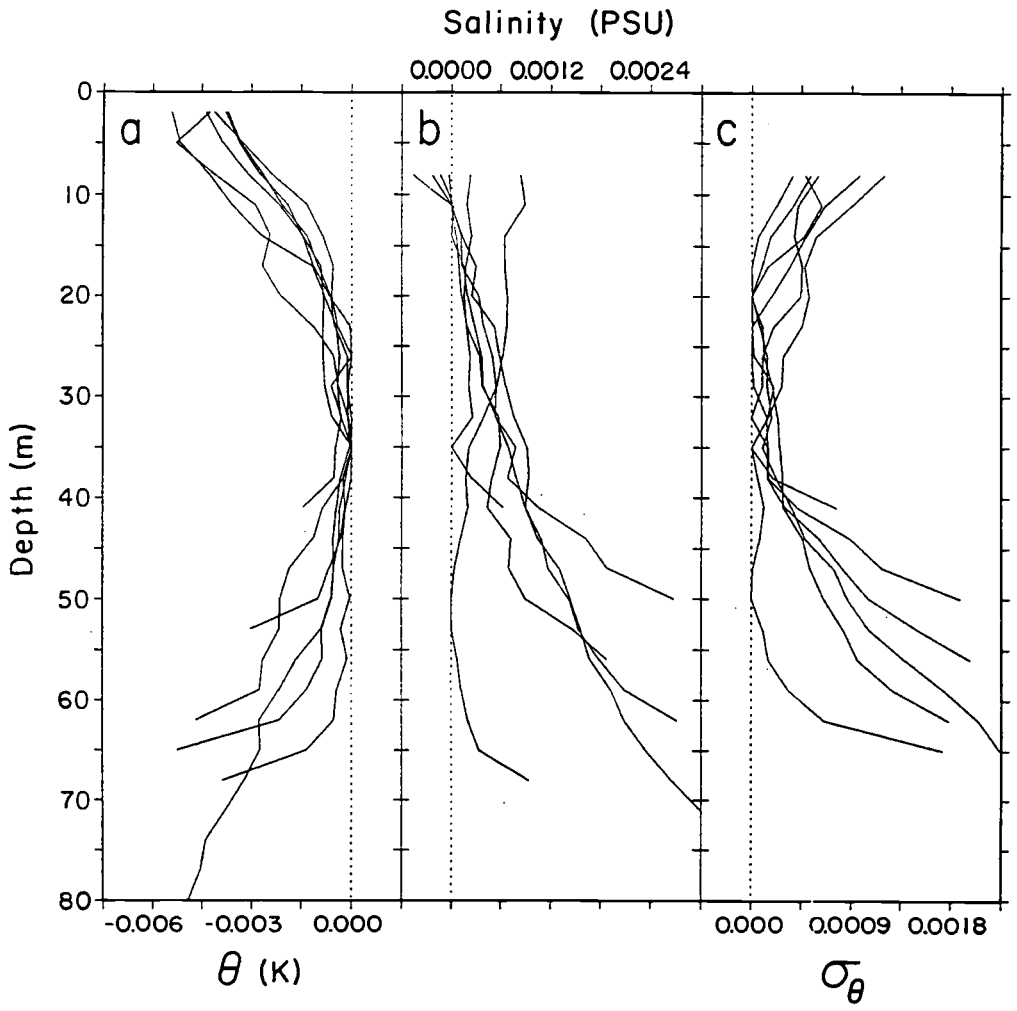

Figure III.4. (a) θ, (b) S, and (c) σ_θ for each of the 6 consecutive nights of the experiment. Data were processed and scales were chosen as described in caption to Figure III.3. Extremum values within the mixed layer were subtracted for comparison of profiles.

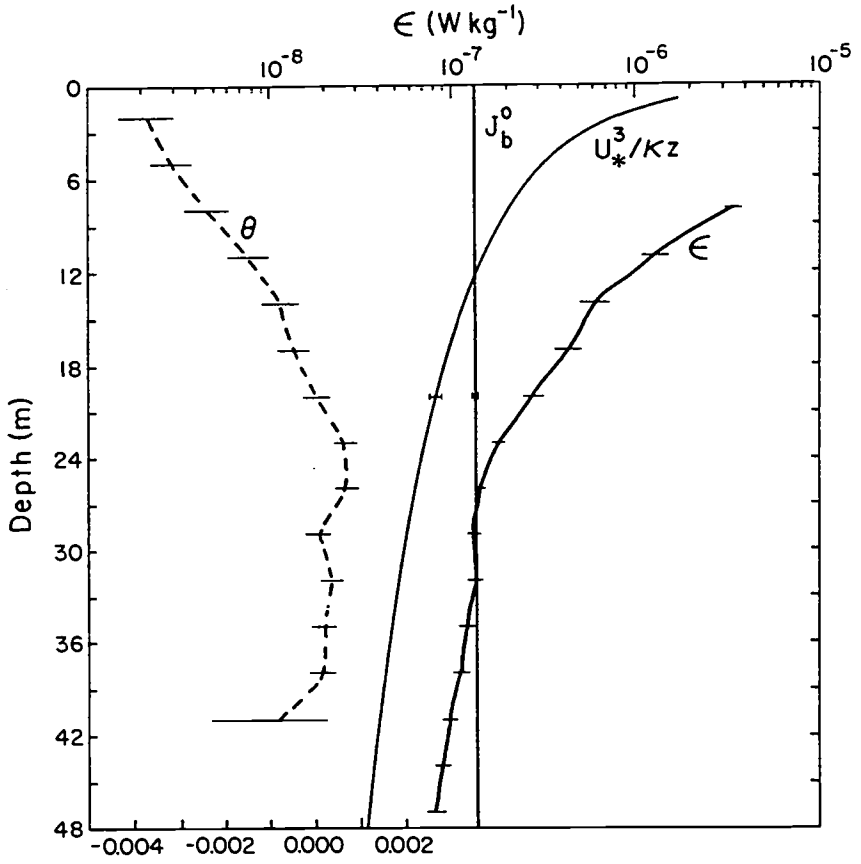

Figure III.5. Referenced and averaged θ profile and averaged $\epsilon(z)$ profile for night 3. The production terms of TKE by surface winds ($u_*{}^3/\kappa z$) and by surface buoyancy flux (J_b^0) are plotted also. Although $\epsilon(z)$ is reasonably constant within the mixed layer, it is not so in the surface layer. $\epsilon(z)$ increases toward the surface at a greater rate than each or the sum of the production terms ($u_*{}^3/\kappa z$ and J_b^0). $\epsilon(z)$ values from depths shallower than 6.5 m were omitted due to possible contamination by the ship's wake. Error bars are 95% bootstrap confidence limits.

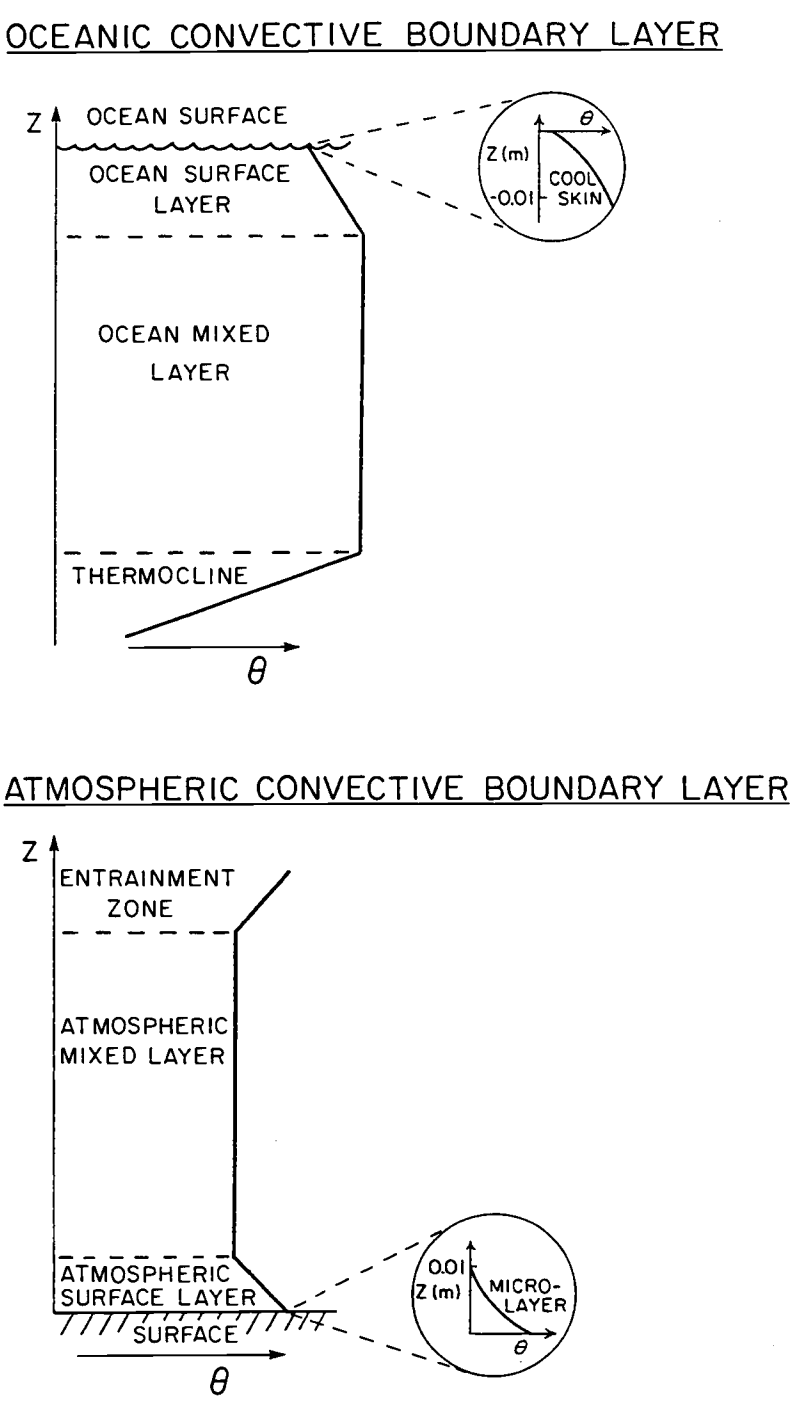

Figure III.6. Schematic showing the mean potential temperature structure of the oceanic and atmospheric CBL's. Table III.2 presents a summary of the main characteristics of each layer.

Table III.1. Nightly averaged values for the six consecutive nights of the experiment and the mean for all nights (last column). Numbers in parentheses are the 95% confidence intervals of the mean determined using the bootstrap method (Efron and Gong 1983). Wind stress, τ, surface heat flux, J_q^0, and surface buoyancy flux, J_b^0, were determined from bulk aerodynamic formulae. The depth of the mixed layer, D, was determined for each profile and averaged for the night. L is the Monin-Obukhov length scale. It is predicted that convective mixing dominates over the depth range $-D < z \ll L$ when $-D/L \gg 1$. The mean potential temperature gradient ($\partial\theta/\partial z$) of the surface layer for each night was determined for the depth range $2L < z < -0.5$ m. The mean ratio $\epsilon(z)/J_b^0$ was determined over the depth range $-D < z < 2L$. Density values used are $\rho_a = 1.25$ and $\rho_w = 1025$ kg m^{-3} and specific heat values are $C_p^a = 1.0 \times 10^3$ and $C_p^w = 4.0 \times 10^3$ J K^{-1} kg^{-1} for air and seawater respectively.

	night						
	1	2	3	4	5	6	mean
No. of profiles	25	42	78	83	75	63	
τ (Nm^{-2})	0.08	0.10	0.08	0.07	0.11	0.11	0.09
J_q^0 (W m^{-2})	212	211	171	166	205	199	189
10^7 J_b^0 (W kg^{-1})	1.6	1.7	1.4	1.3	1.5	1.6	1.5
D (m)	64.4	68.5	50.6	67.5	64.3	82.2	65.1
L (m)	-10.6	-14.2	-11.7	-10.8	-17.3	-17.5	-13.9
10^4 $\partial\theta/\partial z$ (K m^{-1})	-1.5	-2.1	-2.3	-2.1	-1.3	-1.1	-1.8
	(-2.8, -0.02)	(-2.6, -1.5)	(-2.8, -1.7)	(-2.8, -1.4)	(-1.7, -0.9)	(-1.3, -0.8)	
ϵ/J_b^0	0.81	0.82	0.86	0.87	0.79	0.69	0.81
	(0.64, 1.00)	(0.77, 0.86)	(0.81, 0.91)	(0.78, 0.95)	(0.74, 0.84)	(0.66, 0.72)	

Table III.2. Summary of main characteristics of oceanic and atmospheric convective boundary layers. These are depicted schematically in Fig. III.6.

Oceanic Convective Boundary Layer			
Layer	Thickness (m)	θ_z (K m^{-1}) Mixing remarks	References
Cool skin	$O(0.01)$	-300 molecular diffusion	Khundzhua et al. (1977), Paulson and Simpson (1981).
Ocean Surface Layer	$O(10-20)$	-2×10^{-4} $\epsilon/(u_*{}^3/\kappa z) >> 1.$ Wave breaking, Lagmuir cells, plume formation, shear due to wind stress and wave drift.	This study.
Ocean Mixed Layer	$O(50-100)$	~ 0 $\epsilon/J_b^0 \sim 0.44-0.87.$ Well mixed by large scale convective eddies on the order of the mixed layer. Mixed layer scaling applies.	Shay and Gregg (1986), Lombardo and Gregg (1989), Brubaker (1987) Imberger (1985).
Thermocline	$O(100-200)$	>0 Mean values of $\epsilon < -1\times10^{-8}$ W kg^{-1} Intermittent turbulence, internal waves.	

Table III.2. (continued)

Layer	Atmospheric Convective Boundary Layer: Thickness (m)	θ_z (K m^{-1})	Mixing remarks	References
Entrainment zone	$O(100-500)$	>0	Intermittent turbulence, overshooting thermals, K-H waves, internal waves.	Stull (1988), Driedonks and Tennekes (1984).
Atmospheric Mixed Layer	$O(1-2)\times 10^3$	~ 0	$\epsilon/J_b^0 \sim 0.64$. Well mixed by large convective eddies on the order of the mixed layer. Mixed layer scaling applies.	Stull (1988), Driedonks and Tennekes (1984), Caughey and Palmer (1979).
Atmospheric Surface Layer	$O(10-100)$	$-1\times(10^{-2}-10^{-1})$	$\epsilon/({u_*}^3/\kappa z) \sim 1-2$. Small scale turbulent eddies created by forced convection. Monin-Obukhov similarity applies.	Stull (1988), Driedonks and Tennekes (1984), Wyngaard and Cote (1971).
Microlayer	$O(0.01)$	-1×10^4	molecular diffusion	Stull (1988).

IV. PRESCRIPTIONS FOR HEAT FLUX AND ENTRAINMENT RATES IN THE UPPER OCEAN DURING CONVECTION

Abstract

A detailed investigation of the upper ocean during convection reveals:

- the vertical structure of potential temperature, θ, to be steady in time, and
- the current shear to vanish in the bulk of the mixed layer.

These imply that a "slab" type model may be an adequate representation of the convective ocean boundary layer (OBL). In contrast, when convection is not the dominant forcing mechanism, the OBL is stratified and can support a significant current shear. This indicates the inadequacy of "slab" models for the non-convective OBL.

Two independent estimates of the vertical heat flux profile in the convective OBL were made. The first estimate results from heat conservation and the steadiness of the vertical structure of potential temperature. The second estimate is based on the TKE balance and the vertical profiles of TKE dissipation rate. The estimates are consistent and suggest that the nondimensional vertical heat flux due to turbulence has a linear depth dependence of the form $1+a_h(z/D)$, where z is the depth, D is the ML depth, and a_h is a constant with a mean value of 1.13, consistent with numerical and laboratory results and with observations in the convective atmospheric boundary layer. An estimate of the entrainment rate, derived from observed quantities, is $\sim 1 \times 10^{-5}$ m s^{-1}. This is within a factor of 2 of estimates derived from alternative formulations.

IV.1. Introduction

Experiments in the convective ocean boundary layer (OBL) indicate that the vertical structures of the time-averaged potential temperature, θ, and TKE dissipation rate, ϵ, in the convective OBL are similar to those in the convective atmospheric boundary layer (ABL) over land. Both systems include four distinct regimes (proceeding from the ocean's surface down and from the land's surface up):

(1) A "cool skin" (a few millimeters thick) near the surface of the ocean (Khundzhua et al. 1977; Paulson and Simpson 1981) which is analogous to the "hot skin" (or microlayer) near the land surface (Stull 1988). Physical processes are governed by molecular diffusion; large vertical gradients of potential temperature are typical ($\partial\theta/\partial z \sim -300$ K m^{-1} for the OBL and $\partial\theta/\partial z \sim -1 \times 10^4$ K m^{-1} for the ABL).

(2) A superadiabatic ocean surface layer (OSL) of O(10-20 m) in which $\partial\theta/\partial z \sim -2 \times 10^{-4}$ K m^{-1} (Anis and Moum 1992 [chapter III]) and a superadiabatic atmospheric surface layer (ASL) of O(10-100 m) in which $\partial\theta/\partial z \sim -1 \times (10^{-2} - 10^{-1})$ K m^{-1}. In some cases ϵ in the OSL followed Monin-Obukhov similarity scaling (Soloviev et al. 1988; Anis and Moum 1993c [chapter V]), similar to what is observed in the ASL (Wyngaard and Coté 1971; Driedonks and Tennekes 1984; Stull 1988). However, an increasing number of field studies shows that mixing can be much more vigorous in the OSL with values of ϵ much larger than expected from Monin-Obukhov similarity scaling (Anis and Moum 1992 [chapter III], 1993c [chapter V]; Agrawal et al. 1992). The enhanced dissipation rates may result from several mechanisms which are unique

to the OSL, such as surface wave breaking and surface wave stress (Anis and Moum 1993c [chapter V]), or Langmuir circulation.

(3) A well-mixed layer (ML) in which $\partial\theta/\partial z \sim 0$ and ϵ scales well on average with the surface buoyancy flux, J_b^0. Mean values of ϵ/J_b^0, are similar in both the ML of the convective OBL ($\overline{\epsilon/J_b^0} = 0.44 - 0.87$; Shay and Gregg 1986; Lombardo and Gregg 1989; Anis and Moum 1992 [chapter III]) and the convective ABL ($\overline{\epsilon/J_b^0} = 0.64$; Caughey and Palmer 1979). Thicknesses of the ML are O(50-150 m) and O(1000-2000 m) for the OBL and the ABL respectively.

(4) A stable thermocline in the OBL of O(100-200 m) and a stable inversion layer in the ABL of O(100-500 m) where $\partial\theta/\partial z > 0$. Turbulence is intermittent and is generated by shear, Kelvin-Helmholtz instabilities, internal waves and overshooting thermals (e.g. Gargett 1989 for the OBL and Stull 1988 for the ABL). This regime is often referred to as the entrainment zone.

The simplest representation of a convective BL is as a uniform "slab". In ABL models, mean profiles of θ, humidity (and other scalars) and wind speed are assumed to be constant with height with quasi-discontinuities at the top of the ML (e.g. Stull 1988). OBL "slab" models assume similarly that the vertical distributions of the mean temperature, salinity and horizontal currents within the ML are uniform, with a quasi-discontinuous distribution across the base of the ML (e.g. Niiler and Kraus 1977). Since the mean profile of θ is assumed to be constant with depth, the heat flux is a linear function of the vertical coordinate z, decreasing from its value at the surface, $\overline{w'\theta'}(0)$, to its value near the top/base of the ML, $\overline{w'\theta'}(D)$ (similarly, turbulence fluxes of quantities such as humidity and pollutants in the ABL and salinity

in the OBL will also depend linearly on z). Linear heat flux profiles were observed in laboratory studies (Willis and Deardorff 1974; Deardorff et al. 1980) and field experiments in the convective ABL (e.g. Zhou et al. 1985; Young 1988) and in numerical simulations (e.g. Deardorff 1974; André et al. 1978). André and Lacarrère (1985), using third-order numerical simulations of a buoyancy driven OBL, have similarly demonstrated the linear decrease of buoyancy flux with depth. A field experiment in the convective aquatic boundary layer of a fresh water reservoir inferred a linear heat flux profile with depth (Imberger 1985; in this instance the system was assumed to be purely 1-D and the heat flux was estimated directly from the time rate of change of temperature of the water column).

Closure of the ML equations requires knowledge of the entrainment processes at the top/base of the ML. Unfortunately, relatively little is known about the details of entrainment in the convective ABL (and even less so in the convective OBL), mainly due to the difficulty of making accurate measurements of the highly intermittent turbulence in the entrainment zone. Generally, three distinct processes are responsible for TKE production and entrainment in the convective ABL (Driedonks and Tennekes 1984): a) convection due to surface heat/buoyancy flux, b) surface wind stress, and c) shear production due to wind shear at the top of the ML. Opposing the entrainment-producing processes in the ABL are the stable inversion layer at the top of the ML and viscous dissipation of TKE.

A widely used closure scheme of the ML equations of "slab" models is by parameterization of the entrainment rate, w_e. Due to the complicated nature of entrainment processes, no general parameterization exists which is valid for all cases (see Deardorff 1983 for a thorough treatment and

comparison of entrainment formulations). Another closure method relates the heat/buoyancy flux at the top/base of the ML to the heat/buoyancy flux at the surface, such that $-\overline{w'\theta'}(0)/\overline{w'\theta'}(D) = A$, where A is a constant. Most of the suggested values for A in convective boundary layers, from theoretical, experimental and laboratory studies are between 0.1 and 0.3, although values ranging from 0 to 1 have appeared (Stull 1976). This spread of values may be just another manifestation of the complicated processes involved.

In this study we examine the details of the vertical structure of θ, ϵ and shear of the horizontal current as revealed by a large number of profiles obtained in the nighttime convective OBL. We focus our attention on the time period when convective forcing was relatively steady (the period during which the ML rapidly deepened is discussed by Anis and Moum 1993a [chapter II]). Throughout the quasisteady convective forcing period (lasting 11.5-13 hours) the vertical structure of θ was observed to remain essentially constant. Two conclusions are drawn from the steadiness of the vertical stucture of θ: a) a "slab" type behavior of the convective OBL and b) a linear depth dependence of the heat flux. Conclusion (a) is furthermore supported by the vanishing vertical shear of the horizontal currents in the bulk of the ML, suggesting a uniform horizontal velocity distribution in the ML. Using a simplified TKE balance at the base of the ML ($z = -D$) we have estimated $\overline{w'\theta'}(-D)$. Based on these estimates the ratio $-\overline{w'\theta'}(0)/\overline{w'\theta'}(-D)$ and the slope of the linear heat flux profile were calculated and found to be similar to values from laboratory, numerical and ABL field studies. As mentioned above the knowledge of $\overline{w'\theta'}(-D)$ provides also a closure condition for the ML equations and enables one to estimate the entrainment rate. A second estimate of the heat flux profile was made using ϵ profiles and the assumption

of a TKE balance between buoyancy flux and dissipation, $J_b(z) \sim \epsilon(z)$. This estimate suggests, independently from the estimate above, a linear heat flux profile with a slope that is consistent with the slope calculated from the ratio $-\overline{w'\theta'}(0)/\overline{w'\theta'}(-D)$.

Experimental details, meteorological background conditions and observations are described in section IV.2, with a specific focus on the vertical structure of θ, ϵ and shear. Two independent estimates of the vertical heat flux profile in the nighttime convective OBL are made in section IV.3 and compared to each other and to results from laboratory, field and numerical studies. An estimate of the entrainment rate is made in section IV.4 and compared to several entrainment formulations. Summary and conclusions are presented in section IV.5.

IV.2. Observations

IV.2.1. Experimental details

A large data set was collected in the upper OBL of the Pacific Ocean between 13 and 20 March 1987 as the R/V *Wecoma* progressed along 140° W at a mean speed of ~ 2.5 m s^{-1} from 17° N to 6° N (Park et al. 1987). For the present study we have analyzed a total of 445 nighttime hydrographic and turbulence vertical profiles collected with the Rapid-Sampling Vertical Profiler (RSVP; Caldwell et al. 1985). From the RSVP profiles the potential temperature and TKE dissipation rates were calculated as functions of depth. The time interval between profiles was about 6-7 minutes, corresponding to a horizontal separation between profiles on the order of 1000 m (for details see Anis and Moum 1993a [chapter II]). Vertical profiles of horizontal velocity components (T. Chereskin, pers. comm.) were estimated from a shipboard acoustic Doppler current profiler (ADCP). Continuous shipboard measurements of meteorological data were taken throughout the experiment and were processed and kindly provided by F. L. Bahr and C. A. Paulson.

IV.2.2. Meteorological and background conditions

Moderate northeast winds prevailed throughout the experiment, and nighttime averages of surface wind stress, $\tau_0 = \rho_a C_d {U_{10}}^2$, (where ρ_a is the air density, C_d is the drag coefficient and U_{10} is the wind speed at a height of 10 m; Large and Pond 1981) varied between 0.07 and 0.11 Nm^{-2} (Table IV.1). Air temperature was cooler than sea surface temperature during the whole experiment with mean nighttime air-sea temperature differences between -0.73 and -1.84 K (Table IV.1). The net upward heat flux from the surface of the ocean, J_q^0, was calculated as the sum of four individual components $J_q^0 = J_q^{sw} + J_q^{lw} + J_q^s + J_q^e$, where J_q^{sw} is the net shortwave

radiation flux, J_q^{lw} is the the net longwave radiation, J_q^s is the sensible heat flux and J_q^e is the latent heat flux. During nighttime the main contributor to J_q^0 was J_q^e (about 75-90% of the total). Nighttime mean values of J_q^0 were between 166 and 212 Wm^{-2} and resulted in convective conditions with mean values of J_b^0 of $1.31 - 1.66 \times 10^{-7}$ m^2 s^{-3} (Table IV.1) (J_b^0 was calculated using Dorrestein's (1979) formulation; the contribution to J_b^0 due to the change of salinity at the ocean's surface was less than 10%). The Monin-Obukhov length, L, which during convective conditions defines the depth at which the wind stress and the surface buoyancy flux are of equal importance (such that for $z >> L$ wind stress is the main TKE source, while for $z << L$ buoyancy production is the main TKE source), had mean nighttime values between -10.6 and -17.5 m (Table IV.1). These values are similar to those observed in other diurnal oceanic convective boundary layers (e.g Shay and Gregg 1986; Lombardo and Gregg 1989). Sea-state conditions were moderate throughout the experiment with swells with significant heights between 1.8 and 2.7 m and wind-waves with significant heights between 0.6 and 0.9 m (Table IV.1).

IV.2.3. The vertical structure of potential temperature, TKE dissipation and velocity shear

Net heat loss from the ocean's surface resulted in destabilizing convective conditions during each of the six nights of the experiment. During the initial phase of the convective period (about 2-3 hours), when J_b^0 increased nearly linearly to its nighttime quasisteady value, the stable daytime stratification between the ocean's surface and the seasonal pycnocline was eroded. The rate of ML deepening was between 8-19 meters per hour (Anis and Moum 1993a [chapter II]) and final nighttime ML depths, limited by the top of the seasonal

pycnocline, were between 50.6 to 82.2 m (Table IV.2; ML depth, D, was estimated from individual profiles as the depth at which the density exceeded the surface value by $\sim$ 0.005 kg m^{-3}, and then averaged for the night). During the major part of each night (lasting $11.5-13$ hours), J_b^0 varied little and D traced the undulations in the depth of the seasonal pycnocline. We refer to this part of the night as the *quasisteady forcing phase*; this phase is the focus of our analysis.

Investigation of the vertical temperature structure, as a function of time, was carried out by first referencing individual profiles of $\theta(z)$ to the average value of θ in the ML (in the depth range $-D < z < 2L$) and then averaging over periods of 2 hours each during the quasisteady convective forcing phase of each night. As an example, the envelopes of the 95% bootstrap confidence interval of 2-hour averages of θ, as function of the scaled depth $z^* = z/D$ (calculated in depth bins of $0.04D$), are presented in Fig. IV.1 for 5 sequential periods during night 4. (We used z^* instead of z since D varied during the night as it followed the undulations of the top of the seasonal pycnocline, probably due to a combination of internal wave activity and local variability: this is, of course, independent of mixed layer physics and hence we scale this variability out of the problem.) This figure suggests a quasisteady state of the vertical structure of $\theta(z)$ with three distinct regimes: a superadiabatic OSL, where $\partial\theta/\partial z < 0$, in the upper 20-40% of the OBL (see also Anis and Moum 1992 [chapter III]); a relatively well-mixed layer beneath it in which $\partial\theta/\partial z \sim 0$ (the lower part of the ML often had a small positive temperature gradient similar in magnitude to that of the superadiabatic OSL: we attribute this to entrainment of cooler water below the ML base into the ML); a stable layer with a sharp positive gradient of θ capping the

OBL from below and coinciding with the top of the seasonal pycnocline. The quasisteady structure of $\theta(z)$ was found to be a persistent feature throughout the quasisteady convective forcing phase of each of the six nights of the experiment (beginning and ending profiles from the quasisteady forcing phase of each night are shown in Figs. IV.2a-f).

The vertical structure of ϵ was nondimensionalized as $\epsilon^*(z^*) \equiv \epsilon(z/D)/J_b^0$ for individual profiles, and ensemble averaged in depth bins of $0.04D$ for each night (as we did for the profiles of θ). The results are shown in Figure IV.3 for each of the 6 nights of the experiment. A similar computation was made by ensemble averaging the individual profiles of all nights (Fig. IV.4). A consistent feature of the averaged profiles was a rapid and roughly exponential decrease of values of $\epsilon^*(z^*)$ in the upper $20-40\%$ ($\sim 1-2L$) of the convective OBL (Anis and Moum 1993c [chapter V]). In the lower half of the ML, roughly between $-z^* = 0.5$ and $-z^* = 0.9$, values of $\epsilon^*(z^*)$ decreased linearly with z^*. Before dropping rapidly by several factors of ten, a slight increase in $\epsilon(z^*)$ was observed near the base of the ML between $-z^* = 0.95$ and $-z^* = 1.05$. This is an indication of enhanced mixing in the entrainment zone, possibly a result of the enhanced shear levels observed near the base of the ML.

Horizontal current velocity measurements from the R/V *Wecoma* hull mounted ADCP were estimated every 4 m vertically, although they are independent approximately only every 12 m, and interpolated in time to match the RSVP casts used in our analysis. The velocity shear was computed from the slopes of linear fits, over a 12-m depth interval, to the U and V velocity components, such that $S^2 = (\partial U/\partial z)^2 + (\partial V/\partial z)^2$. Analysis of nighttime profiles showed that the estimates of S^2 in the bulk of the ML

were equivalent, on average, to the detection limit of $O(1-2\times10^{-6}\ s^{-2})$ in estimating S^2 from the ADCP velocity measurements (Fig. IV.5). That is, the ML shear is not distinguishable from 0 s^{-1}. In the lower 20% of the ML a relatively sharp increase in shear was observed with a maximum of about $S^2 \sim 6\times10^{-5}\ s^{-2}$ near the base of the ML.

To determine if the low shear values were characteristic for the upper OBL during nighttime only, we plotted the time series of hourly averages of S^2 estimated between 19.1 m and 31.1 m and centered at 25.1 m (19.1 m is the shallowest depth at which U and V could be estimated). A clear distinction between nighttime and daytime emerges from inspection of the time series of the squared buoyancy frequency, N^2, (Fig. IV.6b) and S^2 (Fig. IV.6c). Larger values of S^2 during daytime, compared to nighttime, are closely associated with the larger values of N^2 resulting from the increasing stability due to daytime heating.

To illustrate the difference between daytime and nighttime shear, two data sets, one for daytime and one for nighttime, were constructed from near surface values of S^2 (centered at a depth of 25.1 m). The resulting distributions of S^2 are presented in Fig. IV.7. Nighttime was characterized by a large number (almost 40%) of estimates of S^2 below the equivalent detection limit ($\sim 1\times10^{-6}\ s^{-2}$), while during daytime almost none (less than 1%) of the S^2 were smaller than the detection limit. The mean daytime value of S^2 was larger by a factor of about 4 compared to the mean nighttime value. A standard Kolmogorov-Smirnov test (Press et al. 1992), applied to the nighttime and daytime data sets, showed that the distributions of the two data sets were significantly different at a confidence level better than 99.999%. An independent *Student's t-test* and *F-test* confirmed, respectively,

that the variance and mean of the two data sets were significantly different, again at a confidence level better than 99.999%, however, this is to be expected for substantially different distributions.

IV.3. Estimates of the vertical heat flux profile during convection

IV.3.1. Estimate from potential temperature profiles and heat conservation

Using Reynolds time-averaging the equation for the conservation of heat in the OBL can be written as

$$\frac{\partial \theta}{\partial t} + U_i \frac{\partial \theta}{\partial x_i} = \nu_\theta \frac{\partial^2 \theta}{\partial x_i \partial x_i} - \frac{\partial (\overline{u_i' \theta'})}{\partial x_i} - \frac{\partial I}{\partial z}, \tag{1}$$

where θ, U_i, and I are the time-averaged potential temperature, current velocity and penetrating solar radiation, respectively, primed variables are turbulence components, ν_θ is the thermal molecular diffusivity, and z is positive upwards. Assuming horizontal homogeneity and neglecting the mean molecular conduction of heat, equation (1) for nighttime ($I = 0$) simplifies to

$$\frac{\partial \theta}{\partial t} = -\frac{\partial (\overline{w' \theta'})}{\partial z}. \tag{2}$$

Integrating (2) vertically to the surface ($z = 0$) and rearranging terms results in an equation for the vertical heat flux due to turbulence at depth z

$$\overline{w' \theta'}(z) = \overline{w' \theta'}(0) + \int_z^0 \frac{\partial \theta}{\partial t} dz'. \tag{3}$$

The surface heat flux, $J_q^0 = \rho C_p \overline{w' \theta'}(0)$, was estimated from shipboard meteorological measurements (Table IV.1). Equation (3), then, permits an estimate of the vertical heat flux at some depth z by vertical integration of the time rate of change of temperature between the surface and z. However, in practice this is usually impossible to do using oceanic data because of the small temperature changes resulting from convection compared to lateral temperature variability. For example, using a difference form of (2) and assuming a kinematic heat flux difference between the surface and the bottom

of the ML of $\Delta\overline{w'\theta'} \sim 5 \times 10^{-5}$ K m s^{-1} (based on a surface heat flux of $\sim$ 200 W m^{-2} and a negligible heat flux at the base of the ML), a time period of $\Delta t \sim 10$ hours and a mean ML depth $D = 65$ m results in $|\Delta\theta| = |\Delta(\overline{w'\theta'})\Delta t/\Delta z| < 0.03$ K. Horizontal temperature differences, due to either advective effects or due to the spatial separation between profiles, may result in much larger values than 0.03 K and therefore mask those resulting from convective cooling alone. A simple cure to this problem is to vertically differentiate (2) and change the order of the z and t derivatives, resulting in

$$\frac{\partial}{\partial t}\left(\frac{\partial\theta}{\partial z}\right) = -\frac{\partial}{\partial z}\left(\frac{\partial(\overline{w'\theta'})}{\partial z}\right). \tag{4}$$

From (4) the vertical structure of the turbulence heat flux can be found from the time rate of change of the temperature gradient, $\partial\theta/\partial z$. This can be accomplished more readily, since now one is not concerned with the *absolute* temperature differences between two profiles of $\theta(z)$, which are separated in both time and space, but only with the change in their *relative* vertical structure as a function of time.

The quasisteady vertical structure of $\theta(z)$ that we observed throughout the quasisteady convective forcing phase of each of the six nights of the experiment (Fig. IV.2) results in $\partial(\partial\theta/\partial z)/\partial t = 0$. By (4), this implies that the vertical heat flux due to turbulence in the convective OBL is linear in z, i.e.

$$\overline{w'\theta'}(z) = \overline{w'\theta'}(0) + \left[\overline{w'\theta'}(0) - \overline{w'\theta'}(-D)\right]\frac{z}{D}, \tag{5}$$

or in dimensionless form

$$\overline{w'\theta'}^{*}(z^{*}) = 1 + \left[1 - \overline{w'\theta'}^{*}(-1)\right]z^{*} = 1 + a_h z^{*}, \tag{5a}$$

where $\overline{w'\theta'}(0)$ and $\overline{w'\theta'}(-D)$ are the heat fluxes at the surface and the base of the ML respectively, $\overline{w'\theta'}^{*}(z^{*}) \equiv \overline{w'\theta'}(z)/\overline{w'\theta'}(0)$, and $a_h \equiv \left[1 - \overline{w'\theta'}^{*}(-1)\right]$.

Field experiments in the convective ABL (e.g. Zhou et al. 1985; Young 1988), numerical simulations (e.g. Deardorff 1974; André et al. 1978 for a convective ABL; André and Lacarrère 1985 for a convective OBL), laboratory experiments (e.g. Willis and Deardorff 1974) and a field experiment in the convective aquatic boundary layer of a fresh water reservoir (Imberger 1985) all indicate a linear dependence on z of the turbulence heat/buoyancy flux.

An estimate of the upper limit on the magnitude of $\overline{w'\theta'}(-D)$ (or $\overline{w'\theta'}^*(-1)$) can be made assuming a simplified form of the steady state TKE equation near the base of the ML in which the mechanical production of TKE, P, is balanced by TKE dissipation and by buoyancy destruction, J_b, namely $P = -J_b + \epsilon$. The small, observed increase in ϵ at $-z/D \sim 1$ (Fig. IV.3 and Fig. IV.4) and the increase in shear magnitude near the base of the ML (Fig. IV.5) seem to support such a balance during our experiment. Evidence for a balance of this type at the base of the oceanic ML is provided by the numerical simulations of a buoyancy driven OBL by André and Lacarrère (1985) while observational evidence for a similar balance at the top of the convective ABL comes from a field study discussed by Zhou et al. (1985). Using the simplified TKE balance, defining a flux Richardson number as $R_f = -J_b/P$ and using a critical value for R_f of 0.15 (Osborn 1980) results in an upper bound on the magnitude of the buoyancy flux given by

$$|J_b(-D)| \leq 0.2\epsilon(-D). \tag{6}$$

Neglecting salinity effects, the heat and buoyancy fluxes are related through $J_b = g\alpha\overline{w'\theta'}$ (g is the gravitational acceleration and α is the thermal expansion coefficient of seawater with values of $2.9 - 3.2 \times 10^{-4}$ K^{-1} for

our experiment) so that

$$|\overline{w'\theta'}(-D)| = |\frac{J_b(-D)}{g\alpha}| \leq \frac{0.2\epsilon(-D)}{g\alpha}, \tag{7}$$

or in dimensionless form

$$|\overline{w'\theta'}^*(-1)| \leq 0.2\epsilon^*(-1), \tag{7a}$$

where $\epsilon^*(-1) \equiv \epsilon(-D)/J_b^0$. Nighttime means of $\epsilon^*(-1)$ varied between 0.36 and 0.90 with an average value of 0.63 (Table IV.2). Substitution of these values into (7a) resulted in estimates of the upper limit on the magnitude of $\overline{w'\theta'}^*(-1)$ ranging between 0.07 and 0.18 for the individual nights with an overall mean of 0.13 (Table IV.2). Using (5a) and the mean value $|\overline{w'\theta'}^*(-1)| \leq 0.13$ we suggest that a reasonable approximation for the nondimensional heat flux profile in the convective OBL during our experiment may be given by

$$\overline{w'\theta'}^*(z^*) = 1 + 1.13z^*. \tag{8}$$

Note that the heat flux at the base of the ML is negative (i.e. flows out of the ML).

Figures IV.1 and IV.2 indicate a maximum in θ near the middle of the ML, similar to the minimum in θ observed near the middle of the ML of the convective ABL (e.g Stull 1988). This is simply due to cooling from above, by heat loss from the ocean surface, and entrainment of cool water from below, and results in cooler temperatures in those regions and a maximum in θ near the middle of the ML.

The steadiness of the vertical structure of θ also implies that throughout the depth of the convective OBL the change in temperature, as a function of time, has to be uniform. This suggests that, at least in a time-averaged

sense, the convective OBL cools like a "slab". From dimensional analysis an "overturn", in which a convective eddy communicates from top to bottom of the ML, has a time scale of $T_c = (D^2/J_b^0)^{1/3}$, which is on the order of one hour for $D = 65$ m and $J_b^0 = 1.5 \times 10^{-7}$ m^2 s^{-3}. If, during an "overturn", the OBL is completely mixed then potential temperature changes averaged over time periods larger than T_c will be consistent with the picture of the ML cooling as a uniform "slab". However, one has to remember that on time scales smaller than T_c the convective OBL is highly intermittent (consecutive profiles of θ, separated by 6-7 minutes, reveal considerable small-scale variability and complexity; Anis and Moum 1992 [chapter III]). The "slab" type behavior of the ML is further given credence by the fact that the shear magnitude in the bulk of the ML was at the noise level but increased relatively sharply near the ML base (Fig. IV.5).

IV.3.2. Estimate from dissipation profiles and TKE balance

In the convective OBL, away from the ocean's surface and away from the ML base, TKE production is mainly by buoyancy forcing. For a steady-state, neglecting turbulence transport, and since the background shear is indistinguishable from zero, neglecting also mechanical production, we expect a balance between TKE dissipation and buoyancy production such that

$$\epsilon(z) \sim J_b(z). \tag{9}$$

Neglecting salinity effects (9) can be rewritten as

$$\epsilon(z) \sim g\alpha\overline{w'\theta'}(z), \tag{10}$$

or in dimensionless form

$$\epsilon^*(z^*) \sim \overline{w'\theta'}^*(z^*), \tag{11}$$

where we use $J_b^0 = g\alpha\overline{w'\theta'}(0)$.

Equation (11) permits an independent estimate of the depth-dependent heat flux from the dissipation profiles. Within the ML (away from the surface layer and the ML base) we fitted a linear profile, by least squares, of the form

$$\epsilon^*(z^*) = b_\epsilon + a_\epsilon z^*. \tag{12}$$

The coefficients a_ϵ and b_ϵ are equivalent via (11) to those in (5a) and (8). That is, if (11) is true, we expect $b_\epsilon \sim 1$, $a_\epsilon \sim a_h$.

Least square fits to the observed $\epsilon^*(z^*)$ profiles, performed in the lower half of the convective OBL (Figs. IV.3,4), resulted in values of a_ϵ between 0.30 and 1.50 for the individual nights, and an overall mean of $a_\epsilon = 0.93$ (Table IV.2). The uncertainty in the mean value of a_ϵ was estimated in two ways: the first, ± 0.05, is the probable uncertainty (Press et al. 1992) in the least square fit to the mean $\epsilon^*(z^*)$ profile for all nights. The second uncertainty estimate, given by the range 0.73-1.23, was determined by a graphical fit of two straight lines in the 95% confidence envelope (Fig. IV.4). This resulted in one fit with a minimum slope of 0.73 and a second fit with a maximum slope of 1.23. Of the two estimates, the second represents a better way to estimate the probable uncertainty in a_ϵ since it takes into account the spread of values of ϵ^*, around its mean, at each depth bin. Based on this estimate we conclude that a_ϵ is consistent, at the 95% confidence level, with the average value a_h of 1.13.

Estimates of b_ϵ ranged from 0.66 to 1.99 for the individual nights with an overall mean of 1.40 (Table IV.2). The uncertainty was estimated in a

similar way as for a_ϵ and the uncertainty interval for the overall mean value of b_ϵ (estimated from the two graphically fitted straight lines; Fig. IV.4) was 1.25–1.60. Although this interval has values slightly larger than the expected value of 1, we believe that it is not significantly different from 1; for example, estimates of ϵ which are systematically too large by 25% could account for this departure, without causing a change in the slope of $\epsilon^*(z^*)$ (correction of an error producing dissipation values too large by 25% will also slightly reduce the values of a_h, through $\epsilon^*(-1)$, such that the overall mean value of a_h will be 1.10 instead of 1.13). An uncertainty analysis by Oakey (1982), who employed a profiler similar to our RSVP, suggests that uncertainties in estimates of ϵ may be a combination of random errors (maximum of $\pm 27\%$), systematic errors (maximum of $\pm 32\%$), and errors due to the assumption of isotropic turbulence (maximum of $\pm 50\%$). An error may also be introduced by the obvious difficulty in estimating the precise depth of the base of the ML, D. However, we estimate this error to be $\pm 10\%$, at most, for individual profiles and less so when averaged over many profiles.

IV.3.3. Additional considerations and comparison to atmospheric and numerical results

Physical processes in the convective OBL, neglected in our simplified TKE balance, may also account for some of the differences between the two independent estimates of the heat flux profiles. Of these the most important process is the additional production of TKE by either direct wind stress or by surface waves. However, the enhanced TKE dissipation observed in the upper $30 - 40\%$ of the OBL (Anis and Moum 1993c [chapter V]) may effectively balance this additional TKE production. Numerical studies of the convective ABL (André et al. 1978) and the convective OBL (André and

Lacarrère 1985) indicate turbulence transport of TKE from near the surface into the ML. This transport causes a net convergence, effectively production of TKE, in the lower half of the OBL which has to be balanced by TKE dissipation. The additional dissipation resulting from this balance, which unfortunately cannot be estimated from our measurements, may be another reason why our estimates of b_ϵ were slightly larger than unity.

In spite of the simplifying assumptions we have made, the fact that the vertical structure of θ was quasisteady and that ϵ decreased linearly with depth in the lower half of the ML are solid and consistent results, both leading to the same conclusion of a linear heat flux profile. Moreover, the suggested slope of the heat flux profile (i.e. $a_h = 1.13$) is in general agreement with the range of 1.1-1.3 suggested by Stull (1976a) based on a large number of published values. Simulations of the Wangara experiment by Deardorff (1974) and André et al. (1978), using different numerical schemes, resulted in $a_h = 1.13$ and $a_h = 1.15$ respectively. A numerical study of a buoyancy driven OBL (André and Lacarrère 1985) resulted in $a_h = 1.16$. When an additional turbulence generating velocity shear, $\Delta U = 0.1$ m s^{-1} (about twice the magnitude of the mean value of ΔU we observed at the base of the convective OBL; see next section), was imposed at the bottom of the OBL the slope increased to $a_h = 1.20$, due to the enhanced entrainment.

IV.4. Entrainment Rates

The deepening rate of the ML due solely to vertical mixing processes is given by w_e, the entrainment rate. If, at the bottom of the ML, all mixing processes are associated with the entrainment of the deeper and denser fluid into the ML then (e.g. Stull 1988)

$$w_e \Delta\rho = -\overline{w'\rho'}(-D), \tag{13}$$

where $\Delta\rho$ is the density jump at $z = -D$ (we used the density flux representation, instead of heat flux, for the purpose of comparison below). From (8), with aid of the relation $J_b = g\alpha\overline{w'\theta'}$ we have $-\overline{w'\rho'}(-D) = 0.13\overline{w'\rho'}(0) = -0.13\rho J_b^0/g$. Using the representative values $\Delta\rho = 0.16$ kg m^{-3} (estimated as $\Delta\rho = |\partial\rho/\partial z|\Delta z$, where $|\partial\rho/\partial z| = 3.2\times10^{-2}$ kg m^{-4} was calculated for the depth range $-D - 2.5$ m $< z < -D + 2.5$ m and averaged for all nights, and $\Delta z = 5$ m), $\rho = 1023$ kg m^{-3} and $J_b^0 = 1.5 \times 10^{-7}$ m^2 s^{-3}, results in an estimate of $w_e \sim -1.3 \times 10^{-5}$ m s^{-1}. This rate translates to a deepening of the ML of about 0.6 m during a period of 12 hours. Unfortunately, such small entrainment rates are close to impossible to verify experimentally in the ocean because of the much larger changes due to lateral variability and waves in the stratified interior. However, since from (13) the entrainment rate is inversely proportional to $\Delta\rho$, measurements at sites where the latter is much smaller than we have observed may provide a better opportunity for experimental verification.

Deardorff (1983), derived an entrainment rate based on the TKE equation and second-moment equations for the buoyancy flux and the density-fluctuation variance in the entrainment zone of the ML. The TKE equation was closed utilizing various empirical closure functions and constants. Formulation of the normalized entrainment rate, w_e/u_* or

w_e/w_*, was presented (Fig. 3 of Deardorff 1983) as a function of three Richardson numbers: $Ri_\tau = c_i^2/u_*^2$, $Ri_* = c_i^2/w_*^2$ ($w_* = (J_b^0 D)^{1/3}$ is the convective velocity scale), and $Ri_v = c_i^2/(\Delta U)^2$ (ΔU is the magnitude of the velocity jump at the base of the ML). These three Richardson numbers represent, respectively, the importance of the three mechanisms contributing to entrainment, namely surface wind stress, surface buoyancy flux and shear across the ML base, relative to the retarding stable density gradient at the ML base, represented by the velocity scale $c_i = [(g/\rho)\Delta\rho D]^{1/2}$. In the general case, when both the surface stress and convection are important, the formulation for w_* and Ri_* is used with w_* replaced by $w'_* = (w_*^3 + \eta^3 u_*^3)^{1/3}$ and Ri_* by $Ri'_* = (Ri_*^{-3/2} + \eta^3 Ri_\tau^{-3/2})^{-2/3}$, where the coefficient $\eta^3 < 1.8$.

From the mean values $J_b^0 = 1.5 \times 10^{-7}$ m^2 s^{-3}, $D = 65.1$ m, $\tau_0 = 0.09$ N m^{-2} (Table IV.1), and $\Delta\rho = 0.16$ kg m^{-3}, and the definitions of w_*, u_*, c_i, Ri_τ and Ri_*, it is found that $w_* \simeq w'_*$, to about 5%, and $Ri_* \simeq Ri'_*$, to about 10%. This indicates that for our experiment Deardorff's entrainment formulation for a convectively driven ML can be used to a good approximation. Using that formulation in conjunction with the mean values $w_* = 2.1 \times 10^{-2}$ m s^{-1}, $Ri_* = 221$ and $Ri_v = 71$, results in $w_e \sim -2.5 \times 10^{-5}$ m s^{-1} (Ri_v was estimated using $(\Delta U)^2 = S^2(\Delta z)^2 = 1.4 \times 10^{-3}$ m^2 s^{-2}, where $S^2 = 5.6 \times 10^{-5}$ s^{-2} was calculated for the depth range $-D - 2.5$ m $< z < -D + 2.5$ m and averaged for all nights, and $\Delta z = 5$ m).

From dimensional analysis, it is argued that the dimensionless entrainment rate, w_e/u', can be expressed as $w_e/u' = f(Ri_0)$ (e. g. Turner 1973), where $(Ri_0) = gl\Delta\rho/\rho u'^2$ and l and u' are the turbulence length and velocity scales, respectively. The turbulence velocity scale usually assumes the velocity scales of the forcing mechanism, e.g. $u' = w_*$ or $u' = u_*$

for a BL driven, respectively, by convection or surface stress. The length scale is commonly taken to be the ML depth, such that $l = D$. In the respective cases of convective- and stress-driven entrainment one then has $w_e/w_* = f(Ri_*)$ and $w_e/u_* = f(Ri_\tau)$, where Ri_* and Ri_τ were defined above. Laboratory studies of the entrainment zone of a convectively ML by Deardorff et al. (1980) showed that the dimensionless entrainment rate could be represented fairly well by the relation $w_e/w_* = 0.25(Ri_*)^{-1}$. Using this relation and the relevant mean numerical values from our experiment, a value of $w_e \sim -2.4 \times 10^{-5}$ m s^{-1} is found. Note, however, that the relation $w_e/w_* = 0.25(Ri_*)^{-1}$ results directly from the definition of w_* and equation (13), when $-\overline{w'\rho'}(-D) = -0.25\rho J_b^0/g$ is used instead of $-\overline{w'\rho'}(-D) = -0.13\rho J_b^0/g$, the mean estimate for our experiment.

In a formulation by Stull (1976), the potential energy change due to turbulent entrainment was related to the TKE energy equation integrated over the depth of the ML. Applying this to an idealized "slab" type ML model, and making some simplifications and approximations an entrainment rate equation was derived. Values of the coefficients in Stull's equation were then determined by testing the theoretical equation against a large number of laboratory and field experiments. Using Stull's entrainment parameterization for the convective case (presented graphically in Fig. 7 of Deardorff 1983), and the estimates from our study for w_*, Ri_* and Ri_v, results in $w_e \sim -1.2 \times 10^{-5}$ m s^{-1}. In spite of the lack of consensus on the various entrainment formulations, the values of w_e calculated from (13) and from all of the entrainment formulations discussed above are consitent to within a factor of 2.

IV.5. Summary and conclusions

An open ocean site experiment was conducted in the nighttime convective OBL when the surface buoyancy flux was quasisteady. The vertical structure of potential temperature, TKE dissipation rate and shear of the horizontal velocity was investigated using a large number of vertical profiles. The major results of this study are:

- The nighttime convective OBL cooled as a uniform "slab" during the quasisteady forcing phase. This is inferred from the steadiness of the vertical structure of potential temperature, i.e. $\partial(\partial\theta/\partial z)/\partial t = 0$, where θ was averaged over time periods larger than T_c, the convective time scale. The "slab" type behavior is further supported by the vanishing shear of horizontal velocity in the bulk of the ML and the large increase in shear near the base of the ML. In contrast, during daytime, when the upper OBL was slightly stably stratified due to solar heating, and mixing was chiefly driven by the surface wind stress, a clear increase in shear in the upper part of the OBL was observed.

  The clear distinction observed between the nighttime well-mixed layer, which was unable to support a significant shear, and the daytime stratified upper OBL with a noticeable shear, supports André and Lacarrère's (1985) results from a third-order numerical model. Their results indicate that it is not always possible to describe the OBL as a well-mixed layer as is frequently done in most of the simple parameterized models. This was particularly true for the case of a stress-driven OBL, since the mechanically induced turbulence was found to be relatively inefficient in redistributing the momentum introduced at the surface. However, in the case of buoyancy driven turbulence,

heat and momentum mixing was found to be much more efficient, and to lead to a simplified vertical structure. The evidence from our study is consistent with André and Lacarrère's conclusions, and provides experimental justification for the adequacy of the use of "slab" models for the OBL during convection. Conversely, our results demonstrate the inadequacy of such models during periods when the OBL is driven by surface stress, though exceptions may occur in extreme cases such as storms when exceptional high surface stresses induce vigorous mixing and a truly well-mixed layer may result.

- Two independent estimates of the turbulence heat flux profile suggest that the heat flux in the convective OBL decreases linearly with depth. The first method of estimation of the heat flux profile was based on heat conservation and the steadiness of the vertical structure of potential temperature. From this estimate, the dimensionless heat flux is represented by $\overline{w'\theta'}^*(z^*) = 1 + a_h z^*$. Values of the constant a_h, estimated from the ratio $-[\overline{w'\theta'}(-D)]/[\overline{w'\theta'}(0)]$, were between 1.07 and 1.18 with a mean of 1.13. The second method of estimation of the heat flux profile was based on profiles of TKE dissipation rate and a simplified TKE balance between the buoyancy flux and dissipation in the bulk of the ML, away from the surface of the ocean and the base of the ML. This estimate suggests, similarly, a linear heat flux profile where $\overline{w'\theta'}^*(z^*) = b_\epsilon + a_\epsilon z^*$. Estimates of b_ϵ ranged from 0.66 to 1.99 with an overall mean of 1.40, and estimates of a_ϵ were between 0.30 and 1.50, with an overall mean of 0.93. As discussed in section IV.3, the estimates of b_ϵ are not significantly different from 1, while the estimates of a_ϵ are not significantly different from those of a_h. The linear heat flux

profile, suggested by the two methods, is in good agreement with results from laboratory studies, numerical models (for both the OBL and the ABL) and field studies in the convective ABL.

- Estimates of the ratio $-[\overline{w'\theta'}(-D)]/[\overline{w'\theta'}(0)]$ ranged between 0.07 and 0.18 with a mean of 0.13, and are in good agreement with most of the values quoted for the convective ABL (e.g. Stull 1976). Knowledge of the heat flux at the base of the ML, $\overline{w'\theta'}(-D)$, is of crucial importance in "slab" models since it provides a closure condition for the ML equations and permits an estimate of the entrainment rate.

- The entrainment rate, estimated from the equation for the transport across an interface (13) and the mean heat flux and density jump at the base of the ML, was found to be $\sim -1.3 \times 10^{-5}$ m s^{-1}. Entrainment rates calculated from different formulations, using the relevant numerical values from our experiment, were found to be within a factor of 2 of our estimate. This rather good agreement may be related to the fact that the simplifying assumptions underlying some of the entrainment formulations, such as an idealized "slab" type mixed layer, seem to hold for convective ocean boundary layers.

Although there appear to be clear similarities between the mixed layers of both the ocean and atmosphere during convection, there is a growing body of evidence that the upper part of the OBL, or the surface layer, is distinctly different (e.g. Agrawal et al. 1992; Anis and Moum 1993c [chapter V]). Specifically, mixing is enhanced in the OSL over predictions for the ASL and the superadiabatic potential temperature gradient is comparatively smaller (Anis and Moum 1993c [chapter V]). Both the short time scale variability (i.e. less than the convective time scale) of the vertical heat flux and its

relation to the unique processes in the upper OBL such as wave-turbulence interactions and Langmuir circulation will have to await future availability of direct heat flux measurements.

Acknowledgments. We are grateful to the Captain and crew of the R/V *Wecoma* for their help during the experiment. This work was supported by National Science Foundation Grants OCE-8608256.

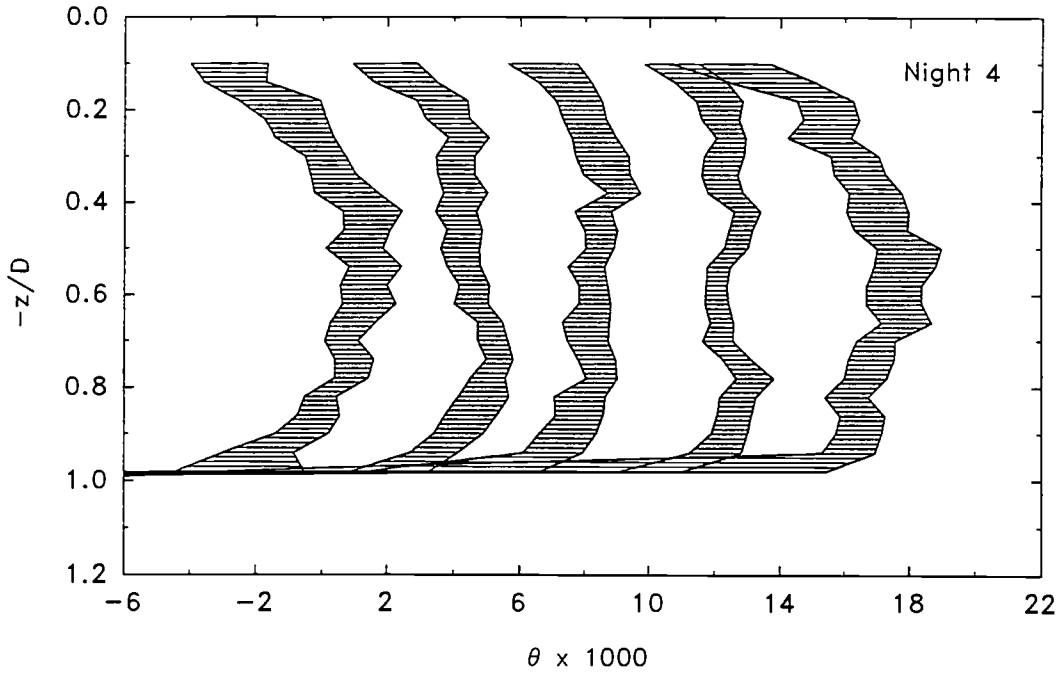

Figure IV.1. Referenced and averaged profiles of $\theta(z)$ as a function of the nondimensional depth, $-z/D$, during the quasisteady convective forcing phase of night 4 (data was averaged in scaled depth bins of $-z/D = 0.04$). The quasisteady convective forcing phase of the night was subdivided into 5 sequential periods of 2 hours, each starting about 2 hours after J_b^0 changed sign from negative to positive and ending about 2 hours before J_b^0 changed sign again. Shading represents 95% bootstrap (Efron and Gong 1983) confidence intervals. The profiles are sequentially offset by 0.004 K.

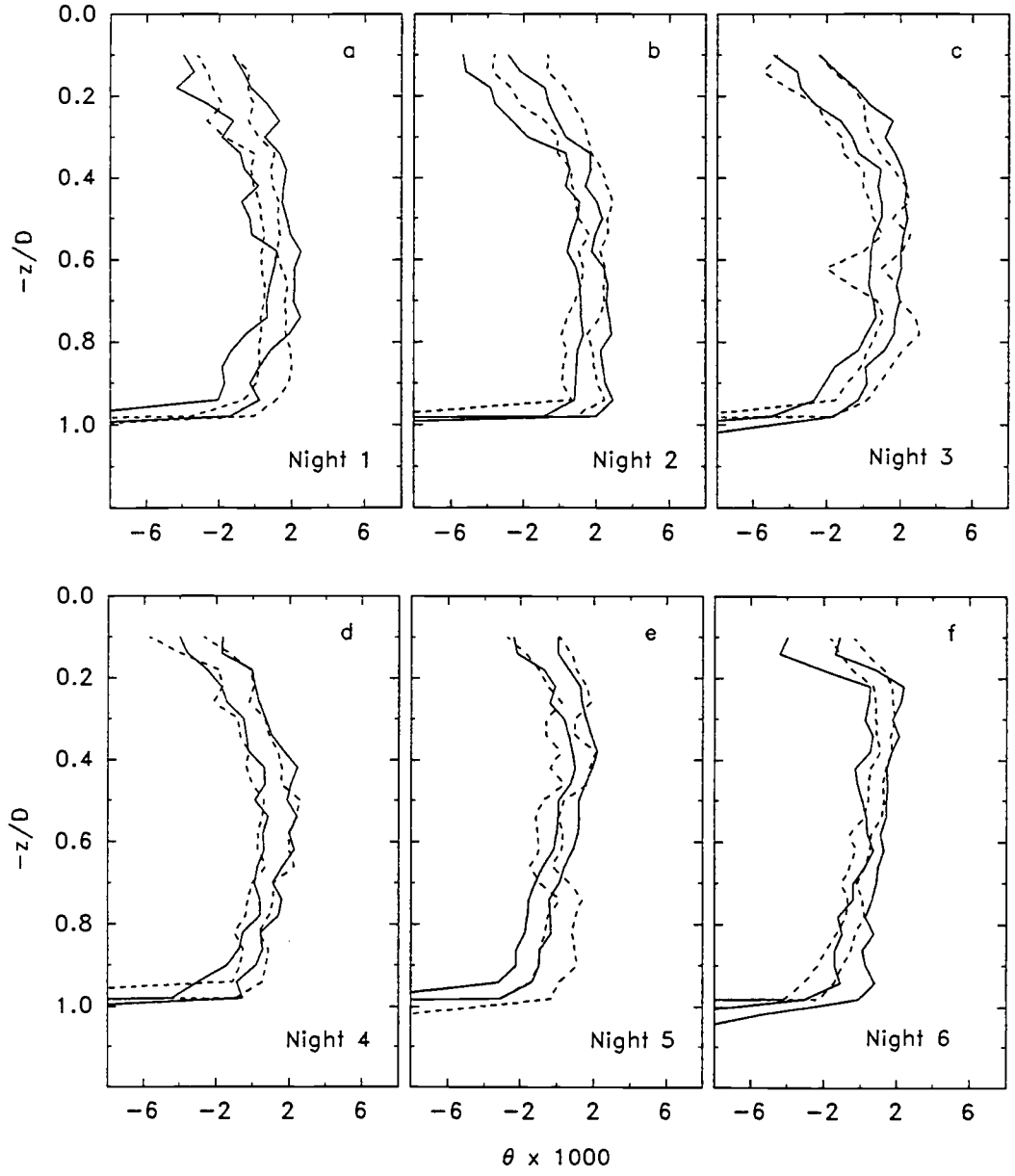

Figure IV.2. Similar to Fig. IV.1 but for the first (solid lines) and last (dashed lines) 2-hour periods of the quasisteady convective forcing phase of each of the six nights of the experiment: (*a*) night 1, (*b*) night 2, (*c*) night 3, (*d*) night 4, (*e*) night 5, (*f*) night 6. The vertical structure of $\theta(z)$ was steady throughout each of the nights of the experiment at the 95% confidence level.

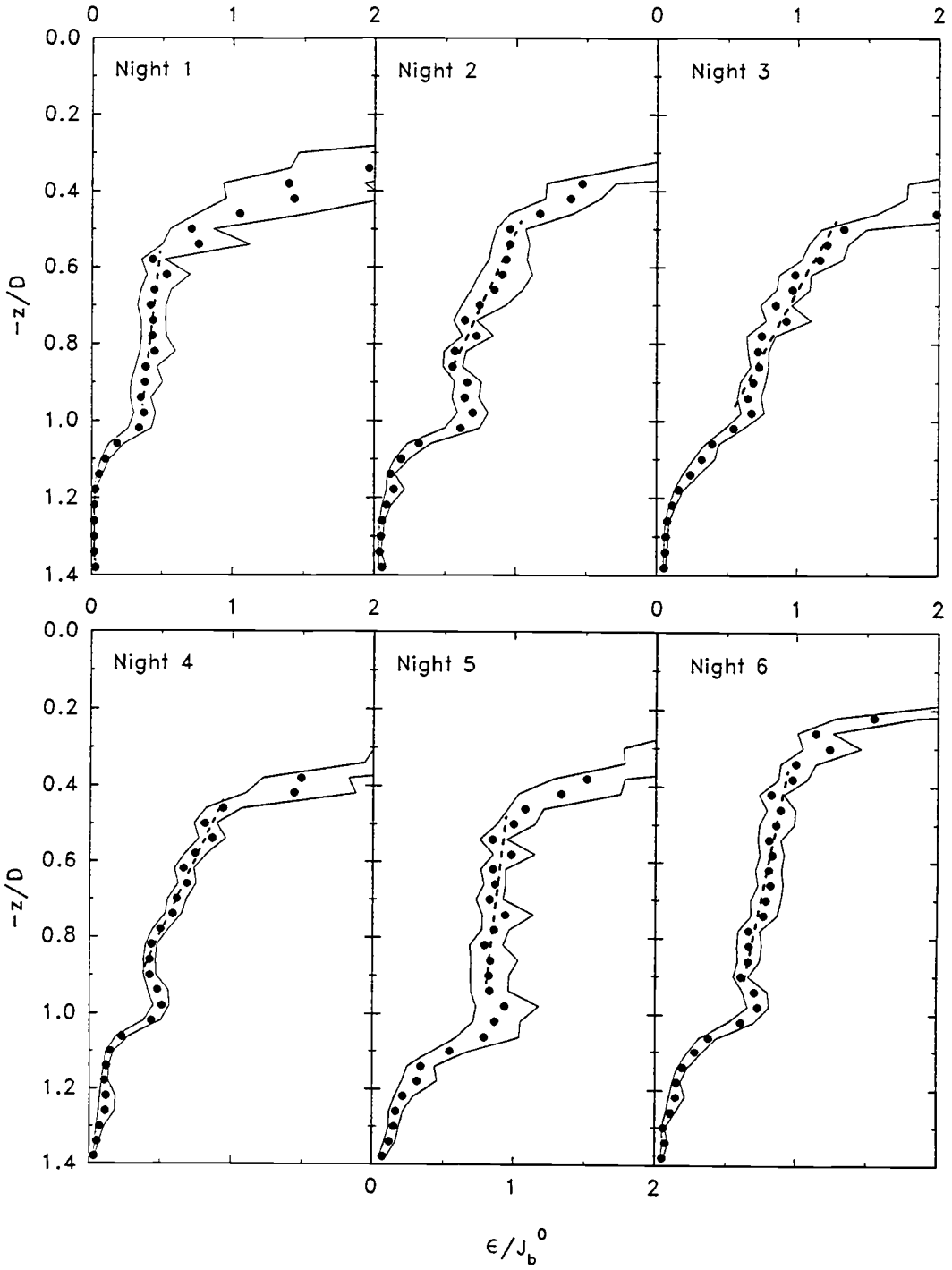

Figure IV.3. Scaled turbulence kinetic energy dissipation rate, ϵ/J_b^0, as a function of nondimensional depth, $-z/D$, for the six nights of the experiment. The filled circles and solid lines represent the mean and the 95% bootstrap confidence envelopes, respectively. The broken lines are least-square fits of the form $b_\epsilon + a_\epsilon z^*$ to the mean values (Eq. 12 and Table IV.2).

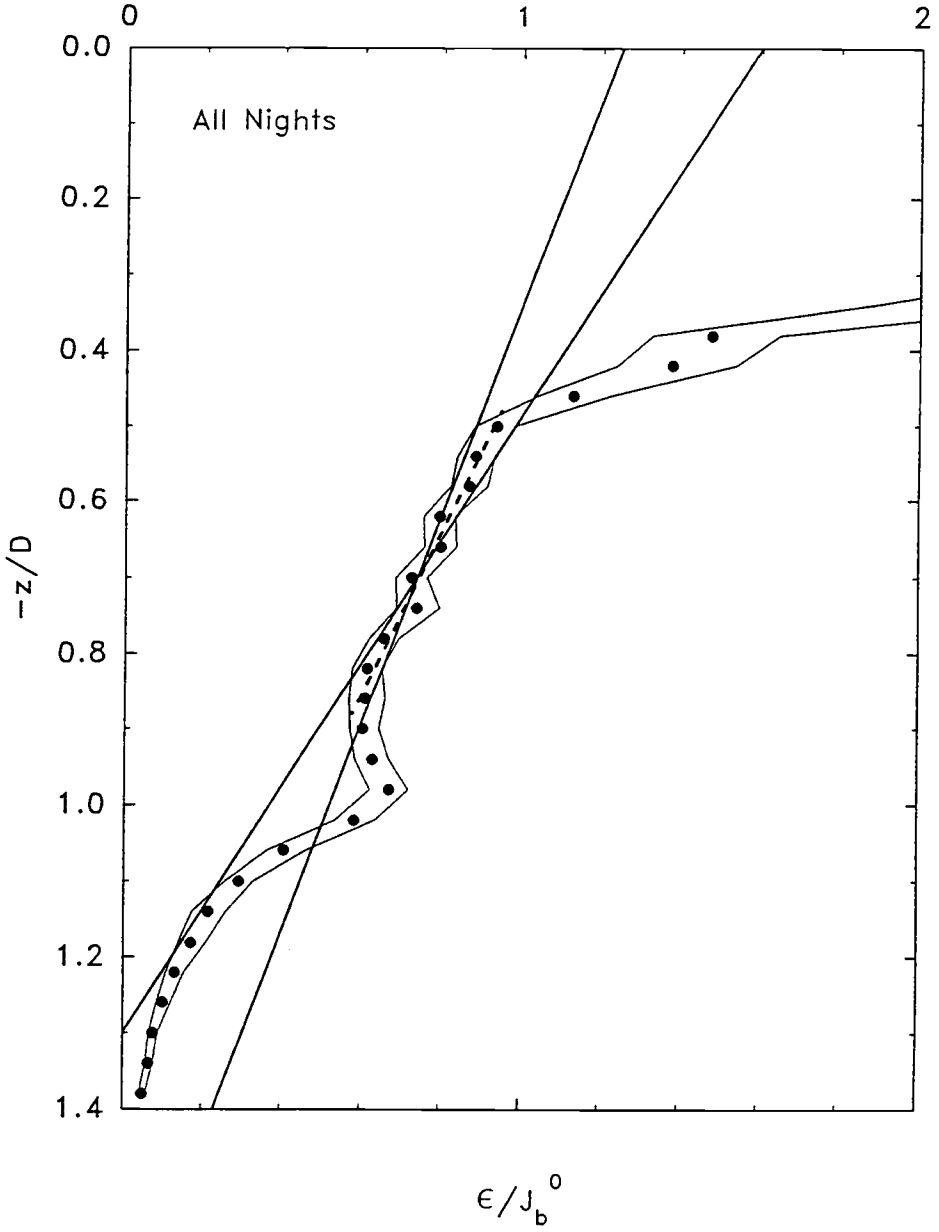

Figure IV.4. Similar to Fig. IV.3 but for the average of all the nights of the experiment. Two straight solid lines were fitted by eye in the 95% confidence envelope such that their slopes represent the minimum and maximum values permissible by this envelope. This provides an uncertainty estimate on a_ϵ (see Table III.2) which takes into account the 95% confidence intervals of the mean values of ϵ. Note also the increase in ϵ/J_b^0 near the base of the mixed layer (i.e near $-z/D \sim 1$).

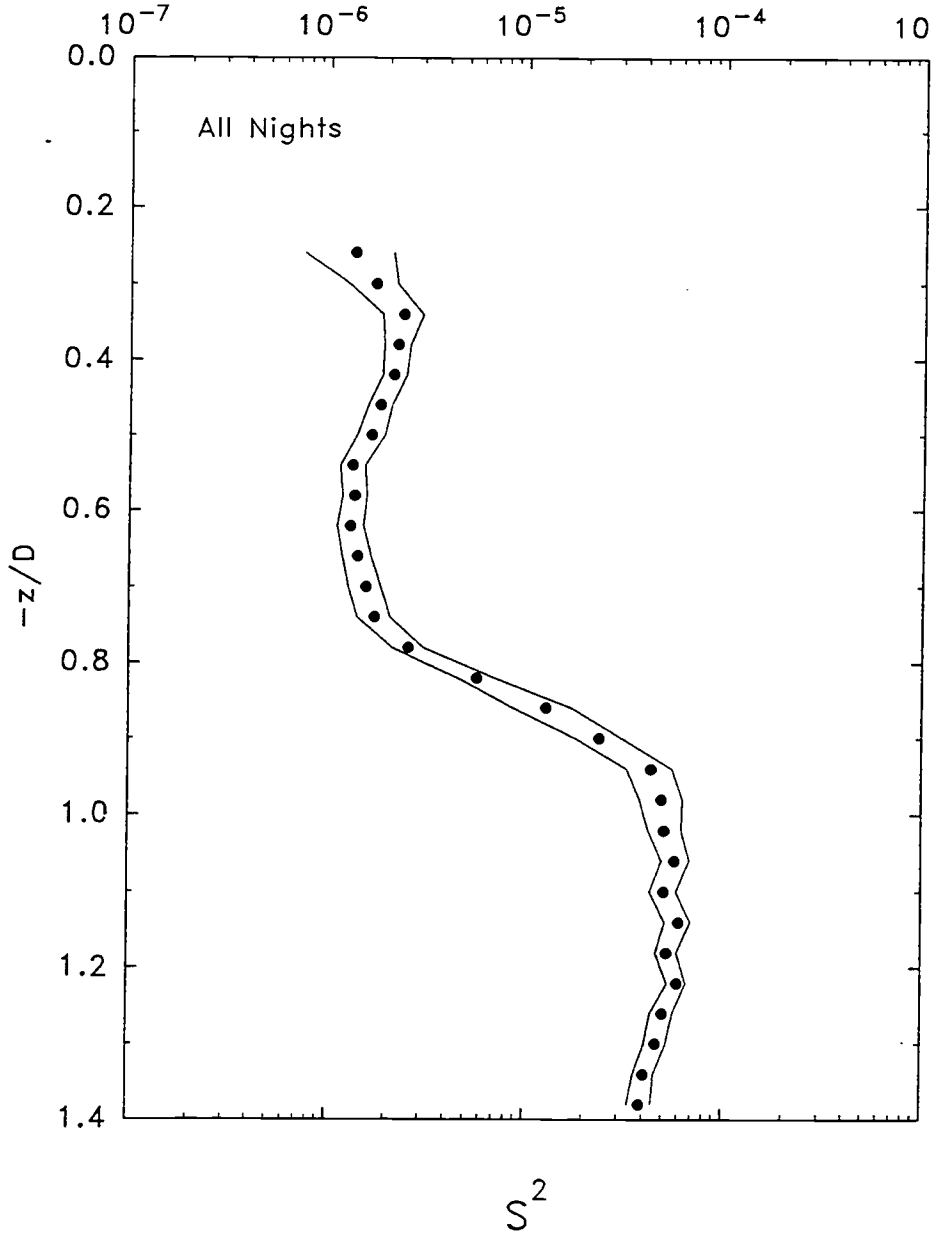

Figure IV.5. Squared shear, $S^2 = (\partial U/\partial z)^2 + (\partial V/\partial z)^2$, as a function of nondimensional depth, $-z/D$. S^2 was calculated from individual profiles, binned in scaled depth bins of $-z/D = 0.04$ and ensemble averaged across all nighttime profiles. The filled circles represent the mean and solid lines the 95% bootstrap confidence envelopes. Values of S^2 in the bulk of the mixed layer are low and not significantly different from the equivalent detection limit ($1 - 2 \times 10^{-6}$ s^{-2}) due to computing S^2 from ADCP velocity measurements. However, a rapid increase in S^2, of almost two orders of magnitude, is noticed in the lower 20% of the mixed layer. The slight increase in S^2 for $0.3 < -z/D < 0.5$ is attributed to a few profiles during nights 1 and 2 and is removed when these nights are excluded from the mean nighttime profile.

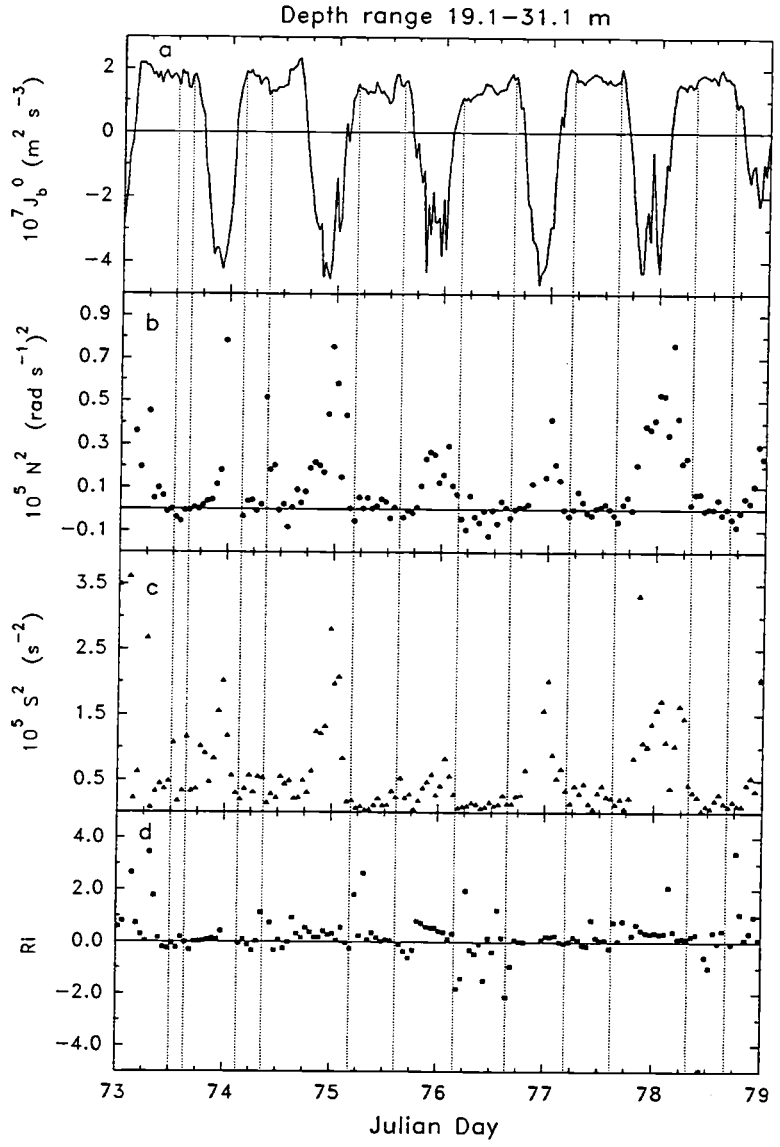

Figure IV.6. Time series of hourly averages of the surface buoyancy flux, (a) J_b^0 (positive during nighttime), squared buoyancy frequency, (b) N^2, squared shear magnitude, (c) S^2, and Richardson number, (d) Ri. N^2, S^2 and Ri were estimated from individual profiles in the depth range -19.1 m $> z > -31.1$ m and then hourly averaged. A clear diurnal cycle in both N^2 and S^2 is apparent; during daytime the increase in S^2 followed closely the increase in stratification (and hence increase in N^2), while during nighttime S^2 decreased to relative small values, which, on average, were not significantly different from the equivalent detection limit. No clear diurnal cycle in Ri is noticed since an increase in S^2 was generally compensated by an increase in N^2, while a decrease in S^2 was compensated by a decrease in S^2. The dotted vertical lines define, sequentially from night 1 to night 6, the period of each night for which RSVP profiles were analyzed.

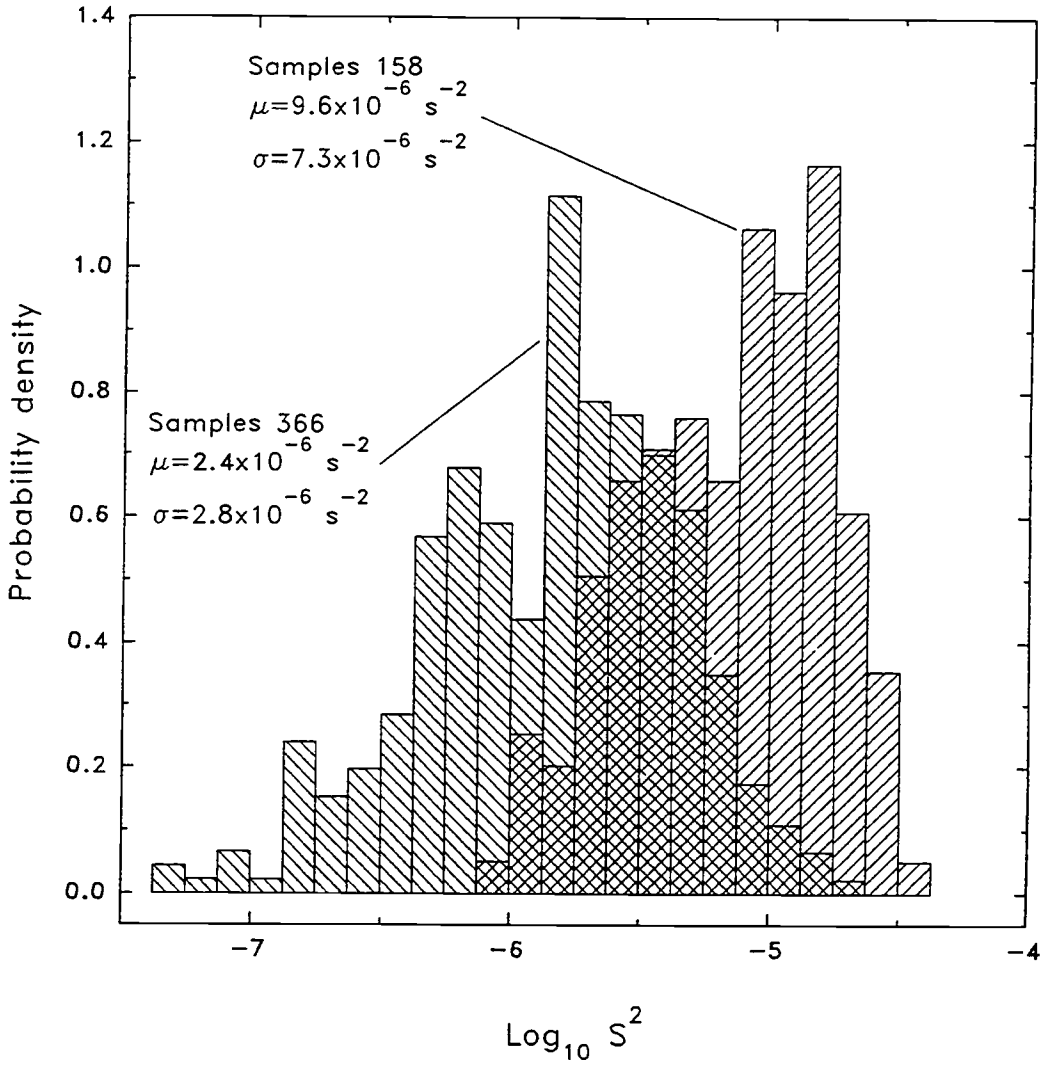

Figure IV.7. Distributions of the daytime and nighttime estimates of S^2 from individual profiles in the depth range -19.1 m $> z > -31.1$ m. Rightward rising hatched areas represent daytime while leftward rising hatched areas represent nighttime. Values of S^2 smaller than 1×10^{-6} s^{-2} are below equivalent detection limit. μ and σ are the sample arithmetic mean and standard deviation, respectively.

Table IV.1. Nighttime average values of meteorological parameters. The surface wind stress, τ_0; the difference between the air temperature (measured from the R/V *Wecoma*'s mast at 8-m height) and the sea surface temperature (SST; measured from the ship's hull mounted Doppler's thermistor at 5-m depth), $T_{air} - SST$; the net surface heat flux, J_q^0; the net surface buoyancy flux, J_b^0; the Monin-Obukhov length scale, $L = -u_*^3/\kappa J_b^0$ (where $u_* = \sqrt{\tau_0/\rho}$ is the ocean surface friction velocity); the significant wave height, H_s for swell and wind-waves(from R/V *Wecoma*'s ship's officers' log). Averages of the above quantities were calculated for the time period during which J_b^0 was quasisteady (starting about 2 hours after J_b^0 changed sign from negative to positive and ending about 2 hours before J_b^0 changed sign back).

	night						
	1	2	3	4	5	6	mean
τ_0 (N m^{-2})	0.08	0.10	0.08	0.07	0.11	0.11	0.09
$T_{air} - SST$ (K)	−1.84	−1.23	−1.53	−0.88	−0.73	−0.86	−1.09
J_q^0 (W m^{-2})	212	211	171	166	205	199	189
10^7 J_b^0 (m^2 s^{-3})	1.61	1.66	1.37	1.31	1.54	1.61	1.48
L (m)	−10.6	−14.2	−11.7	−10.8	−17.3	−17.5	−13.9
H_s swell (m)	2.4	2.7	2.0	1.8	2.2	2.1	2.1
H_s wind-waves (m)	0.8	0.9	0.7	0.6	0.9	0.9	0.8

Table IV.2. Nighttime average values of mixed layer related quantities. D is the depth of the ML; $\epsilon(-D)$ is the TKE dissipation rate at the base of the ML (calulated over the depth range $-D-2.5\text{m} < z < -D+2.5\text{m}$); $\epsilon^*(-1) \equiv \epsilon(-D)/J_b^0$ is the nondimensional TKE dissipation rate (calculated for each profile over the scaled depth range $0.98 < -z/D < 1.02$ and then ensemble averaged for a particular night; values in parentheses are the 95% bootstrap confidence limits); $|\overline{w'\theta'}^*(-1)|$ is the upper bound on the nondimensional vertical heat flux near the base of the ML (calculated as $|\overline{w'\theta'}^*(-1)| \leq 0.2\epsilon^*(-1)$, using the mean values of $\epsilon^*(-1)$); $a_h \equiv 1 - \overline{w'\theta'}^*(-1)$ is the rate of decrease with depth of the nondimensional vertical linear heat flux; a_ϵ and b_ϵ are the values resulting from a least square fit of the form $b_\epsilon + a_\epsilon z^*$ to $\epsilon^*(z^*)$ (where $\epsilon^*(z^*) \equiv \epsilon(z)/J_b^0$ and $z^* \equiv z/D$) in the lower half of the ML (Figs. IV.3 and IV.4; the $\pm$ values are the probable uncertainties in b_ϵ and a_ϵ resulting from the fit to individual nightly mean profiles and to the overall mean profile. For the latter, written in parentheses, are error estimates as determined from two graphically fitted straight lines in the 95% bootstrap confidence envelope (see Fig. IV.4)).

	night						
	1	2	3	4	5	6	mean
D (m)	64.4	68.5	50.6	67.5	64.3	82.2	65.1
$10^7\epsilon(-D)$ (m^2 s^{-3})	0.56	1.14	0.79	0.62	1.36	1.15	0.95
$\epsilon^*(-1)$	0.36	0.65	0.61	0.47	0.90	0.67	0.63
	(0.28, 0.44)	(0.54, 0.77)	(0.54, 0.69)	(0.42, 0.53)	(0.72, 1.12)	(0.58, 0.76)	(0.58, 0.68)
$\lvert\overline{w'\theta'}^*(-1)\rvert$	0.07	0.13	0.12	0.09	0.18	0.13	0.13
a_h	1.07	1.13	1.12	1.09	1.18	1.13	1.13
a_ϵ	0.30 ± 0.10	1.26 ± 0.13	1.50 ± 0.14	1.25 ± 0.08	0.32 ± 0.13	0.57 ± 0.07	0.93 ± 0.05
							(0.73, 1.23)
b_ϵ	0.66 ± 0.07	1.64 ± 0.09	1.99 ± 0.10	1.49 ± 0.06	1.10 ± 0.10	1.15 ± 0.04	1.40 ± 0.04
							(1.25, 1.60)

V. SCALING $\epsilon(z)$ NEAR THE SURFACE OF THE OCEAN

Abstract

An extensive set of vertical microstructure profiles has been collected in the upper oceanic boundary layer (OBL) under various atmospheric and sea conditions. The rate of viscous dissipation of turbulence kinetic energy, ϵ, exhibited a range of behaviours under different forcing conditions. In some of our experiments, in the vicinity of the ocean's surface, ϵ was closely balanced by the wind stress production of turbulence kinetic energy. In the mixed-layer of the nighttime convective OBL, beneath the superadiabatic surface layer, ϵ followed convective similarity scaling. In contrast, a relatively large number of cases revealed enhanced dissipation rates, with an exponential depth decay, in the upper part of the OBL. In these instances the simple scaling laws predicted for turbulence near a solid surface severely underestimate turbulence mixing near the ocean surface.

We suggest, for those cases, that wave-turbulence interactions are important and propose two different mechanisms to explain the behaviour of ϵ near the surface, leading to two scaling schemes. The first mechanism requires high levels of turbulence kinetic energy, created by wave breaking at the surface, to be transported downwards away from the surface by the motion of the swell. This transport is then locally balanced by ϵ. Estimates of the energy lost by breaking surface waves, were consistent with the vertically integrated dissipation rate observed in the upper part of the OBL. In contrast, constant stress layer predictions are far too small. The second mechanism requires a rotational wave field and significant wave stresses that balance the turbulence Reynolds stresses. Energy drawn from the wave field

to the mean flow, via the wave stresses, is in turn drawn from the mean flow by the turbulence production term, which is balanced by ϵ.

V.1. Introduction

The ocean boundary layer (OBL) is defined as that part of the ocean which is directly influenced by surface forcing such as the heat flux, the wind stress, and surface waves. As a result the OBL responds directly to changes in surface forcing with time scalse on the order of diurnal time scales (e.g. the diurnal heating/cooling cycle) and shorter. The upper boundary of the OBL is the ocean's surface, while the lower boundary is often defined by the top of the seasonal thermocline.

In spite of the crucial role of the OBL in atmosphere-ocean dynamics our understanding of the physics in the OBL is rudimentary at best. In a recent review of air-sea interaction, Donelan (1990) concluded that the largest gap in our knowledge of air-sea interaction is in the relationship between the OBL and surface waves. A major obstacle to the understanding of processes in the OBL is the scarcity of accurate measurements. They are difficult to accomplish due to the need for a stable platform from which to make the observations and due to the harsh environment in which the sensors need to operate. Moreover, the analysis is usually complicated as one has to evaluate independently the motions due to the mean flow, waves and turbulence.

To date, studies carried out in the ocean, lakes and laboratories show that in many cases the aquatic boundary layer has similar scaling laws (for definition of scaling laws see section V.4.1) to those in the atmospheric boundary layer (ABL) over land (the ABL is commonly defined as that part of the atmosphere bounded by the land surface from below, and by the first temperature inversion from above, e.g. Stull 1988). Some investigators have shown that wind-driven near surface layers of oceans and lakes exhibit scaling laws consistent with constant stress layers over solid boundaries. Jones and

Kenney (1977) found that turbulence velocity fluctuations appear to have a velocity scale proportional to the friction velocity in water, $u_* = \sqrt{\tau_0/\rho_w}$ (τ_0 is the surface wind stress and ρ_w is the density of sea water), and a length scale proportional to the depth, z. Surface velocity measurements using drifters and drogues (Churchill and Csanady 1983), showed the velocity to decrease nearly logarithmically with depth from the surface to a depth of about 1 m. Field measurements in a fresh water lake (e.g. Dillon et al. (1981), and in the ocean (Soloviev et al. 1988, 1989), showed that turbulence kinetic energy (TKE) dissipation rate, $\epsilon(z)$, scales as $u_*^3/\kappa z$ (Von Karman's constant, $\kappa \approx 0.4$).

Observations during convective conditions revealed a statically unstable superadiabatic layer in the upper 20-40% of the OBL (Anis and Moum 1992 [chapter III]). For comparison, the superadiabatic atmospheric surface layer (ASL) occupies usually only the lower 10% or so of the convective ABL over land. Generally the ASL is defined as the lower 10% of the ABL, where fluxes vary less than 10% of their magnitude, whether it is part of a convective or a stable boundary layer (e.g. Stull 1988). Definition of an oceanic surface layer (OSL) based on the constancy of fluxes cannot be made due to the lack of direct flux measurements. Usage of the term OSL in the oceanographic literature is therfore not uniform. However, since a superadiabatic layer was clearly identified in our studies, we define that part of the nighttime convective OBL as the OSL.

Field studies during convective conditions in aquatic boundary layers revealed well mixed layers in which mean quantities, such as temperature, were nearly constant with depth. Mixed layers (ML) are unique to convectively boundary layers and are rarely, if ever, observed in boundary

layers driven solely by wind stress. To avoid confusion, the term ML will be used when referring to the well-mixed part of the convective boundary layer, where $\partial\sigma_\theta/\partial z \approx 0$ (potential temperature, θ, and potential density, σ_θ, are defined in the caption of Fig V.1). The ML was found to occupy the middle 50-80% of the nighttime convective OBL (Anis and Moum 1993b [chapter IV]). In the ML, $\epsilon(z)$ was found to be relatively uniform with depth and to follow convective similarity scaling for the ocean (e.g. Shay and Gregg 1984a, 1984b, 1986; Anis and Moum 1992 [chapter III]) and for a fresh water reservoir (Imberger 1985), where Brubaker (1987) showed that the rate of dissipation of temperature variance, χ, also followed convective similarity scaling. Lombardo and Gregg (1989) observed a range of conditions in a convective OBL, concluding that ϵ could be normalized very well by the sum of convective and surface layer (SL) similarity scalings. Scaling of χ was less successful and applied only in part of the OBL when turbulent production was dominated either by convection or wind stress.

On the other hand, evidence for enhanced turbulence and mixing in the upper part of the aquatic BL comes from a growing number of experimental field and laboratory studies. Field studies in the upper part of the OBL under different forcing conditions (Shay and Gregg 1984a; Gregg 1987; Gargett 1989; Anis and Moum 1992 [chapter III]; Osborn et al. 1992) showed enhanced TKE dissipation rates which were much larger than predicted by SL and/or convective scalings. Kitaigorodskii et al. (1983) and Agrawal et al. (1992) reported enhanced dissipation rates beneath surface waves, observed during two separate field experiments in Lake Ontario. Thorpe (1984), using acoustic measurements of bubbles near the surface of the ocean, suggested the importance of turbulence generated by breaking waves. In a laboratory

experiment with no imposed winds, Rapp and Melville (1990) showed that, as a result of wave breaking, mean surface currents in the range 0.02-0.03C (where C is the characteristic phase speed) were generated and took about 60 wave periods to decay to 0.005C. Turbulence rms velocities on the order of 0.02C were measured, decaying to 0.005C after more than 60 wave periods, and were still significant to a depth of k^{-1} (where k is the characteristic wavenumber). In light of these experiments it seems reasonable that breaking of surface waves is an important source of TKE and mixing in the OBL, and needs to be considered.

Another source of TKE may be due to downward wave momentum flux. Shonting (1964, 1967, 1968, 1970), Cavaleri et al. (1978), Cavaleri and Zecchetto (1985) and Yefimov and Khristoforov (1969, 1971) observed in field experiments that the horizontal and vertical wave velocities were consistently out of quadrature, leading to downward wave momentum flux. Similar results, from laboratory experiments, were reported by Dobroklonskiy and Lesnikov (1975) and by Bliven et al. (1984), who also showed that TKE decayed exponentially with depth, penetrating to a depth on the order of the wavelength. In a recent laboratory experiment, Cheung and Street (1988) carefully examined turbulence in the water at an air-water interface for different cases of surface gravity waves. They showed that, although turbulence parameters followed constant stress layer scaling in the wind-generated waves case, they behaved very differently in the case of wind-ruffled mechanically-generated waves, for which: 1) increased turbulence levels were observed, away from the surface to a depth of about $1/k$ (k is the wavenumber of the mechanically-generated waves), and the depth decay of turbulence rms velocities followed the decay of wave rms velocities

closely; 2) the phase difference between $\tilde{u}$ and $\tilde{w}$, the horizontal and vertical wave velocities respectively, was consistently less than 90°; 3) in both the wind-ruffled mechanically-generated waves and the high wind speed wind-wave experiments, the mean velocity profiles had slopes less than $1/\kappa$, the slope predicted by the law-of-the-wall, suggesting that the waves affect the mean flow. An ocean with swell and wind-waves might closely resemble the laboratory wind-ruffled mechanically-generated waves of Cheung and Street's experiment. If this is true, we might expect that for a combination of swell and wind-waves the layer near the surface of the ocean will reveal similar departures of turbulence from the predicted behaviour of a turbulent boundary layer near a solid surface.

Although the recent experimental field and laboratory studies, referred to above, provide the most convincing evidence of the importance of surface waves in upper OBL dynamics, treatment of wave-turbulence interactions started much earlier. More than 40 years ago Bowden (1950) suggested, on dimensional grounds, an eddy viscosity as a function of the wave parameters to explain the observed rate of decay of ocean swell. Phillips (1961) suggested generation of turbulence by the straining associated with the nonbreaking random wave motion and viscous diffusion; however the intensity of turbulence was of second order and too weak to account for wave attenuation or mixing in the OBL. Kitaigorodskii (1961), using dimensional arguments, proposed an eddy viscosity coefficient based on the vertical shear of the wave orbital velocity to calculate the vertical temperature profile in the upper OBL. Jacobs (1978), using numerical simulations with alternative forms of eddy viscosity coefficients, showed that an eddy viscosity based on Kitaigorodskii's 1961 formulation proved to be

significantly better in predicting the vertical temperature structure when compared to observations carried out during BOMEX. Benilov (1973), again using dimensional reasoning, proposed analytic expressions for TKE and ϵ as functions of depth and sea state, assuming surface waves as the main source of turbulence. Benilov's model was used by Soloviev (1986) to explain the observations of ϵ that he made in the upper Atlantic OBL. Huang (1986) proposed an exponential depth decay of $\epsilon(z)$ by assuming a similar depth decay of TKE and wave KE; however, a solid physical explanation for this assumption was not presented.

Numerical models, which predict the response of the ocean to different atmospheric forcing conditions, are crucially dependent on accurate parameterizations of momentum, heat and gas exchange between the atmosphere and the ocean. As most of these parameterizations are based on results from the ABL over land and do not account for possible implications due to the free surface of the ocean, these exchanges may be severely underestimated. In the following we examine the results from several sets of turbulence profiling measurements in the OBL, conducted under different meteorological and sea conditions. In section V.2 the necessary theoretical background and the governing equations are presented. Experimental details, meteorological conditions, observational results, and some statistical aspects of the data are presented in section V.3. In section V.4 we discuss the results, possible mechanisms for TKE production and transport, and prospects for scaling ϵ in the OBL. Conclusions and a summary are presented in section V.5.

V.2. Theoretical Background

V.2.1. General considerations

Unlike the rigid boundary of the ABL over land, the OBL is bounded by a free surface through which momentum, heat and gas are exchanged with the lower atmosphere. In the traditional treatment of boundary layers, the equations of momentum and continuity are treated without inclusion of surface waves. However, the existence of the free surface, with waves as an intermediary in the momentum and energy exchange with the atmosphere, has to be taken into account when considering the OBL. In the following analysis an incompressible, Boussinesq flow is assumed and the summation notation in a right hand cartesian system is used. The continuity equation is

$$\frac{\partial u_i}{\partial x_i} = 0; i = 1,2,3. \tag{1}$$

The momentum equation, assuming a nonrotating fluid (i.e. no Coriolis force), is given by

$$\frac{\partial u_i}{\partial t} + u_j \frac{\partial u_i}{\partial x_j} = -\frac{1}{\rho}\frac{\partial p}{\partial x_i} - \delta_{i3} g(1 + \frac{\rho'}{\rho}) + \nu \frac{\partial^2 u_i}{\partial x_j^2}, \tag{2}$$

where ν is the fluid's kinematic viscosity and δ_{ij} is Kronecker's Delta, such that $\delta_{ij} = 1$ if $i = j$ and $\delta_{ij} = 0$ if $i \neq j$.

To explicitly separate the relative influences of mean, wave and turbulence components of the flow field, we decompose all variables (e.g. velocity, pressure) of the flow as

$$a = \overline{a} + \tilde{a} + a', \tag{3}$$

where $\overline{a}$ is the time average component, $\tilde{a}$ the periodic wave-induced component and a' the turbulence component of the motion. Time averages are understood to be performed over time scales much larger than the

characteristic wave period. The combined wave-turbulence fluctuating component of the flow is defined by $a^{w,t} = \tilde{a} + a'$. From the definition of the time average we have

$$\overline{\tilde{a}} = 0 \tag{4.1}$$

and

$$\overline{a'} = 0. \tag{4.2}$$

If we further assume that the mean, the periodic wave-induced and the turbulence components of the motion are uncorrelated

$$\overline{\overline{a}\tilde{b}} = 0, \tag{4.3}$$

$$\overline{\overline{a}b'} = 0, \tag{4.4}$$

$$\overline{\tilde{a}b'} = 0, \tag{4.5}$$

where b represents some other flow variable, including a. Averaging (1) and using (3), (4.1) and (4.2), the continuity equation for the mean component of the flow is

$$\frac{\partial \overline{U}_i}{\partial x_i} = 0. \tag{5.1}$$

Subtracting (5.1) from (1), the continuity equation for the combined wave-turbulence component of the flow is

$$\frac{\partial u_i^{w,t}}{\partial x_i} = 0. \tag{5.2}$$

Averaging equation (2), using (3), (4.1), (4.2), (4.5) and (5.2), results in the momentum equation for the mean flow

$$\frac{\partial \overline{U}_i}{\partial t} + \overline{U}_j \frac{\partial \overline{U}_i}{\partial x_j} = -\frac{1}{\rho}\frac{\partial \overline{P}}{\partial x_i} - \delta_{i3} g + \nu \frac{\partial^2 \overline{U}_i}{\partial x_j^2} - \frac{\partial}{\partial x_j}(\overline{u_j' u_i'}) - \frac{\partial}{\partial x_j}(\overline{\tilde{u}_j \tilde{u}_i}). \tag{6}$$

The last term on the right hand side of this equation represents the interaction of the wave field with the mean flow. The momentum equation

for the combined wave-turbulence component of the flow is arrived at by subtracting (6) from (2) and using (5.2)

$$\frac{\partial u_i^{w,t}}{\partial t} + \overline{U}_j \frac{\partial u_i^{w,t}}{\partial x_j} = -\frac{1}{\rho}\frac{\partial p^{w,t}}{\partial x_i} - \delta_{i3} g \frac{\rho'}{\rho} - \frac{\partial}{\partial x_j}(u_j^{w,t}\overline{U}_i) - \frac{\partial}{\partial x_j}(u_j^{w,t}u_i^{w,t}) + \nu\frac{\partial^2 u_i^{w,t}}{\partial x_j^2} + \frac{\partial}{\partial x_j}(\overline{u_j' u_i'}) + \frac{\partial}{\partial x_j}(\overline{\tilde{u}_j \tilde{u}_i}). \quad (7)$$

To assess the possible interactions between the mean, wave and turbulence components of the flow it is necessary to separate the three components of the flow. We consider this problem in the following two sections. In section V.2.2 we consider an irrotational wave field, derived from a scalar velocity potential. We use an irrotational wave field firstly to demonstrate that one of the two wave-turbulence interaction mechanisms we propose (section V.4.2) may exist in an irrotational wave field, and secondly, irrotationality is used as a means of separating the three components of the flow. In section V.2.3 we assume a rotational wave field, observed in field (e.g Cavaleri et al. 1978) and laboratory (e.g. Cheung and Street 1988) experiments, to develop the necessary background for the second wave-turbulence interaction mechanism proposed. In the case of a rotational wave field the phase averaging technique is used to separate the mean, wave-induced, and turbulence components of the flow.

V.2.2. Turbulence in an irrotational wave field

We assume an irrotational wave field derived from a scalar velocity potential, Φ, by

$$\tilde{u}_i = \frac{\partial \Phi}{\partial x_i}, \quad (8)$$

and a rotational turbulence field derived from a vector potential, $\mathbf{V}$, by

$$u_i' = \epsilon_{ijk}\frac{\partial V_k}{\partial x_j}. \quad (9)$$

Applying the vector identity *div curl* $(\mathbf{V}) \equiv 0$ to equation(9) produces automatically the continuity equation for the turbulence component of the flow

$$\frac{\partial u_i'}{\partial x_i} = 0. \tag{10}$$

Subtracting (10) from (5.2) results in the continuity equation for the wave field

$$\frac{\partial \tilde{u}_i}{\partial x_i} = 0, \tag{11}$$

hence, from (8) and (11), the wave field satisfies Laplace's equation

$$\frac{\partial^2 \Phi}{\partial x_j^2} = 0. \tag{12}$$

We can now consider how the mean flow (6) interacts with an irrotational wave field. For simplicity we consider a statistically homogeneous flow in the horizontal plane with the x-axis aligned in the direction of the mean flow and a wave field propagating in the x direction. The mean flow is described by

$$\overline{U}_i = [U(z,t), 0, 0], \tag{13.1}$$

$$\overline{P} = P(z,t). \tag{13.2}$$

Using the above assumptions and the fact that time averages of the form $\overline{\tilde{u}_i \tilde{u}_j}$ vanish for $i \neq j$ for an irrotational wave field, the x-component of the mean momentum equation (6) is

$$\frac{\partial \overline{U}}{\partial t} = \frac{\partial}{\partial z}(\nu \frac{\partial \overline{U}}{\partial z} - \overline{w'u'}). \tag{14}$$

The terms in parenthesis represent the viscous stress and the turbulence Reynolds stress, respectively. The z-component of the mean flow is given by

$$-\frac{1}{\rho}\frac{\partial \overline{P}}{\partial z} - g - \frac{\partial}{\partial z}(\overline{w'w'} + \overline{\tilde{w}\tilde{w}}) = 0. \tag{15}$$

The x-component equation, (14), is the same as for a flow over a rigid boundary but the z-component equation, (15), involves an additional term, $\overline{\tilde{w}\tilde{w}}$, which is unique to the problem of flows in the presence of a surface wave field. From (15) it is already clear that for this type of flow we cannot simply ignore wave-turbulence interactions; however, better insight can be obtained by considering the KE equations of the mean, wave and turbulence components of the flow.

The mean kinetic energy (MKE) equation is obtained by multiplying the mean momentum equation (6) by $\overline{U}_i$ and averaging

$$\frac{\partial}{\partial t}(\frac{1}{2}\overline{U}_i\overline{U}_i) + \overline{U}_j\frac{\partial}{\partial x_j}(\frac{1}{2}\overline{U}_i\overline{U}_i) = -\frac{1}{\rho}\frac{\partial}{\partial x_i}(\overline{U}_i\overline{P}) - \overline{U}_i\delta_{i3}g + \nu\overline{U}_i\frac{\partial^2\overline{U}_i}{\partial x_j^2}$$
$$- \frac{\partial}{\partial x_j}(\overline{u_j'u_i'\overline{U}_i}) + \overline{u_i'u_j'}\frac{\partial\overline{U}_i}{\partial x_j}$$
$$- \frac{\partial}{\partial x_j}(\overline{\tilde{u}_j\tilde{u}_i\overline{U}_i}) + \overline{\tilde{u}_i\tilde{u}_j}\frac{\partial\overline{U}_i}{\partial x_j}. \qquad (16)$$

The wave kinetic energy (WKE) equation is obtained by multiplying equation (7) by $\tilde{u}_i$, averaging and using (4.3), (4.5) and (11)

$$\frac{\partial}{\partial t}(\frac{1}{2}\overline{\tilde{u}_i\tilde{u}_i}) + \overline{U}_j\frac{\partial}{\partial x_j}(\frac{1}{2}\overline{\tilde{u}_i\tilde{u}_i}) = -\overline{\tilde{u}_i\tilde{u}_j}\frac{\partial\overline{U}_i}{\partial x_j} - \overline{\tilde{u}_i\tilde{u}_j\frac{\partial u_i'}{\partial x_j}} - \frac{\partial}{\partial x_j}(\overline{u_j'\frac{1}{2}\tilde{u}_i\tilde{u}_i})$$
$$- \frac{\partial}{\partial x_j}(\overline{u_j'u_i'\tilde{u}_i}) + \overline{u_i'u_j'\frac{\partial\tilde{u}_i}{\partial x_j}}. \qquad (17)$$

Note that the molecular wave diffusion term, $\nu\partial^2\tilde{u}_i/\partial x_j^2$, vanishes by (12) and the transport term, $\overline{\tilde{u}_j\partial(\tilde{p}/\rho + \frac{1}{2}\tilde{u}_i\tilde{u}_i)/\partial x_j}$, vanishes by the assumption of an irrotational wave field. The TKE equation, obtained by multiplying equation (7) by u_i' and averaging, is

$$\frac{\partial}{\partial t}(\frac{1}{2}\overline{u_i'u_i'}) + \overline{U}_j\frac{\partial}{\partial x_j}(\frac{1}{2}\overline{u_i'u_i'}) = -\frac{\partial}{\partial x_j}\overline{[u_j'(\frac{p'}{\rho} + \frac{1}{2}u_i'u_i')]} - \frac{g}{\rho}\overline{w'\rho'} + \nu\frac{\partial^2}{\partial x_j^2}(\frac{1}{2}\overline{u_i'u_i'})$$
$$- \overline{u_i'u_j'}\frac{\partial\overline{U}_i}{\partial x_j} - \frac{\partial}{\partial x_j}(\overline{u_j'\frac{1}{2}\tilde{u}_i\tilde{u}_i})$$
$$- \frac{\partial}{\partial x_j}(\overline{\tilde{u}_j\frac{1}{2}u_i'u_i'}) - \overline{u_i'u_j'\frac{\partial\tilde{u}_i}{\partial x_j}} - \epsilon, \qquad (18)$$

where we have used relations (4.3), (4.4) and (4.5), continuity equations (10) and (11), the irrotationality condition for the wave field (12), and the definition $\epsilon = \nu\overline{(\partial u_i'/\partial x_j)^2}$ for the TKE dissipation rate. Simplified versions of equations (16), (17) and (18) can be written using our assumptions of statistical homogeneity in the horizontal plane and a mean current and surface wave field propagating in the x direction. This results in the following equations

$$\frac{\partial}{\partial t}(\frac{1}{2}\overline{UU}) = +\nu\overline{U}\frac{\partial^2\overline{U}}{\partial z^2} - \frac{\partial}{\partial z}(\overline{w'u'U}) + \overline{w'u'}\frac{\partial\overline{U}}{\partial z}, \tag{16.1}$$

$$\frac{\partial}{\partial t}(\frac{1}{2}\overline{\tilde{u}_i\tilde{u}_i}) = -\overline{\tilde{u}_i\tilde{u}_j\frac{\partial u_i'}{\partial x_j}} - \frac{\partial}{\partial z}(\overline{w'\frac{1}{2}\tilde{u}_i\tilde{u}_i}) - \frac{\partial}{\partial z}(\overline{w'u_i'\tilde{u}_i}) + \overline{u_i'u_j'\frac{\partial\tilde{u}_i}{\partial x_j}}, \tag{17.1}$$

$$\begin{aligned}\frac{\partial}{\partial t}(\frac{1}{2}\overline{u_i'u_i'}) = &-\frac{\partial}{\partial z}\overline{[w'(\frac{p'}{\rho} + \frac{1}{2}u_i'u_i')]} - \frac{g}{\rho}\overline{w'\rho'} - \overline{w'u'}\frac{\partial\overline{U}}{\partial z} - \frac{\partial}{\partial z}(\overline{w'\frac{1}{2}\tilde{u}_i\tilde{u}_i}) \\ &- \frac{\partial}{\partial z}(\overline{\tilde{w}\frac{1}{2}u_i'u_i'}) - \overline{u_i'u_j'\frac{\partial\tilde{u}_i}{\partial x_j}} - \epsilon,\end{aligned} \tag{18.1}$$

for the MKE, WKE, and TKE, respectively. Note that we have dropped the term $\nu\partial^2(\frac{1}{2}\overline{u_i'u_i'})/\partial x_j^2$ from the TKE equation; we expect it to be several orders of magnitude smaller than the other terms in the TKE budget.

V.2.3. Turbulence in a rotational wave field

Although in many cases the surface wave field is assumed to be irrotational, a number of field and laboratory studies have shown instances where the surface wave field departed from irrotationality. The earliest reports are from Shonting's observations of the velocities beneath the ocean free surface (1964, 1967, 1968, 1970). These observations showed the vertical and horizontal wave orbital velocities to be out of quadrature, leading to a downward momentum flux which decayed rapidly with depth. Similar

results from field observations were reported by Cavaleri et al. (1978), and Cavaleri and Zecchetto (1985). Yefimov and Khristoforov (1969, 1971) found that the most important contribution to the large vertical momentum fluxes they observed in the near surface layer was due to the swell, since the frequency spectrum of the wave stress coincided with the frequency spectrum of the swell. Laboratory studies by Dobroklonskiy and Lesnikov (1975) showed similar results of large wave stresses due to the nonorthogonality of the horizontal and vertical wave velocities. In their laboratory studies Cheung and Street (1988) found that the wave-induced stress $-\overline{\tilde{w}\tilde{u}}$ in wind-wave experiments was generally negative but smaller in magnitude than the turbulence Reynolds stress, $-\overline{w'u'}$. However, in the case of wind-ruffled mechanically-generated waves the wave-induced stress was negative and larger in magnitude than the turbulence Reynolds stress, resulting in energy transfer from the wave field to the mean flow through the term $\overline{\tilde{w}\tilde{u}}\partial\overline{U}/\partial z$ (see equation 24.1). Another laboratory study (Bliven et al. 1984) showed that the Reynolds stress increased with wave steepness and decreased exponentially with depth.

Due to the apparent departure of the wave field from the classical notion of irrotationality, we cannot use the same wave-turbulence separation method as in section V.2.2. However, separation can be achieved by the phase averaging technique (Hussain and Reynolds 1970). This method is suitable for extracting the wave-induced motion when the wave field is characterized by a specific wavelength in the spectrum. An example is the laboratory case of wind-ruffled mechanically-generated waves (Cheung and Street 1988), or the ocean in which the surface wave field is a combination of wind-waves and dominant swell. It should be noted that the turbulence component

of the flow in this case may include random wave components which are mainly attributed to short wind-waves and therefore important only close to the surface of the ocean. If on the other hand the wave field is completely random, for example wind-waves in a fetch limited lake when swell is absent, the phase averaging technique fails.

The phase average, $\langle a \rangle$, is defined as the average over a large ensemble of values of a that are realized at some specified phase of the reference wave. From this definition and the definition of the time average we have the following properties:

$$\langle a \rangle = \tilde{a} + \overline{a}, \tag{19.1}$$

$$a' = a - \langle a \rangle, \tag{19.2}$$

$$\langle a' \rangle = 0, \tag{19.3}$$

$$\langle \tilde{a} b \rangle = \tilde{a} \langle b \rangle, \tag{19.4}$$

$$\langle \overline{a} b \rangle = \overline{a} \langle b \rangle, \tag{19.5}$$

$$\langle \overline{a} \rangle = \overline{\langle a \rangle} = \overline{a}. \tag{19.6}$$

Phase averaging the continuity equation for the combined fluctuating component (5.2), we arrive at the continuity equation for the wave component of the motion

$$\frac{\partial \tilde{u}_i}{\partial x_i} = 0. \tag{20}$$

Subtracting (20) from (5.2) produces the continuity equation for the turbulence component

$$\frac{\partial u_i'}{\partial x_i} = 0. \tag{21}$$

Phase averaging the momentum equation for the combined fluctuating component of the motion (7), and using (20) and (21), we obtain the wave

momentum equation

$$\frac{\partial \tilde{u}_i}{\partial t} + \overline{U}_j \frac{\partial \tilde{u}_i}{\partial x_j} + \tilde{u}_j \frac{\partial \overline{U}_i}{\partial x_j} = -\frac{1}{\rho}\frac{\partial \tilde{p}}{\partial x_i} + \nu \frac{\partial^2 \tilde{u}_i}{\partial x_j^2} + \frac{\partial}{\partial x_j}(\overline{\tilde{u}_j' u_i'} - \langle u_j' u_i' \rangle) + \frac{\partial}{\partial x_j}(\overline{\tilde{u}_j \tilde{u}_i} - \tilde{u}_j \tilde{u}_i). \quad (22)$$

Subtraction of the wave momentum equation (22) from the momentum equation for the combined fluctuating component (7), and using (21), results in the momentum equation for turbulence in the presence of waves

$$\frac{\partial u_i'}{\partial t} + \overline{U}_j \frac{\partial u_i'}{\partial x_j} + \tilde{u}_j \frac{\partial u_i'}{\partial x_j} + u_j' \frac{\partial \overline{U}_i}{\partial x_j} + u_j' \frac{\partial \tilde{u}_i}{\partial x_j} = -\frac{1}{\rho}\frac{\partial p'}{\partial x_i} - \delta_{i3} g \frac{\rho'}{\rho} + \nu \frac{\partial^2 u_i'}{\partial x_j^2} + \frac{\partial}{\partial x_j}(\langle u_j' u_i' \rangle - u_j' u_i'). \quad (23)$$

The KE equations for the mean, wave and turbulence components of the flow are obtained by multiplying the momentum equations (6), (22) and (23) by $\overline{U}_i$, $\tilde{u}_i$, and u_i', respectively, and then phase and time averaging. The MKE equation is

$$\frac{\partial}{\partial t}(\frac{1}{2}\overline{U}_i \overline{U}_i) + \overline{U}_j \frac{\partial}{\partial x_j}(\frac{1}{2}\overline{U}_i \overline{U}_i) = -\frac{1}{\rho}\frac{\partial}{\partial x_i}(\overline{U}_i \overline{P}) - \overline{U}_i \delta_{i3} g + \nu \overline{U}_i \frac{\partial^2 \overline{U}_i}{\partial x_j^2} - \frac{\partial}{\partial x_j}(\overline{u_j' u_i'} \overline{U}_i) + \overline{u_i' u_j'} \frac{\partial \overline{U}_i}{\partial x_j} - \frac{\partial}{\partial x_j}(\overline{\tilde{u}_j \tilde{u}_i} \overline{U}_i) + \overline{\tilde{u}_i \tilde{u}_j} \frac{\partial \overline{U}_i}{\partial x_j}, \quad (24)$$

the WKE equation is

$$\frac{\partial}{\partial t}(\frac{1}{2}\overline{\tilde{u}_i \tilde{u}_i}) + \overline{U}_j \frac{\partial}{\partial x_j}(\frac{1}{2}\overline{\tilde{u}_i \tilde{u}_i}) = -\frac{\partial}{\partial x_j}\overline{[\tilde{u}_j(\frac{\tilde{p}}{\rho} + \frac{1}{2}\tilde{u}_i \tilde{u}_i)]} + \nu \overline{\tilde{u}_i \frac{\partial^2 \tilde{u}_i}{\partial x_j^2}} - \overline{\tilde{u}_i \tilde{u}_j} \frac{\partial \overline{U}_i}{\partial x_j} - \frac{\partial}{\partial x_j}(\overline{\langle u_j' u_i' \rangle \tilde{u}_i}) + \overline{\langle u_i' u_j' \rangle \frac{\partial \tilde{u}_i}{\partial x_j}}, \quad (25)$$

and the TKE equation is

$$\frac{\partial}{\partial t}(\frac{1}{2}\overline{u_i'u_i'}) + \overline{U}_j\frac{\partial}{\partial x_j}(\frac{1}{2}\overline{u_i'u_i'}) = -\frac{\partial}{\partial x_j}\overline{[u_j'(\frac{p'}{\rho} + \frac{1}{2}u_i'u_i')]} - \frac{g}{\rho}\overline{w'\rho'}$$
$$+ \nu\frac{\partial^2}{\partial x_j^2}(\frac{1}{2}\overline{u_i'u_i'}) - \overline{u_i'u_j'}\frac{\partial\overline{U}_i}{\partial x_j}$$
$$- \frac{\partial}{\partial x_j}\overline{[\tilde{u}_j\langle\frac{1}{2}u_i'u_i'\rangle]} - \overline{\langle u_i'u_j'\rangle\frac{\partial\tilde{u}_i}{\partial x_j}} - \epsilon. \quad (26)$$

Assuming statistical homogeneity in the horizontal plane, taking the x axis in the direction of the mean current and using (13.1), the KE equations (24) (25) and (26) reduce to

$$\frac{\partial}{\partial t}(\frac{1}{2}\overline{U}\overline{U}) = +\nu\overline{U}\frac{\partial^2\overline{U}}{\partial z^2} - \frac{\partial}{\partial z}(\overline{w'u'\overline{U}}) + \overline{w'u'}\frac{\partial\overline{U}}{\partial z}$$
$$- \frac{\partial}{\partial z}(\overline{\tilde{w}\tilde{u}\overline{U}}) + \overline{\tilde{w}\tilde{u}}\frac{\partial\overline{U}}{\partial z}, \quad (24.1)$$

$$\frac{\partial}{\partial t}(\frac{1}{2}\overline{\tilde{u}_i\tilde{u}_i}) = -\frac{\partial}{\partial z}\overline{[\tilde{w}(\frac{\tilde{p}}{\rho} + \frac{1}{2}\tilde{u}_i\tilde{u}_i)]} + \nu\overline{\tilde{u}_i\frac{\partial^2\tilde{u}_i}{\partial x_j^2}} - \overline{\tilde{w}\tilde{u}}\frac{\partial\overline{U}}{\partial z}$$
$$- \frac{\partial}{\partial z}(\overline{\langle w'u_i'\rangle\tilde{u}_i}) + \overline{\langle u_i'u_j'\rangle\frac{\partial\tilde{u}_i}{\partial x_j}}, \quad (25.1)$$

$$\frac{\partial}{\partial t}(\frac{1}{2}\overline{u_i'u_i'}) = -\frac{\partial}{\partial z}\overline{[w'(\frac{p'}{\rho} + \frac{1}{2}u_i'u_i')]} - \frac{g}{\rho}\overline{w'\rho'} - \overline{w'u'}\frac{\partial\overline{U}}{\partial z}$$
$$- \frac{\partial}{\partial z}\overline{[\tilde{w}\langle\frac{1}{2}u_i'u_i'\rangle]} - \overline{\langle u_i'u_j'\rangle\frac{\partial\tilde{u}_i}{\partial x_j}} - \epsilon. \quad (26.1)$$

Equations (24.1), (25.1) and (26.1) are, respectively, the reduced KE equations for the mean, wave and turbulence components of the flow. The term $\nu\partial^2(\frac{1}{2}\overline{u_i'u_i'})/\partial x_j^2$ was neglected from the TKE equation as before.

Experimental field results are presented in the next section to illustrate the behaviour of turbulence observed in the OBL under different surface

forcing conditions. The observational results will be discussed in section V.4 in the context of the theoretical background presented above.

V.3. Observational results

V.3.1. Experimental details

This study is based on four experiments conducted under a variety of atmospheric forcing and sea-state conditions. Vertical profiles, in all four experiments, were made using the Rapid-Sampling Vertical Profiler (RSVP; Caldwell et al. 1985). This instrument provides microscale measurements of temperature and conductivity, from which salinity and density were computed, and microscale velocity shear, from which $\epsilon(z)$ was computed. The physical size of the airfoil probes (diameter 0.4 cm; length 1.4 cm) poses an upper limit on the on the spatial resolution of the microscale velocity structure, and the inherent spatial averaging of the probe results in an underestimate of the true dissipation. Because the shear spectrum shifts to smaller scales as ϵ increases, the error due to the spatial averaging of the probe increases with the dissipation level. The probe's response was corrected by applying an empirical transfer function (Ninnis 1984) to the measured estimates of the TKE dissipation rates. Estimates of ϵ were also corrected for variance lost due to incomplete resolution of the shear spectrum by comparing to the universal form of Nasmyth (1970). (The full procedure is described by Moum et al. 1994.)

The first experiment, out of the four, was conducted during March 1987 in the upper Pacific Ocean (140^0 W between 17^0 N and 7^0 N), while the R/V *Wecoma* was steaming south toward the equator as part of the Tropic Heat 2 (TH2 hereafter) experiment. The RSVP was used in a free fall mode and the horizontal spatial separation between profiles was on the order of 1000 m for our profiling rate of 6-10 profiles per hour and ship speed of 2.5 m s^{-1}. Data from depth shallower than 6.5 m were omitted to allow

the RSVP to reach it's nominal stable free fall speed (0.8 m s^{-1}) and to avoid possible contamination of the data by the ship's wake. Currents were determined from the R/V *Wecoma* hull mounted acoustic Doppler current profiler (ADCP). Estimates of the horizontal velocity components were made at depth intervals of 4 m, starting at 19.1 m, and are considered independent approximately every 12 m (T. Chereskin, personal communication).

In order to collect data closer to the surface of the ocean, the other three experiments utilized the RSVP in a free rising mode. Two of the experiments were conducted off the Oregon coast during the summers of 1989 and 1990, herafter OR89 and OR90, and one in Howe Sound, British Columbia, in February 1990, hereafter BC90. In these experiments the RSVP was lowered with the aid of an attached weight which upon release caused the RSVP to freely rise, due to its positive buoyancy, while taking microstructure measurements on its way to the ocean surface. During the OR89 and OR90 experiments the RSVP was deployed from the R/V *Wecoma*, while during BC90 the RSVP was deployed from the Canadian research vessel CSS *Vector*. In all three experiments the ship's bow was headed into the sea while she maintained a low speed of < 0.3 m s^{-1} relative to the water. Surfacing of the RSVP was spotted visually and was usually about 100-150 meter away from the ship. When the RSVP was suspected to have surfaced anywhere near the ship's wake the profile was excluded from our analysis. The profiles used, from those collected in the free rising mode, are believed therefore to be free from contamination by the ship's wake up to very close to the surface, and for analysis we used data starting at a depth of 0.5 m.

Continuous shipboard measurements of meteorological parameters were taken during TH2 (C. Paulson and F. Bahr, personal communication), OR89

and OR90. These included wind velocity, air temperature and humidity, solar and long wave radiation, and sea surface temperature and conductivity. Surface wind stress, τ_0, surface heat flux, J_q^0, and surface buoyancy flux, J_b^0, were calculated using bulk aerodynamic formulae (Large and Pond 1981). The significant wave height, H_s, of swell and wind waves and their direction were estimated by the mate on watch every two hours during TH2, every 15 min during OR89, and every hour during OR90. For the latter two experiments, the periods of the swell and wind waves were also estimated. Single estimates of the significant wave height are to the nearest foot, and an uncertainty of ± 1 foot may be expected. However, for each day or night we averaged at least 5-6 wave height estimates reducing the uncertainty in the average wave height to about 0.1 m. Meteorological data for BC90, from a local wave buoy, included wind speed and direction, sea surface temperature, and significant wave heights and periods, and was kindly provided by the Atmospheric Environment Service of Canada (H. T. Beal, personal communication). Uncertainties in the significant wave heights from the wave buoy are estimated to be less than 0.1 m. Unfortunately, the surface heat and buoyancy flux could not be estimated since humidity and short and longwave radiation were not measured. The surface wind stress was calculted, as before, from the bulk aerodynamic formulae.

The OSL, OBL, and ML were defined in the introduction and to complete the discussion the operational distinctions between these terms, as used in this study, are given. First, the operational use of OSL is equivalent to the definition in the introduction, i.e. it refers only to the superadiabatic part of the nighttime convective OBL. The depth of the OBL, for daytime and nighttime, and the depth of the ML, for nighttime convective conditions

only, was estimated subjectively from individual profiles of salinity, θ, and σ_θ, and then averaged for the respective day or night. This resulted in OBL and ML depths, D, roughly equivalent to the depth at which σ_θ exceeded the surface value by 0.005 kg m^{-3}. For OR89, when salinity estimates were unavailable, the ML depth is the depth at which θ exceeded the surface value by about 0.01 K. We note that the ML depth and the depth of the OBL during nighttime are equivalent.

V.3.2. Tropic Heat 2

The analysis in this section is based on meteorological data and a total of 535 RSVP profiles taken during daytime and nighttime of six diurnal cycles (transition periods of 2-3 hours, from daytime to nighttime conditions and vice versa, were excluded from the analysis).

During daytime, winds were moderate with surface stresses of 0.04-0.12 N m^{-2}. surface gravity waves were in the general direction of the wind with significant wave heights of 1.7-2.4 m for swell, and 0.6-0.9 m for wind-waves. Daytime heating with, with surface heat fluxes between -585 and -230 W m^{-2} and surface buoyancy fluxes of -3.8 to -1.7×10^{-7} m^2 s^{-3} (Table V.1), resulted in a slightly stably stratified OBL (Figs V.1a-V.1f) with $D = 24.7 - 64.7$ m. The mean potential density gradient, $\overline{\sigma_{\theta_z}}$, in the upper 25 m of the OBL, was between -2.64 and -0.72×10^{-4} kg m^{-4} (Table V.2). Inspection of TKE dissipation rates in the same depth range, showed that the estimates of ϵ were much higher than $u_*^3/\kappa z$, and that the depth decay of ϵ followed more closely an exponential than $1/z$ (see section V.4.1 for a discussion of SL and ML similarity scaling definitions and applicability). Estimates of the mean squared velocity shear, $\overline{S^2} = \overline{(\partial U/\partial z)^2 + (\partial V/\partial z)^2}$,

calculated from *Wecoma's* ADCP velocity measurements, ranged from 3.4 to 17.2 $\times 10^{-6}$ s^{-2} for a 12 m bin centered at $z = -25.1$ m (Table V.2).

Deepening of the ML started each night with the onset of convective conditions and was completed in about $2-3$ hours (Anis and Moum 1993a [chapter II]). Surface buoyancy flux increased roughly linearly with time during the ML deepening phase, while throughout the major part of each night (about 12 hours) it was quasisteady with $J_b^0 = 1.3 - 1.7 \times 10^{-7}$ m^2 s^{-3} (Table V.1). Changes in ML depth during this period were probably due to local variability and internal wave activity. Winds, with smaller night-to-night than day-to-day variability, produced surface stresses of 0.07-0.11 N m^{-2}. The wave field was similar to that during daytime with waves in the general direction of the wind and significant heights of 1.8-2.7 m and 0.6-0.9 m for swell and wind-waves, respectively. Nightly averaged profiles of σ_θ and ϵ (Figs. V.1g-V.1l) revealed the following consistent vertical structure (proceeding from the surface down):

i) A statically unstable superadiabatic OSL (Anis and Moum 1992 [chapter III]) occupying about $20-40\%$ of the convective OBL (from the surface to a depth of $15-25$ m or about $1-2|L|$, where $L = -u_*^3/\kappa J_b^0$ is the Monin-Obukhov length scale and is negative during convection). Mean nighttime potential density gradients in the OSL ranged between 0.26 and 0.67 $\times 10^{-4}$ kg m^{-4} (Table V.2). $\epsilon(z)$ increased toward the free surface more rapidly then either $u_*^3/\kappa z$, J_b^0, or their sum, and similar to daytime, the decay of ϵ with depth followed more closely an exponential than $1/z$.

ii) A near neutrally stratified ML (well mixed in both temperature and salinity), between the OSL and the top of the seasonal thermocline,

occupying roughly 50−80% of the convective OBL. During the period of quasisteady surface buoyancy flux, for which our analysis was done, the ML was at its equilibrium depth, D (Table V.2), which was limited only by the stable stratification of the seasonal thermocline (the ML depth changed only as it followed the undulations of the top of the seasonal thermocline, probably due to a combination of internal wave activity and local variability). $\epsilon(z)$ decreased roughly linearly with depth (Anis and Moum 1993b [chapter IV]) and estimates of ϵ, averaged over the depth of the ML, scaled well with J_b^0. In the bulk of the ML, $\overline{S^2}$, was on the order of the ADCP detection limit ($1 - 2 \times 10^{-6}$ s^{-2}), while near the base of the ML, $\overline{S^2}$ increased rapidly by more than an order of magnitude (Anis and Moum 1993b [chapter IV]).

iii) A stable pycnocline at the base of the diurnal ML, in which density increased rapidly with depth as a result of the large decrease in temperature. $\epsilon(z)$ decreased rapidly with depth to values smaller than 1×10^{-8} m^2 s^{-3}.

The high values of ϵ in the upper $15 - 30$ m of the OBL suggest an imbalance between the dissipation of TKE due to viscous forces and the production of TKE by wind stress during day, or by wind stress and surface buoyancy flux during night. To investigate this apparent imbalance further, the experiments described next were conducted with the profiler in the free rising mode, enabling collection of data closer to the surface.

V.3.3. Oregon 1989

Data for this experiment consists of 29 succesful profiles collected during the first night, and of 20 profiles from the second night, a couple of days later. Since no conductivity sensor was mounted on the RSVP, the stability of the

OBL was inferred from the structure of the vertical potential temperature profile.

During the first night the average surface buoyancy flux was 1.4×10^{-7} m^2 s^{-3} and strong steady northerly winds ($\sim$ 13 m s^{-1}) produced an average surface stress of 0.25 N m^{-2} (Table V.1). Sea state was dominated by two swells, one, heavy, from NW with a period of about 12 sec and 3.0 m significant wave height, and the other from NNW with a shorter period of 6 sec and significant height of 2.5 m. Intense breaking, mainly of wind-waves with significant height of about 1 m, took place throughout the night. The profile of θ for this night (Fig. V.1m) shows a neutrally stratified layer in the upper 10 m or so of the OBL with a sharp thermocline beneath it. TKE dissipation rates, between the surface and the thermocline, were higher than could be accounted for by the wind stress production term, $u_*^3/\kappa z$.

Meteorological and sea state conditions, during the second night, were substantailly different and relatively moderate compared to the rough conditions of the first night. The average surface buoyancy flux was 0.4×10^{-7} m^2 s^{-3} and winds, decreasing from 10.0 to 8.0 m s^{-1}, produced an average surface stress of 0.11 N m^{-2}. A 2.0 m swell with a period of 6-8 sec and wind-waves of 0.6 m (Table V.1), breaking only sporadically, defined the sea state. A neutrally stratified layer, extending from the surface to an average depth of about 12 m, was capped below by a sharp thermocline (Fig. V.1n). In the upper 10 m of the OBL, ϵ followed the predicted constant stress layer scaling within 95% confidence limits, but had slightly values deeper, possibly due to entrainment at the base of the ML.

V.3.4. British Columbia 1990

This experiment provided an opportunity to study the behaviour of turbulence in the layer beneath the wind-waves in the absence of swell (Howe Sound is a fjord isolated from the open ocean by Vancouver Island and the Strait of Georgia). A total of 30 successful profiles were made during the early morning hours of two consecutive days. Meteorological and sea state conditions were similar during the two mornings of this experiment: during the first morning winds decreased from 9.3 to 6.0 m s^{-1}, with an average surface stress of 0.08 N m^{-2}, and during the second morning decreased from 10.6 to 3.5 m s^{-1}, with an average surface stress of 0.11 N m^{-2} (Table V.1). The sea surface was characterized by intense white capping due to breaking of waves with significant heights of 0.8 m (morning 1) and 1.2. to 0.6 m (morning 2). During both mornings waves were relatively short with wavelengths less than 14 m (this is the wavelength of a 3 sec period wave, the lower measurement limit of the wave buoy).

Inflow of cool fresh water into Howe Sound satbilized the water column, except the upper 3 m or so which were relatively well mixed in salinity and potential temperature and hence in density. Values of $\overline{\sigma_{\theta_z}}$ in the OBL were -1.90×10^{-4} kg m^{-4} and -0.76×10^{-4} kg m^{-4} for morning 1 and 2, respectively (Table V.2). ϵ was observed to follow $u_*^3/\kappa z$ not only in the shallow OBL (less than 4 m; Table V.2), but also deeper, to a depth of about 10-12 m (Figs. V.1o,p), when the stable density stratification renders SL scaling inapplicable (see section V.4.1.1).

V.3.5. Oregon 1990

The results reported in this section are from a set of 111 profiles, collected during two daytime an three nighttime profiling sessions. During

the experiment meteorological conditions varied from periods with very light winds and no wind-waves, to periods with strong winds and breaking waves.

The first set of 10 profiles was taken in the late afternoon, when winds were $5-6$ m s^{-1}, after rising steadily from 1 m s^{-1} during a period of about 5 hours. Swell was $1.2-1.5$ m in height, while wind-waves were mainly non-breaking wavelets (Table V.1). A stable OBL, 2.1 m deep and with an average value of $\overline{\sigma_{\theta_z}}$ of -23.89×10^{-4} kg m^{-4} (Table V.2), was established during the day when the surface of the ocean was being heated and winds were light. Although stably stratified, $\epsilon(z)$ followed $u_*^3/\kappa z$ up to a depth of about 8 m, below which $\epsilon(z)$ decreased by almost an order of magnitude (Fig. V.1q).

Another set of daytime casts was carried out in late afternoon 5 days later. Steady winds of 10 m s^{-1}, after rising slowly from 8 m s^{-1} during a 5 hour period, produced an average stress of 0.14 N m^{-2} (Table V.1). A swell with 1.8 m significant height and a period of 6 sec, and wind-waves with 0.9 m significant height and periods between 3 and 4 sec and occasional whitecaps, defined the sea state. The OBL was deeper (7.7 m) and slightly less stratified than the first day, and the average value of σ_{θ_z} was -10.08×10^{-4} kg m^{-4}. $\epsilon(z)$ was smaller than $u_*^3/\kappa z$, and decreased by almost two orders of magnitude near the base of the OBL (Fig. V.1r).

The first nighttime set consisted of 9 profiles taken during the early night hours (19-21 local). Winds, 11.5-12.5 m s^{-1}, were in the last phase of a rising trend from 2 to 13.5 m s^{-1} and the average surface buoyancy flux was 1.4×10^{-7} m^2 s^{-3}. Sea state was developing from a 1.2 m to a 1.8-2.1 m swell with a 5 sec period, and wind-waves rose from ripples to waves of 0.9 m height and 4 sec period with some whitecaps (Table V.1). The average value

of σ_{θ_z} in the OBL ($D = 4.1$ m) was -16.08×10^{-4} kg m^{-4}, and $\epsilon(z)$ was slightly smaller than $u_*^3/\kappa z$ (Fig. V.1s). Between 8 to 18 m, $\epsilon(z) \sim u_*^3/\kappa z$, while deeper than 18 m, ϵ decreased rapidly by more than two orders of magnitude.

During the first part of the second night, winds averaged 10.5 m s^{-1} and then dropped in a couple of hours to an average of 7.5 m s^{-1}. Swell decreased in height from 2.1 to 1.8 m and wind-waves decreased in period from 4 to 3 sec and from 1.2 to 0.6-0.3 m (Table V.1). The 10.1 m deep OBL was only slightly stable with an average value of σ_{θ_z} of -2.99×10^{-4} kg m^{-4} (Table V.2). TKE dissipation rate was smaller than $u_*^3/\kappa z$ throughout the OBL (Fig. V.1t).

Relatively weak winds of about 5 m s^{-1} prevailed during most of the third night, an exception being one hour at the beginning when winds rose from 2.5 m s^{-1} to 5 m s^{-1} and one hour at the end when winds decreased to 3.5 m s^{-1}. The surface buoyancy flux was the smallest of all nights, averaging 0.2 $\times 10^{-7}$ m^2 s^{-3} (Table V.1). A swell with 1.8 m significant height and a period of 6-7 sec and wind-waves less than 0.3 m in height with periods between 1-2 sec defined the sea state. No whitecaps were noticed. The OBL ($D = 3.7$ m) was slightly stably stratified with $\overline{\sigma_{\theta_z}} = -3.89 \times 10^{-4}$ kg m^{-4}. $\epsilon(z)$ was slightly larger than $u_*^3/\kappa z$ in the OBL, and decreased gradually throughout the water column (Fig. V.1u).

V.3.6. Statistical aspects of ϵ

For the purpose of statistical analysis, data was grouped according to the four experiments (Table V.3). Examination of data from TH2 showed that the statistics of both $\epsilon/\bar{\epsilon}$ and $\epsilon/(u_*^3/\kappa z)$ were not significantly different, during daytime or nighttime, for -6.5 m $> z > -24.5$ m. However, a

significant difference between the statistics of TH2 and OR89 night 1 and those of the other data sets can be noticed, and is probably caused by the difference in atmospheric forcing and sea-state conditions during the various experiments. Generally, for data sets for which mean profiles showed $\epsilon/(u_*^3/\kappa z) \gg 1$ (TH2 and the first night of OR89), $\epsilon(z)/\bar{\epsilon}$ had a smaller median, and a larger average deviation (AD; defined in the caption of Table V.3), and $\epsilon/(u_*^3/\kappa z)$ had a larger mean (by about an order of magnitude), median, and AD, compared to data sets for which mean profiles showed $\epsilon/(u_*^3/\kappa z) \sim 1$.

To explore further the statistical behaviour of the dissipation rates, the distribution of $\epsilon/(u_*^3/\kappa z)$ was calculated. For this purpose data in the OBL was divided into two groups: one group for which mean profiles showed $\epsilon/(u_*^3/\kappa z) \gg 1$ (Fig. V.2a) and another group for which mean profiles showed $\epsilon/(u_*^3/\kappa z) \sim 1$ (Fig. V.2b). Although the distributions of both groups follow roughly a lognormal, the distribution corresponding to the first group (Fig. V.2a) is translated along the horizontal axis towards larger values of $\epsilon/(u_*^3/\kappa z)$ and is significantly more positively skewed.

To characterize the depth dependence of the statistics of the dissipation rates, the distribution of $\epsilon/(u_*^3/\kappa z)$ was examined as a function of depth. The TH2 data set, which was large and had a relatively deep OBL, was chosen to represent the group for which mean profiles showed $\epsilon/(u_*^3/\kappa z) \gg 1$ and the upper part of the OBL was divided into 4 layers: 6.5-12.5 m, 12.5-18.5 m, 18.5-24.5 m, and 24.5-30.5 m. The main trend revealed a monotonic decrease in the values of the mean and the AD of $\epsilon/(u_*^3/\kappa z)$ with depth; i.e. the deviation from wind stress scaling decreased while proceeding deeper into the OBL. The mean value of $\epsilon/(u_*^3/\kappa z)$ in the layer at 24.5-30.5 m

depth was 2.38 and the AD was 1.46. The group for which mean profiles showed $\epsilon/(u_*^3/\kappa z) \sim 1$ was generally limited by a shallower OBL (2.1 – 14.5 m; Table V.1), however, examination of data closer to the surface was possible because the profiles were taken with the freely rising instrument. The distribution of $\epsilon/(u_*^3/\kappa z)$, in the depth range $0.5 - 5.5$ m and limited to $z > -D$, revealed a slightly positively skewed lognormal distribution. Implications of the statistical behaviour described above are discussed in section V.4.2.

V.4. The TKE budget and prospects for scaling $\epsilon(z)$ in the OBL

V.4.1. TKE excluding wave-turbulence interactions

If the upper boundary of the ocean is treated as a solid surface (e.g. when surface waves are nonexistent or can be neglected), the terms in the momentum and kinetic energy equations describing interactions with the wave field vanish. The equations become those used for a boundary layer over a solid surface, as for the ABL over land, and one expects similar scaling laws to hold for the OBL. The TKE equation for a steady state, neglecting transport terms, results from either equation (18.1) or (26.1)

$$-\frac{g}{\rho}\overline{w'\rho'} - \overline{w'u'}\frac{\partial \overline{U}}{\partial z} - \epsilon = J_b + P - \epsilon = 0. \tag{27}$$

P, the shear production, is the rate of TKE production by the interaction of the turbulence Reynolds stress and the mean shear, and is almost always positive. The buoyant production, J_b, is the rate of work done by/against the buoyancy forces, and might be either a source/sink of TKE, depending on the sign of the vertical buoyancy flux, $\overline{w'\rho'}$. In the OBL this term is negative (a sink) during daytime heating, while during convective conditions (nighttime, cold air outbreaks) it is positive (a source). The TKE dissipation rate, ϵ, is always positive.

V.4.1.1. Surface layer similarity

In the ASL over land (the lower 10% of either the stable or unstable ABL) turbulence fluxes are approximately constant with height (Haugen et al. 1971). Constancy of momentum flux (stress), $\overline{w'u'}$, can be readily obtained from (14) and a steady state. That is,

$$\frac{\partial}{\partial z}(\nu\frac{\partial \overline{U}}{\partial z} - \overline{w'u'}) = 0, \tag{28}$$

so that

$$\nu\frac{\partial\overline{U}}{\partial z}-\overline{w'u'}=\frac{\tau_0}{\rho_w}, \tag{29}$$

The first term in (29), representing the viscous stress, is important only very close to the surface ($O(0.01$ m$)$) and can be neglected farther away, resulting in

$$-\overline{w'u'}=\frac{\tau_0}{\rho_w}=u_*^2. \tag{30}$$

Similarly it can be shown that for steady state the buoyancy (or heat) flux in the SL is constant

$$-\frac{g}{\rho}\overline{w'\rho'}=J_b^0. \tag{31}$$

Since the ASL is approximately a constant-flux layer, its structure is determined by the surface wind stress, τ_0 (or u_*), the surface heat flux, J_q^0, and the buoyancy parameter, g/T (g is the gravitational acceleration and T is a representative ASL temperature). J_q^0 and g/T can be combined into the buoyancy flux, $J_b^0=(g/T)J_q^0/\rho c_p$, where c_p is the specific heat at constant pressure. Since the land surface provides a rigid boundary, the height z above the surface defines the maximal length scale of the large eddies. Normalization of SL variables by the controlling parameters, z, u_*, g/T and J_q^0 (or J_b^0), and formation of dimensionless groups is defined as SL similarity scaling (or Monin-Obukhov similarity scaling or constant stress layer scaling). The dimensionless groups formed with these parameters are expected to be universal functions of z/L.

If SL scaling is applicable, the TKE budget (27) can be nondimensionalized through division by $u_*^3/\kappa z$. With the aid of (30) and (31) we have

$$\frac{z}{L}+\frac{\kappa z}{u_*}\frac{\partial\overline{U}}{\partial z}-\frac{\kappa z}{u_*^3}\epsilon=0. \tag{32}$$

SL similarity theory, then, predicts that the terms in (32) will be universal functions of z/L (note that (32) also assumes stationary and horizontally uniform conditions which are hardly ever met in reality).

Scaling regimes in the stable and unstable ABL are commonly defined by the parameters z/D, z/L (e.g. Nichols and Readings 1979), or by z/D and D/L (Holtslag and Nieuwstadt 1986). D/L is a bulk stability parameter describing the overall structure of the ABL, while z/L can be considered a local stability parameter at some specific height z. For small $|D/L|$ (or $|z/L|$) the stratification is close to neutral, while for increasing values the effects of stability become more important. Following Holtslag and Nieuwstadt, the SL scaling regime in the unstable ABL ($0 > L$) is defined for $0.1 > z/D > 0.01$ and $5 - 10 > -D/L > 1$. For $0.8 > z/D > 0.1$ and $5 - 10 > -D/L > 1$ a near neutral upper layer (NNUL) is indicated. This layer exists often above the sea (Nichols and Readings 1979), and in addition to D, the SL scaling parameters are also relevant in this regime. In the stable ABL ($L > 0$), SL scaling is considered applicable for $0.1 > z/D > 0$ and $10 > D/L > 0$. The region $1.0 > z/D > 0.1$ and $1 > D/L > 0$ is considered a NNUL. In terms of the local stability parameter z/L, SL scaling in the ABL is found to be generally valid in the range $1 > z/L > -2$ (e.g. Wyngaard 1973).

The stability parameters D/L and z/L depend on the the value of L, which, in turn, is completely determined by atmospheric forcing, namely the surface wind stress and surface buoyancy/heat flux. Since the ASL responds relatively fast to changes in surface forcing, D/L and z/L are generally a suitable measure of stability in the ASL. However, the OBL responds much slower to changes in surface forcing, and D/L and z/L may not always represent the actual stability of the upper OBL (additional processes, such

as surface wave activity, might render the comparison between the OBL and the ABL, based on the parameters D/L or z/L, even less applicable). In our opinion, a comparison of background stratification, and shear, in the upper OBL and in the ASL can be better made using the dimensionless temperature gradient, $\Phi_h \equiv (\kappa z/\theta_*)\overline{\theta_z}$, where $\theta_* = J_q^0/\rho c_p u_*$, and the dimensionless shear, $\Phi_m \equiv (\kappa z/u_*)\sqrt{\overline{S^2}}$. Φ_h and Φ_m have an advantage since they take the actual background stratification and shear into account. Examination of our experiments in terms of SL scaling applicability follows and is compared to ASL results.

TH2

During daytime, values of Φ_h were between 0.08 and 0.80 and z/L ranged from 0.6 to 10.7 (both Φ_h and z/L were evaluated for $-6.5 > z > -24.5$ m; Table V.2). For comparison, in the ASL $\Phi_h \sim 1$ for $z/L \sim 0$ (i.e. neutral stratification), and increases linearly with z/L to $\Phi_h \sim 6$ for $z/L \sim 1$ (Businger et al. 1971). This suggests that the OBL, at least in the upper 25 m or so, was less stratified than may be expected from consideration of z/L alone. The shallowest estimate of the dimensionless shear was limited to a depth of 25.1 m and resulted in $\Phi_m = 2.19 - 4.20$, with a mean of 3.39 (Table V.2). A similar range of values of Φ_m is observed in the ASL when $z/L = 0.3 - 0.7$ (Businger et al. 1971), i.e. for much smaller values of the local stability parameter, z/L, when compared to $z/L = 2.2 - 10.9$ (estimated at $z = -25.1$ m) in our case.

During nighttime, the slightly unstably stratified superadiabatic OSL occupied the upper $20 - 40\%(1 - 2L)$ of the OBL. Estimates of Φ_h as a function of z/L in the OSL revealed Φ_h to be consistently smaller in magnitude than in the ASL for $0 > z/L > -1$, and either roughly equal

or smaller than in the ASL for $-1 > z/L > -2$ (Fig. V.3). Φ_h in the range $-6.5 > z > -24.5$ m (equivalent to $-0.5 > z/L > -1.8$) was, on average, between 0.10 and 0.38 (Table V.2). Φ_m, estimated at a depth of 25.1 m, ranged from 1.22 to 2.11, i.e slightly smaller than during daytime. However, since the observed shear was not significantly different from the detection limit of the ADCP (see section V.3.2), Φ_m may eventually be smaller. For comparison, in the ASL $\Phi_m \sim 1$ for $z/L \sim 0$ and decreases to $\Phi_m \sim 0.4$ when $z/L \sim -2$ (Businger et al. 1971).

If the OBL follows similar scaling laws as the ABL, then, SL scaling is expected to apply in the range $1 > z/L > -2$. This would be equivalent to the depth range $0 > z > 21 - 35$ m in the convective OBL (the vertical extent of the OSL), and $0 > z > 2-11$ m in the daytime OBL (estimates of L used are from Table V.1). On the other hand, the dimensionless background temperature gradient and shear, during daytime and nighttime, were smaller than predicted by SL scaling. This may the result of either z/L not being an applicable stability predictor in this case, as discussed above, or more probably due to additional turbulence and mixing processes in the upper OBL. If the latter is true we expect the TKE dissipation rate, ϵ, a measure of turbulence intensity, to exhibit larger values than expected from SL scaling alone.

Inspection of the behaviour of ϵ in the upper 30 m or so of the OBL showed that during daytime ϵ was consistently larger than the wind stress production, $u_*^3/\kappa z$ (Figs. V.1a-V.1f; although SL similarity scaling in the stable ASL is applicable only up to $z/L \sim 1$, we extended our comparison of ϵ and $u_*^3/\kappa z$ to a depth of 30 m since the OBL was only marginally stably stratified in this depth range, as shown above). During nighttime, ϵ

was systematically larger than either the production of TKE by winds, by surface buoyancy flux, J_b^0, or by their sum (Figs. V.1g-V.1l). Moreover, during daytime and nighttime the decay of ϵ with depth in the upper $20-30$ m followed more closely an exponetial than $1/z$. To quantify the excess in dissipation over $u_*^3/\kappa z$, we calculated the ratio of the depth-integrated dissipation rate to the depth-integrated wind stress production in the depth interval $6.5-24.5$ m, $\int_{-24.5}^{-6.5}\rho\epsilon\,dz/\int_{-24.5}^{-6.5}\rho(u_*^3/\kappa z)\,dz$. Values of this ratio, presented in Table V.2, ranged between 3.7 and 16.6 with daytime and nighttime average values of 9.3 and 7.7, respectively. For comparison, measurements under stable conditions in the range $0.5 > z/L > 0$ of the ASL indicated that wind stress production and viscous dissipation were the dominant terms in the TKE budget, and essentially balanced each other, while the buoyant term was only a small loss (Wyngaard and Coté 1971). Under unstable conditions, in the range $0 > z/L > -2.0$, viscous dissipation in the ASL was found to approximately balance the sum of shear and buoyant production, with the latter becoming more important for increasing instability (i.e. for more negative values of z/L).

OR89

Following ABL nomenclature, the estimates of z/L (Table V.2) classify the OBL as being close to neutral for the two nights of the experiment, and SL scaling applicable in the range -0.5 m $> z > -D$. Inspection of Figs. V.1m and V.1n shows that θ was uniform in the upper 12 m or so of the OBL, supporting the notion of neutral stratification. Unfortunately, no current velocity measurements were available in this depth range (as was the case for BC90 and OR90), and background shear could not be estimated. Comparison of $\epsilon(z)$ to $u_*^3/\kappa z$ shows a clear distinction between the two nights:

for night 2 $\epsilon/(u_*^3/\kappa z) \sim 1$ in the upper 10 m or so (Fig. V.1n), as expected from SL scaling, while for night 1 ϵ was larger than expected from SL scaling alone (Fig. V.1m). This difference is similarly reflected in the values of $\int \rho\epsilon\, dz / \int \rho(u_*^3/\kappa z)\, dz$ for the two nights (Table V.2).

BC90

Due to lack of surface heat flux measurements, an accurate estimate of L could not be made. However, since the profiles were taken in the early morning hours, before the sun was over the the mountains, it is fair to assume that the magnitude of J_b^0 was smaller than 3×10^{-7} m^2 s^{-3} (the mean daytime value of J_b^0 during TH2). Using this as an upper bound on J_b^0 together with the wind stress from Table V.2 results in a lower bound on L of about 8 m. Then, for the depth range -0.5 m $> z > -D$ we have $0.5 > -z/L > 0.1$, and SL scaling seems applicable between the surface and D. In this depth range values of the ratio $\int \rho\epsilon\, dz / \int \rho(u_*^3/\kappa z)\, dz$ were 0.5 and 1.0 for morning 1 and 2, respectively (Table V.2). The fact that ϵ followed $u_*^3/\kappa z$ closely up to a depth of about 12 m (Figs. V.1o and V.1p), is possibly related to other processes since SL is not expected to apply deeper than D.

OR90

Estimates of z/L (Table V.2) classify the OBL as slightly stable during daytime, and slightly unstable during nighttime, with SL scaling applicable for -0.5 m $> z > -D$. In this depth range, for day 1 and night 3 (Figs. V.1q and V.1u, respectively), $\epsilon(z)$ was slightly larger than $u_*^3/\kappa z$ and $\int \rho\epsilon\, dz / \int \rho(u_*^3/\kappa z)\, dz \sim 2$ (Table V.2), while for night 1 $\epsilon(z)$ was slightly smaller than $u_*^3/\kappa z$ (Fig. V.1s). Considering the 95% confidence intervals and that ϵ is measured within a factor of 2 (Oakey 1982), the departure of $\epsilon(z)$ from $u_*^3/\kappa z$ for day 1 and nights 1 and 3 is probably insignificant. For

day 2 (Fig. V.1r) and night 2 (Fig. V.1t) a larger departure, with values of $\epsilon(z)$ smaller than the predicted wind stress scaling, can be noticed.

Apparent departures of $\epsilon(z)$ from that expected by SL scaling during the different experiments are discussed in section V.4.2.

V.4.1.2. Mixed layer similarity scaling

In the convective ABL, above the surface and below the entrainment zone, observations indicate a well-mixed layer in which the mean potential temperature, humidity, and wind speed are nearly constant with height. Convective conditions in the ABL occur when the land is heated by solar radiation during daytime, or when cold air is advected over a warmer surface. The magnitude of the bulk stability parameter, $-D/L$, is a measure of the strength of convection, with larger values implying stronger convection. Typical values are in the range of $120 - 240$ for the convective ABL over land. However, Deardorff (1974) showed that a value of $-D/L \sim 5$ can be sufficient to drive the ABL into a convective state.

In the ocean, a ML in which the temperature and salinity are well-mixed and independent of depth, usually occurs during convection when unstable conditions develop as a result of the heat lost from the sea surface. This happens mainly during nighttime, although sporadic events of convection might occur due to rapid cooling of the sea surface by cold air outbreaks (e.g. Shay and Gregg 1986). The heat loss, which is largely due to latent heat flux, produces denser fluid which tends to sink and cause the onset of convective cells.

In the well-mixed part of the convective ABL, surface stress is considered unimportant, leading to ML scaling (or convective scaling). The relevant scaling parameters are the ABL height, D, which defines the limiting length

scale of the large eddies, the height, z, the buoyancy parameter, g/T, and the surface heat flux, J_q^0, or the combination of the latter two into $J_b^0 = (g/T)J_q^0/\rho c_p$ (e.g. Driedonks and Tennekes 1984). ML scaling predicts that all variables in the ML are universal functions of z/D when properly nondimensionalized with the convective velocity scale, $w_* = (DJ_b^0)^{1/3}$, the convective temperature scale, $\theta_{ML} = J_q^0/w_*\rho c_p$, and the length scale D. In the ABL, ML scaling is found to apply generally in the region $-D/L > 5-10$ and $0.8 > z/D > 0.1$ (Holtslag and Nieuwstadt 1986).

The TKE equation in the ML, using (27) while neglecting the surface stress production term, assumes a particularly simple form of balance between TKE production by buoyancy and dissipation by viscous forces

$$-\frac{g}{\rho}\overline{w'\rho'} - \epsilon = J_b - \epsilon = 0. \tag{33}$$

Nondimensionalizing (33) with J_b^0 results in

$$\frac{J_b}{J_b^0} = \frac{\epsilon}{J_b^0}, \tag{34}$$

and ML scaling predicts that the nondimensional flux, J_b/J_b^0, and the nondimensional dissipation rate, ϵ/J_b^0, are universal functions of z/D.

Field experiments (e.g. Young 1988) and numerical simulations (e.g. Deardorff 1974; André et al. 1978) in the highly convective ABL indicate that the nondimensional heat/buoyancy flux is linearly dependent on z/D. Scaling of the heat flux for the less convective marine ABL worked less well (Nichols and Readings 1979). ML scaling of ϵ was shown to work well in the highly convective ABL over land (Caughey and Palmer 1979), and the first successful convective scaling of ϵ in the OBL was reported by Shay and Gregg (1984a, 1984b, 1986) for a diurnal ML and for the ML of a warm-core Gulf Stream ring subject to rapid cooling induced by a cold air outbreak. These

studies in the convective ABL and OBL also indicated a gradual decrease of ϵ/J_b^0 with the increase of $|z/D|$, while numerical simulations of the convective OBL (Klein and Coantic 1981; André and Lacarrère 1985) showed an explicit linear decrease with depth of both J_b/J_b^0 and ϵ/J_b^0.

During TH2 we observed the formation of a convective boundary layer during all six nights of the experiment. A well-mixed layer, in both potential temperature and salinity, and hence density (Figs. V.1g-V.1l), formed every night about $2-3$ hours after transition from daytime to nighttime conditions (Anis and Moum 1993a [chapter II]) and eroded rapidly after transition from nighttime to daytime conditions (again in about $2-3$ hours). The bulk stability parameter, $-D/L$, varied between 3.9 and 6.7 (Table V.2), which in ABL terminology classifies the OBL as only mildly convective. However, our range of values of $-D/L$ was similar to the lower range of data analyzed by Shay and Gregg (1986), who found no systematic variation in values of $\epsilon(z)/J_b^0$ in their observed range of $-D/L = 3-76$. Investigation of the vertical structure of θ during TH2, suggests that the heat flux decreased linearly with depth in the convective OBL (Anis and Moum 1993b [chapter IV]). It was also demonstrated in the same study that ϵ/J_b^0 decreased linearly with z/D in the bulk of the ML, away from the OSL and the entrainment zone.

During the 1989 and 1990 experiments off the Oregon coast, the depth of the nightly ML was much smaller than during TH2, possibly as a result of stabilizing conditions during the boreal summer. The relatively large magnitude of L (Table V.1), combined with the small ML depths, resulted in relatively small values of $-D/L$: 0.24 to 0.31 and 0.07 to 0.27 during the

nights of OR89 and OR90, respectively (Table V.2). In this range ML scaling is considered not applicable, and explains why ϵ did not scale with J_b^0.

V.4.2. TKE including wave-turbulence interactions

Due to the free surface of the OBL, differences from the behaviour of turbulence in the presence of a solid boundary might well be expected. A comparison of our data to those from the ABL over land is made by plotting nondimensionalized dissipation rate, $\epsilon/(u_*^3/\kappa z)$, vs. nondimensionalized depth, z/L, in the OBL of all 4 experiments (Fig. V.4). When compared to the empirical fit for the ABL over land (the dashed line in Fig. V.4, adapted from Wyngaard and Coté (1971)) it is clear that although the majority of the data points are below or near this fit, a large number have values much greater. One way to reconcile the apparent differences is to note that the wind produces not only surface stress but also surface waves, which in turn can produce or interact with turbulence in different ways. We examine several aspects of the influence of surface waves to determine if the observed $\epsilon(z)$ profiles are consistent with theoretical considerations.

Are the high dissipation rates, found during TH2 and the first night of OR89, consistent with the energy lost from breaking waves?

An estimate of the energy lost by breaking surface waves can be made in three ways. The first estimate is based on Longuet-Higgins' (1969) theoretical-statistical model. According to this model the rate of energy lost per unit surface area, R, due to wave breaking is

$$R = \frac{Ep}{\overline{T}}, \tag{35}$$

where E is the total wave energy density per unit horizontal area and p is the proportion of wave energy lost per mean wave cycle, $\overline{T}$. The wave spectrum

in the equilibrium range, when the limiting form of the wave spectrum is dominated by wave breaking, is given by $S(\omega) = \beta g^2 \omega^{-5}$, where β is a constant and ω is radian frequency (Phillips 1977). Using this wave spectrum the value of p is given (Longuet-Higgins 1969) by

$$p = \exp(\frac{-1}{8\beta}). \tag{36}$$

Note that p is quite sensitive to the value of the constant β (see also Table V.4). For a narrow wave spectrum, E is related to the rms wave amplitude $\overline{a}$ by

$$E = \frac{1}{2}\rho g \overline{a}^2. \tag{37}$$

A second estimate of energy lost by breaking surface waves uses the laboratory observations of Lamarre and Melville (1991), that about 10% (and up to 40%) of the total prebreaking energy can be lost through breaking (see also Rapp and Melville 1990). Combined with field observations of the fraction, $f(U_{10})$, of breaking waves as a function of wind speed at 10 m height (Thorpe and Humphries 1980; Holthuijsen and Herbers 1986), the rate of energy lost per unit surface area due to breaking can be written as

$$R = \frac{0.1 E f(U_{10})}{\overline{T}}, \tag{38}$$

The factor 0.1 in (38) results from the use of Lamarre and Melville's observation that about 10% of a wave's energy can be lost by breaking.

The third estimate of energy lost by breaking surface waves uses the rate of energy transfer from the wind to the waves which, following Kitaigorodskii (1983), is given by

$$W = \gamma \tau_0 \overline{C}, \tag{39}$$

where γ is a coefficient on the order of 0.1-1.0 and $\overline{C} = (g/2\pi)\overline{T}$ is the mean phase speed of the waves. If the wave field is stationary and homogeneous

then the rate of energy lost by breaking should equal the rate of energy input from the wind to the waves, i.e. $R = W$.

If most of the wave energy lost by breaking produces turbulence, it might in turn be evidenced in enhanced dissipation rates near the surface. This seems to be supported by laboratory measurements of deep-water breaking waves by Rapp and Melville (1990), who found that more than 90% of the energy lost due to breaking was dissipated within four wave periods. If so, the depth-integrated TKE dissipation rate, $\int \rho\epsilon\, dz$, in the wave-influenced layer near the surface should be on the order of the rate of energy lost by wave breaking. Assuming that the energy lost is largely due to breaking of wind-waves, estimates based on (35), (38) and (39) were made. First, we have estimated R using the wave parameters from *Wecoma's* ship's officers' log (Table V.1) and a short discussion of the adequacy of their use, and the possible uncertainties in R, follows.

Wave related uncertainties in the estimates of R from (35) or (38) may be due to uncertainties in either $\overline{a}$ (since $E \propto \overline{a}^2$) or $\overline{T}$, while uncertainty in the latter is the only wave parameter related uncertainty in estimates of R from (39). Our estimate of the uncertainty in H_s (0.1 m; section V.3.1) leads to an uncertainty in E of $\sim 25\%$ at nominal values of $H_s = 0.8$ m for TH2 and $H_s = 1.0$ m for OR89 night 1 where $\overline{a} \sim H_s/2$ (Table V.1). Since the wave periods from the officer's log are estimated to the nearest full second we may expect an uncertainty of $\sim 25\%$ in the period of the wind-waves of OR89 night 1.

Unfortunately, estimates of $\overline{T}$ were unavailable from the officers' log for TH2; however, an estimate of $\overline{T}$ can be made in several ways. One way is to use Holthuijsen and Herbers' (1986) observations of the wave steepness,

$s \equiv H/(g/2\pi)T^2$. These observations were made in open sea conditions with winds between 8 and 12 m s^{-1}, which are similar to the conditions that prevailed during TH2 and OR89. Their observations indicated an average steepness $s = 0.037$, which results in $\overline{T} \sim 3.7$ sec for TH2 (a similar calculation for OR89 night 1 results in $\overline{T} \sim 4.2$ sec, in good agreement with the value of 4 sec from the log book). Two other methods of estimation of $\overline{T}$ use the wind speed at 10 m height, U_{10}. The first estimate uses the relation $\overline{T} = 0.81 \times 2\pi U_{10}/g$ (Neumann and Pierson 1966). From this relation $\overline{T} \sim 3.6$ sec and $\overline{T} \sim 3.8$ sec for mean winds of 7 and 7.5 m s^{-1}, observed during daytime and nighttime of TH2, respectively. The second estimate uses the relation $\overline{T} = 2\pi\overline{C}/g \sim 2\pi U_{10}/g$ (Longuet-Higgins 1969), resulting in $\overline{T} \sim 4.5$ sec and $\overline{T} \sim 4.8$ sec for daytime and nighttime of TH2, respectively. Since values of $\overline{T}$, based on the estimates above, ranged between 3.6 and 4.8 sec we used $\overline{T} \sim 4$ sec for TH2 (daytime and nighttime), which may introduce an uncertainty of $\sim 25\%$ in the estimates of R. Thus, combining the uncertainties in E (25%) and $\overline{T}$ (25%), the estimates of R from wave parameters are believed to be accurate to within a factor smaller than 2.

Another means of estimation of R is solely from the relations between wind and wave parameters for fully developed seas. Two sets of relations were used for our estimates. The first, based on observations and theoretical considerations of the wave height distribution, (Longuet-higgins 1969) suggests that $\overline{T} = 2\pi\overline{C}/g \sim 2\pi U_{10}/g$, and $\overline{a} \sim 0.088{U_{10}}^2/g$. The second set of relations, based on the spectral form proposed for fully developed wind seas (Neumann and Pierson 1966), suggests that $\overline{T} = 0.81 \times 2\pi U_{10}/g$ and $H_s = 2.12 \times 10^{-2}{U_{10}}^2$ (for our estimates we have taken $\overline{a} = H_s/2$).

Estimates of R based on the wave parameters from R/V *Wecoma*'s log and based on the relations between the wind and the waves are presented in Table V.4. It can be noticed that for daytime and nighttime of TH2 all three estimates of R within a factor of about 2. A larger difference between the estimates of R is apparent for OR89 night 1. However, this may be the result of estimating R from wind-wave parameters only, while swell was probably actively breaking too. It can be seen, indeed, that a relatively good agreement exists between the estimates of R from the swell parameters and from U_{10} (Table V.4). The relatively large range in R, as represented by the upper and lower values for each estimate, is introduced by the range in the estimates of p (a factor ~ 6), $f(U_{10})$ (a factor of $\sim 3-6$), and γ (a factor of ~ 10).

All of the 3 independent estimates made for the energy lost by breaking surface waves are much greater than the turbulence energy generated by the wind stress as predicted by SL scaling (the rightmost column in Table V.4). These estimates are, however, consistent with the observed vertically integrated turbulence dissipation rate, $\int \rho\epsilon\, dz$ (Table V.4).

Influence of wave-turbulence interaations on $\epsilon(z)$ near the surface

Because high values of $\epsilon(z)$ were observed much deeper than e-folding scales of the wind-waves, a possible scenario is that breaking waves (mainly wind-waves) form a layer near the surface (on the order of the wind-wave height) of enhanced TKE which in turn is transported downward by the swell. This could be achieved via the term $-\partial(\overline{\tilde{w}\frac{1}{2}u_i'u_i'})/\partial z$ ((18.1) and (26.1)) which describes the vertical transport of TKE, $\frac{1}{2}\overline{u_i'u_i'}$, by the wave velocity $\tilde{w}$. At first glance it may seem that this term should vanish due to averaging over the sinusoidal vertical wave velocity, $\tilde{w}$. However, consider the following

scenario: during the half cycle when $\tilde{w} > 0$, turbulence near the surface decays with time and diffuses spatially as it cannot be transported upward further through the sea surface; during the half cycle when $\tilde{w} < 0$, turbulence from the surface will be transported downward while decaying and diffusing. The result is a vertical gradient, $-\partial(\overline{\tilde{w}\frac{1}{2}u_i'u_i'})/\partial z$, which will be positive on average. That is, away from the surface the magnitude of $\overline{\tilde{w}\frac{1}{2}u_i'u_i'}$ will decrease due to the combined effects of exponential depth decay of $\tilde{w}$ and the decay and spreading of TKE as it is transported downward.

If a surface layer, with a thickness of $O(k^{-1})$, is governed by wave-turbulence interactions such that the main local balance is between $-\partial(\overline{\tilde{w}\frac{1}{2}u_i'u_i'})/\partial z$ and the TKE dissipation rate, then

$$\epsilon(z) \sim -\frac{\partial}{\partial z}(\overline{\tilde{w}\frac{1}{2}u_i'u_i'}) \sim -\frac{\partial}{\partial z}\overline{[\omega a \exp(kz)\sin(kx-\omega t)\frac{1}{2}u_i'u_i']}, \qquad (40)$$

where ω and a are the radian frequency and amplitude, respectively, and $\tilde{w} = \omega a \sin(kx-\omega t)\exp(kz)$. Although the depth decay of turbulence (represented by $\frac{1}{2}\overline{u_i'u_i'}$) is not known, the vertical gradient of $\overline{\tilde{w}\frac{1}{2}u_i'u_i'}$ will decay with depth at least as fast as $\exp(kz)$, as a result of the decay of the vertical wave velocity $\tilde{w}$ alone.

An upper bound on $\epsilon(z)$ in the wave dominated surface layer can now be found. Assuming, for the simplicity of differentiation, a depth independent (or in turn a depth averaged) correlation coefficient, r, between $\tilde{w}$ and $u_i'u_i'$, and taking $\frac{1}{2}\overline{u_i'u_i'} \sim \frac{3}{2}u_{rms}^2 \sim \frac{3}{2}(0.02C)^2$ as an upper bound on the TKE (Rapp and Melville 1990), we find from (40)

$$\epsilon(z) \leq a\frac{1}{\pi}g^{1/2}k^{3/2}r\frac{3}{2}(0.02C)^2\exp(kz), \qquad (41)$$

where $\omega^2 = kg$, and averaging is performed over half the cycle of downward transport, i.e. when $\tilde{w} < 0$. It should be noted that if breaking of wind-waves

is the main source for TKE, the phase speed C of the wind-waves has to be used to estimate the TKE, $\frac{1}{2}\overline{u_i' u_i'}$, in (41), while the other wave parameters are derived from the swell.

If on the other hand the wave field is not truly irrotational, as reported by some investigators (see section V.2.3), the resulting wave stresses may indirectly enhance turbulence in the wave influenced layer near the surface. Assuming steady state and neglecting the molecular diffusion term, the KE equation of the mean flow (24.1) reduces to

$$-\overline{w'u'} - \overline{\tilde{w}\tilde{u}} = constant = \frac{\tau_0}{\rho}. \tag{42}$$

Cheung and Street (1988) found that $-\overline{\tilde{w}\tilde{u}}$ and $-\overline{\tilde{w}\tilde{u}}\partial\overline{U}/\partial z$ were generally negative, decaying rapidly with depth. Thus, energy is transferred from the wave field to the mean field via the term $\overline{\tilde{w}\tilde{u}}\partial\overline{U}/\partial z$, which appears in (24.1) and (25.1) with opposite signs. If in the wave-dominated layer near the surface the wave stresses are much larger than the surface wind stress (e.g. Shonting 1964; Cavaleri et al. 1978) such that $\overline{\tilde{w}\tilde{u}} >> \tau_0/\rho$ then, in order to satisfy the balance in (42), one arrives at

$$-\overline{w'u'} \sim \overline{\tilde{w}\tilde{u}} >> \tau_0/\rho. \tag{43}$$

This balance, depicted schematically in Fig. V.5, does not violate the continuity of tangential stress across the air-water interface, but rather allows for much larger respective wave and turbulence stress terms than would be predicted from an estimate τ_0/ρ derived from surface winds.

If the wave stress is simply a result of $\tilde{u}$ and $\tilde{w}$ being out of quadrature (e.g. Yefimov and Khristoforov 1969; Cavaleri et al. 1978), the orbital wave velocities can be defined as follows:

$$\tilde{u} = a\omega \cos(kx - \omega t)\exp(kz), \tag{44a}$$

$$\tilde{w} = a\omega \sin(kx - \omega t + \phi) \exp(kz), \tag{44b}$$

where ϕ is the phase shift from quadrature (although ϕ may be depth dependent, we assume for simplicity that ϕ is a constant considered here as a representative value for the wave stress influenced layer). From (44a) and (44b) and with the aid of trigonometric identities

$$\overline{\tilde{w}\tilde{u}} \approx \frac{1}{2} a^2 gk \exp(2kz) \sin\phi, \tag{45}$$

where $\omega^2 = gk$. An exponential decay of mean wave stress was observed by Cheung (1985) for wind-ruffled mechanically-generated waves, and similar results were reported by Bliven et al. (1984), for both paddle-generated waves and paddle-generated waves with an imposed wind stress. Assuming that the main balance in (26.1) is between the TKE dissipation rate, ϵ, and the shear production, $-\overline{w'u'}\partial\overline{U}/\partial z$, and using (43) and (45), results in

$$\epsilon = -\overline{w'u'}\frac{\partial \overline{U}}{\partial z} \approx \frac{1}{2} a^2 gk \exp(2kz) \sin\phi \frac{\partial \overline{U}}{\partial z}. \tag{46}$$

Although the two mechanisms proposed above to explain the observed high ϵ values in the near surface layer, namely the transport of TKE by swell and the indirect production of TKE via wave stresses, are physically different, both processes might affect turbulence and mixing in a surface layer of $O(k^{-1})$.

An additional wave-turbulence interaction term that needs to be considered is $-\overline{u_i' u_j' \partial \tilde{u}_i / \partial x_j}$ (equations 18.1 and 26.1), which describes TKE production by the interaction of the turbulence Reynolds stress and the periodic wave shear. This type of interaction might be important for turbulence with time scales, $T_t << T$, i.e. much shorter than the wave period, T, such that the turbulence perceives the wave field as a slowly varying shear flow (Kitaigorodskii and Lumley 1983). If the turbulence

velocity scale is u_t and the length scale l_t, we find from the condition $T_t << T$ that $l_t/u_t << T$. Using the empirical relation, $\epsilon \approx {u_t}^3/l_t$, we arrive at the condition for the turbulence velocity, $u_t << (T\epsilon)^{1/2}$. For representative values of $\epsilon \sim 10^{-6}$ m^2 s^{-3}, observed at a depth of about 10 m during TH2, and $T \sim 10$ sec we get $u_t << 3 \times 10^{-3}$ m s^{-1}. This velocity scale is even smaller than u_*, which is $O(0.01)$ m s^{-1}, and is too small and inconsistent with the increased turbulence levels we observed near the surface. Moreover, an estimate of the turbulence length scale, based on the above considerations, results in $l_t << 3 \times 10^{-3}$ m. This relatively short turbulence length scale required for the wave-shear production mechanism, $-\overline{u_i' u_j' \partial \tilde{u}_i/\partial x_j}$, to be effective probably renders it unimportant in vertical mixing in the OBL, compared to the larger eddies which have sizes on the order of meters.

How well do the predicted scalings of wave-turbulence interaction agree with our observations ?

A simple exponential form $\epsilon(z) = \epsilon_0 \exp(\alpha z)$ was fit to the observed dissipation rates in the upper part of the OBL (Figs. V.6a and V.6b). For TH2, α varied between 0.21 and 0.39 m^{-1} (including all days and nights) with an average, weighted by the number of profiles in each day or night, of 0.30 m^{-1}. The surface intercept value, ϵ_0, varied between 2.0×10^{-5} and 10.0×10^{-5} m^2 s^{-3} with a weighted average of 4.1×10^{-5} m^2 s^{-3}. If dissipation locally balances the downward transport by swell of enhanced surface turbulence produced by wind-wave breaking (equation 40), then vertically integrating $\epsilon(z) = \epsilon_0 \exp(\alpha z)$ to the surface should result in a value consistent with the energy lost by wave breaking. Integration from a depth of 24.5 m to the surface results in a range of values from 0.093 to 0.262 W m^{-2} with an average of 0.140 W m^{-2} for TH2. These values are higher

than those obtained by integrating the observed $\epsilon(z)$ (Table V.4), which represent a lower bound on the depth-integrated dissipation rate; however, they are consistent with the estimates of the rate of energy lost by wind-wave breaking in Table V.4. The wavelengths resulting from the exponential fit are $\lambda = 16.1 - 29.9$ m with $\lambda = 20.9$ m corresponding to the average wavenumber $k = 0.30$ m^{-1} (in this case $\alpha = k$). Although we have no measurements of the dominant wavelengths, these values are representative of the lower bound associated with swell patterns in the North Pacific.

We first consider the mechanism described by (40) and (41), by which TKE generated by breaking wind-waves is transported downwards by the swell. The depth decay of $\epsilon(z)$ is dictated by that of the orbital velocity of the swell; if the turbulence also undergoes significant diffusion and dissipation over half a wave cycle, then the vertical decay rate will be greater than (41). Since (41) invokes a correlation coefficient, r, of unknown magnitude, it is important to demonstrate that r need not be large in order that (41) be an effective mechanism.

An estimate of r_0 (r at $z = 0$) can be made by vertically integrating (40) and evaluating at $z = 0$. We assume a swell wavenumber equal to the average value of the exponential fit, $k_s = \alpha = 0.30$ m^{-1}, and a swell amplitude $a_s = 1.05$ m^{-1} (Table V.1). TKE, $\frac{1}{2}\overline{u_i' u_i'}$, is estimated as $\sim \frac{3}{2} u_{rms}^2$ with $u_{rms} \sim 0.02 C_w$ (Rapp and Melville 1990), where C_w is the phase speed of breaking wind-waves calculated using a mean period of $\overline{T}_w = 4.0$ sec. ϵ at $z = 0$ is taken as the average surface intercept value of the fit, $\epsilon_0 = 4.1 \times 10^{-5}$ m^2 s^{-3}. This results in $r_0 \sim 0.01$. Even if we use $u_{rms} \sim 0.005 C_w$, the value of the rms turbulence velocity observed by Rapp and Melville (1990) 60 wave periods after breaking (a likely underestimate in our case, since for the

winds of TH2 the average time predicted between breaking events is $\sim 11\overline{T}_w$ (Holthuijsen and Herbers 1986) or $\sim 33\overline{T}_w$ (Thorpe and Humphries 1980)), we find $r_0 \sim 0.16$, which is still considerably less than 1.

The first night of OR89 revealed a change in slope of $\epsilon(z)$ at a depth of ~ 6 m (Fig. V.6b). The change in the slope, with a more rapid depth decay in the upper 6 m of the OBL, might be due to dominance of wind-waves near the surface as a result of higher wind and seas compared to the TH2 experiment (even if such a layer existed near the surface during TH2 we would have missed it since we profiled with a free falling instrument as opposed to OR89 when we profiled in a free rising mode). Below 6 m, we might still associate the decay scale with the swell. In this case we divided the exponential fit to $\epsilon(z)$ into two separate depth intervals (Fig. V.6b), resulting in $\alpha_1 = 0.66$ m^{-1} and $\alpha_2 = 0.18$ m^{-1} for the depth intervals of 1.5-5.5 m and 5.5-14.5 m, respectively. If in this case downward transport of turbulence is dominated by wind-wave transport in the upper part and swell transport in the lower part, then $k_w = \alpha_1 = 0.66$ m^{-1} and $k_s = \alpha_2 = 0.18$ m^{-1}, where k_w and k_s are the wind-wave and swell wavenumbers, respectively. These wavenumbers correspond, respectively, to $\lambda_w = 9.5$ m and $\lambda_s = 34.9$ m or to $T_w = 2.5$ sec and $T_s = 4.7$ sec, compared to the ship's officer's log estimates of $T_w = 4$ sec and $T_s = 6$ sec (for the shorter of the two swells observed). An estimate of the correlation coefficient at $z = 0$ results in $r_0 \sim 0.12$. Although the value of the correlation coefficient is larger than that for TH2, it is consistent with the higher rate of wave breaking observed during OR89 as a result of stronger winds (Thorpe and Humphries 1980; Holthuijsen and Herbers 1986).

The velocity scale, u_t, for turbulence resulting from wave breaking is estimated next and compared to laboratory observations. Assuming an eddy

length scale $l_t \sim H$, where H is the height of the breaking waves, and using the relation $\epsilon = u_t^3/l_t$, with $\epsilon \sim \epsilon_0$, where ϵ_0 is the surface intercept value of the exponential fit, we obtain $u_t = 3.2 \times 10^{-2}$ m s^{-1} and $u_t = 6.6 \times 10^{-2}$ m s^{-1} for TH2 and OR89 night 1, respectively. Expressed in terms of the phase velocity, C_w, of the wind-waves this is equivalent to $u_t = 0.006C_w$ and $u_t = 0.011C_w$ for TH2 and OR89 night 1, respectively, in agreement with the range of $0.005 - 0.02C_w$ of rms turbulence velocities resulting from wave breaking observed by Rapp and Melville (1990). The higher value of u_t for OR89 night 1, in terms of fractions of C_w, is consistent with the higher sea state and breaking rate observed. For comparison; if near the surface $u_t \sim u_*$, we find $u_t \sim 9.4 \times 10^{-3}$ and $u_t \sim 1.6 \times 10^{-2}$ m s^{-1} for TH2 and OR89 night 1, respectively. The latter values of u_t are smaller by a factor of 4, compared with those estimated above, resulting in an underestimate of ϵ by almost two orders of magnitude.

Next we consider the mechanism described by (46), by which wave-induced shear stresses in a rotational wave field interact with the mean flow and the turbulence to effect a depth decay rate of $\epsilon(z$ determined by the decay rate of the wave stress (45). In this case, $\epsilon(z) \propto \exp(2kz)$ (or $\alpha = 2k$ for comparison to the data). The exponential fit results in an average value of $k = \alpha/2 = 0.15$ m^{-1} for TH2, corresponding to $\lambda = 41.8$ m ($T = 5.2$ sec), in agreement with the general swell patterns in the North Pacific. Assuming that the change in slope of the exponential for OR89 night 1 (Fig. V.6b) is due to dominance of wind-waves near the surface and swell deeper, we find $k_w = \alpha_1/2 = 0.33$ m^{-1} and $k_s = \alpha_2/2 = 0.09$ m^{-1} corresponding to $\lambda_w = 19.0$ m ($T_w = 3.5$ sec) and $\lambda_s = 69.8$ m ($T_s = 6.7$ sec), respectively. A lower limit on $\sin\phi$, in the wave-stress dominated surface layer, can be

estimated from the balance in (46) (see appendix) as

$$\sin\phi > \frac{2\int_h^0 \epsilon\, dz}{a^2 g k \overline{U}(0)}. \tag{47}$$

Using mean values for TH2 of $a_s \sim 1.05$ m (Table V.1), $k_s g = (\alpha/2)g \sim 1.5$ (rad s^{-1})^2, $\int_{-24.5}^0 \epsilon\, dz = \int_{-24.5}^0 \epsilon_0 \exp(\alpha z)\, dz \sim 1.3 \times 10^{-4}$ m^3 s^{-3} (with mean exponential fit parameters $\epsilon_0 = 4.1 \times 10^{-5}$ m^2 s^{-3} and $\alpha = 0.30$ m^{-1}), and assuming a mean surface current $\overline{U}(0) = 0.01$ m s^{-1} results in $\sin\phi > 0.016$. In other words, to explain the observed TKE dissipation rates near the surface, only a small departure from quadrature of $\sim 1^0$ is needed. A similar calculation for OR89 night 1 results in $\sin\phi > 0.11$ ($\phi > 6^0$), where we used the wind-wave amplitude $a_w \sim 0.5$ m (Table V.1), and $k_w g = (\alpha_1/2)g \sim 3.2$ (rad s^{-1})^2 and $\int_{-5.5}^0 \epsilon\, dz \sim 4.4 \times 10^{-4}$ m^3 s^{-3} (calculated from the parameters of the exponential fit in the 1.5-5.5 m depth interval), and $\overline{U}(0) = 0.01$ m s^{-1}. A similar estimate, with a swell amplitude of $a_s \sim 1.2$ m (Table V.1), $k_s g = (\alpha_2/2)g \sim 0.9$ (rad s^{-1})^2, $\int_{-14.5}^0 \epsilon\, dz \sim 1.1 \times 10^{-4}$ m^3 s^{-3} (calculated from the parameters of the fit in the 5.5-14.5 m depth interval), and $\overline{U}(0) = 0.01$ m s^{-1}, results in $\sin\phi > 0.018$ ($\phi > 1^0$). For comparison; Shonting (1970), Yefimov and Khristoforov (1969), and Cavaleri et al. (1978) have reported phase shifts from quadrature as large as $20^0 - 30^0$ in the upper few meters of the OBL.

Statistics of $\epsilon/(u_*^3/\kappa z)$

The roughly lognormal distributions of $\epsilon/(u_*^3/\kappa z)$ observed (section V.3.6) are the result of the inherently intermittent nature associated with most turbulent flows. Other investigators have similarly demonstrated lognormal distributions of ϵ, at least when forcing was relatively steady (e.g. Oakey 1985; Osborn and Lueck 1985; Shay and Gregg 1986; Moum et al.

1989; Yamazaki et al. 1990; Agrawal et al. 1992). Although the distributions of $\epsilon/(u_*^3/\kappa z)$ of the two different groups of data discussed in section V.3.6 were roughly lognormal, they hint at a key difference in forcing in the two cases.

The bulk of the dissipation rates of the group for which mean profiles showed $\epsilon/(u_*^3/\kappa z) \sim 1$ (Fig. V.2b), were in general agreement with wind stress scaling estimates (about 60% of the values of ϵ were within a factor of 3 of $u_*^3/\kappa z$ and only 4% of the values were larger than $u_*^3/\kappa z$ by a factor of 10 or more). The excess of larger values of $\epsilon/(u_*^3/\kappa z)$ observed closer to the surface (0.5-5.5 m and limited to $z > -D$), which resulted in a positively skewed lognormal distribution, may be contributed by the energetic events of wave breaking which become more important upon approaching the surface. The picture that emerges from this data set is of an OBL forced by wind stress, to which the bulk of the dissipation rates are related, and by additional intermittent events of wave breaking. This observation is consistent with that of Agrawal et al. (1992) who observed, at 1-m depth in Lake Ontario, a background level of dissipation rates close to the constant stress layer estimates, and intermittent intense events resulting in enhanced dissipation rates (about 10% of the values showed $\epsilon/(u_*^3/\kappa z) > 10$). They argued that a likely source of these intense but intermittent events, which dominate the average values, is wave breaking.

In contrast to the background level of $\epsilon \sim u_*^3/\kappa z$ found by Agrawal et al. (1992) and observed by us for the data set for which mean profiles showed $\epsilon/(u_*^3/\kappa z) \sim 1$, an important difference is apparent in the data set of Fig. V.2a for which mean profiles showed $\epsilon/(u_*^3/\kappa z) \gg 1$. Examination of a subset in the depth range 6.5-10.5 m showed a background level of ϵ

which was more than an order of magnitude larger than expected from wind stress scaling (only 16% of the values of ϵ were within a factor of 3 of $u_*^3/\kappa z$ while 62% of the values showed $\epsilon/(u_*^3/\kappa z) > 10$). This observation suggests that the near surface layer in this case is dominated by a background forcing which is completely inconsistent with wind stress scaling.

Decrease of the mean value of $\epsilon/(u_*^3/\kappa z)$ from values of $O(10)$ to values near unity with the increase in depth, and the accompanying narrowing of the distribution (section V.3.6), support a model of an OBL with a two layer structure: a surface layer on the order of k^{-1} (several tens of meters for a long swell) in which TKE is enhanced by waves, while beneath this layer either wind stress and/or convection are responsible for TKE production. Based on measurements of the velocity field in the upper meter of Lake Ontario, Kitaigorodskii et al. (1983) proposed a similar two layer structure: an upper layer, with thickness on the order of 10 times the rms wave height in which intense generation of turbulence by waves takes places, while below this region a constant stress layer is appropriate (note, however, that Kitaigorodskii et al. examined cases of active wind-wave generation for short fetches, i.e. swell was absent).

The influence of wave age on wave-turbulence interaction

Compared to the equilibrium phase, when the rate of energy lost by wave breaking balances the energy input by the wind, during the development phase of a wave field a relatively larger part of the wind energy might go into the wave field than is lost by wave breaking. Thus, during the growing phase of the wind-wave field, energy and momentum transfer from the wind to the OBL below the wind-waves may be less efficient and u_*, inferred from the wind speed at 10 m, may be an overestimate of the turbulence velocity

scale and result in overestimates of ϵ in the constant stress layer formulation. This argument provides an explanation for the lower than predicted ϵ values we observed during OR90 day 2 (Fig. V.1r), when winds stabilized after a period of rising, and during OR90 night 1 (Fig. V.1s), when winds were in the last phase of a rising trend.

Although this explanation seems plausible, it cannot explain the lower values of ϵ than predicted by $u_*^3/\kappa z$ observed during night 2 of OR90 (Fig. V.1t), when winds decreased during the second half of the night.

V.4.3. Comparison with recent measurements of ϵ in the presence of waves

Some recent experimental studies in the aquatic near surface zone showed ϵ to follow the predicted SL scaling, while others showed dissipation rates to be much larger. Vertical profiles of high-frequency temperature fluctuations were made by Dillon et al. (1981) in the neutrally stratified near surface layer of a reservoir, with no remotely-generated swell, when winds averaged 4.8 m s^{-1}, surface wave heights were 0.1-0.2 m, and occasional white-capping was observed. Dissipation rates, estimated from the high-frequency temperature profiles, followed $u_*^3/\kappa z$ rather well between 1-m depth and the base of the ML at about 6 m. However, from the surface to a depth of 1 m, turbulence was so intense that dissipation rates could not reliably be resolved. From data collected in a reservoir, when winds were between 2-6.5 m s^{-1}, Imberger (1985) suggested that ϵ followed the predicted z^{-1} decay in the upper 30% of the ML, although with a great deal of scatter. Soloviev et al. (1988, 1989), using a tethered free-rising profiler, made velocity microstructure measurements in the upper OBL during night under relatively calm conditions of wind speeds of 1.9 to 6.5 m s^{-1}, and wind-

waves ranging from ripples to 0.5 m in height and periods up to 4 sec and swells 0.5-1.0 m in height and periods of 6-7 sec. Dissipation rates, estimated from the vertical component of the turbulence velocity fluctuations, were near or just above $u_*^3/\kappa z$ in the depth range of a few centimeters to about 5 m. Convection was found to play an appreciable role only at depths greater than 5 m. Lombardo and Gregg (1989) demonstrated that ϵ followed wind stress scaling when $1 > -D/L$ with a mean value of $\epsilon/(u_*^3/\kappa z)$ of 1.76 for $0.8 > -z/L > 0.15$ and depths greater than 5 m.

In direct contrast to the results described above, an increasing body of observations in the aquatic near surface zone shows that ϵ is often much larger than predicted by SL and/or ML scaling. Kitaigorodskii et al. (1983) measured TKE dissipation rates beneath wind-waves in Lake Ontario that were two orders of magnitude larger than $u_*^3/\kappa z$. Moreover, the depth dependence of ϵ was inconsistent with pure shear-produced turbulence, and the rms turbulence velocities had a strong dependence on wave energy which could not be explained by SL similarity theory. Kitaigorodskii and Lumley (1983) explored possible wave-turbulence interactions, suggesting that the term $-\overline{\partial(w'\frac{1}{2}\tilde{u}_i\tilde{u}_i)/\partial z}$, which appears in (18.1) for the TKE of an irrotational wave field, might explain the enhanced dissipation rates they observed. They argue that one of the mechanisms which can explain why w' and $\tilde{u}_i\tilde{u}_i$ may be correlated is associated with the process of wave-breaking in a random surface wave field. Breaking events increase the probability that the vertical turbulence velocity, w', is directed downwards, leading to a downward surface energy flux. An exponential fit to one data set (Kitaigorodskii et al. 1983) showed ϵ to be approximated very well by an exponential in z with a decay constant of $3k_p$, where k_p is the wavenumber of the peak of the

wave spectrum. This behaviour of ϵ appeared to be consistent with the parameterization of $\overline{w'\tilde{u}_i\tilde{u}_i}$ suggested by Kitaigorodskii and Lumley (1983).

Dissipation rates in a strongly convecting ML (Gregg 1987), showed that although ML similarity scaling described ϵ well in the convective regime deep in the ML, it failed closer to the surface. Intense near-surface dissipation rates, with averages several decades larger than the sum of J_b^0 and $u_*^3/\kappa z$, extended as deep as 30 m. Below this depth ϵ decreased abruptly to levels approximating J_b^0. Gregg suggested that at least one of the following mechanisms: convective plumes, breaking surface waves, or Langmuir cells, were responsible for producing the intense dissipation rates. From data collected in the northeast Pacific throughout a week and a half of intermittently stormy weather, and over a wide range of wind forcing, Gargett (1989) presented vertical profiles of ϵ near the surface that consistently showed a depth dependence closer to z^{-4} than the predicted z^{-1}. However, during the last day of the experiment, when wind speed and sea state decreased, ϵ showed an approximate z^{-1} dependence. Gargett stated that "although fragmentary data suggest that there may be times when the OBL can be described by a constant-stress layer, unfortunately these times may not coincide with the times when the bulk of the stress-driven air-sea transport occurs".

Osborn et al. (1992) reported results from measurements near the ocean surface during weakly convective conditions, mean winds of 5-9 m/s and waves of 4 s period, using submarine-mounted turbulence probes and sonars. They found values of ϵ in excess of 10 times those expected from SL and ML scaling and which were closely related to acoustically-detected bubble clouds generated by breaking waves. Dissipation rates from data acquired by three

different types of velocimeters during the WAVES program in Lake Ontario (Agrawal et al. 1992), showed ϵ to be highly intermittent. The background level of ϵ was close to values predicted by SL scaling, however, a fairly large number of dissipation estimates exceeded $u_*^3/\kappa z$ by more than an order of magnitude. The mode of the distribution of ϵ, which was approximately the value expected from SL scaling, corresponded to 1/5 of the mean. A possible explanation offered for the apparently different results reported by different investigators is the highly intermittent nature of wave breaking, which is poorly sampled by profiling devices.

To summarize the comparison of ϵ estimates from our studies and those discussed above, we plotted (Fig. V.7) the dissipation rates scaled by $u_*^3/\kappa z$ versus the depth scaled by u_*^2/g, in a manner consistent with the presentation of Soloviev et al. (1988). Vertically integrated dissipation rates in the OBL, $\epsilon_I = \int_{-D}^{0} \epsilon \, dz$, from different experiments, are compared to the wind power, $E_{10} = \tau_0 U_{10}$, in Fig. V.8. The solid line, adapted from an empirical fit by Oakey and Elliott (1982), estimates that about 1% of E_{10} is dissipated in the OBL. Although this estimate seems to work well for OBLs obeying SL scaling, quite a few of the data lie above this line with representative values of ϵ_I on the order of 10% of E_{10}. In this context it is of interest to note that Richman and Garrett (1977), using field and laboratory experiments in combination with a model of momentum and energy transfer by the wind to the ocean, estimated an input to the ocean of $4 - 9\%$ of E_{10} (including the energy that goes into wave breaking). Figs. V.7 and V.8 support the conclusion that we cannot ignore the many cases where simple SL scaling grossly underestimates the observed TKE dissipation rates in the near surface layer. Even if enhanced dissipation levels prove to be relatively scarce, the

physics needs to be resolved since such events frequently dominate the overall average dissipation rate.

V.5. Conclusions

Extensive measurements of turbulence in the OBL were made using a vertical profiling instrument. These covered a wide range of atmospheric forcing and sea states. Some of our experiments showed that $\epsilon \sim u_*^3/\kappa z$, even in slightly stably stratified layers. This seemed to be true even when short wind-waves were breaking and whitecapping activity was observed but swell was absent. In this case the absence of long waves excludes the possibility of the existence of an effective mechanism of downward transport of TKE produced by wave breaking near the surface. Dissipation rate estimates in the well-mixed part of the nighttime convective OBL ($2L > z > -D$) followed ML similarity scaling with nightly mean values of ϵ/J_b^0 ranging between 0.69 and 0.87 and an overall mean value of 0.81 (Anis and Moum 1992 [chapter III]). A closer inspection of ϵ/J_b^0 as a function of depth indicated that ϵ/J_b^0 decreased linearly with z/D in the ML, away from the OSL and the entrainment zone (Anis and Moum 1993b [chapter IV]). During convective periods the stability parameter, $-D/L$, varied between 3.9 and 6.7, which is relatively low when compared to the convective ABL where typical values of $-D/L$ are on the order of 100.

On the other hand, some of our observations showed dissipation rates larger (by one to two orders of magnitude) than predicted for TKE produced solely by surface wind stress and buoyancy flux. The enhanced dissipation rates reached depths up to about 25 m in the nighttime superadiabatic OSL and the slightly stable daytime OBL during the TH2 experiment. Similarly, enhanced levels of ϵ were observed to a depth of about 12 m in the neutrally stratified OBL during the first night of the OR89 experiment. This suggests enhanced mixing in the near surface layer of the ocean when compared to

the ASL, and is consistent with the smaller than predicted nondimensional temperature gradients observed in the nighttime OSL and in the upper part of the OBL during daytime. The presence of swell in conjunction with wind-waves, and the fact that the depth dependence of $\epsilon(z)$ was close to exponential with a decay rate on the order of the inverse wavenumber of the swell, suggest wave-related turbulence in the upper part of the OBL.

Two scenarios are suggested as possible explanations for the enhanced dissipation rates :

i) As a result of surface wave breaking, high levels of TKE are produced in a thin surface layer on the order of the height of the breaking waves. Turbulence is then transported downward by the motion of the swell, while probably decaying with time and diffusing spatially. This results in the divergence $-\partial(\overline{\tilde{w}\frac{1}{2}u_i'u_i'})/\partial z$ to assume positive values. If this divergence term is balanced by the TKE dissipation rate, an upper bound $\epsilon(z) < 3 \times 10^{-6} a_s g^{1/2} k_s^{3/2} {C_w}^2 \exp(k_s z)$ is found, where the exponential depth decay is due to the vertical swell velocity. The actual depth decay of ϵ will be greater than $\exp(k_s z)$ if spatial diffusion and dissipation of turbulence are significant over a wave period; and in the stable case also due to destruction of TKE by buoyancy forces. Independent estimates we made of the energy lost by breaking surface waves were consistent with the vertically integrated dissipation rates.

ii) If the wave field is rotational, as has been suggested by many studies, an additional mechanism of TKE production via wave-stresses might be possible. Kinetic energy, transferred from the wave field to the mean field via the wave production term, $-\overline{\tilde{w}\tilde{u}}\partial\overline{U}/\partial z$, can in turn be drawn from the mean field by turbulence via the turbulence production term,

$-\overline{w'u'}\partial\overline{U}/\partial z$. It is suggested that $\epsilon \approx \frac{1}{2}a^2gk\exp(2kz)\sin\phi\partial\overline{U}/\partial z$, resulting from the balance between the turbulence Reynolds stress, $-\overline{w'u'}$, and the wave stress, $\overline{\tilde{w}\tilde{u}}$. Only a small departure from quadrature ($\phi \sim O(1^0)$ on average) is needed to account for the enhanced levels of ϵ we observed.

Although physically different, both processes may affect the near surface layer to a depth on the order of k^{-1} (some tens of meters for a long swell). Beneath this layer either SL or ML similarity scalings, or a combination of the two, may be more appropriate. The suggested two layer structure of the OBL is consistent with the observed statistical behaviour of $\epsilon/(u_*^3/\kappa z)$: data for which mean profiles showed $\epsilon/(u_*^3/\kappa z) \gg 1$, revealed a background level of ϵ near the surface ($6.5-10.5$ m) which was more than an order of magnitude larger than the expected wind stress estimates. However, background levels of ϵ approached $u_*^3/\kappa z$ with the increase in depth, consistent with a wind stress driven layer beneath the layer affected by waves.

Due to the limitations of vertical profiling, which are at best snapshots of the variables we measure in the water column, and because of the intermittent nature of turbulence, statistically significant results will need very large data sets. It is for future work to combine vertical with horizontal profiling or moored measurements, under a variety of sea states, to test the hypothetical mechanisms suggested here and to determine the conditions for which different scaling laws for turbulence hold true.

Acknowledgments. We are grateful to the Captains and crews of the R/V *Wecoma* and CSS *Vector* for their efforts during the experimental phase of this study and to Ann Gargett, who agreed to allow us ship time in the midst of another experiment to obtain the BC90 data set. Long and helpful

discussions with Dave Hebert over the course of this work and comments on an earlier version of this paper by Laurie Padman are acknowledged. This work was funded by the National Science Foundation (OCE-8608256 and OCE-8716719) and the Office of Naval Research (N00014-89J3211). A. A. was also supported by a personal grant from the Gerson Meerbaum Foundation for Oceanography, the Hebrew University of Jerusalem, Israel.

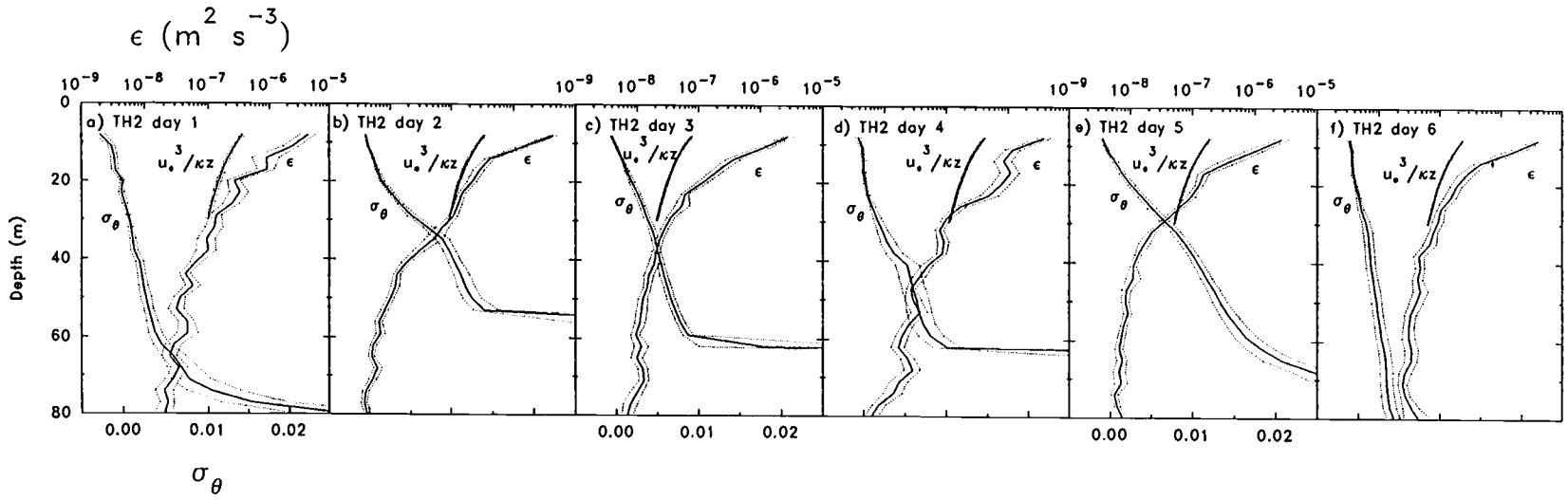

Figure V.1. Referenced and averaged profiles of potential density, σ_θ, and TKE dissipation rate, ϵ. σ_θ is defined as $\rho_w(s,\theta,0) - 1000$ kg m^{-3}, where ρ_w, the density of seawater at atmospheric pressure (i.e. $p = 0$), is given as a function of salinity, s, and potential temperature, θ. The effect of adiabatic heating or cooling is removed by using θ instead of the *in situ* temperature, and is useful when comparing fluid parcels at different depths. The number of profiles in each average, and atmospheric and sea-state conditions are presented in Tables V.1 and V.2. For comparison purposes, the influence of horizontal gradients was removed as follows: values of σ_θ (or θ for OR89) for single profiles were first referenced to their average value in the OBL and then depth binned and averaged. This is slightly different from the analysis presented by Anis & Moum (1992) where θ (considered for nightly profiles only) was referenced to its average value in the layer $-D < z < 2L$. Depth bins are 3 m for TH2 and 2 m for all other experiments. Also plotted are $u_*^3/\kappa z$ and the nighttime surface buoyancy flux, J_b^0 (see section V.4.1 for SL and ML scaling applicability). Dotted lines represent the 95% bootstrap confidence limits (Efron & Gong 1983). Note that the scales of the σ_θ axes are not the same for all experiments, although they are the same for each group within experiments.

a–f) Daytime profiles from TH2. In the upper 25 m ϵ is consistently larger than $u_*^3/\kappa z$. Data from depths shallower than 6.5 m were omitted due to possible contamination by the ship's wake.

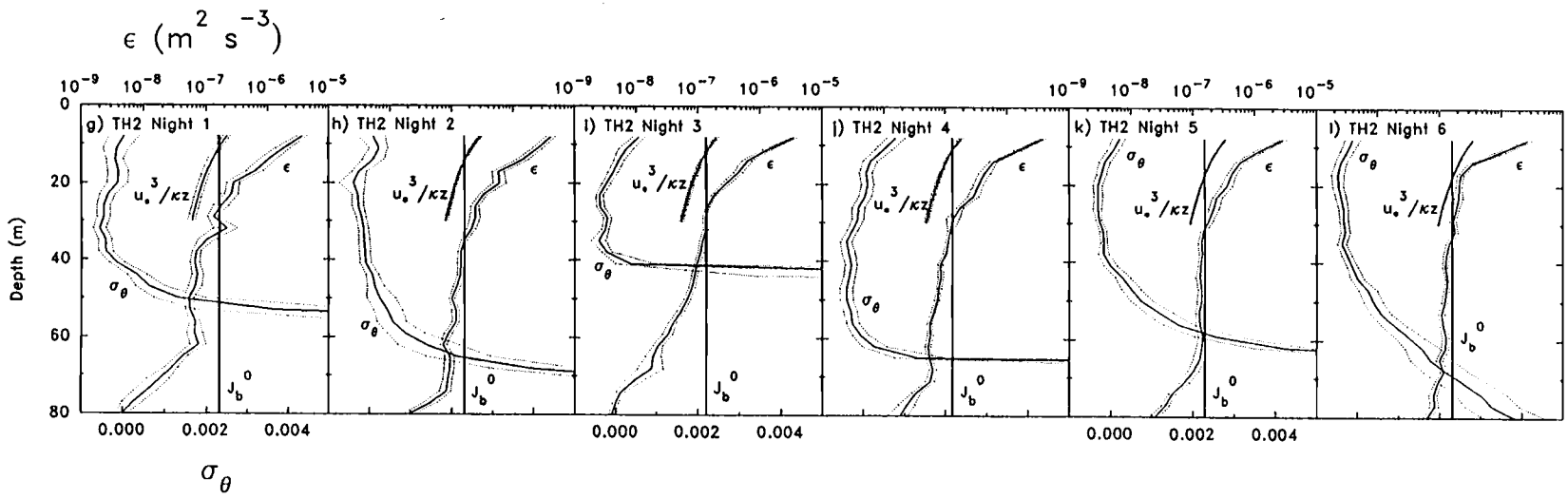

Figure V.1. (continued) g–l) Nighttime profiles from TH2. Although $\epsilon(z)$ is reasonably constant within the ML, it is not so in the OSL. $\epsilon(z)$ increases toward the surface at a rate greater than each or the sum of the production terms ($u_*^3/\kappa z$ and J_b^0). Data from depths shallower than 6.5 m were omitted due to possible contamination by the ship's wake.

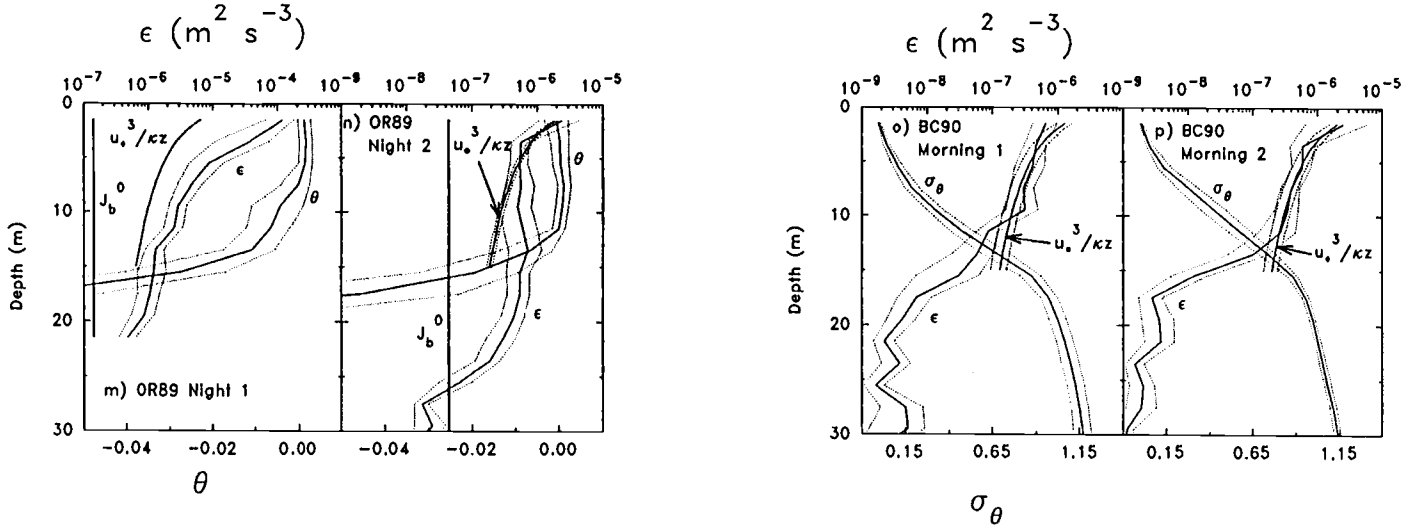

Figure V.1. (continued) m–n) OR89 profiles. No conductivity sensor was mounted on the profiler during this experiment, hence the referenced potential temperature (θ) profile is presented instead of σ_θ (a constant salinity value from conductivity measurements at 5 m depth was used in the calculation of θ). During night 1 (m), when winds and seas were high (Table V.1), the dissipation rate in the neutral OBL was larger than the wind stress production, $u_*^3/\kappa z$, while during night 2 (n), when conditions were moderate, $\epsilon(z)$ scaled with $u_*^3/\kappa z$ in the upper 10 m of the OBL. The somewhat higher values of ϵ near the base of the OBL during the second night, may be due to processes not related directly to wind forcing such as entrainment (note the different range of values of the ϵ axes for the two nights).

o–p) BC90 profiles. Although the OBL was relatively shallow (about 3 m; Table V.1), and $\epsilon(z)$ is not expected to follow SL scaling deeper than the base of the OBL (section V.4.1.1), we plotted $u_*^3/\kappa z$ to a depth of 15 m from curiosity reasons. This data set is distinctive from the other data sets by the fact that wind-wave breaking and whitecapping activity were observed while no swell was present.

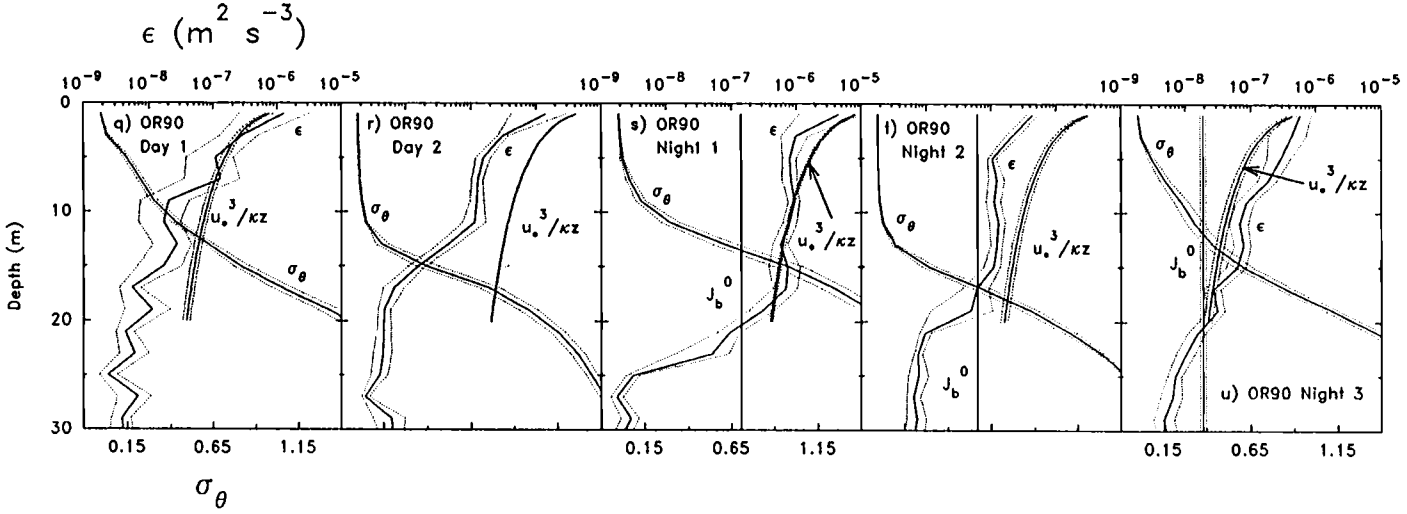

Figure V.1. (continued) q–u) OR90 profiles.

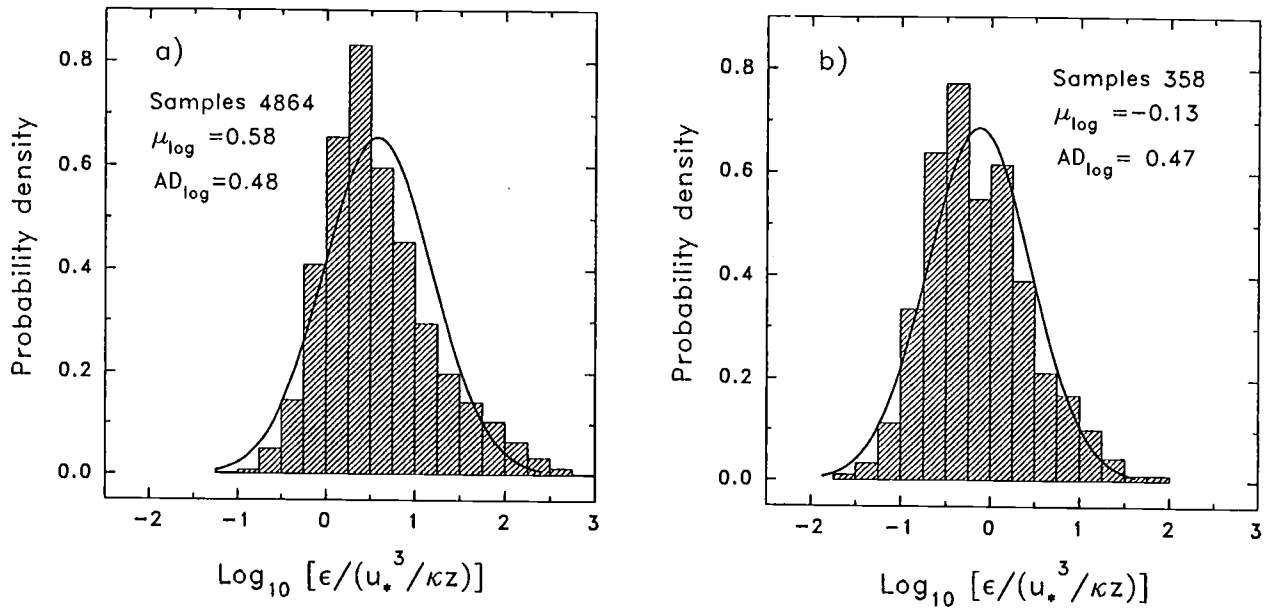

Figure V.2. Probability densities (hatched area) of $\epsilon/(u_*^3/\kappa z)$. The mean and standard deviation, $\mu_{\log}$ and $\sigma_{\log}$, respectively, of the observed distributions of $\log_{10}[\epsilon/(u_*^3/\kappa z)]$ were computed and used to superimpose lognormal distributions (solid lines). The average deviation of $\log_{10}[\epsilon/(u_*^3/\kappa z)]$, $\mathrm{AD}_{\log}$, is also cited (AD is defined in the caption of Table V.3).

a) 4864 samples from TH2 and OR89 night 1 for which mean profiles showed $\epsilon/(u_*^3/\kappa z) \gg 1$. TH2 data is from the depth interval -6.5 m $> z > -24.5$ m and OR89 night 1 data is from -0.5 m $> z > -D$. For this data set $\bar{\epsilon} = 31.61 \times 10^{-7}$ m^2 s^{-3}, and the median and average deviation of $\epsilon/\bar{\epsilon}$ are 0.12 and 1.40, respectively. The mean, median, and average deviation of $\epsilon/(u_*^3/\kappa z)$ are 13.64, 2.97, and 17.03.

b) 358 samples from OR89 night 2, BC90 mornings 1 and 2, and OR90 day 1 and nights 1 and 3 for which mean profiles showed $\epsilon/(u_*^3/\kappa z) \sim 1$. For this set $\bar{\epsilon} = 7.87 \times 10^{-7}$ m^2 s^{-3}, and the median and average deviation of $\epsilon/\bar{\epsilon}$ are 0.40 and 1.04, respectively. The mean, median, and average deviation of $\epsilon/(u_*^3/\kappa z)$ are 2.75, 0.42 and 3.64. Data used is from the depth interval -0.5 m $> z > -D$.

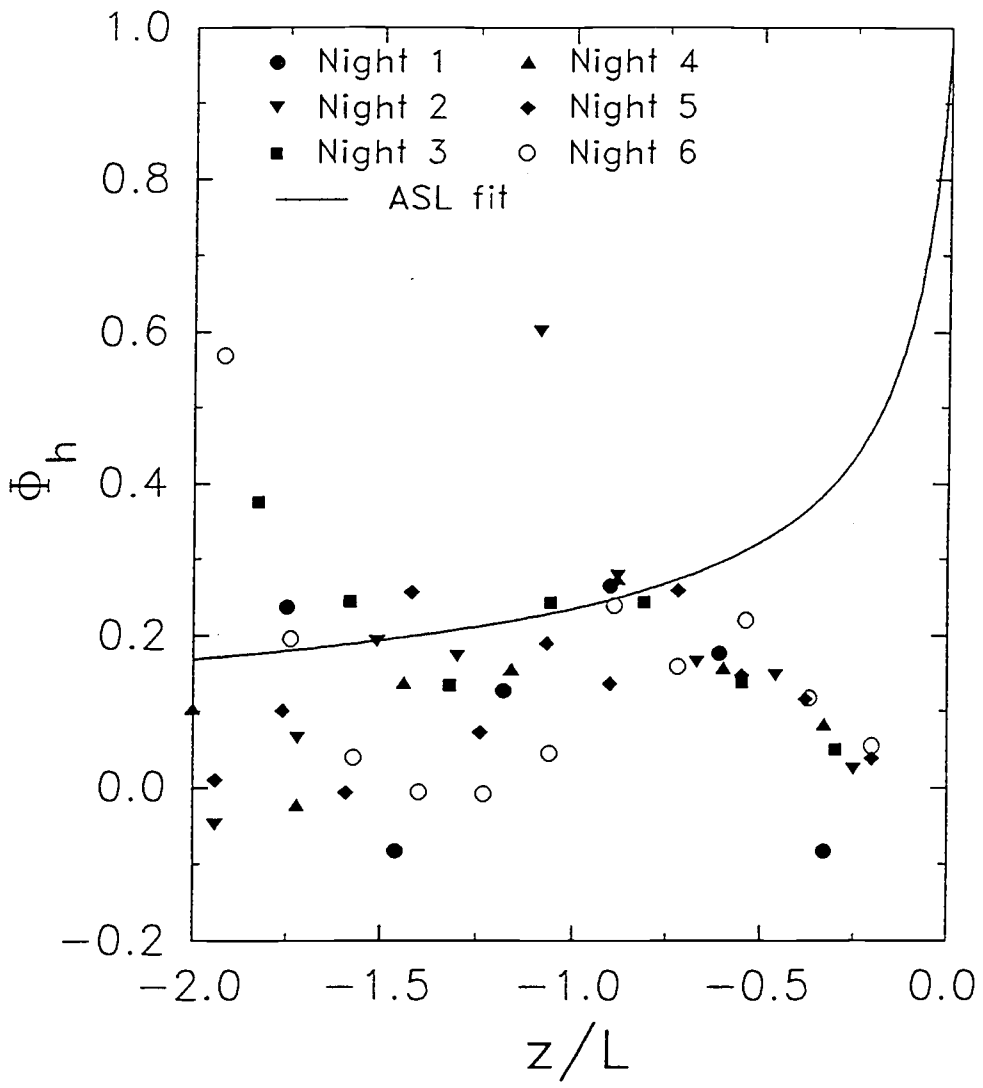

Figure V.3. Dimensionless vertical gradient of potential temperature, $\Phi_h \equiv (\kappa z/\theta_*)\overline{\theta_z}$, as a function of dimensionless depth, z/L. The symbols represent gradients of the nightly mean values of $\theta(z)$ observed in the OSL during TH2, and the solid line represents the relationship $\Phi_h = (1 - 16(z/L))^{-1/2}$ suggested by Dyer (1974) for the ASL during convection.

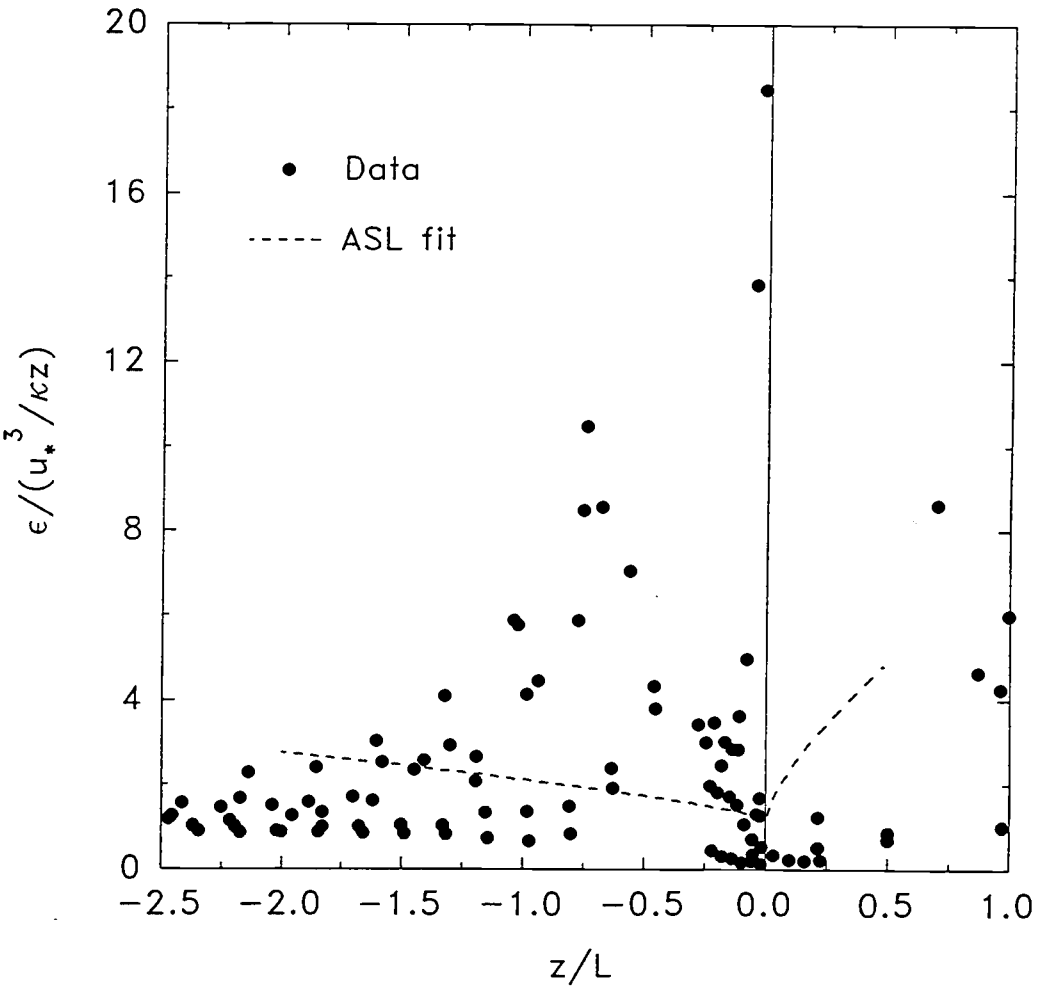

Figure V.4. $\epsilon/(u_*^3/\kappa z)$ as a function of z/L in the OBL, for all our experiments. Positive values of z/L represent stable conditions, while negative values represent unstable, i.e. convective, conditions. The vertical solid line represents neutral stability, when $z/L = 0$, and the dashed line is adapted from Wyngaard & Coté's (1971) fit to their data in the ASL. Although some of our oceanic data are close to the dashed line, a large number of data have values much larger compared to those in the ASL.

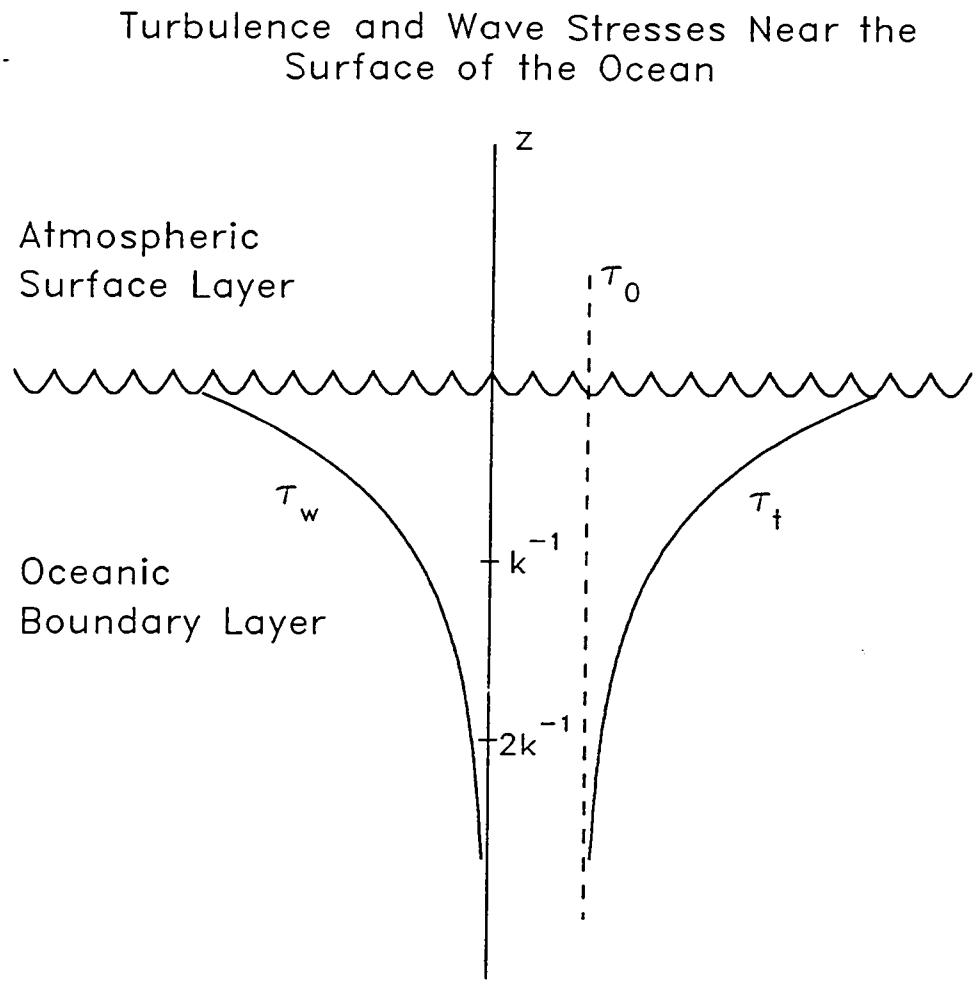

Figure V.5. Schematic depicting the stress balance, $\tau_t + \tau_w = \tau_0$, near the surface of the ocean allowing for wave generated stresses (see section V.4.2, equation 42). $\tau_t = -\rho_w \overline{w'u'}$ is the turbulence Reynolds stress, $\tau_w = -\rho_w \overline{\tilde{w}\tilde{u}}$ is the wave stress, and $\tau_0 = \rho_w C_D {U_{10}}^2$ is the wind stress calculated using U_{10}, the wind speed at 10 m height, and C_D is the drag coefficient. This balance does not violate the requirement of stress continuity across the air-sea interface. If this balance exists and can be modeled as in (45) then the depth decay of τ_t, or for that matter of τ_w, is exponential with a decay constant of $2k$ (the vertical scale is exaggerated to highlight the exponential depth decay).

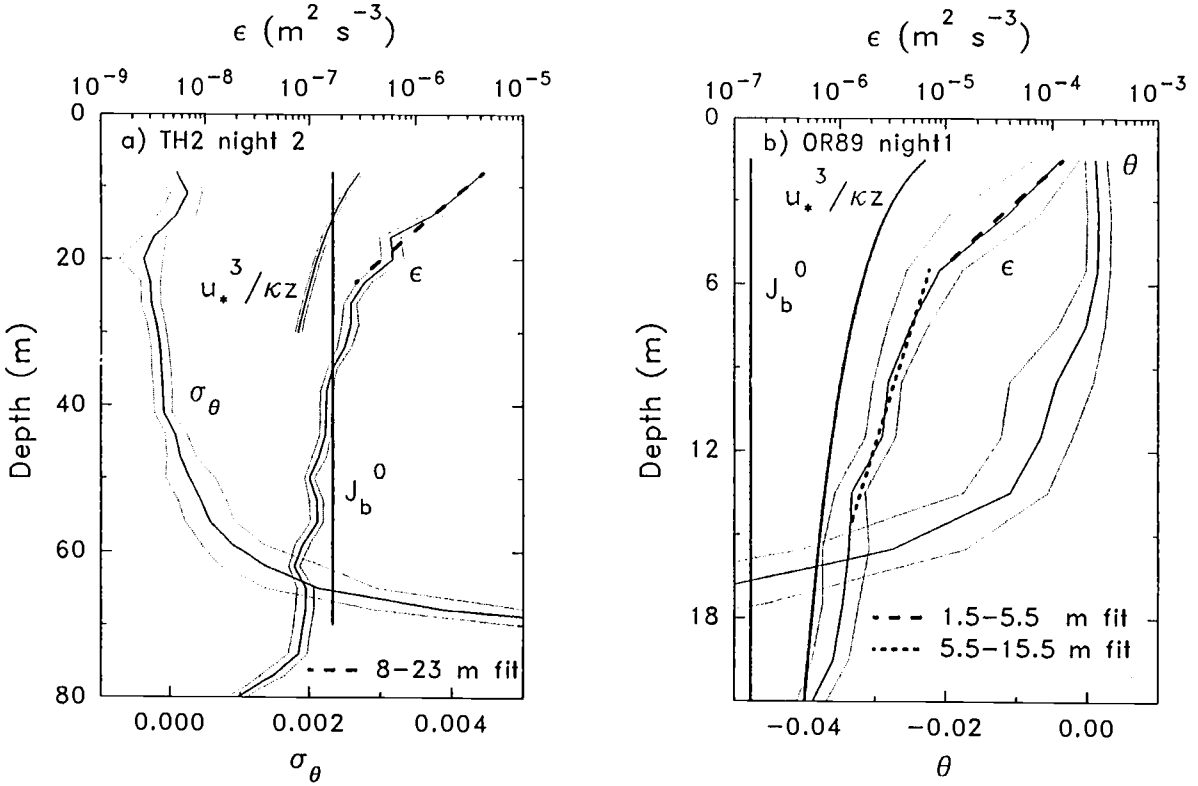

Figure V.6. Fit of the form $\epsilon(z) = \epsilon_0 \exp(\alpha z)$ to the estimated values of ϵ in the upper part of the OBL. For TH2 night 2 (a) a fit in the depth range 8-23 m (long dashes) results in $\epsilon_0 = 1.8 \times 10^{-5}$ m^2 s^{-3} and $\alpha = 0.18$ m^{-1}. In the depth range of the fit $\epsilon(z)$ is larger than predicted by either constant stress or convective scaling, or their sum. Below this depth $\epsilon(z) \sim J_b^0$ to the base of the ML ($\sim$ 70 m) where $\epsilon(z)$ decreases rapidly with depth. For OR89 night 1 (b), a fit in the depth range 1.5-5.5 m (long dashes) results in $\epsilon_0 = 2.9 \times 10^{-4}$ m^2 s^{-3} and $\alpha = 0.66$ m^{-1}, and a fit in the depth range 5.5-14.5 m (short dashes) results in $\epsilon_0 = 2.0 \times 10^{-5}$ m^2 s^{-3} and $\alpha = 0.18$ m^{-1}. Note that down to the base of the ML ($\sim$ 13 m) $\epsilon(z)$ is larger than predicted by constant stress layer scaling.

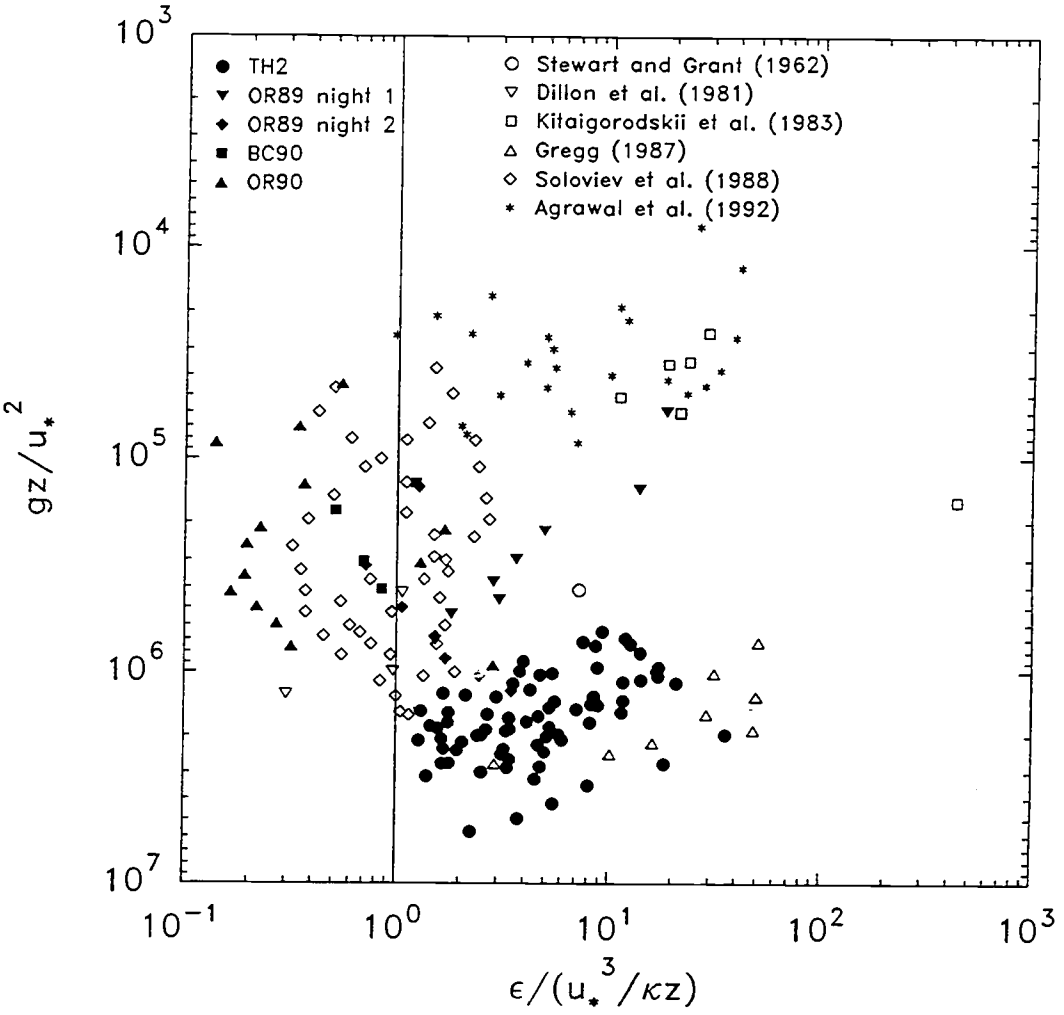

Figure V.7. Dimensionless dissipation rate, $\epsilon/(u_*^3/\kappa z)$, as a function of dimensionless depth, gz/u_*^2. The constant stress layer is represented by the vertical line $\epsilon/(u_*^3/\kappa z) = 1$. Data sets are labelled on the plot with their reference.

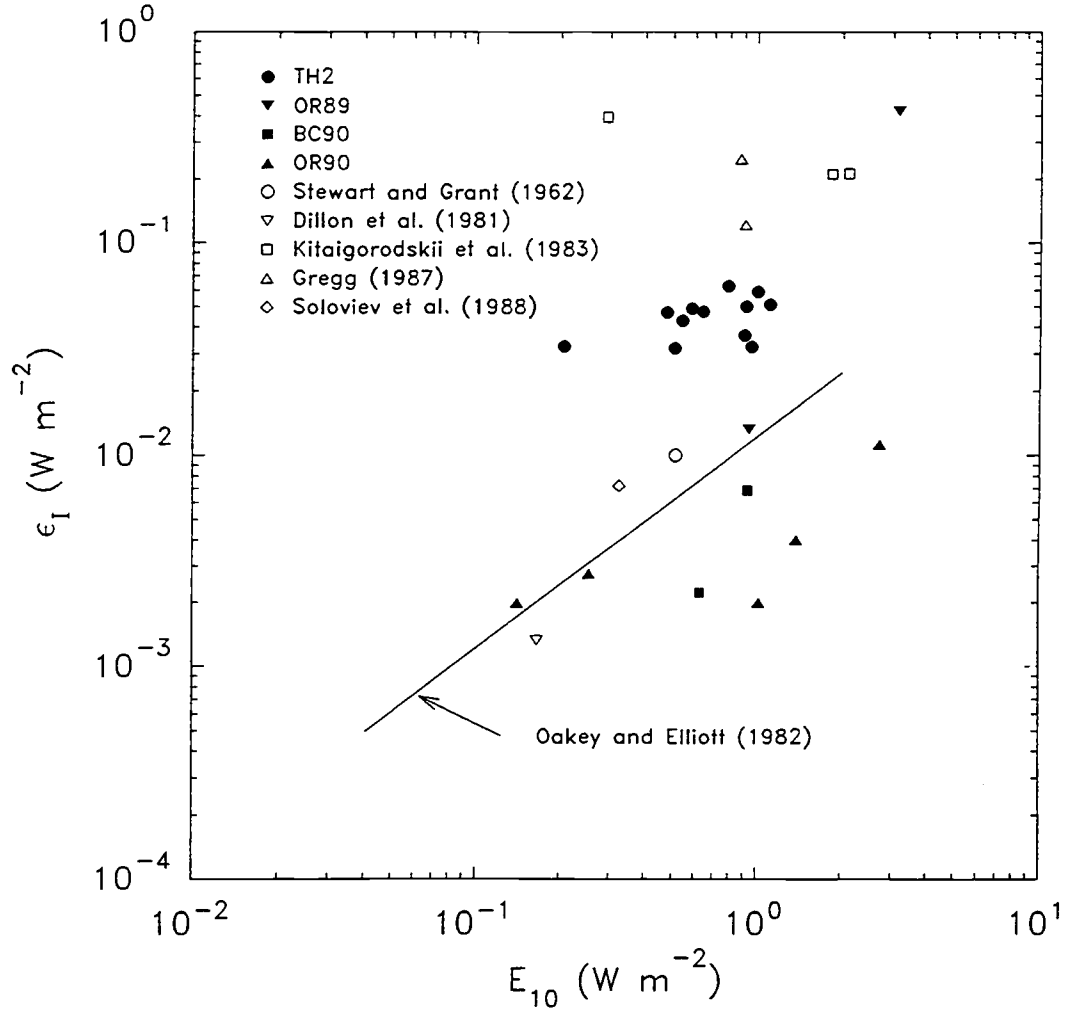

Figure V.8. Depth integrated dissipation rate in the OBL, ϵ_I, vs. wind power at 10 m height, $E_{10} = \tau_0 U_{10}$. Data sets are labelled according to their source. The solid line is adapted from Oakey & Elliott (1982) and indicates 1% of E_{10} dissipated in the ML. This prediction seems to work well for cases where ϵ scales as $u_*^3/\kappa z$; however, a number of data sets have dissipation rates on the order of 10% of E_{10}. Although the number of these cases may be relatively small, they need to be taken into account since average values of ϵ in the OBL may be completely dominated by the higher values.

Table V.1. Daytime and nighttime averaged values of the atmospheric and sea state conditions for the TH2, OR89, BC90, OR90 experiments. For TH2 the overall daytime and nighttime means are also presented. Surface wind stress, τ_0, surface heat flux J_q^0 (positive upward), and surface buoyancy flux, J_b^0 (positive upward), were determined from bulk aerodynamic formulae (Large & Pond 1981). The Monin-Obukhov length scale is defined as $L \equiv -u_*^3/\kappa J_b^0$, where $u_* \equiv \sqrt{\tau_0/\rho_w}$ is the friction velocity in water, ρ_w is the density of seawater, and $\kappa = 0.4$ is von Karman's constant; L is negative during convection. The significant wave height, H_s, and period, T (when given), for TH2, OR89, and OR90 are from R/V *Wecoma*'s ship's officers' log and are given for swell and wind waves. Meteorological parameters and significant wave heights for BC90 are from Pam Rocks wave buoy in Howe Sound. Wave periods during the experiment were less than 3 sec (14 m wavelength), which is the lower measurement limit of the wave buoy. No heat flux estimates could be made from the buoy's measurements.

	No. of profiles	τ $\mathrm{Nm^{-2}}$	J_q^0 $\mathrm{W\ m^{-2}}$	$10^7\ J_b^0$ $\mathrm{m^2\ s^{-3}}$	L m	Swell H_s (m), T (s)	Wind-waves H_s (m), T (s)
TH2							
day 1	15	0.12	−585	−3.8	8.0	2.4, –	0.7, –
day 2	40	0.11	−507	−3.6	7.9	2.4, –	0.9, –
day 3	48	0.04	−392	−2.8	2.3	1.7, –	0.6, –
day 4	17	0.12	−524	−3.7	9.2	1.9, –	0.9, –
day 5	29	0.07	−377	−2.9	5.9	2.2, –	0.9, –
day 6	20	0.09	−230	−1.7	11.4	2.1, –	0.9, –
mean		0.08	−428	−3.1	6.5	2.1, –	0.8, –

Table V.1. (continued)

	No. of profiles	τ Nm^{-2}	J_q^0 $W\ m^{-2}$	$10^7\ J_b^0$ $m^2\ s^{-3}$	L m	Swell H_s (m), T (s)	Wind-waves H_s (m), T (s)
TH2							
night 1	25	0.08	212	1.6	−10.6	2.4, –	0.8, –
night 2	42	0.10	211	1.7	−14.2	2.7, –	0.9, –
night 3	78	0.08	171	1.4	−11.7	2.0, –	0.7, –
night 4	83	0.07	166	1.3	−10.8	1.8, –	0.6, –
night 5	75	0.11	205	1.5	−17.3	2.2, –	0.9, –
night 6	63	0.11	199	1.6	−17.5	2.1, –	0.9, –
mean		0.09	189	1.5	−13.9	2.1, –	0.8, –
OR89							
night 1	29	0.25	223	1.4	−67.7	3.0, 12 2.5, 6	1.0, 4 –
night 2	20	0.11	73	0.4	−63.0	2.0, 6 – 8	0.6, 4 – 5

Table V.1. (continued)

	No. of profiles	τ Nm^{-2}	J_q^0 $W\ m^{-2}$	$10^7\ J_b^0$ $m^2\ s^{-3}$	L m	Swell H_s (m), T (s)	Wind-waves H_s (m), T (s)
BC90							
morning 1	9	0.08	–	–	–	–	0.8, –
morning 2	21	0.11	–	–	–	–	1.2 – 0.6, –
OR90							
day 1	10	0.05	−32	−0.2	49.5	1.2 – 1.5, –	wavelets
day 2	9	0.14	−266	−1.7	31.1	1.8, 6	0.9, 4
night 1	9	0.23	197	1.4	−57.8	1.8 – 2.1, 5	0.9, 4
night 2	43	0.12	124	0.6	−49.8	2.1 – 1.8, 6	0.9 – 0.6, 4 – 3
night 3	40	0.03	42	0.2	−26.0	1.8, 7 – 8	0.3, 1 – 2

Table V.2. Daytime and nighttime values of OBL parameters for TH2, OR89, BC90, and OR90. D is the OBL thickness; D/L is a bulk stability parameter; $u_* \equiv \sqrt{\tau_0/\rho_w}$ is the ocean surface friction velocity; $\theta_* \equiv -J_q^0/\rho_w C_p u_*$ is the ocean surface temperature scale (C_p is the specific heat); $\overline{\theta_z}$ and $\overline{\sigma_{\theta_z}}$ are the mean vertical gradients of the potential temperature θ and the potential density σ_θ, respectively, and were evaluated by a linear regression to the curves of θ and σ_θ of each profile and then averaged for the day or the night (θ and σ_θ are defined in the caption of Fig. V.1); $-z/L$ is a surface layer stability parameter (positive, when $L > 0$, implies statically stable and negative, when $0 > L$, implies statically unstable); $\Phi_h \equiv (\kappa z/\theta_*)\overline{\theta_z}$ is a dimensionless temperature gradient; $\overline{S^2} = \overline{(\partial U/\partial z)^2 + (\partial V/\partial z)^2}$ is the squared shear computed from a linear regression to individual profiles of U and V over the depth interval -19.1 m $> z > -31.1$ m centered at a depth of 25.1 m and then averaged for the day or night; $\Phi_m \equiv (\kappa z/u_*)\sqrt{\overline{S^2}}$ is a dimensionless shear; $\int \rho\epsilon\, dz / \int (\rho u_*^3/\kappa z)\, dz$ is the ratio of the depth-integrated dissipation to the depth integrated wind stress production. $\overline{\theta_z}$, $\overline{\sigma_{\theta_z}}$, $\int \rho\epsilon\, dz / \int (\rho u_*^3/\kappa z)\, dz$, $-z/L$, and Φ_h were estimated for the depth interval -6.5 m $> z > -24.5$ m for TH2, and for the depth interval -0.5 m $> z > -D$ for all other experiments.

	D	D/L	$10^2 u_*$	$10^2\theta_*$	$10^4\overline{\theta_z}$	$10^4\overline{\sigma_{\theta_z}}$	$10^6\overline{S^2}$	$-z/L$	Φ_h	Φ_m	$\frac{\int \rho\epsilon\, dz}{\int (\rho u_*^3/\kappa z)\, dz}$
	m		m s^{-1}	K	K m^{-1}	kg m^{-4}	s^{-2}				
TH2											
day 1	63.4	7.9	1.06	1.35	5.14	−1.90	8.8	0.8—3.1	0.10—0.37	2.75	7.0
day 2	26.7	3.4	1.03	1.20	7.04	−2.12	17.1	0.8—3.1	0.15—0.57	4.00	5.6
day 3	29.5	12.8	0.63	1.53	7.93	−2.16	3.4	2.8—10.7	0.13—0.51	2.96	16.6
day 4	41.4	4.5	1.10	1.17	4.15	−1.18	17.2	0.7—2.7	0.09—0.35	3.82	5.6
day 5	24.7	4.2	0.85	1.09	8.88	−2.64	12.4	1.1—4.2	0.21—0.80	4.20	6.6
day 6	64.7	5.7	0.91	0.62	1.90	−0.72	4.2	0.6—2.1	0.08—0.30	2.19	7.9
mean	36.4	7.0	0.88	1.21	6.54	−1.87	9.7	1.0—3.8	0.14—0.53	3.39	9.3

Table V.2. (continued)

	D	D/L	$10^2 u_*$	$10^2 \theta_*$	$10^4 \overline{\theta_z}$	$10^4 \overline{\sigma_{\theta_z}}$	$10^6 \overline{S^2}$	$-z/L$	Φ_h	Φ_m	$\frac{\int \rho \epsilon \, dz}{\int (\rho u_*^3/\kappa z) \, dz}$
	m		m s^{-1}	K	K m^{-1}	kg m^{-4}	s^{-2}				
TH2											
night 1	64.4	−6.7	0.89	−0.58	−1.70	0.26	6.2	−2.3— −0.6	0.08—0.29	2.80	10.0
night 2	68.5	−5.0	0.98	−0.53	−2.68	0.43	4.3	−1.7— −0.5	0.13—0.50	2.11	9.2
night 3	50.6	−4.6	0.87	−0.48	−2.12	0.67	1.3	−2.1— −0.6	0.11—0.43	1.29	8.8
night 4	67.5	−6.7	0.83	−0.49	−1.82	0.65	1.2	−2.3— −0.6	0.10—0.36	1.33	10.9
night 5	64.3	−3.9	1.02	−0.49	−1.67	0.45	2.8	−1.4— −0.4	0.09—0.34	1.62	4.8
night 6	82.2	−3.9	1.04	−0.47	−1.60	0.36	1.6	−1.4— −0.4	0.09—0.34	1.22	3.7
mean	65.1	−5.3	0.94	−0.49	−1.91	0.50	2.3	−1.8— −0.5	0.10—0.38	1.55	7.7
OR89											
night 1	13.5	−0.24	1.57	−0.35	8.07	—	—	−0.24— −0.01	0.05—1.26	—	13.0
night 2	14.5	−0.31	1.04	−0.17	3.23	—	—	−0.31— −0.01	0.04—1.08	—	1.3

Table V.2. (continued)

	D m	D/L	$10^2 u_*$ m s^{-1}	$10^2 \theta_*$ K	$10^4 \overline{\theta_z}$ K m^{-1}	$10^4 \overline{\sigma_{\theta_z}}$ kg m^{-4}	$10^6 \overline{S^2}$ s^{-2}	$-z/L$	Φ_h	Φ_m	$\frac{\int \rho\epsilon\, dz}{\int (\rho u_*^3/\kappa z)\, dz}$
BC90											
morning 1	3.7	—	0.91	—	—	−13.51	—	—	—	—	0.5
morning 2	3.6	—	1.06	—	—	−13.89	—	—	—	—	1.0
OR90											
day 1	2.1	0.06	0.67	0.12	38.81	−23.89	—	0.01—0.06	0.67—2.80	—	1.9
day 2	7.7	0.25	1.18	0.55	28.68	−10.08	—	0.02—0.25	0.10—1.60	—	0.3
night 1	4.1	−0.07	1.49	−0.32	35.21	−16.08	—	−0.07— −0.01	0.22—1.78	—	0.5
night 2	10.1	−0.27	1.08	−0.28	12.08	−2.99	—	−0.27— −0.01	0.09—1.73	—	0.2
night 3	3.7	−0.24	0.56	−0.18	15.02	−3.89	—	−0.24— −0.02	0.16—1.22	—	1.8

Table V.3. Columns 4 and 5 are statistics of $X = \epsilon/\bar{\epsilon}$, the TKE dissipation rate normalized by its mean value for the respective data set. Columns 6-8 are statistics of $X = /(\kappa z\epsilon/u_*^3)$, the TKE dissipation rate normalized by wind stress scaling. The median is the value X_{med} for which larger and smaller values of X are equally possible. The average deviation (AD) (or mean absolute deviation) for a quantity X is defined by $ADev(x_1...x_N) = \frac{1}{N}\sum_{j=1}^{N}|x_j - \overline{x}|$, and is a more robust estimate of the variability around the mean than the standard deviation (Press et al. 1986).

Experiment	Depth interval	$10^7\bar{\epsilon}$	$\epsilon/\bar{\epsilon}$			$\kappa z\epsilon/u_*^3$	
	m	$m^2\ s^{-3}$	Median	AD	Mean	Median	AD
TH2 daytime	$6.5 - 24.5$	23.1	0.12	1.37	15.22	2.69	19.89
TH2 nighttime	$6.5 - 24.5$	23.9	0.15	1.35	12.86	3.00	15.84
TH2 all data	$6.5 - 24.5$	23.7	0.14	1.36	13.56	2.89	17.05
OR89 night 1	$0.5 - D$	247.0	0.12	1.37	6.38	1.72	7.53
OR89 night 2	$0.5 - D$	7.97	0.45	1.00	1.61	0.73	1.51
BC90 morning 1	$0.5 - D$	5.73	0.65	0.70	0.78	0.40	0.71
BC90 morning 2	$0.5 - D$	16.70	0.24	1.29	1.00	0.33	1.13
OR90 daytime	$0.5 - D$	5.35	0.32	1.14	0.31	0.17	0.25
OR90 nighttime	$0.5 - D$	6.02	0.14	1.44	1.83	0.16	2.92
OR90 all data	$0.5 - D$	5.95	0.17	1.41	1.66	0.16	2.62

Table V.4. Estimates of the rate of energy lost by wind-wave breaking, R, calculated from equations (35), (38), and (39), the depth integrated dissipation rates, $\int \rho\epsilon\, dz$, and the depth integrated wind stress production term $\int(\rho u_*^3/\kappa z)\, dz$ (all units are Wm^{-2}). There are three rows of estimates of R for each of the experiments tabulated. In the firts row we have used the wave parameters from R/V *Wecoma*'s ship's officers' log (Table V.1). Estimates of R in the second row are based on values of $\overline{T}$ and E as determined from the wind speed, U_{10}, and the formulation suggested by Longuet-Higgins (1969). Values of R in the third row are estimated from the relations between the wave parameters and U_{10} as suggested by Neumann & Pierson (1966). For OR89 night 1 we have added, in the fourth and fifth rows, estimates of R using the parameters of the two swells from *Wecoma*'s log (see also text). Values in the left column of the estimate based on equation (35) were calculated using $p = 2.4 \times 10^{-4}$, where $\beta = 1.5 \times 10^{-2}$ (Hasselmann et al. 1973)) was used, and those in the right column using $p = 13.9 \times 10^{-4}$, where $\beta = 1.9 \times 10^{-2}$ (Forristall 1981) was used. Values in the left column of the estimate based on equation (38) were calculated using $f(U_{10})$, the fraction of breaking waves as a function of U_{10}, as observed by Holthuijsen & Herbers (1986), and those in the right column using $f(U_{10})$ as observed by Thorpe & Humphries (1980). Values in the left and right columns of the estimate based on equation (39) were calculated using $\gamma = 0.1$ and $\gamma = 1.0$, respectively (Kitaigorodskii 1983). For TH2, $\int \rho\epsilon\, dz$ was evaluated between 0.5-24.5 m and the value of ϵ at a depth of 6.5 m was used also for depths shallower than 6.5 m (this represents a lower limit on the depth integrated dissipation rate). Tabulated are the overall mean values of daytime and nighttime, while in parentheses are the extreme values of the individual days and nights. For OR89, $\int \rho\epsilon\, dz$ was integrated between 0.5-13.5 m. For comparison with constant stress layer scaling, $\int(\rho u_*^3/\kappa z)\, dz$ was calculated for the same depth intervals for which $\int \rho\epsilon\, dz$ was calculated.

Table V.4. (continued)

Experiment	Energy lost by breaking R						$\int \rho\epsilon\, dz$	$\int(\rho u_*^3/\kappa z)\, dz$
	Eq. (35)		Eq. (38)		Eq. (39)			
TH2 daytime								
Wecoma's wind-waves	0.048	0.28	0.60	1.60	0.050	0.50	0.041 (0.031, 0.056)	0.008 (0.006, 0.013)
U_{10} (Longuet-Higgins 1969)	0.052	0.30	0.65	1.74	0.056	0.56		
U_{10} (Neumann & Pierson 1966)	0.089	0.52	1.12	2.98	0.045	0.45		
TH2 nighttime								
Wecoma's wind-waves	0.048	0.28	0.60	1.60	0.056	0.56	0.041 (0.031, 0.060)	0.008 (0.006, 0.011)
U_{10} (Longuet-Higgins 1969)	0.064	0.37	0.80	2.14	0.068	0.68		
U_{10} (Neumann & Pierson 1966)	0.110	0.64	1.37	3.66	0.055	0.55		
OR89 night 1								
Wecoma's wind-waves	0.075	0.44	1.25	6.89	0.16	1.56	0.362	0.033
U_{10} (Longuet-Higgins 1969)	0.30	1.72	4.96	27.28	0.31	3.13		
U_{10} (Neumann & Pierson 1966)	0.51	2.94	8.47	46.57	0.25	2.54		
swell 1 ($H_s = 3.0$ m, $T = 12$ s)	0.23	1.31	3.76	20.68	0.47	4.68		
swell 2 ($H_s = 2.5$ m, $T = 6$ s)	0.31	1.81	5.22	28.72	0.23	2.34		

VI. GENERAL CONCLUSIONS

In four studies presented in chapters II through V we have investigated several key features of the OBL with the aid of an extensive data set collected by vertically profiling the OBL between the surface and a depth of $\sim$ 100 m. The first three studies focused on the convective OBL while the fourth study investigated turbulence in the OBL during different atmosperic and sea state conditions. The major results are summarized in the following:

- A clear distinction exists between the convective OBL and the wind mixed OBL; the convective OBL appears to be the only truly well-mixed OBL while the wind mixed OBL is actually stratified (even if only weakly). This has implications for modeling and indicates that a "slab" model is a fair representation of the convective OBL but may be a rather poor representation of a wind stress forced OBL. In the wind stress driven OBL mechanically induced turbulence is relatively inefficient in redistributing the momentum introduced at the surface. However, in a convectively driven OBL the buoyancy produced turbulence is much more efficient in momentum mixing, possibly due to the large overturning convective eddies.

- The "slab" type behavior of the convective OBL is inferred from the steadiness of the vertical structure of potential temperature, i.e. $\partial(\partial\theta/\partial z)/\partial t = 0$, where θ is averaged over time periods larger than T_c, the convective time scale (i.e. the time for a complete convective overturn $O(1)$ hr). This "slab" type behavior is further supported by the vanishing shear of horizontal velocity in the bulk of the ML and the large increase in shear near the base of the ML. The well-mixed convective

OBL is unable to support any significant shear while, in contrast, the wind stress driven OBL is able to support a noticeable shear due to its stable stratification.

- The relatively sharp increase in shear observed near the base of the ML of the convective OBL, accompanied by the slight increase in TKE dissipation, suggests a simple TKE balance between shear production and destruction by buoyancy and viscous dissipation. Estimates of the heat flux at the base of the ML, using this simple balance, result in $J_q(-D) \approx -0.13 J_q^0$. Knowledge of the heat flux at the base of the ML is of crucial importance in "slab" models since it provides a closure condition for the ML equations and permits an estimate of the entrainment rate.

- It is shown that the turbulence heat flux in the convective OBL decreases linearly with depth and may be represented by $J_q(z) = J_q^0[1 + a_h(z/D)]$, where D is the ML depth and $a_h = 1.07 - 1.18$ with a mean of 1.13. The linear heat flux profile is in good agreement with results from laboratory studies, numerical models (for both the OBL and the ABL) and field studies in the convective ABL.

- The linear decrease with depth of $\epsilon(z/D)/J_b^0$ in the bulk of the ML of the convective OBL ($0.9 > -z/D > 0.4$), and the fact that a similar rate of decrease with depth of $J_b(z)/J_b^0$ is inferred independently, confirm that a simple TKE balance of the form $\epsilon(z/D) \sim J_b(z/D)$ exists in the bulk of the ML.

- An analysis, in which large-scale horizontal gradients are effectively removed, clearly identifies, for the first time, a persistent statically unstable superadiabatic surface layer in the upper part of the convective

OBL. The mean value of the potential temperature gradient in the superadiabatic layer is $\sim -2 \times 10^{-4}$ K m^{-1}. The existence of a superadiabatic OSL, in conjunction with previous results, indicates that the *mean* structure of potential temperature in the convective OBL resembles that of the ABL during convection.

- In some cases, in the vicinity of the ocean's surface, ϵ is closely balanced by the wind stress production of TKE. In contrast, some of our observations show dissipation rates larger (by one to two orders of magnitude) than predicted for TKE produced solely by surface wind stress and buoyancy flux. This suggests enhanced mixing in the near surface layer of the ocean when compared to the ASL, and is consistent with the smaller than predicted nondimensional temperature gradients observed in those cases in the upper part of the OBL. The presence of swell in conjunction with wind-waves, and the fact that the depth dependence of $\epsilon(z)$ is close to exponential with a decay rate on the order of the inverse wavenumber of the swell, indicates wave-related turbulence in the upper part of the OBL. It is suggested that wave related turbulence may affect the near surface layer to a depth on the order of k^{-1} (some tens of meters for a long swell). Beneath this layer either SL or ML similarity scalings, or a combination of the two, may be more appropriate.

- Two wave-turbulence models are suggested as possible explanations for the enhanced dissipation rates observed in the vicinity of the ocean's surface:

  i) As a result of surface wave breaking, high levels of TKE are produced in a thin surface layer on the order of the height of

the breaking waves. Turbulence is then transported downward by the motion of the swell, while probably decaying with time and diffusing spatially. This results in the divergence $-\partial(\overline{\tilde{w}\frac{1}{2}u_i'u_i'})/\partial z$ to assume positive values. If this divergence term is balanced by the TKE dissipation rate, an upper bound $\epsilon(z) < 3 \times 10^{-6} a_s g^{1/2} k_s^{3/2} {C_w}^2 \exp(k_s z)$ is found, where the exponential depth decay is due to the vertical swell velocity. The actual depth decay of ϵ will be greater than $\exp(k_s z)$ if spatial diffusion and dissipation of turbulence are significant over a wave period; and in the stable case also due to destruction of TKE by buoyancy forces. Independent estimates of the energy lost by breaking surface waves are consistent with the vertically integrated dissipation rates.

ii) If the wave field is rotational, as has been suggested by many studies, an additional mechanism of TKE production via wave-stresses might be possible. Kinetic energy, transferred from the wave field to the mean field via the wave production term, $-\overline{\tilde{w}\tilde{u}}\partial\overline{U}/\partial z$, can in turn be drawn from the mean field by turbulence via the turbulence production term, $-\overline{w'u'}\partial\overline{U}/\partial z$. It is suggested that $\epsilon \approx \frac{1}{2}a^2 g k \exp(2kz)\sin\phi\,\partial\overline{U}/\partial z$, resulting from the balance between the turbulence Reynolds stress, $-\overline{w'u'}$, and the wave stress, $\overline{\tilde{w}\tilde{u}}$. Only a small departure from quadrature ($\phi \sim O(1^0)$ on average) is needed to account for the enhanced levels of ϵ we observed.

- Predictions of the time dependent ML depth, $D(t)$, from consideration of convective forcing alone underestimate the observed ML depth. Wind related processes, such as wind stress, surface waves, and Langmuir

circulations, are suggested to balance the energy budget, and are shown to be consistent with the additional energy required. A simple estimate in terms of the wind power suggests that about $0.04E_{10}$ enter the OBL. From this $\sim 0.034E_{10}$ is effectively dissipated, while about $0.006E_{10}$ is available for mixing. Unfortunately our measurements cannot identify the dominating wind related mechanism, however, it is reasonable to expect that during moderate sea conditions a combination of these mechanisms needs to be considered.

BIBLIOGRAPHY

Agrawal, Y. C., E. A. Terray, M. A. Donelan, P. A. Hwang, A. J. Williams III, W. M. Drennan, K. K. Kahma, and S. A. Kitaigorodskii, 1992: Enhanced dissipation of kinetic energy beneath surface waves. *Nature*, **359**, 219-220.

Alexander, R. C., and J. W. Kim, 1976: Diagnostic model study of mixed-layer depths in the summer North Pacific. *J. Phys. Oceanogr.*, **6**, 293-298.

Anati, D., and H. Stommel, 1970: The initial phase of deep water formation in the Northwest Mediteranean during MEDOC '69, on the basis of observations made by "Atlantis II". *Cah. Oceanogr.*, **22**, 343-352.

André, J. C., G. De Moor, P. Lacarrère, G. Therry, and R. du Vachat, 1978: Modeling the 24-hour evolution of the mean and turbulent structures of the planetary buondary layer. *J. Atmos. Sci.*, **35**, 1861-1883.

André, J. C., and P. Lacarrère, 1985: Mean and turbulent structures of the oceanic surface layer as determined from one-dimensional, third-order simulations. *J. Phys. Oceanogr.*, **15**, 121-132.

Anis, A., and J. N. Moum, 1992: The superadiabatic surface layer of the ocean during convection. *J. Phys. Oceanogr.*, **22**, 1221-1227.

Anis, A., and J. N. Moum, 1993a: Diurnal mixed layer deepening. Submitted to *J. Geophys. Res.*.

Anis, A., and J. N. Moum, 1993b: Prescriptions for the heat flux and entrainment rates in the upper ocean during convection. Submitted to *J. Phys. Oceanogr.*.

Anis, A., and J. N. Moum, 1993c: Scaling $\epsilon(z)$ near the surface of the ocean. Submitted to *J. Fluid Mech.*

Assaf, G., R. Gerard, and A. L. Gordon 1971: Some mechanisms of oceanic mixing revealed in aerial photographs. *J. Geophys. Res.*, **76**, 6550-6572.

Banner, M. L., and D. H. Pregrine, 1993: Wave breaking in deep water. *Annu. Rev. Fluid Mech.*, **25**, 373-397.

Benilov, A. Yu., 1973: Generation of ocean turbulence by surface waves. *Izv. Akad. Nauk. SSSR, Atmos. Ocean. Phys.*, **9**, 160-164.

Bliven, L. V., N. E. Huang, and S. R. Long, 1984: A laboratory study of the velocity field below surface gravity waves. In *Gas Transfer at Water Surfaces* (ed. W. Brutseart & G. H. Jirka). Reidel, 181-190.

Bowden, K. F., 1950: The effect of eddy viscosity on ocean waves. Phil. Mag., **41** No. 320, 907-917.

Brubaker, J. M., 1987 : Similarity structure in the convective boundary layer of a lake. *Nature*, **330**, 742-745.

Businger, J. A., J. C. Wyngaard, Y. Izumi, and E. F. Bradley, 1971: Flux-profile relationships in the atmospheric surface layer. *J. Atmos. Sci.*, **28**, 181-189.

Caldwell, D. R., T. M. Dillon, and J. N. Moum, 1985: The rapid sampling vertical profiler: an evaluation. *J. Atmos. Ocean. Technol.*, **2**, 615-625.

Caughey, S. J., and S. G. Palmer, 1979: Some aspects of turbulence structure through the depth of the convective boundary layer. *Quart. J. Roy. Meteor. Soc.*, **105**, 811-827.

Cavaleri, L., J. W. Ewing, and N. D. Smith, 1978: Measurements of the pressure and velocity field below surface waves. In *Turbulent Fluxes through the Sea Surface, Wave Dynamics, and Prediction* (ed. A. Favre & K. Hasselmann). Plenum, 257-272.

Cavaleri, L., and S. Zecchetto, 1985: Reynold Stresses. In *The Ocean Surface* (ed. Y. Toba & H. Mitsuyasu). Reidel, 443-448.

Cheung, T. K., 1985: A study of the turbulent layer in the water at an air-water interface. *Technical Report No. 287*, Department of Civil Engineering, Stanford University.

Cheung, T. K., and R. L. Street, 1988: The turbulent layer in the water at an air-water interface. *J. Fluid Mech.*, **194**, 133-151.

Churchill, J. H., and G. T. Csanady, 1983: Near surface measurements of quasi-Lagrangian velocities in open water. *J. Phys. Oceanogr.*, **13**, 1669-1680.

Clarke, R. A., and J.-C. Gascard, 1983: The formation of Labrador sea water. Part I: Large-scale processes. *J. Phys. Oceanogr.*, **13**, 1764-1778.

Deardorff, J. W., 1974: Three-dimensional numerical study of the height and mean structure of a heated planetary boundary layer. *Bound.-layer Meteor.*, **7**, 81-106.

Deardorff, J. W., 1983: A multi-limit mixed-layer entrainment formulation. *J. Phys. Oceanogr.*, **13**, 988-1002.

Deardorff, J. W., G. E. Willis, and D. K. Lilly, 1969: Laboratory investigation of non-steady penetrative convection. *J. Fluid Mech.*, **31**, 7-31.

Deardorff, J. W., G. E. Willis, and B. H. Stockton, 1980: Laboratory studies of the entrainment zone of a convectively mixed layer. *J. Fluid Mech.*, **100**, 41-64.

Denman, K. L., 1973: A time-dependent model of the upper ocean. *J. Phys. Oceanogr.*, **3**, 173-184.

Denman, K. L., and M. Miyake 1973: Upper layer modification at ocean station *Papa*: observations and simulation. *J. Phys. Oceanogr.*, **3**, 185-1954.

Dillon, T. M., J. G. Richman, C. G. Hansen, and M. D. Pearson, 1981: Near surface turbulence measurements in a lake. *Nature*, **290**, 390-392.

Dobroklonskiy, S. V., and B. M. Lesnikov, 1975: A laboratory study of the dynamic characteristics of drift currents in the presence of wind-driven waves. *Izv. Akad. Nauk. SSSR, Atmos. Ocean. Phys.*, **11**, 942-950.

Donelan, M., 1990: Air sea interaction. In *The Sea: Ocean Engineering Science*, vol. 9, part A, (ed. B. Le Mehaute & D. M. Hanes). J. Wiley and Sons Inc., New York, 239-292.

Dorrestein, R., 1979: On the vertical buoyancy flux below the sea surface as induced by atmospheric factors. *J. Phys. Oceanogr.*, **9**, 229-231.

Dyer, A. J., 1974: A review of flux-profile relationships. *Bound.-layer Meteorol.*, **7**, 363-372.

Driedonks, A. G. M., and H. Tennekes, 1984: Entrainment effects in the well-mixed atmospheric boundary layer. *Bound.-Layer Meteor.*, **30**, 75-105.

Efron, B., and G. Gong, 1983: A leisurely look at the bootstrap, the jacknife and cross-validation. *Amer. Statist.*, **37**, 36-48.

Forristall, G. Z., 1981: Measurements of a saturated range in ocean wave spectra. *J. Geophys. Res.*, **86**, 8075-8084.

Gargett, Ann E., 1989: Ocean Turbulence. *Ann. Rev. Fluid Mech.*, **21**, 419-451.

Garnich, N. G., and S. A. Kitaigorodskii, 1977: On the rate of deepening of the oceanic mixed layer. *Izv. Akad. Nauk. SSSR, Atmos. Ocean. Phys.*, **13**, 888-893.

Gascard, J.-C, and R. A. Clarke, 1983: The formation of Labrador sea water. Part II: Mesoscale and smaller-scale processes. *J. Phys. Oceanogr.*, **13**, 1779-1797.

Garwood, R. W. Jr., 1977: An oceanic mixed layer model capable of simulating cyclic states. *J. Phys. Oceanogr.*, **7**, 455-468.

Gibson, C. H., C. A. Friehe, and S. O. McConnel, 1977: Structure of sheared turbulent fields. *Phys. Fluids*, **20** (Suppl.), s156-167.

Gordon, A. L., 1970: Vertical momentum flux accomplished by Langmuir circulation. *J. Geophys. Res.*, **75**, 4177-4179.

Gregg, M. C. 1987: Structures and fluxes in a deep convecting mixed layer. In *Dynamics of the Oceanic Mixed Layer* (ed. P. Müller and D. Henderson). Hawaii Institute of Geophysics Special Publication 1987, 1-23.

Halpern, D., 1974: Observations of the deepening of the wind-mixed layer in the northeast Pacific Ocean. *J. Phys. Oceanogr.*, **4**, 454-466.

Hasselmann, K., T. P. Barnett, E. Bouws, H. Carlson, D. E. Cartwright, K. Enke, J. A. Ewing, H. Gienapp, D. E. Hasselmann, P. Krusemann, A. Meerburg, P. Müller, D. J. Olbers, K. Richter, W. Sell, and H. Walden, 1973: Measurements of wind-wave growth and swell decay during the Joint North Sea Wave Project (JONSWAP). *Dtsch. Hydrogr. Z.*, Suppl. **A8**, No. 12, 95 pp.

Haugen, D. A., J. C. Kaimal, and E. F. Bradley, 1971: An experimental study of Reynolds stress and heat flux in the atmospheric surface layer. *Quart. J. Roy. Meteor. Soc.*, **97**, 168-180.

Holthuijsen, L. H., and T. H. C. Herbers, 1986: Statistics of breaking waves observed as whitecaps in the open ocean. *J. Phys. Oceanogr.*, **16**, 290-297.

Holtslag, A. A. M., and F. T. M. Nieuwstadt, 1986: Scaling the atmospheric boundary layer. *Bound.-layer Meteorol.*, **36**, 201-209.

Huang, N. E., 1986: An estimate of the influence of breaking waves on the dynamics of the upper ocean. *Wave Dynamics and Radio probing of the Ocean Surface*, O. M. Phillips and K. Hasselmann, Eds., Plenum Press, 295-313.

Hussain, A. K. M. F., and W.C. Reynolds, 1970: The mechanics of an organized wave in turbulent shear flow. Part 2. Experimental results. *J. Fluid Mech.*, **41**, 241-258.

Imberger, J., 1985 : The diurnal mixed layer. *Limnol. Oceanogr.*, **30**, 737-770.

Jacobs, A. J., 1978: Numerical simulations of the natural variability in water temperature during BOMEX using alternative forms of the vertical eddy exchange coefficients. *J. Phys. Oceanogr.*, **8**, 119-141.

Jones, I. S. F., and B. C. Kenney, 1977: The scaling of velocity fluctuations in the surface mixed layer. *J. Geophys. Res.*, **82**, 1392-1396.

Joyce, Terrence M., and Marvel S. Stalcup, 1985: Wintertime convection in a Gulf Stream warm core ring. *J. Phys. Oceanogr.*, **15**, 1032-1042.

Kato, H., and O. M. Phillips, 1969: On the penetration of a turbulent layer into stratified fluid. *J. Fluid Mech.*, **37**, 643-655.

Khundzhua, G. G., A. M. Gusev, Ye. G. Andreyev, V. V. Gurov, and N. A. Skorokhvatov, 1977: Structure of the cold surface film of the ocean and heat transfer between the ocean and the atmosphere. *Izv. Atmos. and Oceanic Phys.*, (Engl. Transl.), **13**, 506-509.

Kitaigorodskii, S. A., 1961: On possibility of theoretical calculation of vertical temperature profile in upper layer of the sea. *Bull. Acad. Sci. USSR, Geophys. Ser.*, **3**, 313-318.

Kitaigorodskii, S. A., 1983: On the theory of the equilibrium range in the spectrum of wind-generated gravity waves. *J. Phys. Oceanogr.*, **13**, 816-827.

Kitaigorodskii, S. A., and J. L. Lumley, 1983: Wave-turbulence interactions in the upper ocean. Part I: The energy balance of the interacting fields of surface wind waves and wind-induced three-dimensional turbulence. *J. Phys. Oceanogr.*, **13**, 1977-1987.

Kitaigorodskii, S. A., M. A. Donelan, J. L. Lumley, and E. A. Terray, 1983: Wave-turbulence interactions in the upper ocean. Part 2: Statistical characteristics of wave and turbulent components of the random velocity field in the marine surface layer. *J. Phys. Oceanogr.*, **13**, 1988-1999.

Klein, Patrice, and Michel Coantic, 1981: A numerical study of turbulent processes in the marine upper layers. *J. Phys. Oceanogr.*, **11**, 849-863.

Lamarre, Eric, and W. K. Melville, 1991: Air entrainment and dissipation in breaking waves. *Nature*, **351**, 469-472.

Langmuir, I., 1938: Surface water motion induced by wind. *Science*, **87**, 119-123.

Large, W. G., and S. Pond, 1981: Open ocean momentum flux measurements in moderate to strong winds. *J. Phys. Oceanogr.*, **11**, 324-336.

Large, W. G., and S. Pond, 1982: Sensible and latent heat flux measurements over the open ocean. *J. Phys. Oceanogr.*, **12**, 446-462.

Leaman, K. D., and Schott F., 1991: Hydrographic structure of the convection regime in the Gulf of Lions: winter 1987. *J. Phys. Oceanogr.*, **21**, 574-598.

Leibovich, S., 1983: The form and dynamics of Langmuir circulations. *Ann. Rev. Fluid Mech.*, **15**, 391-427.

Leibovich, S., and S. Paolucci, 1980: The Langmuir circulation instability as a mixing mechanism in the upper ocean. *J. Phys. Oceanogr.*, **10**, 186-207.

Levitus, S., 1982: Climatological atlas of the world ocean, seasonal analyses. NOAA Professional Paper No. 13, Rockville, Md., December 1982 (on digital data tapes).

Lombardo, C. P., and M. C. Gregg, 1989: Similarity scaling of viscous and thermal dissipation in a convecting surface boundary layer. *J. Geophys. Res.*, **94**, 6273-6284.

Longuet-Higgins, M. S., 1969: On wave breaking and the equilibrium spectrum of wind-generated waves. *Proc. R. Soc. Lond.*, A**310**, 151-159.

Miropolskii, Y. Z., 1970: Nonstationary model of the wind-convection mixing layer in the ocean. *Izv. Akad. Nauk. SSSR, Atmos. Ocean. Phys.*, **6**, 1284-1294.

Morison, J. H., M. G. McPhee, T. B. Curtin, and C. A. Paulson, 1992: The oceanography of winter leads. *J. Geophys. Res.*, **97**, 11199-11218.

Moum, J. N., D. R. Caldwell, and C. A. Paulson, 1989: Mixing in the equatorial surface layer and thermocline. *J. Geophys. Res.*, **94**, 2005-2021.

Moum, J. N., M. C. Gregg, R. C. Lien, and M. E. Carr, 1994: Comparison of ϵ from two microstructure profilers. Submitted to *J. Atmos. Ocean Tech.*

Nasmyth, P., 1970: Oceanic turbulence. Ph.D. thesis. University of British Colombia, Vancouver, 69 pp.

Neumann, G., and W. J. Pierson Jr., 1966: *Principles of Physical Oceanography*. Prentice Hall, Inc., Englewood Cliffs, N. J., 545 pp.

Nicholls, S., and C. J. Readings, 1979: Aircraft observations of the structure of the lower boundary layer over the ocean. *Q. J. R. Met. Soc.*, **105**, 785-802.

Niiler, P. P., and E. B. Kraus, 1977: One-dimensional models of the upper ocean. *Modelling and Prediction of the Upper Layers of the Ocean*, E. B. Kraus, Ed., Pergamon Press, 143-172.

Ninnis, R., 1984: The effects of spatial averaging on airfoil probe measurements of oceanic velocity microstructure. Ph.D. thesis. University of British Colombia, Vancouver, 109 pp.

Oakey, N. S., 1982: Determination of the rate of dissipation of turbulent energy from simultaneous temperature and velocity shear microstructure measurements. *J. Phys. Oceanogr.*, **12**, 256-271.

Oakey, N. S., and J. A. Elliott, 1982: Dissiption within the surface mixed layer. *J. Phys. Oceanogr.*, **12**, 171-185.

Osborn, T. R., 1980: Estimates of the local rate of vertical diffusion from dissipation measurements. *J. Phys. Oceanogr.*, **10**, 83-89. Oakey, N. S., 1985: Statistics of mixing parameters in the upper ocean during JASIN phase 2. *J. Phys. Oceanogr.*, **15**, 1662-1675.

Osborn, T. R, and R. G. Lueck, 1985: Turbulence measurements from a towed body. *J. Atmos. Ocean. Technol.*, **2**, 517-527.

Osborn, T., D. M. Farmer, S. Vagle, S. A. Thorpe, and M. Cure, 1992: Measurements of bubble plumes and turbulence from a submarine. *Atmosphere-Ocean*, **30**, 419-440.

Park, M. M., J. N. Moum, D. R. Caldwell, and M. D. Brown, 1987: Tropic Heat II 1987-Leg 1 rapid sampling vertical profiler observations. *Ref. 87-22*, 378 pp., Coll. of Oceanogr., Oregon State Univ., Corvallis.

Paulson, C. A., and J. J. Simpson, 1981: The temperature difference across the cool skin of the ocean. *J. Geophys. Res.*, **86**, 11044-11054.

Payne, R. E., 1972: Albedo of the sea surface. *J. Atmos. Sci.*, **29**, 959-970.

Phillips, O. M., 1961: A note on the turbulence generated by gravity waves. *J. Geophys. Res.*, **66**, 2889-2893.

Phillips, O. M., 1977: *The Dynamics of the Upper Ocean.* Cambridge University Press, New York, 336 pp.

Pollard, R. T., 1977: Observations and theories of Langmuir circulations and their role in near surface mixing. In: *A voyage of discovery: G. Deacon 70th anniversary volume.* Ed M. Angel, Pergamon Press, New York, 235-251.

Press, W. H., B. P. Flannery, S. A. Teukolsky, and W. T. Vetterling, 1986: *Numerical Recipes.* Cambridge University Press, Cambridge, 818 pp.

Press, W. H., S. A. Teukolsky, W. T. Vetterling, and B. P. Flannery, 1992: *Numerical Recipes* (Second edition). Cambridge University Press, 963 pp.

Rapp, R. J., and W. K. Melville, 1990: Laboratory measurements of deep-water breaking waves. *Phil. Trans. R. Soc. Lond.*, A**331**, 735-800.

Richman, J., and C. Garrett, 1977: The transfer of energy and momentum by the wind to the surface mixed layer. *J. Phys. Oceanogr.*, **7**, 876-881.

Rohr, J., and C. Van Atta, 1987: Mixing efficiency in stably stratified growing turbulence. *J. Geophys. Res.*, **92**, 5481-5488.

Schott, F., and K. D. Leaman, 1991: Observations with moored acoustic Doppler current profilers in the convective regime in the Golfe du Lion. *J. Phys. Oceanogr.*, **21**, 558-574.

Shay, T. J., and M. C. Gregg, 1984a: Turbulence in an oceanic convective layer. *Nature*, **310**, 282-285.

Shay, T. J., and M. C. Gregg, 1984b: Turbulence in an oceanic convective layer (Corrigendum). *Nature*, **311**, 84.

Shay, T. J., and M. C. Gregg, 1986: Convectively driven turbulent mixing in the upper ocean. *J. Phys. Oceanogr.*, **16**, 1777-1798.

Shonting, D. H., 1964: A preliminary investigation of momentum flux in ocean waves. *Pure Appl. Geophys.*, **57**, 149-152.

Shonting, D. H., 1967: Measurements of particle motions in ocean waves. *J. Mar. Res.*, **25**, 162-181.

Shonting, D. H., 1968: Autospectra of observed particle motion in wind waves. *J. Mar. Res.*, **26**, 411-419.

Shonting, D. H., 1970: Observations of Reynolds stresses in wind waves. *Pure Appl. Geophys.*, **81**, 202-210.

Smith, J., R. Pinkel, and R. A. Weller, 1987: Velocity structure in the mixed layer during MILDEX. *J. Phys. Oceanogr.*, **17**, 425-439.

Soloviev, A. V., 1986: Dissipation of turbulent energy in the wind-generated wave layer of the ocean. *Izv. Akad. Nauk. SSSR, Atmos. Ocean. Phys.*, **22**, 286-292.

Soloviev, A. V., 1990: Coherent structures at the ocean surface in convectively unstable conditions. *Nature*, **364**, 157-160.

Soloviev, A. V., N. V. Vershinsky, and V. A. Bezverchnii, 1988: Small scale turbulence measurements in the thin surface layer. *Deep-Sea Res.*, **35**, 1859-1874.

Soloviev, A. V., N. V. Vershinsky, and V. A. Bezverchnii, 1989: Small scale turbulence measurements in the thin surface layer of the ocean (Corrigenda). *Deep Sea Res.*, **36**, 1283-1284.

Stewart, R. W., and H. L. Grant, 1962: Determination of the rate of dissipation of turbulent energy near the sea surface in the presence of waves. *J. Geophys. Res.*, **67**, 3177-3180.

Stull, R. B., 1976: The energetics of entrainment across a density interface. *J. Atmos. Sci.*, **33**, 1260-1267.

Stull, R. B., 1988: *An Introduction to Boundary Layer Meteorology.* Kluwer Academic Publishers, Dordrecht, 666 pp.

Swallow, J. C., and G. F. Caston, 1973: The preconditioning phase of MEDOC 1969–I. Observations. *Deep-sea Res.*, **20**, 429-448.

Tennekes, H., and J. L. Lumley, 1972: *A First Course in Turbulence.* The MIT Press, 300 pp.

Thorpe, S. A., 1984: On the determination of K_v in the near surface ocean from acoustic measurements of bubbles. *J. Phys. Oceanogr.*, **14**, 855-863.

Thorpe, S. A., 1985: Small scale processes in the upper ocean boundary layer. *Nature*, **318**, 519-522.

Thorpe, S. A., 1992: Bubble clouds and the dynamics of the upper ocean. *Q. J. R. Meteorol. Soc.*, **118**, 1-22.

Thorpe, S. A., and P. N. Humphries, 1980: Bubbles and breaking waves. *Nature*, **283**, 463-465.

Thorpe, S. A., M. Cure and M. White, 1991: The skewness of temperature derivatives in the oceanic boundary layers. *J. Phys. Oceanogr.*, **21**, 428-433.

Turner, J. S., 1969: A note on wind mixing at the seasonal thermocline. *Deep-sea Res.*, **16** (Suppl.), 297-300.

Turner, J. S., 1973: *Buoyancy Effects in Fluids*. Cambridge University Press, 368 pp.

Weller, R. A., and J. F. Price, 1988: Langmuir circulation within the oceanic mixed layer. *Deep-Sea Res.*, **35**, 711-747.

Willis, G. E., and J. W. Deardorff, 1974: A laboratory model of the unstable planetary boundary layer. *J. Atmos. Sci.*, **31**, 1297-1307.

Wyngaard, J. C., 1973: On surface layer turbulence. In *Workshop on Micrometeorology* (ed. P. M. Haugen). Amer. Meteor. Soc., Boston, Mass. 101-149.

Wyngaard, J. C. and O. R. Cote, 1971: The budgets of turbulent kinetic energy and temperature variance in the atmospheric surface layer. *J. Atmos. Sci.*, **28**, 190-201.

Wyrtki, K., and B. Kilonsky, 1984: Mean water and current structure during the Hawaii-to-Tahiti shuttle experiment. *J. Phys. Oceanogr.*, **14**, 242-254.

Yamazaki, H., R. G. Lueck, and T. Osborn, 1990: A comparison of turbulence data from a submarine and a vertical profiler. *J. Phys. Oceanogr.*, **20**, 1778-1786.

Yefimov, V. V., and G. N. Khristoforov, 1969: Some features of the velocity field in the layer of wind-driven swell. *Izv. Akad. Nauk. SSSR, Atmos. Ocean. Phys.*, **5**, 597-602.

Yefimov, V. V., and G. N. Khristoforov, 1971: Spectra and statistical relations between the velocity fluctuations in the upper layer of the sea and surface waves. *Izv. Akad. Nauk. SSSR, Atmos. Ocean. Phys.*, **7**, 841-851.

Young, George S., 1988: Turbulence structure of the convective boundary layer. Part I: variability of normalized turbulence statistics. *J. Atmos. Sci.*, **45**, 719-735.

Zhou, Ming Yu, D. H. Lenschow, B. B. Stankov, J. C. Kaimal, and J. E. Gaynor, 1985: Wave and turbulence structure in a shallow baroclinic convective boundary layer and overlying inversion. *J. Atmos. Sci.*, **42**, 47-57.

APPENDIX

APPENDIX

A lower limit on the phase shift from quadrature

Vertical integration of (46) from h, the bottom of the layer influenced by wave stresses, to the surface, results in

$$\int_h^0 \epsilon\, dz = \int_h^0 -\overline{w'u'}\frac{\partial \overline{U}}{\partial z}\, dz \approx \int_h^0 \frac{1}{2}a^2 gk \exp(2kz)\sin\phi \frac{\partial \overline{U}}{\partial z}\, dz. \qquad (A1)$$

assuming $\sin\phi$ to be constant, yields

$$\sin\phi \approx \frac{2\int_h^0 \epsilon\, dz}{\int_h^0 a^2 gk \exp(2kz)\frac{\partial \overline{U}}{\partial z}\, dz}. \qquad (A2)$$

but

$$\frac{\partial}{\partial z}(\exp(2kz)\overline{U}) = \exp(2kz)\frac{\partial \overline{U}}{\partial z} + 2k\exp(2kz)\overline{U}, \qquad (A3)$$

so that

$$\exp(2kz)\frac{\partial \overline{U}}{\partial z} = \frac{\partial}{\partial z}(\exp(2kz)\overline{U}) - 2k\exp(2kz)\overline{U} < \frac{\partial}{\partial z}(\exp(2kz)\overline{U}), \qquad (A4)$$

since $2k\exp(2kz)\overline{U} > 0$.

Hence

$$\int_h^0 \exp(2kz)\frac{\partial \overline{U}}{\partial z}\, dz < \int_h^0 \frac{\partial}{\partial z}(\exp(2kz)\overline{U})\, dz$$
$$= \exp(2kz)\overline{U}\Big|_h^0 = \overline{U}(0) - \exp(2kh)\overline{U}(h) < \overline{U}(0) \qquad (A5)$$

and substitution of A5 in A2 results in a lower limit on ϕ given by

$$\sin\phi > \frac{2\int_h^0 \epsilon\, dz}{a^2 gk\overline{U}(0)}. \qquad (A6)$$